AN EXPERIMENTAL INVESTIGATION ON UNIAXIAL TENSILE, SLIP-BOND AND CREEP BEHAVIOR OF CARBON TEXTILE REINFORCED CEMENTITIOUS COMPOSITES (C-TRCC)

A THESIS SUBMITTED TO
THE GRADUATE SCHOOL OF NATURAL AND APPLIED SCIENCES
OF
MIDDLE EAST TECHNICAL UNIVERSITY

BY

IRAJ SHARIFI

IN PARTIAL FULFILLMENT OF THE REQUIREMENTS
FOR
THE DEGREE OF DOCTOR OF PHILOSOPHY
IN
CIVIL ENGINEERING

JANUARY 2025

Approval of the thesis:

An Experimental Investigation on Uniaxial Tensile, Slip-Bond and Creep Behavior of Carbon Textile Reinforced Cementitious Composites (C-TRCC)

submitted by **Iraj Sharifi** in partial fulfillment of the requirements for the degree of **Doctor of Philosophy** i**n Civil Engineering, Middle East Technical University** by,

Prof. Dr. Naci Emre Altun
Dean, **Graduate School of Natural and Applied Sciences** _____

Prof. Dr. Erdem Canbay
Head of the Department, **Civil Engineering, METU** _____

Prof. Dr. İsmail Özgür Yaman
Supervisor, **Civil Engineering, METU** _____

Dr. Burhan Alam
Co-Supervisor, **Civil Engineering, METU** _____

Examining Committee Members:

Prof. Dr. Erdem Canbay
Civil Engineering, METU _____

Prof. Dr. İsmail Özgür Yaman
Civil Engineering, METU _____

Prof. Dr. Mustafa Şahmaran
Civil Engineering, Hacettepe University _____

Prof. Dr. Serdar Göktepe
Civil Engineering, METU _____

Prof. Dr. Özgür Anıl
Civil Engineering, Gazi University _____

Date: 16.01.2025

I hereby declare that all information in this document has been obtained and presented by academic rules and ethical conduct. I also declare that, as required by these rules and conduct, I have fully cited and referenced all material and results that are not original to this work.

Iraj Sharifi

Signature :

ABSTRACT

AN EXPERIMENTAL INVESTIGATION ON UNIAXIAL TENSILE, SLIP-BOND AND CREEP BEHAVIOR OF CARBON TEXTILE REINFORCED CEMENTITIOUS COMPOSITES (C-TRCC)

Sharifi Iraj
Doctor of Philosophy, Civil Engineering
Supervisor: Prof. Dr. İsmail Özgür Yaman
Co-Supervisor: Dr. Burhan Alam

January 2025, 177 pages

Textile reinforced cementitious composite (TCRC) is an innovative composite material consisting of a non-metallic fabric mesh reinforcement and a fine-grained cementitious mortar and has been used as a repair and strengthening material in reinforced concrete and masonry structures over the last two decades. This study particularly aims to investigate the mechanical properties of a flexible grid-like woven carbon (C-) textile with two different cementitious mortars; M7, commonly used in TRCC production, and M45, a specialized mortar developed for Engineered Cementitious Composites (ECC®) with the absence of short discrete PVA fibers. The research aims to provide a comprehensive investigation on the mechanical performance and long-term tensile creep performance of such C-TRCC systems.

A three-phase experimental program was conducted as part of this study. The first phase includes uniaxial direct tensile characterization and aims to understand the failure mechanisms of C-TRCC, focusing on the influences of yarn direction, reinforcement ratio, and mortar type. In the second phase, the slip bond performance of C-TRCC is evaluated with pull-out tests to determine the slip bond characteristics, focusing on the correlation between yarn direction, embedment lengths, yarn-mortar

interaction, and failure modes. In the third phase, the tensile creep behavior is evaluated under sustained loading applied at different temperatures (20ºC, and 50ºC).

Results revealed that the tensile performance of C-TRCC is significantly influenced by textile yarn architecture with warp yarns demonstrating higher tensile strength and failure resistance than weft yarns, attributed to their denser and more stable architecture. The slip-bond tests demonstrated a clear relationship between embedment length and pull-out load capacity, also underscores the importance of accurately characterizing textile geometry in order to reliably predict the developed shear strength within the C-TRCC. Finally, tensile creep tests under sustained loading and elevated temperatures (50°C) showed accelerated deformation, emphasizing the critical role of SBR coatings on yarns, which soften at higher temperatures, leading to reduced bonding performance.

Keywords: Textile Reinforced Cementitious Composites (TRCC), Carbon Textile, Uniaxial Tensile Behavior, Slip-Bond Characteristics, Tensile Creep.

ÖZ

KARBON TEKSTİL TAKVİYELİ ÇİMENTOLU KOMPOZİTLERİN (K-TTÇK) TEK EKSENLİ ÇEKME, KAYMA-BAĞ VE SÜNME DAVRANIŞININ DENEYSEL İNCELENMESİ

Sharifi, Iraj
Doktora, İnşaat Mühendisliği
Tez Yöneticisi: Prof. Dr. İsmail Özgür Yaman
Ortak Tez Yöneticisi: Dr. Burhan Alam

Ocak 2025, 177 sayfa

Tekstil takviyeli çimentolu kompozit (TTÇK), metalik olmayan bir kumaş örgü donatısı ve ince taneli çimentolu harçtan oluşan yenilikçi bir kompozit malzemedir ve son yirmi yılda betonarme ve yığma yapılarda bir onarım ve güçlendirme malzemesi olarak kullanılmaktadır. Bu çalışma özelinde, esnek ve ızgara benzeri bir dokuma ile üretilen karbon (K-) tekstilin iki farklı çimentolu harç ile birleştirilmesiyle elde edilen K-TTÇK'in mekanik özelliklerinin araştırılması hedeflenmiştir. K-TTÇK'in üretiminde, bu tür sistemlerde yaygın olarak kullanılan M7 harcı ile ve tasarlanmış çimentolu kompozitler (ECC®) için geliştirilmiş özel bir harç olan M45 baz alınmıştır. Araştırma, K-TTÇK sistemlerinin mekanik performansı ve uzun vadeli çekme sünmesi performansı hakkında kapsamlı bir inceleme yapmayı amaçlamaktadır.

Bu çalışma kapsamında üç aşamalı bir deneysel program yürütülmüştür. İlk aşama K-TTÇK'in tek eksenli doğrudan çekme karakterizasyonunu içermekte ve dokuma yönü, donatı oranı ve harç tipinin etkilerine odaklanarak K-TTÇK'in göçme mekanizmalarını anlamayı amaçlamaktadır. İkinci aşama, K-TTÇK'in kayma-bağ performansını, dokuma yönü, bağ dayanımı, dokuma-harç etkileşimi ve göçme

modları arasındaki korelasyona odaklanarak kayma-bağ özelliklerini belirlemek için çekme testleri ile değerlendirmektedir. Üçüncü ve son aşamada ise K-TTÇK'in farklı sıcaklıklarda (20ºC ve 50ºC) uygulanan sabit yükler altındaki çekme sünmesi altındaki davranışı incelenmiştir.

Sonuçlar, K-TTÇK'in çekme performansının tekstil donatısı mimarisinden önemli ölçüde etkilendiğini, çözgü ipliklerinin daha yoğun ve daha kararlı mimarilerine atfedilen atkı ipliklerine göre daha yüksek çekme mukavemeti ve kopma direnci gösterdiğini ortaya koymuştur. Kayma-bağ testleri, gömme uzunluğu ile çekme yükü kapasitesi arasında net bir ilişki olduğunu göstermiş, ayrıca K-TTÇK içinde oluşan bağ dayanımının güvenilir bir şekilde tahmin edilebilmesi için tekstil geometrisinin doğru bir şekilde karakterize etmenin önemini vurgulamıştır. Son olarak, sürekli yükleme ve yüksek sıcaklık (50°C) altında yapılan çekme sünmesi testleri, sünme deformasyonlarının artmasına neden olmuş ve yüksek sıcaklıklarda bozunarak yapışma performansının düşmesine neden olan SBR kaplamaların K-TTÇK performansı üzerindeki kritik rolünü vurgulamıştır.

Anahtar Kelimeler: Tekstil Takviyeli Çimentolu Kompozitler (TTÇK), Karbon Tekstil, Tek Eksenli Çekme Davranışı, Kayma-Bağ Özellikleri, Çekme Sünmesi

This thesis is dedicated to my beloved parents,

For their endless love, unwavering support, and sacrifices that have shaped my journey.
Your encouragement and belief in me have been my greatest source of strength.
I am forever grateful for everything you have done to help me reach this milestone.

ACKNOWLEDGMENTS

The successful completion of this thesis owes much to the invaluable support and encouragement extended by special people in my life. First, I sincerely thank my supervisor, Prof. Dr. Ismail Özgür Yaman, for his invaluable guidance, unwavering support, and diligent supervision.

I am grateful to Dr. Burhan Alam, my co-advisor, but more than an advisor, my brother. I appreciate his trust and the reassurance that he is always there for me.

I would like to express my deepest and endless gratitude to my parents and my brothers, Moharram Ali, Mohammad Ali, Ali, and Touraj, for their unwavering support and encouragement throughout my life, especially during the demanding years of my doctoral studies. Their belief in my potential has been a constant source of strength and motivation.

I am deeply indebted to my thesis monitoring committee members, Prof. Dr. Erdem Canbay and Prof. Dr. Mustafa Şahmaran, for their insightful guidance, constructive feedback, and encouragement throughout the course of my doctoral studies. Their expertise and advice have been instrumental in shaping the direction and quality of this research

My heartfelt appreciation also goes to Mohammad Hamahang Sherzai, Arsalan Javanmard, and Furkan Yalçındağ for their indispensable assistance during the experimental tests. Their dedication, collaboration, and expertise were pivotal in completing the experiments, and this research would not have reached its conclusion without their support.

I am sincerely thankful to Cuma Yıldırım and Gülşah Bilici, esteemed staff members of the METU Construction Materials Laboratory, for their kind and tireless support.

Their technical expertise, generosity, and willingness to assist at every stage have greatly facilitated the research process and ensured its successful completion.

This research was funded by the Scientific and Technological Research Council of Türkiye (TÜBİTAK) under Project No. 121N240. I gratefully acknowledge the financial support provided, which was essential for the successful execution of this work. Additionally, I extend my gratitude to Fibrobeton, Baştaş Çimento, Master Builders Solutions, and Solidian companies for their valuable in-kind support, which significantly contributed to the experimental phase of this study.

Finally, to all who have supported me in various capacities throughout this journey, I extend my heartfelt gratitude. This achievement is a testament not only to my efforts but also to the invaluable contributions of everyone who stood by me.

.

TABLE OF CONTENTS

ABSTRACT v

ÖZ vii

ACKNOWLEDGMENTS x

TABLE OF CONTENTS xii

LIST OF TABLES xv

LIST OF FIGURES xvi

1 INTRODUCTION 1

1.1 General 1

1.2 Objectives 3

1.3 Scope 5

2 LITERATURE REVIEW 6

2.1 General 6

2.2 The Uniaxial Tensile Performance of TRCC 10

2.2.1 Effect of Textile Type 16

2.2.2 Effect of Mortar Type 21

2.2.3 Effect of Short Fiber Addition 22

2.3 The Slip-Bond Performance of TRCC 23

2.3.1 Pull-out Mechanism of TRCC 24

2.3.2 Single-Sided Pull-out Tests 28

2.3.3 Double-Sided Pull-out Tests 29

2.3.4 Yarn Pull-out Test 30

2.4 TRCC Components Affecting Slip-Bond Performance 32

2.4.1 Textile Material Type 32
2.4.2 Cementitious Mortar 33
2.4.3 Impregnation of the Textile Monofilaments 36
2.4.4 Textile Architecture 39
2.5 Long-Term Performance of TRCC Under the Sustained Loading 43
2.5.1 Creep of Concrete 44
2.5.2 Testing for Creep of Concrete 46
CHAPTER 3 51
3 EXPERIMENTAL PROGRAM 51
3.1 General 51
3.2 Materials 52
3.2.1 Cementitious Materials 52
3.2.2 Sands 53
3.2.3 Chemical Admixture 54
3.2.4 Carbon Textile 55
3.3 Cementitious Mortars 65
3.4 Testing Procedures 66
3.4.1 Phase I: Uniaxial tensile testing of C-TRCC 66
3.4.2 Phase II: Slip-bond Behavior of C-TRCC (Yarn Pull-out tests) 70
3.4.3 Phase III: Creep Behavior of TRCC under Tensile Loading 74
CHAPTER 4 79
4 RESULTS AND DISCUSSION 79
4.1 Phase I: Uniaxial tensile test results 79
4.2 Phase II: Yarn Pull-out Test Results 90

4.2.1 Yarn Pull-out Test Results of C-TRCC with M45 mortar 92
4.2.2 Yarn Pull-out Test Results of C-TRCC with M7 mortar 101
4.2.3 Discussion of results for M7 mortar pull-out tests 107
4.2.4 Discussion of results for M45 mortar pull out tests 115
4.3 Phase III: Tensile Creep Test Results 123
4.3.1 Preliminary Testing and Slippage 123
4.3.2 Uniaxial Tensile Strength of C-TRCC (Warp) 128
4.3.3 Creep Testing of C-TRCC with M45 mortar (Mortar A) 129
4.3.4 Creep Testing of C-TRCC with M7 mortar (Mortar B) 132
4.3.5 Discussion of Results 135
CHAPTER 5 139
5 CONCLUSIONS AND RECOMMENDATIONS 139
6 APPENDIX-I 163
Pull-out Tests Results for M7 Mortar 163
7 APPENDIX – II 171
Pull-out Tests Results for M45 Mortar 171
CURRICULUM VITAE (Only For Doctoral Thesis) 177

LIST OF TABLES

Table 2-1 Fine-grained concrete compositions, masses in kg/m3(Butler et al., 2010) 35
Table 3-1 Chemical composition of Portland cement 52
Table 3-2 Chemical compositions of Class F type fly ash 53
Table 3-3 Physical properties of the two siliceous sands 54
Table 3-4 Properties of the high-range water reducer 54
Table 3-5 Manufacturer data on carbon textile properties 56
Table 3-6. Mixture proportions of the cementitious mortars 65
Table 4-1 Analysis of the load-deformation data in accordance with AC434 82
Table 4-2 Slip-bond test results for M45 when tested in the warp direction 93
Table 4-3 Slip-bond test results for M45 when tested in the weft direction 99
Table 4-4 Slip-bond test results for M7 when tested in the warp direction 103
Table 4-5 Slip-bond test results for M7 when tested in the weft direction 106
Table 4-6 Summary of the uniaxial tensile strength results of C-TRCC creep specimens 129

LIST OF FIGURES

Figure 2-1 Application of TRCC jacketing on RC columns (Bournas et al., 2009) .7
Figure 2-2 Application of TRCC jacketing in the shear spans (a) conventional jacketing and (b) layers of textile and cementitious mortar (T. C. Triantafillou & Papanicolaou, 2006) 8
Figure 2-3 Beam-column joint strengthening with TRCC (Al-Salloum et al., 2011) 9
Figure 2-4 3-D Structure illustration of "Cube" (Vakaliuk et al., 2022)....10
Figure 2-5 Clevis gripping uniaxial test setup (De Santis et al., 2018)....11
Figure 2-6 Clamp gripping uniaxial test setup (De Santis et al., 2018) 11
Figure 2-7 Gripping setup (a) clevis gripping (b) clamp gripping (Arboleda et al., 2016)....12
Figure 2-8 Idealized stress-strain graphs: (a) bare textile (b) clevis gripping (c) clamp gripping (Santis et al., 2018)....13
Figure 2-9 Grid-like, non-crimped textile and picture (Friese et al., 2022) 17
Figure 2-10 Grid-like woven carbon textile structure (Friese et al., 2022)....18
Figure 2-11 Structure and picture of weft-knitted utilized to reinforce fresh concrete (Friese et al., 2022) 19
Figure 2-12 The pultrusion process (Peled & Mobasher, 2007) 20
Figure 2-13 Stress gradient distribution in the vicinity of a macro-crack in TRCC (a) without short fibers and (b) with fiber (Barhum & Mechtcherine, 2013)....22
Figure 2-14 Influencing factors on the bond performance of textile reinforcement (Preinstorfer et al., 2024)....24
Figure 2-15 A schematic illustration of a standard pullout test setup and (b) the assumed shear bond stress at various slip values used for modeling pullout behavior (A. Peled, 2016)....25
Figure 2-16 Cross-section of a yarn inserted in cementitious mortar (a) schematic presentation (b) carbon yarn in mortar (Soranakom & Mobasher, 2009) 26

Figure 2-17 Telescopic pull-out phenomenon of the yarn in a cementitious mortar (a) after pull-out development, and (b) schematic depiction of telescopic failure in a yarn structure (Cohen & Peled, 2010) 27
Figure 2-18 Schematic illustration and setup of single-sided pull-out testing (Preinstorfer et al., 2024) 29
Figure 2-19 Double-sided TRCC pull-out testing setup (Bielak et al., 2018) 30
Figure 2-20 TRCC yarn pull-out test setup test setup (Dalalbashi et al., 2018) 31
Figure 2-21 SEM pictures: bonded part of dry textile within mortar (Donnini et al., 2016) 34
Figure 2-22 SEM pictures: bond of partially coated yarn with mortar (Donnini et al., 2016) 34
Figure 2-23 Stress gradient distribution in yarn cross-section without impregnation (left) and with impregnation(right) (Gries et al., 2016) 37
Figure 2-24 Double-sided pull-out Load-slip curves for different impregnation materials (Gries et al., 2016) 38
Figure 2-25 Illustration of squeezing pressure process in grid-like noncrimp textile (Hahn et al., 2019) 40
Figure 2-26 Influencing characteristics of yarn architecture on splitting failure mode: (a) cross-sectional shape; (b) yarn longitudinal waviness; (c) variation in cross-section of yarn in longitudinal directions; (d) mechanical anchorage due to transverse yarns (Preinstorfer & Kollegger, 2020b) 41
Figure 2-27 Profiled yarn with tetrahedral geometry; (a) picture (b) schematic depiction (Penzel et al., 2022) 42
Figure 2-28 Exemplary force distribution in the textile yarn under tensile loading (Hausding et al., 2011) 42
Figure 2-29 Transverse yarn mechanical anchorage in junction picture: (a) intact stage , (b) failed stage(Alva Peled et al., 2017). 43
Figure 2-30 ASTM C 512 test setup of creep under compression (ASTM 1987) .. 47
Figure 2-31 Tensile creep frame(Poston et al., 2001) 48
Figure 2-32 Tensile creep testing frame at METU (Keskin, 2012a) 49

Figure 2-33 Ball joints in the loading frame (Keskin, 2012b) 50
Figure 3-1 Particle size distribution of the two siliceous sands 54
Figure 3-2 Grid-like woven carbon textile utilized in this study..... 55
Figure 3-3 SEM analysis: (a) weft (90°) yarn, (b) warp (0°) yarns with a leno woven thread 57
Figure 3-4 SEM analysis: (a) yarns junction two warp yarns and one weft (b) illustration of SBR impregnation (defects are visible on filaments surface)..... 58
Figure 3-5 Laser scanning: (a) textile specimen inside laser scanner, (b) its 3-D model 60
Figure 3-6 3-D Models of the textile from laser scanner 61
Figure 3-7 Laser scanning: (a) warp yarn 3-D model (b) dimension and cross-section geometry of warp yarns..... 62
Figure 3-8 Laser scanning: (a) weft yarn 3-D model (b) dimension and cross-section geometry of weft yarns..... 62
Figure 3-9 Schematic description of the uniaxial test setup of the yarns 64
Figure 3-10 Uniaxial tensile stress-strain response of the yarns in both directions 64
Figure 3-11 Schematic illustration of the uniaxial test specimen..... 66
Figure 3-12 Cross-sectional view of the test specimen with two-layer carbon textile 67
Figure 3-13 C-TRCC formwork: (a) textile placement in the forms (b) placement of cementitious mortar 67
Figure 3-14 Uniaxial Tensile Test Set-up 68
Figure 3-15 AVE measurements and correction of axial displacement after testing steel plates 69
Figure 3-16 Schematic description of the yarn pull-out test specimens for three embedment lengths of 50, 100, and 150 mm..... 71
Figure 3-17 Schematic illustration of yarn pull-out testing for one, two, and three yarns 72
Figure 3-18 C-TRCC yarn pull-out tests specimen preparation and testing procedure. 73

Figure 3-19 Yarn pull-out testing setup 74
Figure 3-20 Schematic illustration of C-TRCC tensile creep specimen 75
Figure 3-21 Schematic depiction of the cross-section tensile creep specimens 75
Figure 3-22 Creep test setup 76
Figure 3-23 Schematic illustration of deformation measurement using DEMEC gage 77
Figure 3-24 Schematic illustration of creep testing and the specimen heating system 78
Figure 3-25 Pictures for (a) heating system, (b) Deformation measurement with DEMEC gage 78
Figure 4-1 Load – global strain measurements of TRC specimens 80
Figure 4-2 Effects of matrix type and textile direction on the performance of C-TRCC 83
Figure 4-3 Failure modes in C-TRC specimens 85
Figure 4-4 Slippage phenomenon observed in C-TRCC specimens 85
Figure 4-5 Some other observations on the tested C-TRCC specimens 86
Figure 4-6 SEM pictures of C-TRCC when tested along the warp direction 87
Figure 4-7 SEM pictures of C-TRCC when tested along the weft direction 88
Figure 4-8 Digitally stitched SEM pictures of C-TRC coupons in M7 89
Figure 4-9 Load-slip curves for M45 mortar with 150 mm embedment length 92
Figure 4-10 Load-slip curves for M45 mortar with 100mm embedment length 92
Figure 4-11 Textile rupture failure mode 94
Figure 4-12 Telescopic failure dominant textile rupture failure 95
Figure 4-13 Textile pull-out failure mode 96
Figure 4-14 Splitting failure mode 96
Figure 4-15 Load-slip curves for M45 mortar with 150mm embedment length 97
Figure 4-16 Load-slip curves for M45 mortar with 100 mm embedment length 98
Figure 4-17 Splitting failure mode observed in (a) 2Y (b) 3Y configurations 100
Figure 4-18 The mechanical interlock illustration in the warp and weft junction 101
Figure 4-19 Load-slip curves for M7 mortar with 150mm embedment length 102

Figure 4-20 Load-slip curves for M7 mortar with 100 mm embedment length....102
Figure 4-21 Textile slippage failure mode in M7 mortar 104
Figure 4-22 Load-slip curves for M7 mortar with 150mm embedment length.....104
Figure 4-23 Load-slip curves for M7 mortar with 100mm embedment length.....105
Figure 4-24 Load-slip curves for M7 mortar with 50 mm embedment length.....105
Figure 4-25 Telescopic pull-out dominant textile rupture in 3Y weft with 100 mm embedment length in M7 mortar 107
Figure 4-26 Maximum pull-out loads in the M7 mortar 108
Figure 4-27 Shear bond strength based on manufacturer-provided dimensions for M7 mortar 110
Figure 4-28 Shear bond strength based on laser scanning dimensions for C-TRCC with M7 pull-out tests.....112
Figure 4-29 Tensile strength of C-TRCC with M7 pull-out tests 113
Figure 4-30 Slip@F_max of C-TRCC with M7 pull-out tests.....114
Figure 4-31 Yarn telescopic failure mode in 3Y -150mm with M45 mortar 115
Figure 4-32 Maximum pull-out loads of C-TRCC with M45 mortar 116
Figure 4-33 Shear bond strength calculated by manufacturer data C-TRCC with M45 mortar pull-out tests 117
Figure 4-34 Shear bond strength calculated by laser scanning data C-TRCC with M45 mortar pull-out tests 120
Figure 4-35 Tensile strength of C-TRCC with M45 mortar pull-out tests.....121
Figure 4-36 Slip at maximum pull-out load for C-TRCC with M45 mortar pull-out tests 122
Figure 4-37 Load normalized deformation results of TRECC specimens 124
Figure 4-38 Tensile creep - time data at 50% creep loading for dummy specimens 125
Figure 4-39 Pull out of carbon textile yarns in dummy specimens at 75% loading 126
Figure 4-40 Modification of specimen dimensions for tensile creep testing 127
Figure 4-41 Force-normalized deformation of C-TRCC creep specimens 128

Figure 4-42 Creep loads and the number of cracks observed on each load level. 130
Figure 4-43 Creep test results of the C-TRCC specimens prepared with the M45 mortar 131
Figure 4-44 Creep test results of the C-TRCC specimens prepared with M7 mortar 134
Figure 4-45 Tested Specimen SEM illustration degradation of SBR coating 137
Figure 4-46 Cracking pattern in (a) 50°C,(b) 20°C 138
Figure 6-1 Load-slip curves for 1 yarn carbon textile tested in the warp direction with 150 mm embedment length into the M7 mortar 163
Figure 6-2 Load-slip curves for 2 yarn carbon textile tested in the warp direction with 150 mm embedment length into the M7 mortar 164
Figure 6-3Load-slip curves for 3 yarn carbon textile tested in the warp direction with 150 mm embedment length into the M7 mortar 164
Figure 6-4 Load-slip curves for 1 yarn carbon textile tested in the weft direction with 150 mm embedment length into the M7 mortar 165
Figure 6-5 Load-slip curves for 2 yarn carbon textile tested in the weft direction with 150 mm embedment length into the M7 mortar 165
Figure 6-6 Load-slip curves for 3 yarn carbon textile tested in the weft direction with 150 mm embedment length into the M7 mortar 166
Figure 6-7 Load-slip curves for 1 yarn carbon textile tested in the warp direction with 100 mm embedment length into the M7 mortar 166
Figure 6-8 Load-slip curves for 2 yarn carbon textile tested in the warp direction with 100 mm embedment length into the M7 mortar 167
Figure 6-9 Load-slip curves for 3 yarn carbon textile tested in the warp direction with 100 mm embedment length into the M7 mortar 167
Figure 6-10 Load-slip curves for 1 yarn carbon textile tested in the weft direction with 100 mm embedment length into the M7 mortar 168
Figure 6-11 Load-slip curves for 2 yarn carbon textile tested in the weft direction with 100 mm embedment length into the M7 mortar 168

Figure 6-12 Load-slip curves for 3 yarn carbon textile tested in the weft direction with 100 mm embedment length into the M7 mortar 169
Figure 6-13 Load-slip curves for 1 yarn carbon textile tested in the weft direction with 50 mm embedment length into the M7 mortar 169
Figure 6-14 Load-slip curves for 2 yarn carbon textile tested in the weft direction with 50 mm embedment length into the M7 mortar 170
Figure 6-15 Load-slip curves for 3 yarn carbon textile tested in the weft direction with 50 mm embedment length into the M7 mortar 170
Figure 7-1 Load-slip curves for 1 yarn carbon textile tested in the warp direction with 150 mm embedment length into the M45 mortar 171
Figure 7-2 Load-slip curves for 2 yarn carbon textile tested in the warp direction with 150 mm embedment length into the M45 mortar 172
Figure 7-3 Load-slip curves for 3 yarn carbon textile tested in the warp direction with 50 mm embedment length into the M45 mortar 172
Figure 7-4 Load-slip curves for 1 yarn carbon textile tested in the weft direction with 150 mm embedment length into the M45 mortar 172
Figure 7-5 Load-slip curves for 2 yarn carbon textile tested in the weft direction with 150 mm embedment length into the M45 mortar 173
Figure 7-6 Load-slip curves for 3 yarn carbon textile tested in the weft direction with 150 mm embedment length into the M45 mortar 173
Figure 7-7 Load-slip curves for 1 yarn carbon textile tested in the warp direction with 100 mm embedment length into the M45 mortar 174
Figure 7-8 Load-slip curves for 2 yarn carbon textile tested in the warp direction with 100 mm embedment length into the M45 mortar 174
Figure 7-9 Load-slip curves for 3 yarn carbon textile tested in the warp direction with 100 mm embedment length into the M45 mortar 175
Figure 7-10 Load-slip curves for 1 yarn carbon textile tested in the weft direction with 100 mm embedment length into the M45 mortar 175
Figure 7-11 Load-slip curves for 2 yarn carbon textile tested in the weft direction with 100 mm embedment length 176

Figure 7-12 Load-slip curves for 3 yarn carbon textile tested in the weft direction with 100 mm embedment length..... 176

CHAPTER 1

1 INTRODUCTION

1.1 General

Textile reinforced cementitious composite (TRCC) is an innovative composite material consisting of a non-metallic fabric mesh reinforcement (Carbon, AR-Glass, Basalt, etc.) and fine-grained cementitious mortar, that has emerged in the recent two decades as a feasible strengthening and retrofitting method of reinforced concrete and masonry structures (T. Triantafillou, 2016). Non-metallic fabric mesh reinforcement offers benefits such as corrosion resistance, crack control, design flexibility, sustainability, and reduced weight, making these materials highly attractive to researchers (Xu et al., 2004). This composite material was developed to address the limitations of traditional Fiber-Reinforced Polymer (FRP) methods, particularly the inorganic mortar's poor performance at elevated temperatures (Esmaeili et al., 2019) and the incompatibility with various substrate materials (Erdil et al 2013). Potential applications include, but are not limited to, flexural strengthening (B. T. Truong et al., 2017) and shear strengthening of RC beams (Alrefaei et al., 2018).

The fine-grained cementitious mortar in TRCC presents improved bonding, enhanced durability, better workability, and compatibility with substrate materials. Mortars used in TRCC typically have a water-to-binder ratio of 0.3 to 0.4 and a binder content of approximately 40-50% by volume. To ensure proper penetration into the textile mesh, aggregate size is generally limited to 1 or 2 mm. The high binder content is essential for optimal workability and strong bonding between the fine-grained mortar and the textile mesh. Cementitious materials, such as granulated blast furnace slag, fly ash, and micro-silica, are often incorporated to enhance bond strength and improve the overall mechanical properties and durability of the TRCC. These supplementary cementitious materials help buffer alkalinity and reduce pH

levels, resulting in a denser and more uniform bond with the textile (Butler et al., 2009). Various mortar compositions have been developed considering the requirements, such as suitable bonding between textile and mortar, workability, and durability of these composites (Mechtcherine et al., 2016) .

Since the beginning of TRCC related research, different textile structures have been used to exploit the mechanical and structural properties of textiles. For example, one-dimensional textiles, also known as reinforcing bars, are used to enhance the tensile strength of concrete (Kapsalis et al., 2021). Grid-like non-crimp fabrics and woven fabrics, as well as weft-knitted fabrics, are the most commonly used 2D textile structures in construction projects (Friese et al., 2022). These 2D textiles are composed of warp and weft yarns, each consisting of thousands of continuous filaments. Warp yarns run longitudinally along the textile manufacturing machine, while weft yarns run transversely. The manufacturing processes of warp and weft yarns have a significant influence on their architectural and structural characteristics, resulting in a different mechanical behavior in each direction. Therefore, a comprehensive evaluation of both warp and weft directions is crucial for a thorough understanding of the TRCC performance.

Key mechanical performance characteristics of TRCC, such as tensile strength, ductility, modulus of elasticity and shear bond strength, are critical to the design of reliable and durable structures (Goliath et al., 2023). In addition to textile properties and amount, the type of cementitious mortar and testing methodology (including specimen gripping techniques) significantly influence the mechanical properties of TRCC (Ricker et al., 2022). Of the various test methods available, uniaxial direct tensile testing is widely recognized as the most appropriate technique for evaluating the mechanical behavior of TRCC (Mobasher, 2016). This test method provides valuable data on several factors, including the influence of textile types (e.g. AR glass, carbon and basalt) on post-crack displacement and load levels, the effect of mesh spacing and the number of textile layers on load-bearing capacity and crack propagation (Mattarollo et al., 2023).

Uniaxial tensile tests on TRCC exhibit various failure modes, which are closely related to the material's mechanical properties (Nivetha et al., 2023). One of the most observed failure modes in C-TRCC specimens is the slippage of textile yarns within the mortar matrix. This failure mode is influenced by factors such as testing methodology, the type of cementitious mortar, the textile manufacturing process, and the bond strength between the textile and the mortar (Mattarollo et al, 2023). Therefore, a deeper understanding of the bond between the textile and mortar is crucial for improving the mechanical performance and durability of these composites.

TRCC exhibits enhanced durability compared to traditional reinforced concrete due to its non-metallic reinforcement, which makes it resistant to aggressive environmental conditions and corrosion (Alexander & Shashikala, 2023; Spelter et al., 2019). Although, the degree of impregnation of textile yarns within the mortar matrix has a significant impact on the creep response of TRCC, particularly under elevated temperatures and high relative humidity (Mechtcherine, 2016), the long-term performance of TRCC under sustained loading conditions (creep) remains inadequately understood. This represents a critical knowledge gap in establishing a robust framework for evaluating TRCC's long-term mechanical behavior. The creep response of TRCC is primarily influenced by the time-dependent deformation of the mortar matrix and the progressive development of microcracks, which can lead to the gradual debonding of textile yarns from the matrix and, ultimately, yarn pullout.

1.2 Objectives

To investigate the long-term performance of TRCC, a TÜBİTAK-funded project entitled "Long-term Performance of Textile Reinforced Cementitious Composites (LTP-TRCC)" was undertaken at the Materials of Construction Laboratories within the Department of Civil Engineering at METU. That research focused on evaluating the performance of carbon (C-) and glass (G-) TRCC systems fabricated using various cementitious mortars under diverse environmental conditions. The

experimental program encompassed a series of tests, including uniaxial tensile characterization, bond/slip behavior assessment, creep characterization, and exposure to environmental loading such as cyclic heating/cooling and wet/dry cycles, along with uniaxial tensile creep characterization.

This thesis research, conducted within the framework of a TUBITAK project, aims to provide a comprehensive investigation on the mechanical performance and long-term tensile creep performance of such C-TRCC systems. To this end, a grid-like woven carbon textile fabric, commonly employed in strengthening and retrofitting applications, was selected. The study evaluated the performance of this textile in both longitudinal (warp) and transverse (weft) yarn directions. Two different cementitious mortars were utilized: M7, a standard mortar commonly used in TRCC production, and M45, a specialized mortar typically used in Engineered Cementitious Composites (ECC) with the absence of short discrete PVA fibers.

A three-phase experimental program was designed to achieve a set of objectives.

- The first phase aims to understand the key parameters such as textile yarn orientation (warp and weft direction) and reinforcement ratio on the uniaxial tensile performance of C-TRCC produced with two different cementitious mortars (M7 and M45).
- The second phase of the research investigates the pull-out behavior of C-TRCC, using the same experimental parameters as in the previous phase, to evaluate the slip-bond behavior. In order to comprehensively evaluate the influence of cross-yarn mechanical interlock on slip-bond behavior, the study is extended beyond the conventional 1-Y configuration to include 2-Y and 3-Y configurations. Three embedment lengths (150 mm, 100 mm, and 50 mm) of the textile were selected to investigate shear bond strength and failure modes in the C-TRCC pull-out tests.
- In the final phase, using the same C-TRCC production parameters as in the previous phases, tensile creep tests are performed at two different temperature regimes (20°C and 50°C) to evaluate the coupled effects of creep

and temperature on the long-term performance of the C-TRCC, with particular emphasis on the potential for time-dependent degradation at elevated temperatures.

1.3 Scope

Chapter 1 provides an introduction on the subject to explain why C-TRCC is important in civil engineering, particularly for the repair and strengthening of buildings. It also outlines the objectives of the research and explains the experimental program used in the study. Chapter 2 reviews the literature on TRCC. It highlights the studies that have been carried out and the gaps in the literature relating to these composites, particularly in areas such as uniaxial tensile and slip bond behavior, and its performance under sustained loads. The experimental program associated with this study is described in Chapter 3, which describes the materials, test setups, and methods used to investigate the mechanical behavior of C-TRCC. The chapter focuses on how various factors such as the design of the fabric, the length in which it is embedded, and the environmental conditions affect the performance of the material. Chapter 4 presents the data obtained from the experimental investigation and discusses the observations. Finally, Chapter 5 presents the conclusions, highlighting the importance of the research in advancing knowledge in the field of construction materials, particularly with regard to the mechanical behavior and long-term performance of C-TRCC.

CHAPTER 2

2 LITERATURE REVIEW

2.1 General

Existing reinforced concrete (R/C) structures need to be retrofitted and strengthened to improve their serviceability and resilience to natural hazards such as earthquakes. In addition, durability challenges often arise from material degradation and failure mechanisms, with rebar corrosion being the most common problem leading to deterioration of R/C (Feng et al., 2022). A range of methods has been implemented to mitigate the structural vulnerabilities of existing buildings. The most widely used techniques include epoxy injection or grouting to repair cracks and fill voids, enhancing stability; section enlargement, steel plate bonding, and the application of fiber-reinforced polymers (FRP) to strengthen structural elements and increase their load capacity (Gireesh Kumar & Yeegalapati, 2022). Among these techniques, use of FRP are widely used due to their numerous advantages, including high tensile strength, corrosion resistance, lightweight properties, and ease of application (Durgadevi et al., 2021). However, issues such as interfacial problems, concerns related to long-term durability, and fire performance restrictions primarily rooted in its organic binder necessitate finding novel solutions to these problems (Erdil et al., 2012; Esmaeili et al., 2019). About three decades ago, researchers began to develop an innovative composite material, textile-reinforced cementitious composites (TRCC), to address the challenges associated with using epoxy as a binder. This material combines advanced high-performance non-metallic fibers, such as carbon, AR glass, basalt and aramid, arranged in open mesh fabrics as reinforcement, with inorganic cementitious matrices (Tetta et al., 2015).

Due to its unique properties, TRCC have been used to strengthen existing structures and to create new thin and lightweight constructions, such as pedestrian bridges, parking structures, and self-supporting façades (Williams Portal et al., 2015).

Combining the textile's high tensile strength and non-corrosive properties allows for much thinner structures compared to those reinforced with steel. This reduction in thickness decreases the overall weight, lowers transportation costs during the prefabrication process, and conserves resources (Alexander & Shashikala, 2020) . Moreover, TRCC exhibits ductile behavior with a superior energy absorption capability and an enhanced crack distribution. This section highlights selected case studies demonstrating the use of TRCC in both retrofit applications for strengthening and repairing existing structures and new construction and explores the potential future applications of this innovative material.

Bournas et al., (2009) studied the efficacy of TRCC on seismic retrofitting of R/C columns, compared with FRP as shown in Figure 2-1. The results revealed that applying TRCC considerably increases old columns' deformation capacity and strength, and TRCC indicated more flexibility than FRP during the cyclic loading.

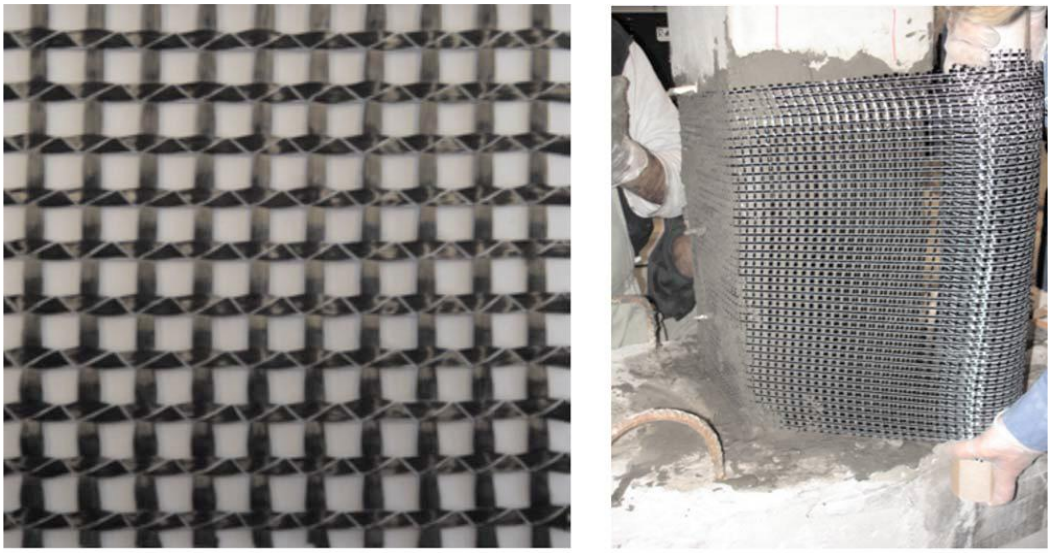

Figure 2-1 Application of TRCC jacketing on RC columns (Bournas et al., 2009)

In another study, the flexural performance of a R/C beam after strengthening with TRCC was studied (Elsanadedy et al., 2013). The research findings indicate that the flexural capacity of R/C beams strengthened with TRCC was significantly improved

compared to control specimens. The results also emphasize the critical role of mortar properties, textile type, and end anchorage in optimizing the effectiveness of these composites.

T.C. Triantafillou & Papanicolaou (2006) investigated the efficacy of shear strengthening of beams by TRCC jacketing (Figure 2-2**)**. The results of this investigation demonstrated that the shear resistance of R/C beams significantly increases when TRCC jackets are applied. Additionally, the application of TRCC layers further enhanced the shear performance of these beams.

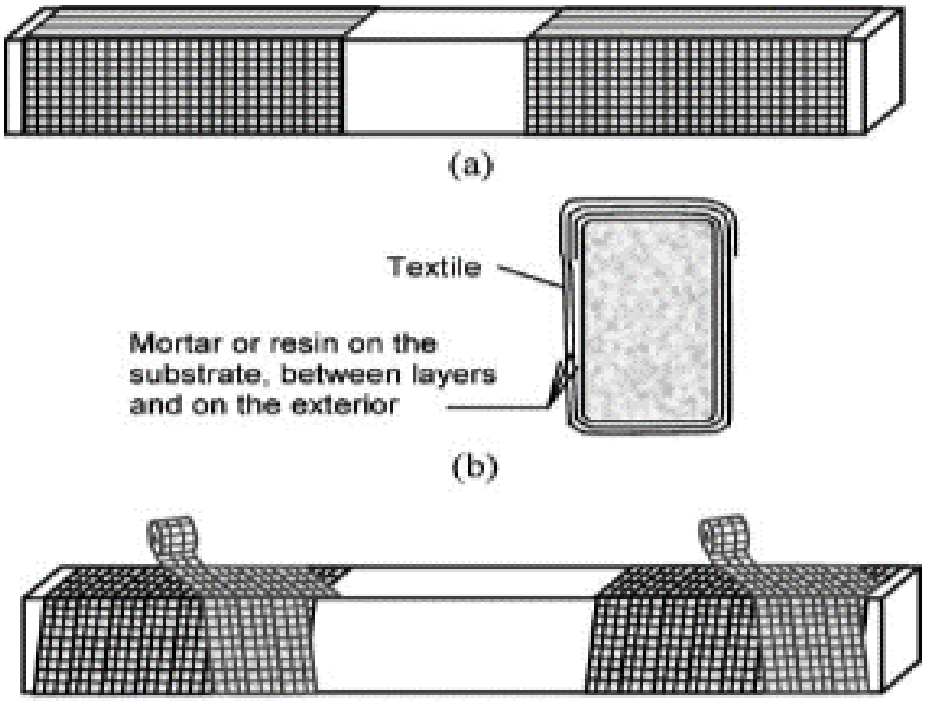

Figure 2-2 Application of TRCC jacketing in the shear spans (a) conventional jacketing and (b) layers of textile and cementitious mortar (T. C. Triantafillou & Papanicolaou, 2006)

In another study, seismically deficient R/C beam-column joints (Figure 2-3) were retrofitted with TRCC to evaluate their efficiency (Al-Salloum et al., 2011). It was observed that TRCC enhanced the strength and flexibility of the joints. Additionally,

a significant increase in energy absorption capacity was observed, which contributes to mitigating structural damage during seismic events. This is crucial for maintaining the serviceability of structures.

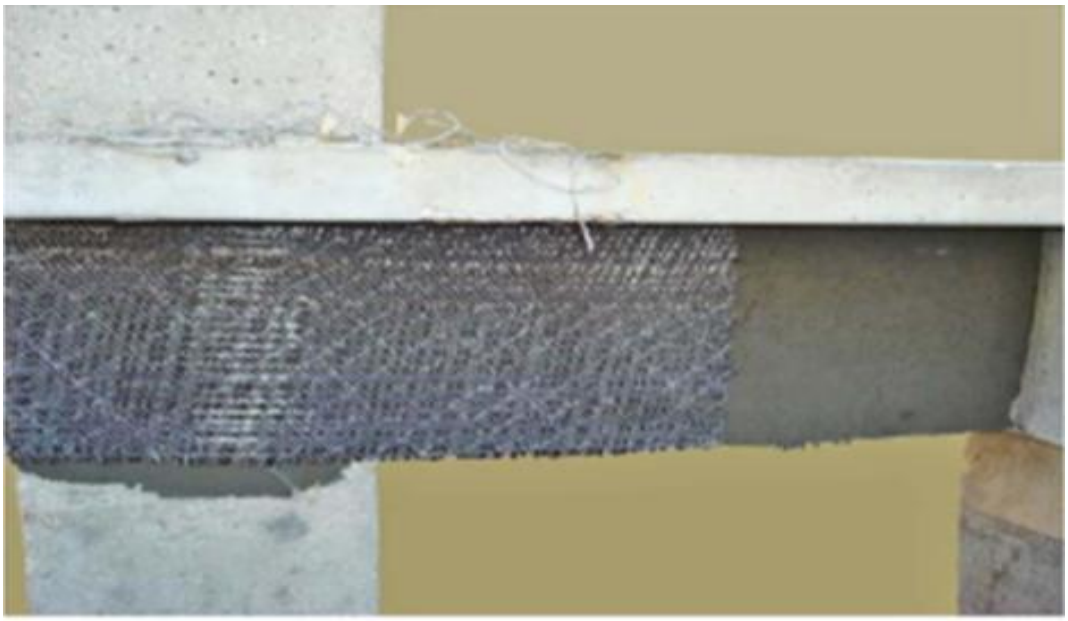

Figure 2-3 Beam-column joint strengthening with TRCC (Al-Salloum et al., 2011)

Moreover, TRCC's unique combination of ductility, durability, and sustainability makes it an attractive option for use as a structural material in thin-wall members (Venigalla et al., 2022). The use of non-metallic reinforcement, such as textile fibers, in R/C structures can enhance durability and sustainability compared to traditional steel reinforcement (Friese et al., 2022). With its superior mechanical performance and durability, the use of carbon fibers in the manufacture of C-TRCC structures offers a compelling option for structural applications compared to other available materials. For example, carbon concrete composite (C3) is a major construction project that started in Germany in 2016 (Tietze et al., 2022). The initiative aims to develop standards and regulations for the structural application of C-TRCC. As a

significant milestone, the first precast C-TRCC building, 'Cube,' depicted in Figure 2.4, was constructed during the initial phase (Vakaliuk et al., 2022).

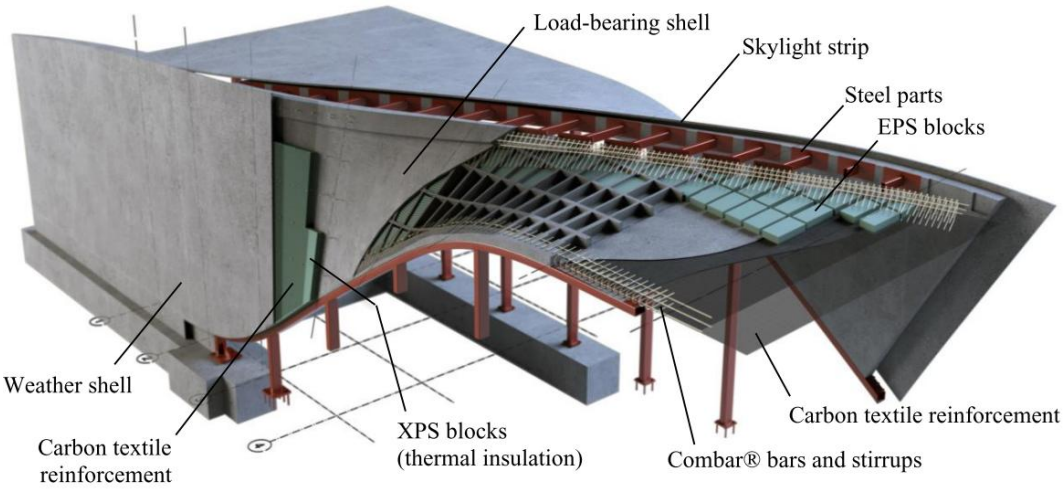

Figure 2-4 3-D Structure illustration of "Cube" (Vakaliuk et al., 2022)

The following sections discuss the mechanical properties of TRCC with reference to the relevant literature.

2.2 The Uniaxial Tensile Performance of TRCC

Uniaxial tensile testing is a fundamental method for characterizing the mechanical behavior of TRCC. By subjecting TRCC specimens to a controlled tensile load, the interaction between the textile reinforcement and the cementitious matrix can be studied, cracking behavior can be observed, and the overall tensile response of the material can be determined. Therefore, this test provides critical information about the material's performance under tensile loading, including its strength, stiffness, and ductility. It is well known that the way in which the TRCC specimens are applied, i.e., the grip, affects the tensile response of the TRCC. Two methods used in the

literature for this purpose are referred to as “clevis grip” (Figure 2-5) and “clamping grip ” (Figure 2-6).

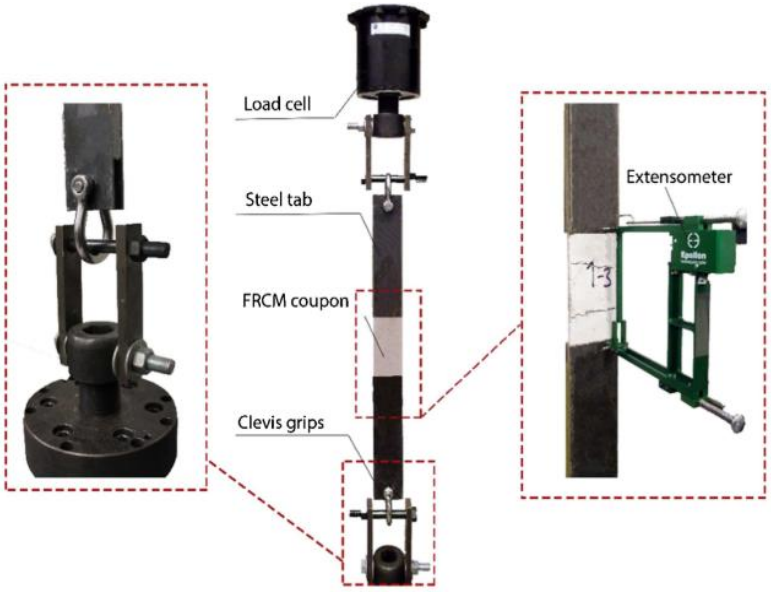

Figure 2-5 Clevis gripping uniaxial test setup (De Santis et al., 2018)

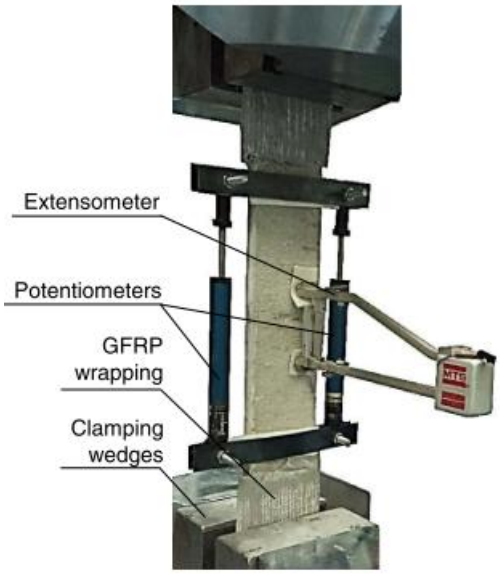

Figure 2-6 Clamp gripping uniaxial test setup (De Santis et al., 2018)

The primary distinction between the two methods relates to the stress state generated by the grips. In the initial case, only shear stresses are transmitted as shown in Figure 2-7 (a). In this type of test, the fabric's full potential is often not utilized due to the failure mode being slippage of the fabric. In the second method which is depicted in Figure 2-7 (b), the clamping grips induce compression and shear in the specimen, restricting slippage between the fabric and matrix at the grip, which results in a trilinear stress-strain curve as presented in Figure 2-8. The tests conducted with clamping grips permit the comprehensive characterization of the composite's mechanical behavior, including identifying tensile failure in each constituent material as. However, in the field applications of TRCC, the ends are not anchored, and failure is often due to slippage of the fibers. Consequently, the tests conducted with clevis grips aim to reproduce the as-installed TRCC behavior, and the stress-strain curve for this type of tensile test depicts bilinear behavior (Arboleda et al., 2016).

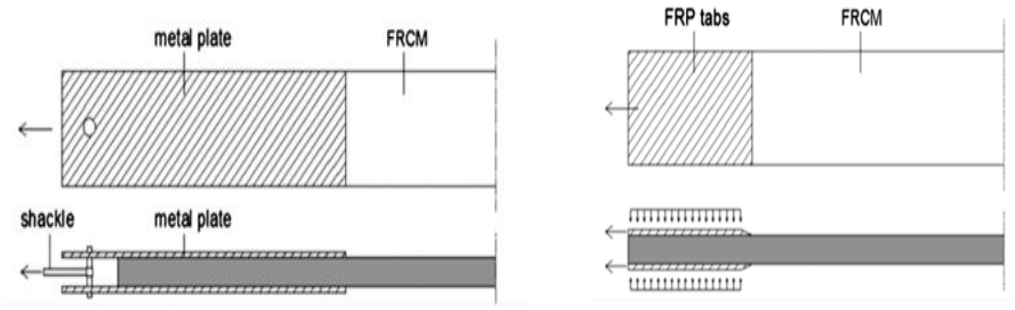

(a) (b)

Figure 2-7 Gripping setup (a) clevis gripping (b) clamp gripping (Arboleda et al., 2016)

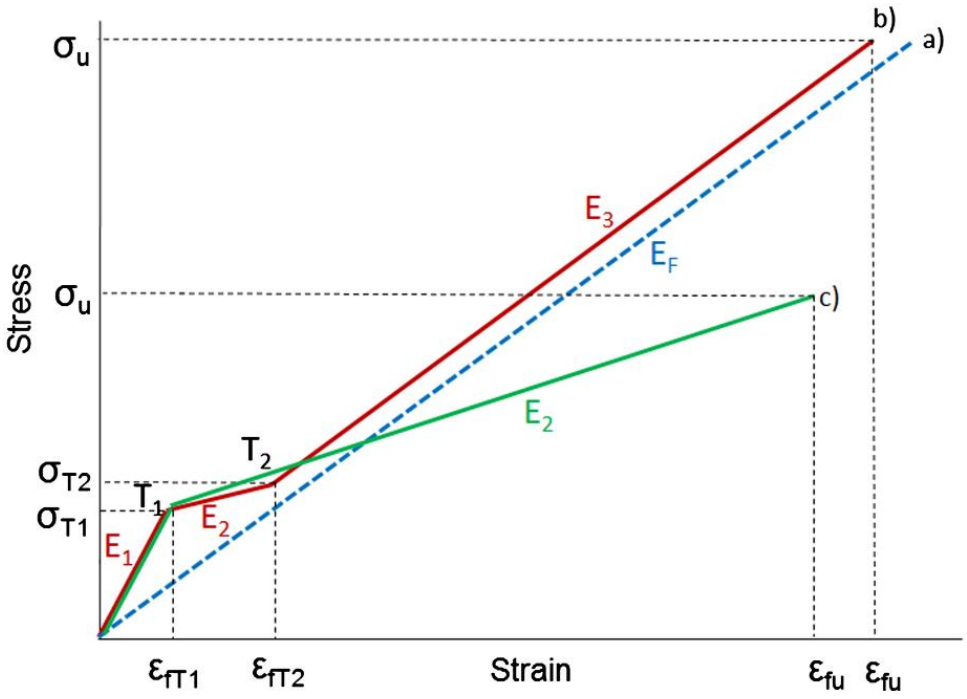

Figure 2-8 Idealized stress-strain graphs: (a) bare textile (b) clevis gripping (c) clamp gripping (Santis et al., 2018)

The typical stress-strain response of TRCC during a uniaxial tensile test is characterized as an idealized trilinear curve as depicted in Figure 2-13 (b) (Jesse et al., 2008). The initial linear section signifies the undamaged condition of the composite material influenced by the matrix characteristics improved by the presence of textile reinforcement. The subsequent part denotes the development and increase of crack number. During this phase, there is a notable decline in rigidity with the formation of relatively small cracks. The extent and steepness of this curve segment are dependent on the effectiveness of the bonding between the textile reinforcement and the matrix and the percentage of filaments engaged in load transfer. The third phase is characterized as the crack-widening region, during which the pre-existing cracks expand until final failure occurs, either by reaching the fabric's ultimate tensile strength and by the textile's slippage from the mortar, or a combination of both. This particular phase is defined by various factors, including the specimen gripping methods and textile properties like volume percentage,

geometry, and yarns impregnation conditions. In this phase, the fabric merely acts against the applied load. Hence, the curve's slope typically illustrates the bare textile's elastic modulus. Under specific circumstances, a tension-stiffening phenomenon is observable where the modulus in this phase aligns parallel, although at a slightly increased stress level compared to the fabric Figure 2-8(a). This phenomenon is attributed to the involvement of the uncracked matrix existing between the cracks. When the specimens in the gripping area were not under side pressure, the matrix exhibits deficient strength, or the yarn experiences slippage, the modulus of the third phase may be indistinguishable from the second phase, resulting in a bilinear behavior instead (Figure 2-8(c)).

The parameters reported from TRCC uniaxial direct tensile tests are first cracking strength (σ_{cr}), ultimate tensile strength (σ_u), strain at ultimate tensile strength (ε_u), and tensile modulus (E_i) (Truong & Kim, 2021).The cracking strength of TRCC (σ_{cr}) up to the point which cover mortar cracks, in which the mortar is the dominant load-carrying unit, is calculated by dividing the delivered force (F) by the cross-section of the specimenA_{TRCC} using following Eq1 (RILEM Technical Committee 232-TDT (Wolfgang Brameshuber) et al., 2016):

$$\sigma_{cr} = \frac{F_{cr}}{A_C} \quad (1)$$

The cracking strength is the tensile stress at the point where linear behavior ends in the stress-strain curve, T_1 ($\sigma_{T_1}, \varepsilon_{T_1}$) in Figure 2-8

After cracking, the load-carrying capacity of TRCC is primarily recognized in the presence of fabric reinforcements. As a result, determining the direct tensile stress experienced by the textile (σ_f) involves dividing the applied force (F) by the cross-sectional area of the textile reinforcement (A_f) (Santis et al., 2018).

$$\sigma_f = \frac{F}{A_f} \quad (2)$$

TRCC's ultimate tensile strength is the peak point in the stress-strain curve at which the TRCC specimen fails, shown as $(\sigma_u, \varepsilon_{fu})$ in Figure 2-8 for both bilinear and trilinear responses.

The strain of TRCC in uniaxial direct tensile tests is calculated by dividing the deformation of the region of interest (ΔL) by the region of interest length (RGL) (Carozzi & Poggi, 2015).

$$\varepsilon = \frac{\Delta L}{RGL} \tag{3}$$

The tensile elastic modulus of TRCCs is identified through the gradient of the stress-strain curve and computed by dividing the discrepancy in the tensile stress between two specific points ($\Delta\sigma_i$) by the difference in the tensile strain of the respective points ($\Delta\varepsilon_i$). This is expressed in the below equation.

$$E_i = \frac{\Delta\sigma_i}{\Delta\varepsilon_i} \tag{4}$$

In the trilinear stress-strain response scenario, it is necessary to determine the elastic moduli corresponding to the initial elastic phase (E_1), the crack propagation phase (E_2), and the crack widening phase (E_3). E_1 is the slope of the line segment between points O and T_1, E_2 is the slope of the line segment between points T_1 and T_2, and E_3 is the slope of the line section between points T_2 and the peak $(\sigma_u, \varepsilon_{fu})$, as shown in Figure 2-8(b).

In the state of bilinear response, it is essential to determine the tensile elastic modulus of both the initial elastic phase (E_1) and the post-cracking phase (E_2). E_1 is the line slope connecting point O to point T_1, as illustrated in Figure 2-8 (c) As indicated by previous studies (Santis et al., 2018) the gradient of the line drawn between two points selected on the stress-strain plot at stress levels of $0.9\sigma_u$ and $0.6\sigma_u$ corresponds to the tensile modulus of the post-cracking phase (E_2). Consequently, E_2 can be computed using the subsequent equation.

$$E_2 = \frac{0.9 * \sigma_{f_u} - 0.6 * \sigma_{f_u}}{\varepsilon_{f_{@0.9\sigma_{f_u}}} - \varepsilon_{f_{@0.6\sigma_{f_u}}}} \quad (5)$$

The ultimate tensile stress of TRCCs is denoted as σ_{f_u}, and $\varepsilon_{f_{@0.9\sigma_{f_u}}}$ and $\varepsilon_{f_{@0.6\sigma_{f_u}}}$ representing the corresponding tensile strain of TRCCs at stress levels equivalent to $0.9\sigma_{f_u}$ and $0.6\sigma_{f_u}$, respectively.

The tensile behavior of TRCC is affected by factors such as textile materials, textile architecture, yarns, geometrical properties, mortar compositions, strength, and the manufacturing as well as the testing procedures of TRCC (T. C. Triantafillou, 2016).

2.2.1 Effect of Textile Type

The material type of the textile is one of the determining characteristics that considerably affect the tensile strength of TRCC (Venigalla et al., 2022) . Among the several types of textiles used in TRCC, PBO-TRCCs (Polyparaphenylene Benzobisoxazole) demonstrated superior ultimate tensile strength. In contrast, TRCCs reinforced with natural fibers such as Flax (F-), Sisal (S-), Cotton (CO-), and Hemp (H) exhibited the lowest ultimate tensile strength. Additionally, the tensile strength of TRCCs reinforced with Carbon (C-), Glass (G-), and Basalt (B-) varies significantly. These differences in performance can be attributed to the unique properties of the reinforcement materials used. Specifically, PBO fibers stood out among the various fibers with a significant tensile strength of 3900 MPa (Tran Manh et al., 2021). However, natural fibers displayed the lowest tensile strength with around 400 MPa (Mercedes et al., 2018). The C-TRCC tensile strength is reported to range from 834 MPa to 2556 MPa (Arboleda,et al., 2016; Wei et al., 2020). For G-TRCC, this value ranges from 1120 to 1400 MPa (D'Antino & Papanicolaou, 2018) and for B-TRCC ultimate tensile strength is 1042 MPa (Caggegi et al., 2017).

Various textile manufacturing methods proposed for construction applications, including grid-like non-crimp fabrics (NCF), grid-like woven, and weft knitted, are the most suitable fabric formations for retrofitting and structural aims (Friese et al., 2022). NCFs are the preferred option for reinforcement textiles in concrete construction. The fabrication process of these textiles involves a warp-knitting technique, where a knitting thread interconnects multiple layers of reinforcing fibers. Unlike woven fabrics, these reinforcing fibers are manufactured without crimping, producing the term "non-crimp fabric" (Figure 2-9). Owing to the absence of crimping in the reinforcing fibers, NCFs exhibit superior elongation stiffness compared to regular woven fabrics (Friese et al., 2022).

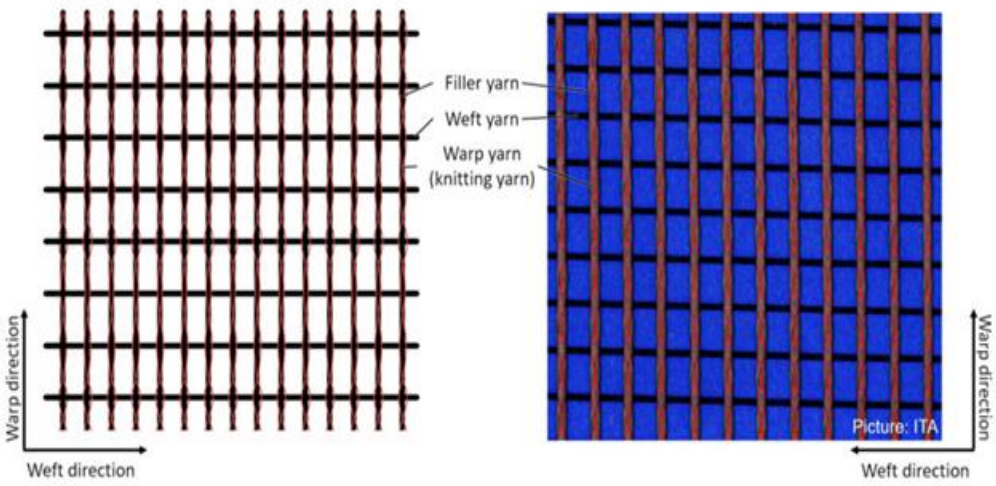

Figure 2-9 Grid-like, non-crimped textile and picture (Friese et al., 2022)

Grid-like woven (Figure 2-10) fabrics in the fabrication process are similar to grid-like NCF; however, the crimping and geometrical change in longitudinal directions of yarns cause them to show quite different mechanical properties and textile/mortar bonding performance(Friese et al., 2022).

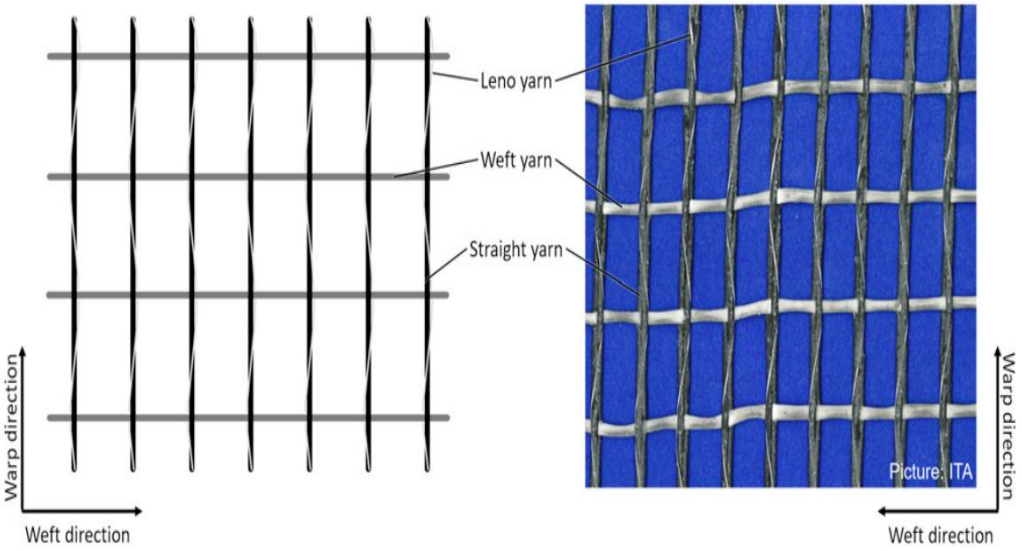

Figure 2-10 Grid-like woven carbon textile structure (Friese et al., 2022)

Weft-knit fabrics (Figure 2-11) are derived from one or multiple thread systems through stitch formation, where threads are transformed into loops and interconnected with adjacent loops. This manufacturing technique produces a pliable textile with minimal gap sizes, making weft-knit textiles an unconventional option for concrete. Nevertheless, weft-knit fabrics can be utilized in concrete construction to reinforce fresh concrete. In such instances, weft-knitted structures serve as stay-in-place formworks, also known as KnitCrete (Friese et al., 2022).

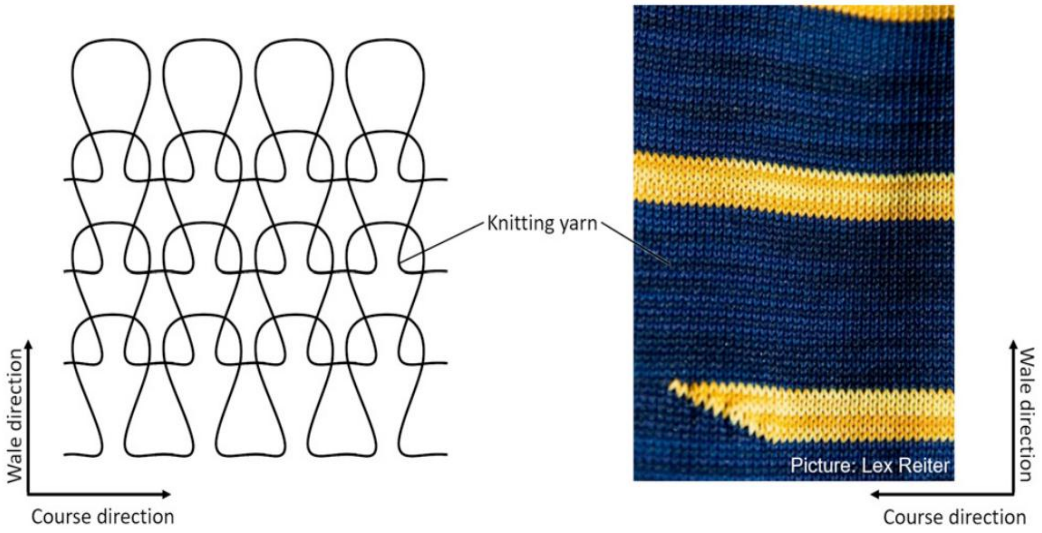

Figure 2-11 Structure and picture of weft-knitted utilized to reinforce fresh concrete (Friese et al., 2022)

The manufacturing process of TRCC plays a significant role in its mechanical performance. The production method can influence the alignment of the fibers and general composite uniformity and directly impact the microstructure of TRCC. Various regular production techniques in structural elements construction, such as casting, laminating, spraying, and pulturation, have been used to producing the TRCCs. Fabrication methods of TRCC influence the mechanical characteristics of these composites (Brameshuber, 2016). The impact of two production techniques, specifically pultrusion and casting processes, on the tensile characteristics of TRCCs was studied by (Peled & Mobasher, 2007). In the pultrusion (Figure 3-8) process, fabrics were submerged in a slurry infiltration chamber and pulled through rollers to compress the mortar matrix within the mesh apertures and remove excess cement paste. Conversely, in the casting process, fabrics were manually placed in the mortar matrix using hand lay-up techniques (Rawat et al., 2022).

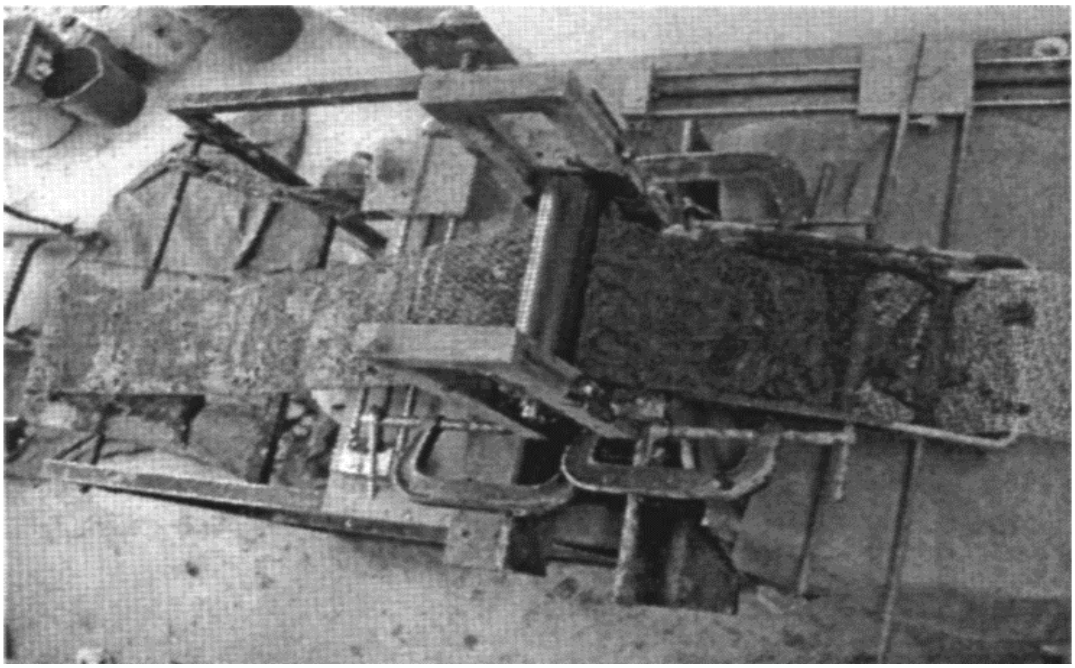

Figure 2-12 The pultrusion process (Peled & Mobasher, 2007)

The improved mechanical properties of pultruded TRCCs compared to cast TRCCs can be primarily attributed to the shear stress induced in the pultrusion process, which facilitates the infiltration of cement particles between the filaments (Peled & Mobasher, 2007). Thus, the anchorage and adhesion of the textiles within the mortar matrix was significantly improved during the pultrusion process, resulting in an increase in the tensile strength of the pultruded composites (Peled & Mobasher, 2007). In addition, the pressure applied to the surface of the newly formed laminated composites associated with the pultrusion technique increased the ability of the cement to penetrate the gaps between the filaments and fabric layers. This resulted in increased bond strength and reduced filament pullout during tensile testing, thereby increasing the tensile strength of the pultruded composite (Peled & Mobasher, 2005).

2.2.2 Effect of Mortar Type

Another significant factor that affects the mechanical response of TRCC is the mortar type which can be changed based on the requirements of the usage area (Mechtcherine, 2016). The fine-grained concrete which is normally is used in the TRCC production contains a water/binder (w/b) ratio ranging from 0.3 to 0.4, with a binder content of 40-50% in terms of volume. A significant quantity of binder is essential for ensuring adequate bonding between the fine concrete and the filaments that form the textile reinforcement, while also contributing to the workability of the fresh concrete (Mechtcherine et al., 2016). The size of the aggregates is usually limited to 1 and 2 mm, a range influenced by factors such as the distance separating the textile reinforcement's yarns, the textile reinforcement layers' arrangement, and the structural component's dimensions (Mechtcherine et al., 2016). Additional requirements appear from specific application situations. For instance, achieving high efficiency in the manufacturing of slender, large-scale components necessitates highly fluid and self-leveling properties, along with the capability to permeate through intricate reinforcing fabrics, sometimes in multiple tiers, and the aptitude to encase the individual filaments (Venigalla et al., 2022). The incorporation of pozzolans into the cement matrix results in a change of matrix alkalinity. Nonetheless, there are no issues regarding maintaining pH equilibrium, given that the fabric utilized in TRCC exhibits resistance to alkalis. Commonly employed mineral admixtures in TRCC encompass fly ash, micro silica, and metakaolin. These materials, characterized by their minute particle dimensions and high pozzolanic reactivity, enhance their adhesion and mechanical properties. Furthermore, their reduced permeability contributes significantly to the enhancement of durability. The characteristics of hardened concrete are evaluated based on its mechanical behavior under both compressive and tensile forces. Literature indicates that the typical compressive strength of TRCC matrices for structural applications ranges from 50 to 60 MPa. Additionally, compressive strengths reaching up to 120 MPa are

employed in precast construction and load-bearing architectural applications (Mechtcherine et al., 2016).

2.2.3 Effect of Short Fiber Addition

Furthermore, the addition of short fibers to cementitious mortar can also enhance the mechanical properties of TRCC by contributing to micro-cracks bridging (Figure 2-13) which improves the stress value needed to propagate to macro-cracks (Barhum & Mechtcherine, 2012; Deng et al., 2020; Zhang & Deng, 2022). A set of uniaxial, deformation-controlled tension tests was conducted by Barhum & Mechtcherine, 2013 to analyze the strength, deformation, and fracture characteristics of slender, thin plates constructed from TRCC with and without short fibers (glass and carbon). A notable enhancement of the initial cracking stress was attained, with the value rising by 1.5 and 2 times due to the short glass and carbon fibers, respectively. Although the increased quantity and fineness of cracks were evident in the samples with added short fibers, a moderate enhancement in tensile strength was recorded.

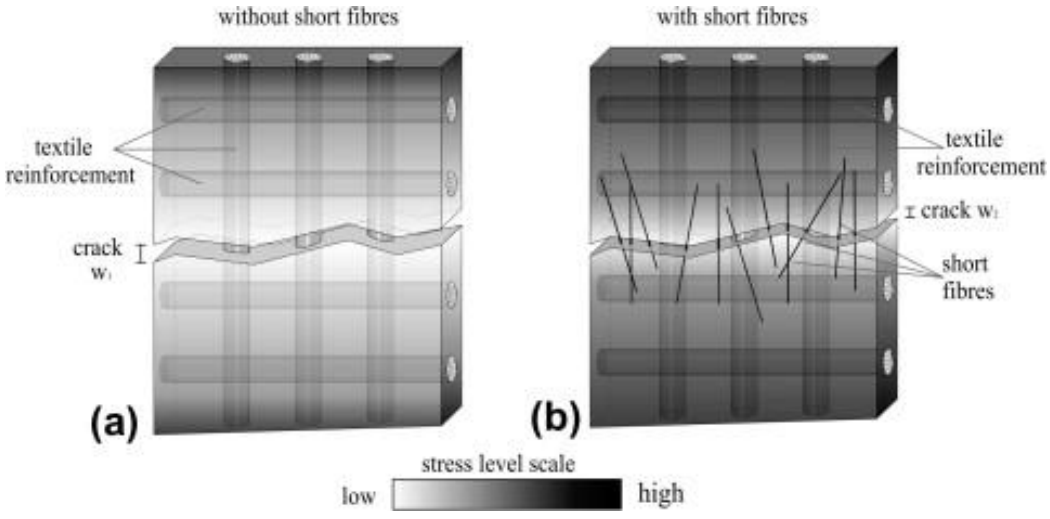

Figure 2-13 Stress gradient distribution in the vicinity of a macro-crack in TRCC (a) without short fibers and (b) with fiber (Barhum & Mechtcherine, 2013)

The effect of PVA fiber addition to TRCC tensile response was investigated by (Zhang & Deng, 2022). The results revealed that with the rise in the content of PVA fibers and the increase in the reinforcing ratio, the specimens demonstrated a progressive manifestation of multiple cracking behavior and a decrease in the distance between cracks. The enhancement in stress transfer across the cracks could be attributed to the bridging impact of short PVA fibers and longitudinal yarns. The alteration of the failure mechanism from slippage to fracture of the textile can be attributed to the presence of short PVA fibers. The ultimate stress and peak strain increase with the increase of PVA fiber content under the same textile reinforcing ratio.

2.3 The Slip-Bond Performance of TRCC

The slip-bond characteristics of TRCC are of critical importance with regard to its structural performance, influencing both its structural stability and functional performance. The bonding mechanisms observed in steel-reinforced concrete, such as adhesion, friction, and mechanical interlock, can be identified in a similar manner in TRCC (Preinstorfer et al., 2024). Moreover, the size of each factor's impact varies notably owing to various factors, including the testing methodology, amount of textile, the type and structure of the yarn, surface roughness, the composition of the impregnation, fiber sizing, mortar type, additives in the binder, and the geometrical structure of the textile. Some of those factors are schematically shown in Figure 2-14. When natural fibers are used in textile manufacturing, inadequate adhesion between the fibers and the binder can occur due to fiber expansion upon exposure to moisture in the fresh concrete, followed by contraction during drying (Preinstorfer et al., 2024).

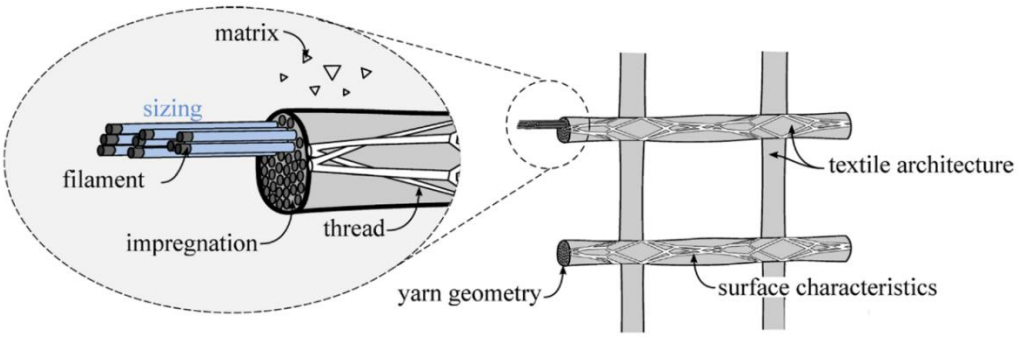

Figure 2-14 Influencing factors on the bond performance of textile reinforcement (Preinstorfer et al., 2024)

A lack of standardization has necessitated the investigation of bonding performance between textile and cementitious mortar through the implementation of diverse test methods. Among these, the single-sided pull-out test (SSPO), double-sided pull-out test (DSPO), and yarn pull-out tests have emerged as the most frequent and reliable. (Preinstorfer et al., 2024).

2.3.1 Pull-out Mechanism of TRCC

Various analytical models have been developed to describe how pull-out load interacts with slip deformation in a fiber embedded in a cement-based matrix (A. Peled, 2016). These models typically explain two primary phases: an initial elastic phase referred to as chemical bonding and a subsequent slip phase dominated by friction. In the typical pull-out test setup illustrated in Figure 2-15 (a), when the force, P, is applied to the fiber, which is embedded over a specified length, l_e , within the cementitious matrix. Figure 2-15 (b) presents the interfacial shear stress versus fiber slip relationship modeled in this setup. The initial portion of this curve is characterized by a linear elastic response, continuing up to the maximum adhesive bond strength τ_{au}. Once this peak is surpassed, the response shifts to a frictional

phase τ_{fu}, where a steady frictional shear stress is maintained over the full range of slip.

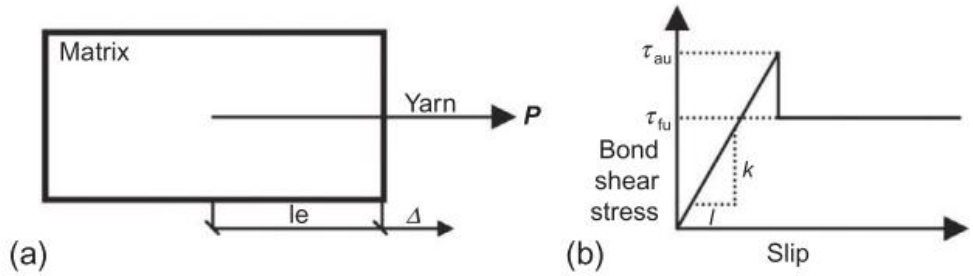

Figure 2-15 A schematic illustration of a standard pullout test setup and (b) the assumed shear bond stress at various slip values used for modeling pullout behavior (A. Peled, 2016)

However, the complex structure of the yarns and their interaction with the mortar leads to a specific phenomenon known as telescopic pull-out of the textile within the mortar. To better understand this phenomenon, the yarn structure will first be explained in the following section.

2.3.1.1 Yarn structure (microstructure)

In numerous instances, fabrics are constructed from multifilament yarns (rovings), which are comprised of hundreds or thousands of filaments with a relatively narrow diameter. This type of yarn presents a variety of benefits as a reinforcement material, which makes it suitable for the creation of high-performance cementitious composites. Nevertheless, the utilization of multifilament reinforcements in cementitious composites is inherently challenging, primarily due to the particulate nature of the cementitious matrix. The internal spaces between the filaments of the yarn (with internal dimensions of less than 5 μm) consist of relatively large particles (5–70 μm particles), which are larger than the internal dimensions of the spaces themselves. Consequently, the cement particles are unable to fully penetrate the internal spaces between the inner filaments of the strand. This results in a distinctive

microstructure, wherein the external filaments (sleeve) are in direct contact with the hydration products (owing to the effective penetration of cement grains), while the internal filaments (core) remain relatively free due to the limited cement penetrability or even the absence of the cement matrix between the core filaments (A. Peled, 2016). In this type of microstructure, the reinforcement unit is not a discrete filament fully surrounded by a cementitious mortar, rather it is a multifilament yarn with internal voids between the filaments enclosed by a particulate mortar as depicted in Figure 2-16 (A. Peled, 2016).

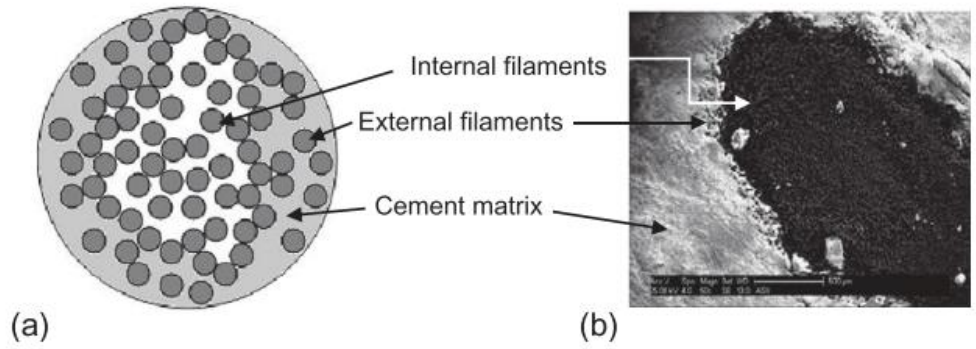

Figure 2-16 Cross-section of a yarn inserted in cementitious mortar (a) schematic presentation (b) carbon yarn in mortar (Soranakom & Mobasher, 2009)

2.3.1.2 Telescopic pull-out mechanism

This distinctive form of partial cement penetration (depicted above) gives rise to unique bonding mechanisms, characterized by direct contact between the external filaments (sleeve filaments) and the cement matrix, resulting in a strongly bonded matrix-filament interface. Therefore, they become subject to fracturing during the loading process, which results in the delivery of high first-crack stress. After the external filaments have failed, a telescopic type of pullout is generated, in which the internal (core) filaments slip against the external (sleeve) filaments. Subsequently,

stresses are transferred and distributed exclusively through surface interactions between the components (Banholzer, 2006; Brockmann & Brameshuber, 2006). It can be concluded that the core filaments are not utilized effectively for stress transfer and may be considered as less efficient use of resources. The inadequate utilization of the inner filaments is evident when comparing the tensile behavior of cement composites reinforced with carbon fabric to that of the fabric itself (not embedded in a cement matrix). The tensile strength of the cement composite is significantly lower than that of the fabric alone, due to the low cement penetrability Figure 2-17. Furthermore, the composite displayed a greater strain compared to the strain observed in the standalone fabric, due to the pullout of the core filaments from the composite bundle. Notably, the composite filaments, lacking direct contact with the matrix, were free to slide (A. Peled, 2016).

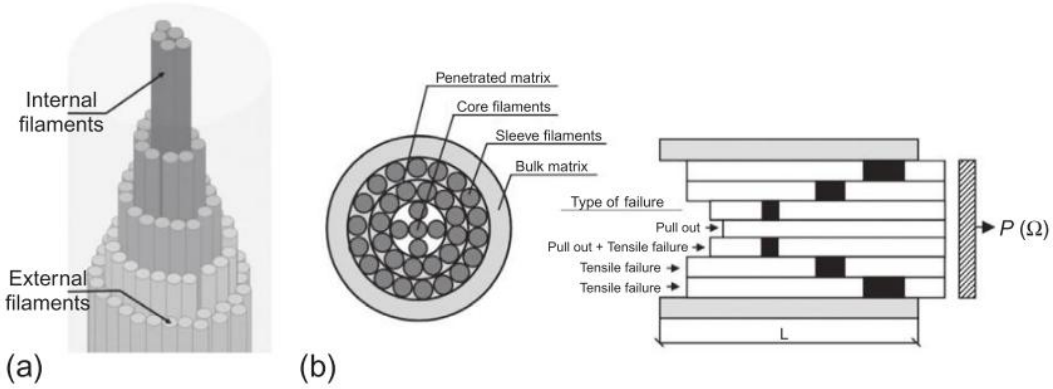

Figure 2-17 Telescopic pull-out phenomenon of the yarn in a cementitious mortar (a) after pull-out development, and (b) schematic depiction of telescopic failure in a yarn structure (Cohen & Peled, 2010)

2.3.2 Single-Sided Pull-out Tests

The test setup and schematic depiction of single-sided pull-out tests for TRCC are depicted in Figure 2-18 (Preinstorfer & Kollegger, 2020). Within saw cuts on both sides, the outer yarns are separated, leaving the central yarn as the sole link between the two sections of the specimen. The lower segment has an extensive bonding length, whereas the upper segment possesses a specified bonding length equivalent to the distance of a single weft yarn. While extensive bonding length ensures complete yarn anchorage with no anticipated yarn displacement, the upper side experiences failure. Accurate inspection is essential during the evaluation process, as the specimens affected by cutting must be identified and separated. Utilizing metal rings as formwork guides prior to the mortar application aids in positioning samples within the testing frame. The testing procedure involves securing the lower portion of the specimens with clamps while subjecting the upper portion to load via a bolted joint. This distinctive methodology enables the assessment of the bond characteristics of fabrics while considering the possibility of a splitting failure. The extent of crack opening is commonly measured using the Linear Variable Differential Transformer (LVDT) in all circumstances (Figure 2-18).

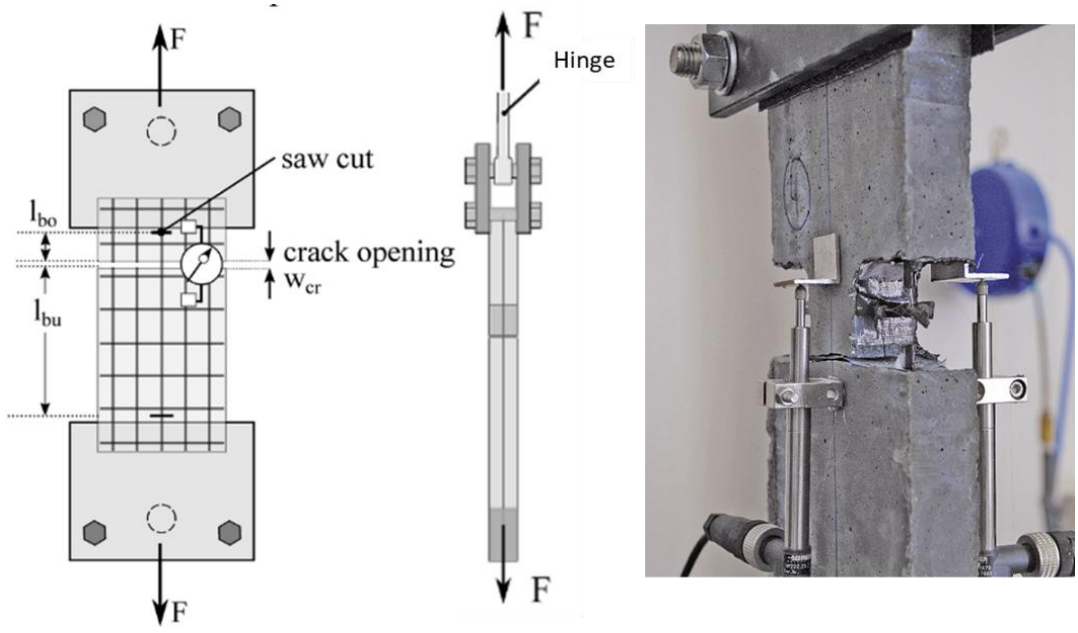

Figure 2-18 Schematic illustration and setup of single-sided pull-out testing (Preinstorfer et al., 2024)

2.3.3 Double-Sided Pull-out Tests

The TRCC double-sided pull-out (DSPO) test, as illustrated in Figure 2-19, was originally developed to determine the anchorage length required for flexible textiles, such as SBR-impregnated carbon fabrics and dry fabrics (Bielak et al., 2018; Butler et al., 2009, 2010; Silva et al., 2014). This test simulates the circumstances of a reinforcement crossing a crack with multiple yarns and a thin layer of fine-grained mortar covering it. A specimen used in the DSPO test comprises of TRCC specimens with a horizontal notch on both sides, indicating the location of the intended crack. The depth of this notch is linked to how the reinforcement is arranged in the cross-sectional area. An alternative setup for the DSPO test involves a symmetrically narrowed prism with a 1-mm midspan notch. In both cases, the specimen's top and bottom sections are separated by steel plates that are attached to the specimen either through adhesion or by being fastened using screws or a hydraulic force. The rigidity

of textiles like epoxy-impregnated carbon fabric could be impacted by the pressure exerted during clamping in the test. Moreover, such reinforcement typically forms a stronger bond with concrete, which can result in longitudinal cracks. This cracking tendency is suppressed by applying high clamping pressures, leading to a reduced anchorage length requirement and altering the bonding properties.

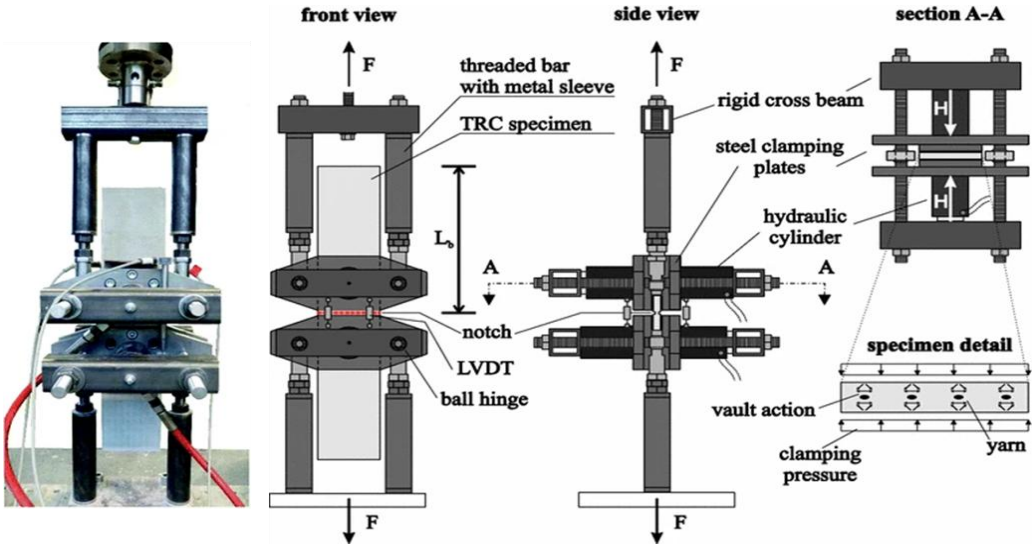

Figure 2-19 Double-sided TRCC pull-out testing setup (Bielak et al., 2018)

2.3.4 Yarn Pull-out Test

Yarn pull-out tests (Figure 2-20) are known as the most common test method for investigating bond performance in TRCC due to the simplicity of conducting the tests (Dalalbashi et al., 2021a; Lepenies, 2003; Peled et al., 2006, 2008; Zhu et al., 2020). The primary outcome of these tests is a set of force-slip curves, which can then be used to develop bond-slip laws for use in analytical or numerical models (Dalalbashi et al., 2021; Y. Li et al., 2018; Tran et al., 2021; Venigalla et al., 2023). A critical part of this procedure is ensuring the accuracy of the solution with respect to the bond-slip laws, which requires accurate measurement of slip at both the loaded and free ends of the specimen. Given the challenges associated with measuring the

strain distribution along the embedded length, it is a common practice to assume a stress/strain distribution. In order to reduce the impact of contact compression force experienced at the support, introducing a tube in the concrete positioned at the loaded section of the yarn is recommended. This approach aligns with the established bond test for determining the bond strength of conventional RC, resulting in a less disrupted bonded area and a more realistic representation of bond behavior. However, owing to the considerable thickness of the samples, which often do not mirror the thickness of actual TRCC specimens, the probability of splitting failure is typically minimized, and the force-slip correlation derived from these tests typically represents an upper bound of the bond strength.

Figure 2-20 TRCC yarn pull-out test setup test setup (Dalalbashi et al., 2018)

2.4 TRCC Components Affecting Slip-Bond Performance

2.4.1 Textile Material Type

The type of textile material employed has a substantial impact on the bonding performance of TRCC, particularly when the yarn has not had an impregnation process. This effect can be attributed to a direct interaction between the filament and the mortar, which in practice determines the bonding mechanism. This is dependent on the adhesion and friction between the two main elements, but this is also subject to alteration by the filling of the space between the filaments. In general, the strength of the bond increases with a more compact microstructure in the vicinity of the filaments. (Preinstorfer et al., 2024). In an experimental study conducted by Williams et al. (2014), a one-sided testing procedure was developed to assess the bonding efficacy of basalt and carbon fabrics. The results indicated comparable bond performance for both carbon and basalt fabrics. However, the two types of textile exhibited different failure mechanisms. Carbon fabrics failed primarily through yarn extraction, while basalt fabrics showed failure modes involving both yarn rupture and yarn pull-out. Another study found out that dry carbon textile and a coated AR-glass textile exhibited similar bond strengths, highlighting the influence of coatings on slip-bond behavior in TRCCs (Mader et al., 2004). While carbon fibers demonstrate resistance to alkaline environments, AR-Glass fibers are susceptible to deterioration through two primary mechanisms: chemical degradation and physical embrittlement. Exposure to alkaline conditions in concrete gradually degrades AR-glass fibers, primarily due to the filling of spaces between the filaments, which strengthens interfilament adhesion. This enhanced bonding reduces the yarn's flexibility, especially when its orientation is not perpendicular to newly formed cracks in the matrix.

2.4.2 Cementitious Mortar

The water to binder ratio in cementitious mortars is a crucial factor in TRCC bonding performance (Barhum & Mechtcherine, 2012). A single-sided pull-out test revealed that a lower water-to-binder ratio shifts the fracture mechanism from yarn pull-out to yarn rupture, leading to increased cracking stress. Additionally, a reduced water-to-binder ratio results in a denser microstructure with lower porosity, enhancing the bond between the mortar and textile yarns. It's well-established that compressive strength significantly influences bonding performance in conventional reinforced concrete, with higher compressive strength correlating to increased bending stiffness and strength. In order to reinforce textiles, it is necessary to consider the specific characteristics of the mesh size of the fabric and the complex geometry of the cross-section structure. Therefore, in many cases, this requires the use of TRCC matrices consisting of fine-grained concrete with a higher strength, in order to ensure appropriate interaction between the cementitious composites and textile components (Preinstorfer et al., 2024). In this context, Donnini et al. (2016) used three distinct types of mortar, labeled as "Mortar-15", "Mortar-30", and "Mortar-45" representing mortar class strengths of 15, 30, and 45 MPa, respectively. These were utilized together with dry and partially impregnated textile fabrics. The results showed that while increasing mortar strength improves bond performance, bonding in dry textiles relies solely on the interaction between the mortar and the outer filaments. The mortar and inner filaments can easily slip during loading due to the relatively large size of hydration products, which prevents them from effectively penetrating the spaces between the inner filaments, as illustrated in Figure 2-21 (Donnini et al., 2016).

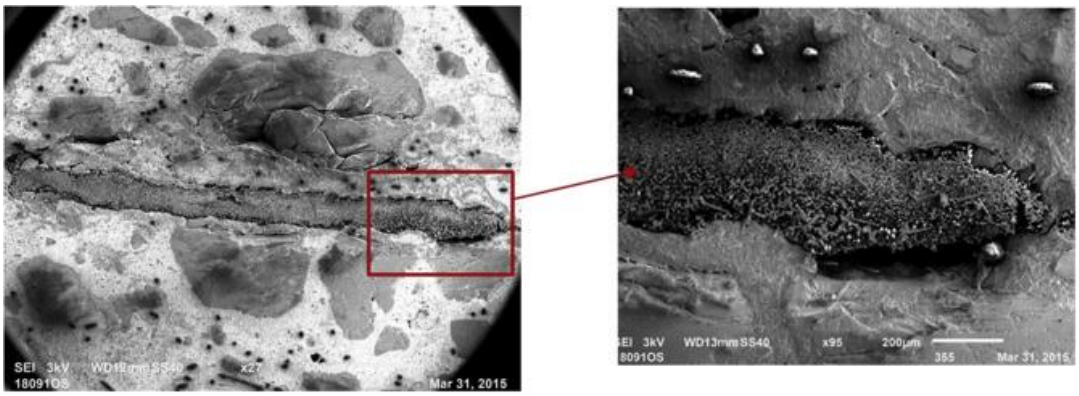

Figure 2-21 SEM pictures: bonded part of dry textile within mortar (Donnini et al., 2016)

Partially impregnated yarns (Figure 2-22), conversely, demonstrate enhanced bonding due to improved cohesion in the load-carrying capacity among the filaments of the yarns.

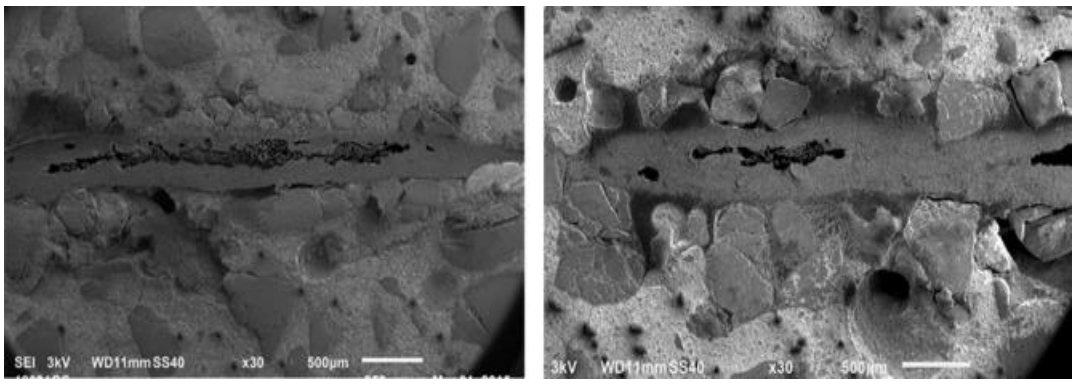

Figure 2-22 SEM pictures: bond of partially coated yarn with mortar (Donnini et al., 2016)

Butler et al., (2010) investigated the impact of matrix composition and accelerated aging on the bonding characteristics of dry glass textile reinforcement. Three fine-grained concrete mixtures, labeled M1, M2, and M3, were employed in that study as

binder materials. The fine-grained mortar featured a maximum aggregate size of 1 mm and a substantial binder amount. Each mortar type distinguished itself from the rest based on alkalinity, rate of hydration, and particle size distribution of the binder. The composition of the matrices is provided in Table 2-1

Table 2-1 Fine-grained concrete compositions, masses in kg/m3(Butler et al., 2010)

Matrix composition (kg/m^3)	**M1**	**M2**	**M3**
CEM I 32.5 R	–	557	861
CEM III/B 32.5 NW-HS-NA	550	–	–
Fly ash	248	251	–
Microsilica suspension (50 mass% powder, 50 mass% water)	55	56	–
Sand 0–1 mm	1101	1114	1148
Water	248	251	287

Results showed that the mortar with the highest amount of cement (M3) showed better initial bonding performance, which is attributed to the formation of a dense microstructure by the C-S-H phase. On the other hand, M1 displayed a more porous microstructure at the bond interface, reducing bonding efficacy. Following accelerated aging, matrix M3 experienced a significant decline in bonding performance and a brittle failure mode, whereas matrix M1 retained good bonding properties and demonstrated a more ductile behavior. The authors connected this phenomenon with the diminished formation of portlandite crystals among the filaments with lower OPC content, which could fracture and create cracks in the filaments under tensile deformation (Butler et al., 2010).

Alternative binder usage, such as geopolymers mortars, presents a potentially promising tool for investigating new forms of TRCC that were previously unnoticed because of the high alkalinity of ordinary Portland cement binder solutions. However, there is a lack of literature focusing on the bonding characteristics of geopolymer concrete reinforced with textiles (Preinstorfer et al., 2024). An investigation was conducted by De Santis et al. (2017) on the application of

metakaolin-slag-sodium-silicate GeoPolymer (GP) grout as a matrix for the bonding of four fabrics composed of basalt, glass, carbon fibers, and two ultra-high tensile strength steel fabrics to soft mud and strong clay bricks for structural reinforcement purposes. The geopolymer was subjected to a thorough chemical and physical analysis, demonstrating the completion of the geopolymerization process and the robust stability of the material against leaching, freeze-thaw cycles, and high-temperature exposures, in addition to possessing satisfactory mechanical properties. Pull-off tests verified that the geopolymer grout exhibited exceptional adhesion strength, effectively bonding the meshes and fabric to both clay bricks. To find a promising alternative in TRCC production for retrofitting and strengthening of masonry structures, Arce et al. (2023) used Alkali-activated materials (AAM). They tested various mortars that contain fly ash, ladle furnace slag (LFS), and metakaolin to assess the composite's compressive and flexural strength, the critical characteristics for their possibility of use in TRCC applications. The results indicated that the utilization of pure, high-calcium fly ash as a primary component of the binder resulted in an insufficient bonding performance between mortar and textile. However, the use of potassium-based activators resulted in superior bonding performance compared to sodium-based activators.

2.4.3 Impregnation of the Textile Monofilaments

The impregnation materials which is used to coat the textile significantly influence the bonding characteristics of TRCC as shown in Figure 2-23. The coating procedure satisfies various purposes, such as facilitating the transfer of loads between the individual filaments, bonding between yarns and mortar, covering imperfections on the filament surfaces, protecting the fibers' surfaces from corrosive environments, and maintaining the uniformity of the yarn as a single element throughout the manufacturing and load application phases (Preinstorfer et al., 2024).

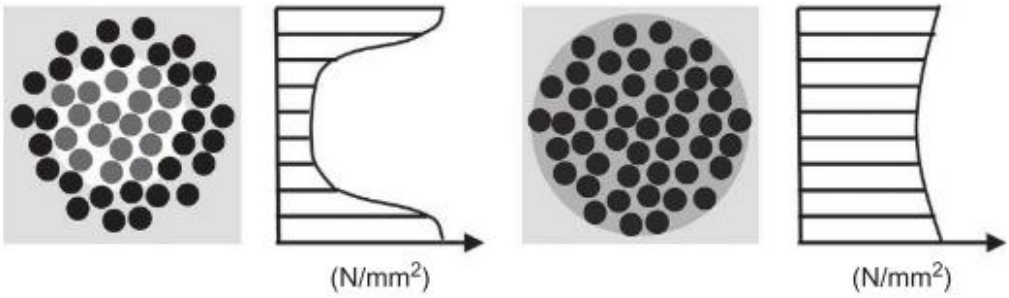

Figure 2-23 Stress gradient distribution in yarn cross-section without impregnation (left) and with impregnation(right) (Gries et al., 2016)

The impact of the applied impregnation on the TRCC behavior relies on the coating material type. Polymers with a high Young's modulus increase the maximum force the component can persist while reducing its ductility. The crack opening under the stress of various coatings is illustrated in Figure 2-24. Unimpregnated yarns exhibit separate filament extraction during crack opening. Although the maximum load level is relatively low compared to impregnated yarns, the deformation is substantially high. Impregnated yarns obtain a more rigid response from the members and can carry higher loads. Nevertheless, failure in TRC members reinforced with coated textile yarns tends to occur at an earlier stage.

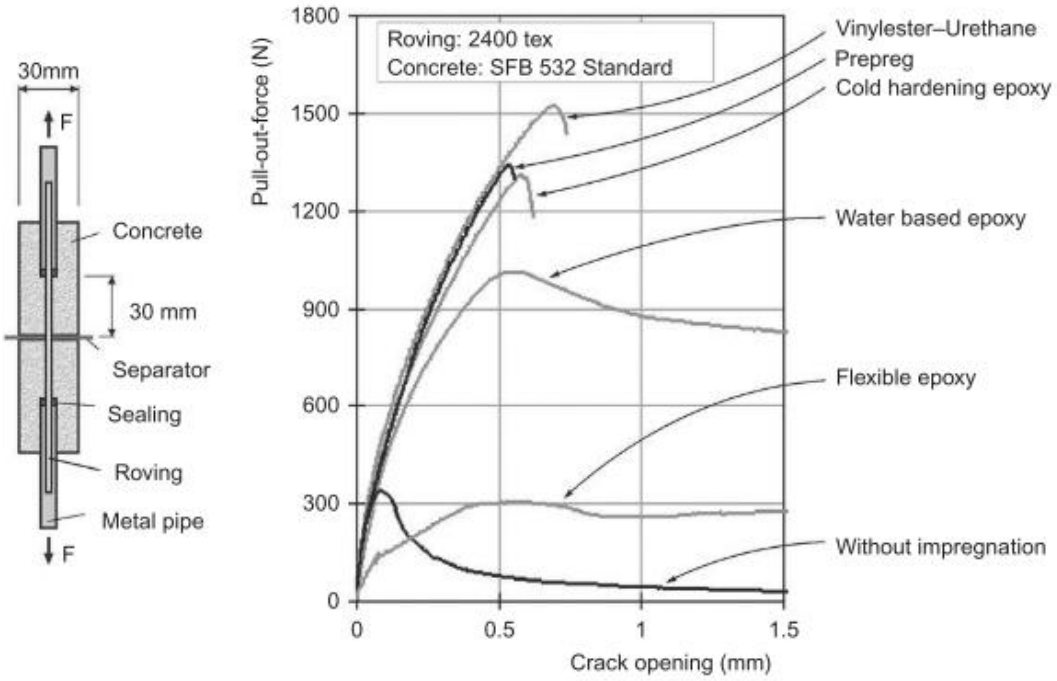

Figure 2-24 Double-sided pull-out Load-slip curves for different impregnation materials (Gries et al., 2016)

In selecting an appropriate impregnation material, the main factors to consider are its effects on chemical and mechanical characteristics and its ability to bear the temperature range and exposure duration during application. The impregnation process, whether resulting in full or partial impregnation, creates a sealed layer on the fabric that significantly influences bond performance. For example, Donnini et al. (2016) investigated the influence of different types and dosages of organic impregnations applied to carbon fabric on its bond behavior with mortar. Direct tensile, pull-off and shear-bond double-lap tests were conducted. By altering the degree of impregnation of the fabric during its manufacture, experiments are conducted on various combinations of textiles and mortars, namely dry fabric, light impregnation, medium impregnation, and high impregnation. While the failure mode did not alter, the peak load increased by 75% in the double shear test results when

the fabric exhibited a medium or high impregnation level. Very light impregnation levels resulted in behavior similar to that of dry fabrics.

In another study, epoxy resin or styrene-butadiene rubber (SBR) are used as polymeric impregnation material in an industrial scale (Preinstorfer et al., 2024). Textiles impregnated with SBR are characterized as having a "weak" impregnation, where the bond between the yarn and matrix is determined by a combination of friction and chemical bonding at the surface. This is evidenced by the presence of a greater amount of hydration reaction products on the surface of the fabric. On the other hand, epoxy resin-based impregnations typically exhibit limited chemical bonding with the cementitious matrix. Bond performance in these cases relies primarily on friction and mechanical interlock, which is dependent on the presence of geometrical irregularities along the yarn (Preinstorfer et al., 2024).

2.4.4 Textile Architecture

In addition to the composition, the architecture and geometry of the textile reinforcement also affect their bonding performance. The manufacturing process impacts the textile’s geometry. The most common shape for impregnated textiles is a flat elliptical shape rooted in the production procedure as shown in Figure 2-25 . In this process, the impregnation material is forced into the voids between filaments under pressure, resulting in an elliptical yarn shape with a higher circumference-to-cross-sectional area ratio (Hahn et al., 2019).

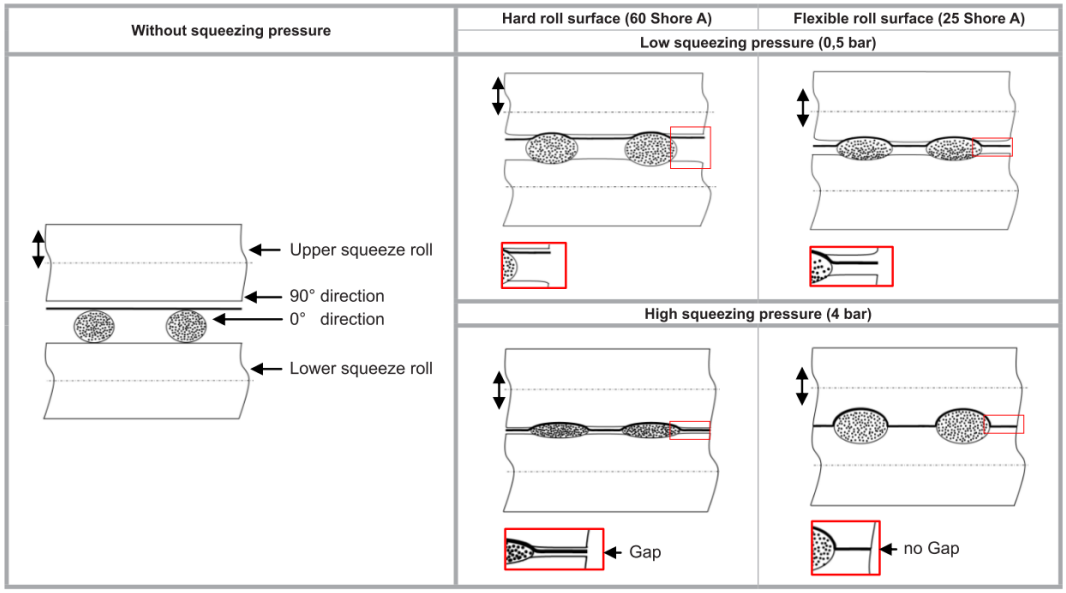

Figure 2-25 Illustration of squeezing pressure process in grid-like noncrimp textile (Hahn et al., 2019)

The larger circumference-to-cross-sectional area ratio increases the contact area with the surrounding cementitious mortar, leading to improved load transfer and bond performance (Quadflieg et al., 2017). However, the elliptical shape can lead to uneven stress distribution within the concrete due to bond stresses. This can result in increased tensile stresses, making the TRCC component more susceptible to bond failure due to concrete splitting. Other influencing characteristics in yarn architecture that lead to splitting failure are geometrical variation in the longitudinal direction, waviness of yarns in the longitudinal direction, and mechanical anchorage because of transverse yarns as depicted in Figure 2-26 (Preinstorfer & Kollegger, 2020). This failure mode can be controlled by using these factors to ensure the required bonding quality in TRCC.

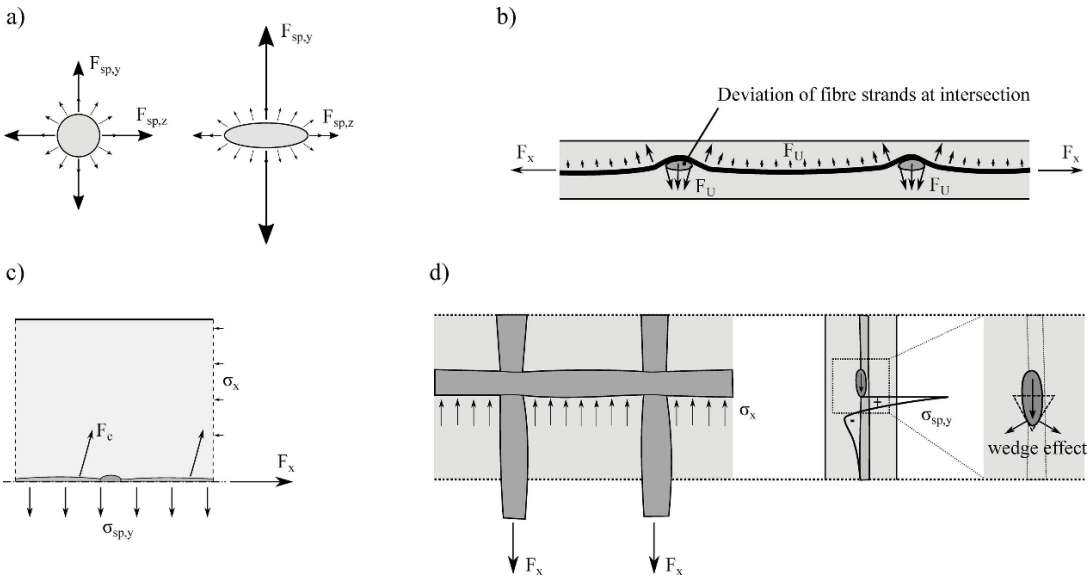

Figure 2-26 Influencing characteristics of yarn architecture on splitting failure mode: (a) cross-sectional shape; (b) yarn longitudinal waviness; (c) variation in cross-section of yarn in longitudinal directions; (d) mechanical anchorage due to transverse yarns (Preinstorfer & Kollegger, 2020b)

It was also shown that geometrical variation in longitudinal yarns increases mechanical interlock between textile and cementitious mortar, leading to better bonding in TRCC (Preinstorfer & Kollegger, 2020). A novel profiling method has been utilized to generate a precise tetrahedral profile. The investigation demonstrates a micrographic examination involving profiled yarns. It is revealed in the analysis that the bonding characteristics of profiled yarns surpass those of traditional yarns lacking profiles. Moreover, the study suggests that a specific bond alteration can be achieved by adjusting the profile geometry and the impregnation and consolidation parameters (Penzel et al., 2022).

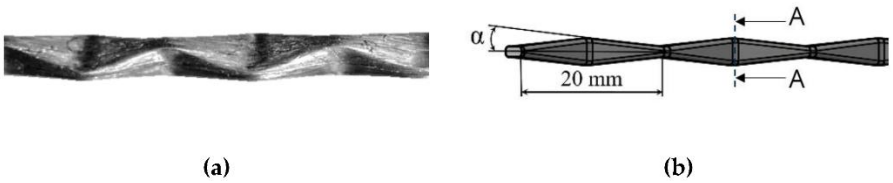

Figure 2-27 Profiled yarn with tetrahedral geometry; (a) picture (b) schematic depiction (Penzel et al., 2022)

The manufacturing process also influences the potential waviness of textiles, which can result from yarns that are not perfectly straight or are asymmetrically joined at the crossing points (Hausding et al., 2011). Textile waviness is critical in enhancing bonding as the mechanical anchorage is attained for high curvatures during the yarn extraction from the mortar. However, the deviation of the yarn axis from the reinforcement layer induces additional splitting tensile stresses (Figure 2-28).

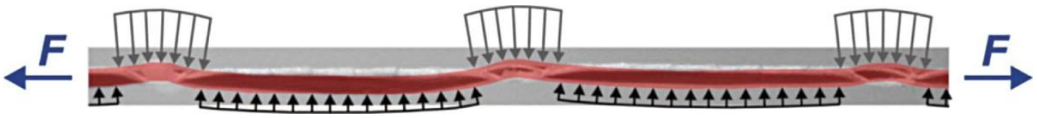

Figure 2-28 Exemplary force distribution in the textile yarn under tensile loading (Hausding et al., 2011)

A significant contribution to the bonding phenomenon in textiles involves the transverse yarn anchorage mechanism, which can be explained as comprising two distinct stages: intact and failed junction bonds as shown in

Figure 2-29 (Peled et al., 2017). The anchorage at the point where yarns intersect is primarily attributed to the connection between warp and fill yarns and the resistance offered by the fill yarns in redistributing the applied load. Furthermore, the anchorage mechanism may also be influenced by the surface curvature of the yarn within a woven textile.

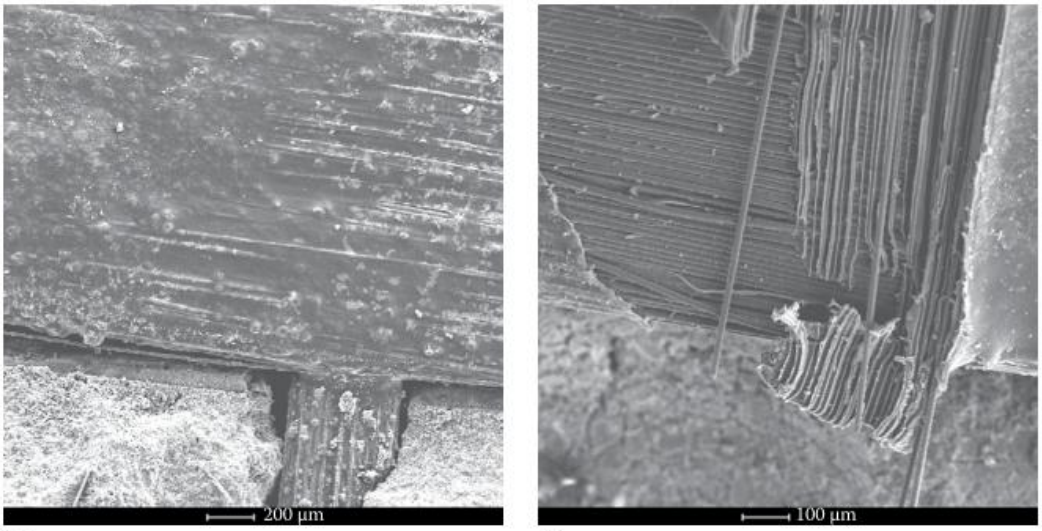

Figure 2-29 Transverse yarn mechanical anchorage in junction picture: (a) intact stage , (b) failed stage(Alva Peled et al., 2017).

2.5 Long-Term Performance of TRCC Under the Sustained Loading

While the previously discussed mechanical properties of TRCC are determined through instantaneous testing, creep behavior—a critical time-dependent factor—plays a significant role in the long-term performance of thin, lightweight structural elements. A thorough understanding of TRCC creep behavior is vital to ensuring the structural integrity of applications such as façades, pedestrian bridges, and retrofitted structures, thereby improving their reliability and sustainability. Given the substantial impact of concrete creep on TRCC performance and the limited research available on this subject, it is crucial to first develop a fundamental understanding of concrete creep. The following section introduces key terminology related to the creep behavior of concrete.

2.5.1 Creep of Concrete

The total deformation of concrete under sustained loading is divided into distinct parts: immediate deformation (instantaneous) and time-dependent deformation. The time-dependent deformation initiates promptly and continues at a diminishing pace throughout the loading process of concrete. This gradual deformation over time in concrete is commonly referred to as creep (Steven H. Kosmatka, Beatrix Kerkhoff et al., 2002). Creep of concrete could be categorized based on the following terminology (Alpes, 2016).

- **Basic creep** is identified as the deformation that occurs in concrete under conditions where there is no movement of moisture between the concrete and its surrounding environment.
- **Drying creep** is the additional deformation that happens in the drying process of concrete under sustained loading.
- **Transitional thermal creep** is the deformation that occurs when concrete exposes an increase in temperature
- **Total creep** is defined as the summation of basic creep, drying creep, and transitional thermal creep.
- **Recovery of creep** is the amount of strain recovered after sustained load removal.
- **Specific creep** is attained by dividing the creep strain on the corresponding applied stress i.e. creep strain due to a unit applied stress.
- **The creep coefficient** is defined as the ratio of the creep strain to the elastic strain.
- **The creep compliance function** is the summation of the elastic and total creep strains that occur due to a unit loading stress.

The creep of concrete is influenced by a combination of intrinsic and extrinsic factors. Intrinsic factors, such as design strength, aggregate content, and aggregate elastic modulus, are inherent to the material and are fixed at the time of casting.

Extrinsic factors, which can vary post-casting, include temperature, age, degree of hydration, relative humidity, and specimen size (Bazant, 1973).

Under normal stress levels, the ratio of creep to stress remains relatively constant. Creep in younger concrete is largely irreversible, whereas older or drier concrete exhibits more recoverable creep (Steven H. Kosmatka, Beatrix Kerkhoff et al., 2002). The creep strain is linearly proportional to the applied stress up to about 50% of the ultimate strength of the concrete. In addition, specific creep increases with higher water/cement (w/c) ratios. In addition, aggregates act as a restraint against deformation, including shrinkage, thus reducing the total amount of creep.

The creep behavior of concrete is influenced by the types of loads applied, which induce compressive, tensile, or flexural stresses (Kim et al., 2019). While concrete is primarily designed to resist compressive stresses, understanding the behavior under tensile loading is also critical, particularly for structural elements subjected to tensile forces(Ranaivomanana et al., 2012). However, accurately quantifying tensile creep is challenging due to concrete's low tensile strength, making it difficult to directly compare tensile and compressive creep. While the initial tensile creep may be more pronounced than compressive creep, especially over shorter durations, compressive creep may become more significant over longer periods. Both compressive and tensile creep are influenced by the same experimental parameters (Bissonnette et al., 2007).

The mechanism of tensile creep, based on microcracking as described by Ward & Cook, (1969), demonstrated that conventional seepage theory incompletely predicts the tensile creep of concrete. Their experimental results, particularly those conducted under varying humidity conditions, deviated significantly from the assumptions and predictions of the theory. The authors suggested that microcrack propagation is important for tensile creep, particularly under drying environments where cracks grow during the test and contribute to deformation. It was shown that the tensile creep of concrete with less paste is higher, confirming that crack development might be affected by aggregate content, which contradicts prior findings on compressive

creep. Bissonnette et al. (2007) investigated the applicability of seepage theory, viscous shear theory, and microcracking—mechanisms commonly used to explain creep under compression—to the phenomenon of tensile creep. Seepage theory was considered a suitable approach for describing tensile creep, as it accounts for the movement of free water within larger capillaries, which is adsorbed by expanding gel pores under tensile load. However, tensile creep was observed to be higher under drying conditions compared to that of sealed conditions, which could not be described by seepage theory. As a result of the drying process, water is transported from the paste, leading to contraction. However, tensile creep under drying conditions has been observed to increase expansion due to tensile creep, which represents a limitation of the seepage theory in accurately describing tensile creep (Bissonnette et al., 2007).

Furthermore, tensile creep can be effectively explained by viscous shear theory. According to this theory, the applied load, in combination with evaporation, disturbs the adsorbed water layer, leading to the removal of water and allowing gel particles to slide or flow over one another. When water movement is restricted, only the adsorbed water is disrupted. This phenomenon explains why basic creep is smaller than drying creep (Bissonnette et al., 2007).

2.5.2 Testing for Creep of Concrete

The standardization for compressive creep testing of concrete with a maximum aggregate size of 50 mm is outlined in ASTM C 512 (ASTM, 1987). Cylindrical specimens with a diameter of 150 mm and an L/D of 2 are used in the tests, as shown in Figure 2-30. This method allows the determination of creep strains up to 40% of the compressive stress, on the assumption that compressive creep is proportional to compressive strength up to this level. Prior to testing, the specimens are moist cured at a temperature of 23±1.7°C for seven days. Following moist curing, the specimens are stored at 23±1.1°C with a relative humidity of 50±4% until the end of the test. The load is maintained using a loading frame consisting of head plates and a load

holding element. When the objective is to determine basic creep, the specimens are sealed to prevent loss of moisture by evaporation.

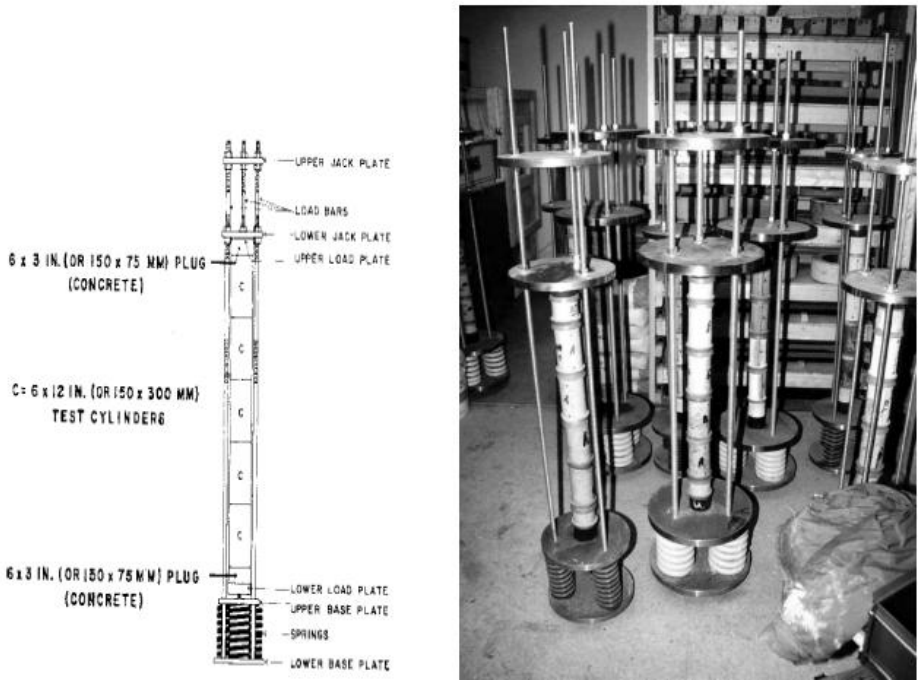

Figure 2-30 ASTM C 512 test setup of creep under compression (ASTM 1987)

A standardized test method for tensile creep determination does not currently exist. However, several direct tensile creep testing setups have been documented in the literature. For example, (Poston et al., 2001) used 76 mm x 76 mm x 305 mm specimens and applied loads up to 40% of the tensile strength determined at 3, 7, and 28 days using a tensile creep test frame, as shown in Figure 2-31. The initial loading was conducted at the three-day mark, with subsequent increases at the seven- and 28-day intervals, maintained until the end of the test. Strains were measured using mechanical strain gauges over a gauge length of 250 mm.

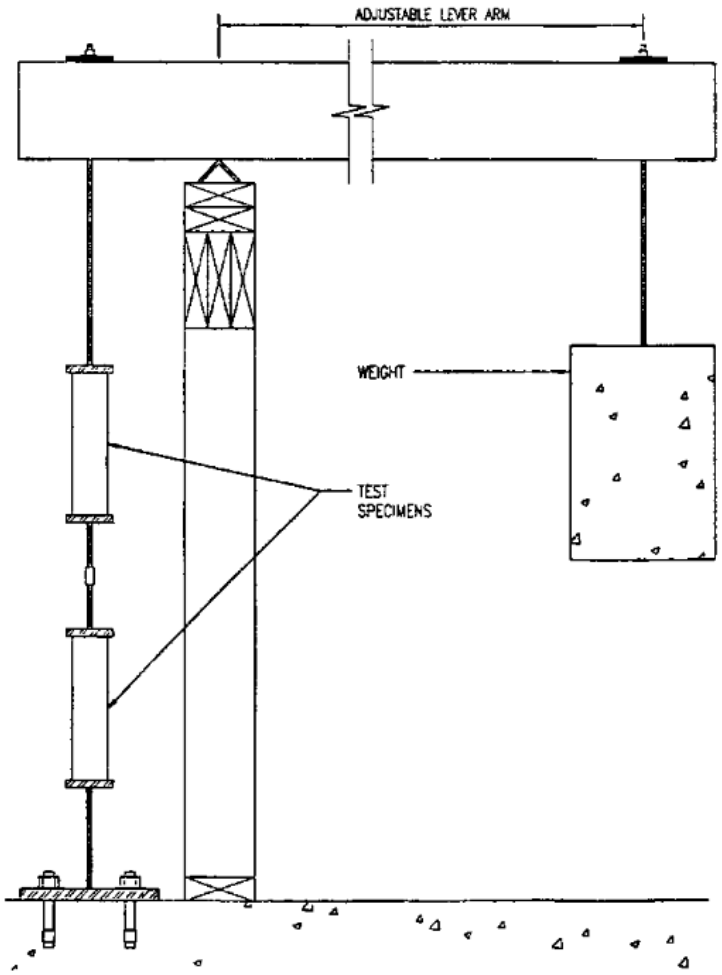

Figure 2-31 Tensile creep frame(Poston et al., 2001)

Similar to the aforementioned test setup, a tensile creep test setup was designed at the Materials of Construction Laboratory of the METU Department of Civil Engineering, in the form of a lever arm, and steel I-beams were employed to construct the tensile creep test frame (Keskin, 2012). Four such frames were constructed, each with the capacity to test three specimens simultaneously. The total height of the loading frames is 1.7 meters, and the total length of the lever is 2.5 meters, with a load ratio of approximately 1/7 (the ratio of the weight placed on the frame to the applied load). The maximum weight that can be placed on the frame is 250 kilograms, which corresponds to approximately 2,000 kilograms of force (kgf)

of the applicable load. The loading apparatus is equipped with steel plates of 5 and 10 kg mass, which provide a sensitivity of approximately 35 kgf. The specimens can be loaded without any eccentricity, as hinge connections are used in the joints between the frame and the specimens. Details of the tensile creep loading frame and its connections can be seen Figure 2-32 and Figure 2-33, respectively. Following assembly in the laboratory, all tensile creep test frames were calibrated using a load cell, and calibration charts were prepared for each frame. Length change measurements were conducted using a DEMEC digital mechanical strain gauge with a measuring range of 250 mm and a sensitivity of 0.001 mm. In this thesis the same loading frames were utilized for creep testing of TRCC specimens with a slight modification.

Figure 2-32 Tensile creep testing frame at METU (Keskin, 2012a)

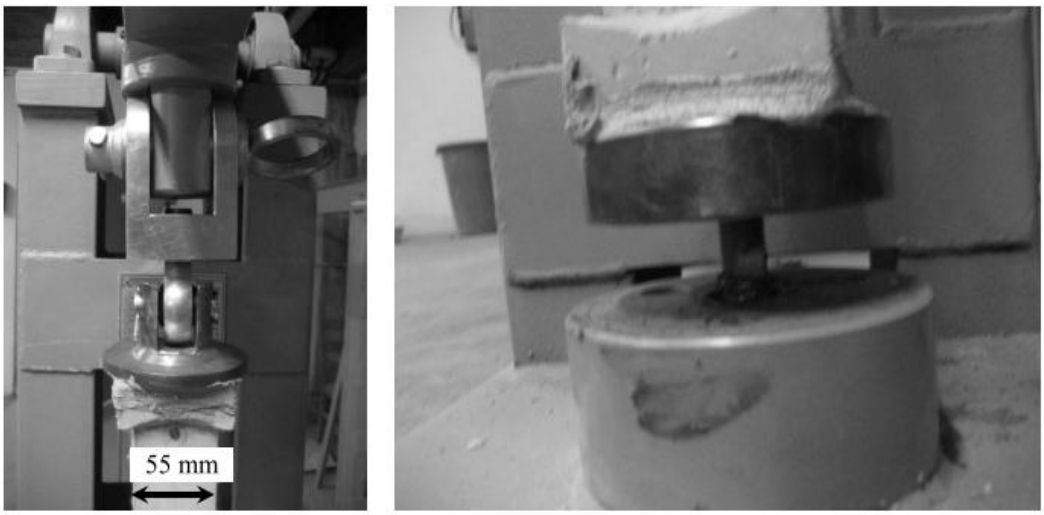

Figure 2-33 Ball joints in the loading frame (Keskin, 2012b)

CHAPTER 3

3 EXPERIMENTAL PROGRAM

3.1 General

This study aims to experimentally evaluate the mechanical behavior of carbon textile-reinforced cementitious composites (C-TRCC), including uniaxial direct tensile performance, slip-bond and tensile creep behavior. To this end, a three-phase study was conducted. In the initial phase, the mechanical characterization of C-TRCC was evaluated through uniaxial direct tensile tests. These tensile tests investigated the influence of several parameters, including the textile reinforcement ratio, textile architecture (specifically the effects of warp and weft yarns), and the use of two different cementitious matrix compositions. The first matrix contained a higher cement content, which was developed by German scientists for TRCC in strengthening applications and named M7 (Mechtcherine et al., 2016). The second mortar contained a high amount of fly ash and finer aggregates, and was based on a matrix which was developed for ECC production, known as M45 (Li & Li, 2019).

The second phase investigated the slip-bond behavior of C-TRCC using a yarn pull-out test method adapted from the direct tensile clevis gripping method, mimicking real-world TRCC applications. These tests evaluated the maximum pull-out force, nominal shear bond strength, and maximum pull-out related properties, considering the influence of mortar composition, warp and weft yarn architecture, and textile structure in both two- and three-yarn pull-out configurations.

The third phase assessed the tensile creep performance of C-TRCC under sustained direct tensile loading (at 25%, 50%, and 75% of tensile capacity) and exposure to different temperature conditions (20°C and 50°C). The influence of the cementitious mortar composition (M7 and M45) was also investigated.

This chapter presents the materials and test methods used in all three phases of the experimental program.

3.2 Materials

This study utilized a range of materials for the preparation of C-TRCC specimens, including Portland cement, siliceous sands, fly ash, superplasticizer, polyvinyl alcohol (PVA) fibers, and a grid-like woven carbon textile. The properties of these materials are described below.

3.2.1 Cementitious Materials

In the experimental investigation, CEM I 42.5R type ordinary Portland cement (equivalent to ASTM Type I) was utilized. This cement, manufactured by Baştaş Çimento A.Ş, has a specific gravity of 3.1 and a Blaine specific surface area of 3411 cm^2/g. Table 3-1 illustrates the chemical analysis results of the cement as performed by TURKCIMENTO.

Table 3-1 Chemical composition of Portland cement

Chemical Composition	**(%)**
SiO_2	18.32
Al_2O_3	4.48
Fe_2O_3	2.84
CaO	61.3
MgO	1.59
SO_3	2.78
Na_2O	0.28
K_2O	0.81
Cl^-	0.04
Loss on Ignition (LoI)	6.82
Insoluble Residue (IR)	0.76

The fly ash used in this research was sourced from the Sugözü Thermal Power Plant and classified as Class F according to ASTM C618. Its chemical composition as

determined by TURKCIMENTO is presented in Table 3-2. The Blaine fineness and specific gravity of the fly ash are 2900 cm^2/g and 2.1, respectively.

Table 3-2 Chemical compositions of Class F type fly ash

Chemical Composition	**(%)**
SiO_2	58.5
Al_2O_3	22.0
Fe_2O_3	6.41
CaO	3.13
MgO	2.15
SO_3	0.28
Na_2O	1.0
K_2O	1.39
TiO2	0.92
Loss on Ignition (LoI)	3.34

3.2.2 Sands

By definition, TRCC requires a fine-grained cementitious matrix with sufficient fluidity to effectively penetrate the textile mesh and provide a strong bond between the mortar and the textile. This principle was the basis for the development of the M7 mortar. Similarly, M45 mortar, recognized for their fine-grained matrices, were used as a reference benchmark. Consequently, in this study, siliceous sands with two different particle size distributions were selected to evaluate the effect of mortar composition on the performance of C-TRCC.

Sieve analysis of the siliceous sands was performed following ASTM C136-06 guidelines, while specific gravity and water absorption tests were conducted in accordance with ASTM C127-15. All tests were carried out in the Materials of Construction Laboratory of the Civil Engineering Department at METU. The physical properties of the two types of siliceous sand are summarized in

Table 3-3 Physical properties of the two siliceous sands

Properties	D_{max}= 1 mm	D_{max}= 0.25 mm
Specific Gravity (Saturated Surface Dry)	2.56	2.65
Specific Gravity (Oven Dry)	2.57	2.67
Specific Gravity (Apparent)	2.59	2.69
Water Absorption (%)	0.54	0.60

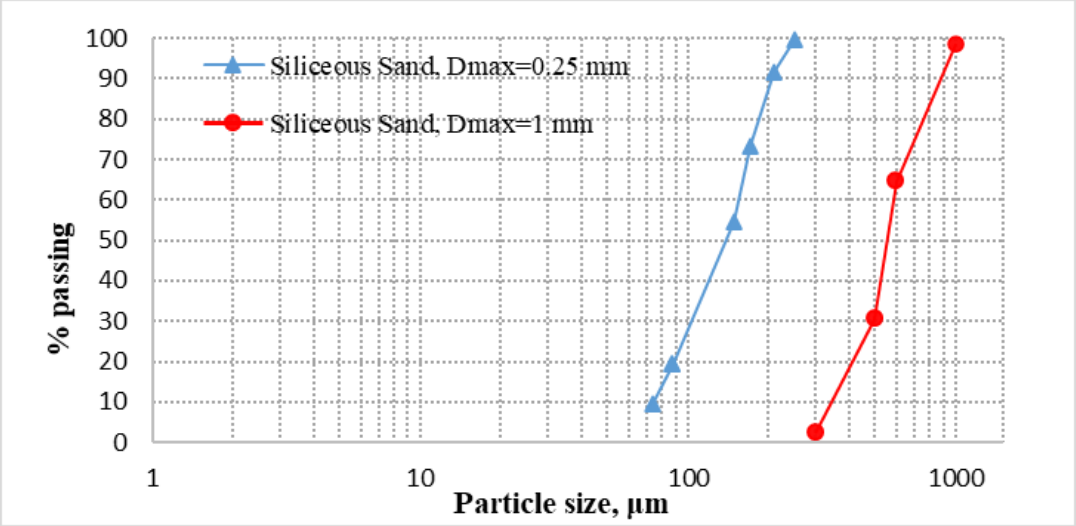

Figure 3-1 Particle size distribution of the two siliceous sands

3.2.3 Chemical Admixture

In TRCC production, a commercially available high-range water-reducing admixture, MasterGlenium 51, was used in all compositions to ensure optimal mortar penetration into textile meshes. The properties, as disclosed by the Master Builders Solutions corporation, are presented in Table 3-4.

Table 3-4 Properties of the high-range water reducer

Structure of the Material	Modified Polycarboxylate Ether Based
Appearance	Brown liquid
Specific gravity @ 20°C	1.082 - 1.142 kg/lt
pH-value	6-7
Alkali content (%)	≤ 3.00 (by mass)
Chloride content (%)	≤ 0.100 (by mass)

3.2.4 Carbon Textile

The carbon textile that was used in the experimental investigation, was grid-like and woven in two perpendicular directions - warp (0°) and weft (90°) - with a spacing of 16.7 × 16.7 mm², as shown in Figure 3-2. It was impregnated with styrene-butadiene rubber (SBR), and was commercially available from Solidian under the name "FLEX GRID-CAR-260-CCS1-14x14". The manufacturer's specifications detailing the properties of the fabric are given in

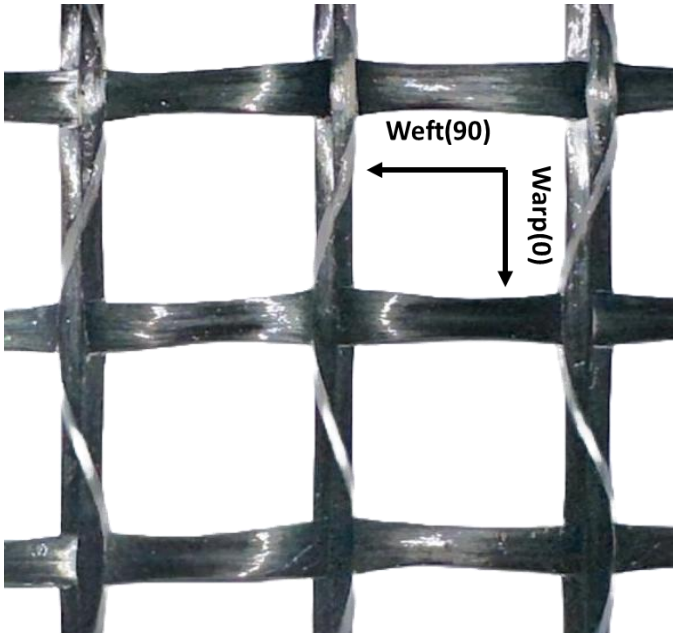

Figure 3-2 Grid-like woven carbon textile utilized in this study

Table 3-5 Manufacturer data on carbon textile properties

Property	Direction	Unit	Value	Tolerance
Impregnation Material	Styrene-butadiene resin (>18)			
Basis Weight	-	g/m²	260	±5%
Cross-Section of the Strands	Warp	mm²	0.9	-
	Weft	mm²	0.9	-
Cross-Section of the Reinforcements	Warp	mm²/m	54	-
	Weft	mm²/m	54	-
Mesh Size (Middle)	Warp	mm	16.7	±0.5%
	Weft	mm	16.7	±0.5%
Tensile Strength	Warp	kN/m MPa	126 2300	-
	Weft	kN/m MPa	120 2200	-

The longitudinal warp carbon yarns are divided, allowing the weft carbon yarn to interlace between these divided yarns at each intersection. Consequently, the warp yarns exhibited an average tex count of 800×2, whereas the weft yarn possessed a tex count of 1600. Additionally, a spiral glass yarn was interlaced in a leno weave pattern through the warp yarn to reinforce the intersections.

In literature, it is reported that the textile architecture has a determining influence on C-TRCC's mechanical properties (Preinstorfer et al., 2024). The difference in textile architecture stems from its manufacturing process (Venigalla et al., 2022). This process leads to quite different structures that filaments establish in warp (0°) yarns and weft (90°) yarns. Woven textiles are produced by intertwining two sets of yarns positioned perpendicularly at 0°/90° angles by weaving each yarn over and under the other in a repetitive pattern. The yarns running along the length of the textile are referred to as warp yarns, while those running across the width are known as weft or fill yarns. Within woven textiles, the yarns are interlinked through friction at the intersections, necessitating a sufficient quantity of these intersection points to maintain the fabric's stability; for this purpose, a leno woven yarn in the warp

direction is placed. Both warp and weft yarns are elliptical in shape, with some substantial differences in their geometrical and architectural characteristics (Hahn et al., 2019). To validate this and gain a deep understanding of the structural architecture of the textile used in this study, scanning electronic microscopy (SEM) analysis and 3-D laser scanning analysis were conducted

3.2.4.1 SEM Analysis

For a better understanding of the textile architecture and structure, SEM analysis was performed at the METU Central Laboratories. The SEM images depict quite different structures and architecture in terms of diameter and yarn alignment between weft (Figure 3-3-a) and warp (Figure 3-3-b) yarns.

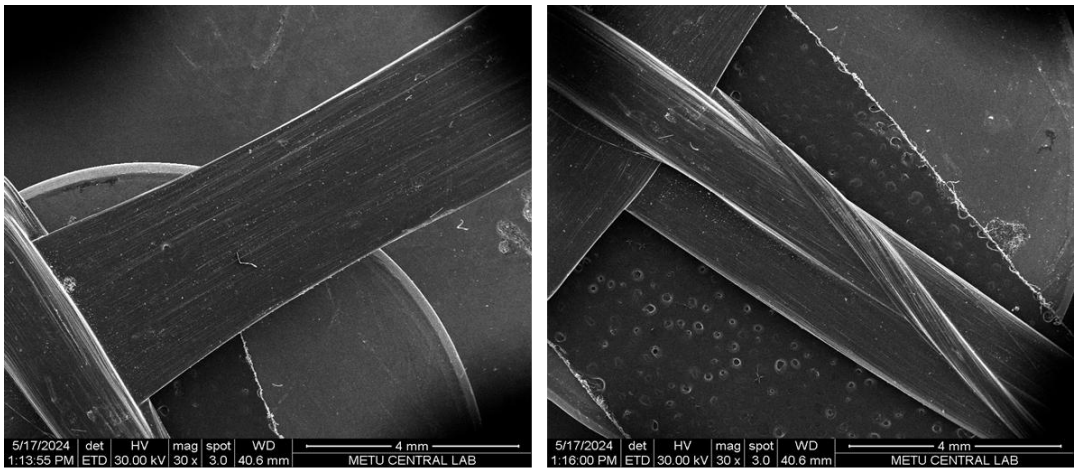

(a) (b)

Figure 3-3 SEM analysis: (a) weft (90°) yarn, (b) warp (0°) yarns with a leno woven thread

As can be seen from SEM images, weft or fill yarns have looser geometrical shapes and more geometric deviation in the longitudinal direction, originating in the squeezing of yarns throughout the fabrication process. The higher circumference is a consequence of the elliptical shape of the weft direction, which provides a greater contact surface between the yarns and the cementitious mortar. However, the

diminished contact area of this yarn in joint locations reduces the likelihood of contact with mortar. The insufficient tension in the production of textiles in the weft direction results in an unstable structure along the length of the textile, and the crimping in the lengthwise direction makes this direction prone to defects and less effective bonding (Hahn et al., 2019). In contrast, two warp yarns that is intersected with the weft yarn, results in a more compact and resilient structural configuration. The incorporation of a glass thread on the warp yarns facilitates the integration of these two yarns, enhancing the overall structural integrity in this direction.

The junction point (Figure 3-4) in grid-like woven carbon textiles, regulated by friction and further enhanced for increased structural stability using a leno woven thread, significantly impacts the mechanical properties of TRCC. It accomplishes this by regulating load distribution, enhancing structural integrity, improving flexibility, promoting bonding with the concrete matrix, and increasing overall durability (Friese et al., 2022)..

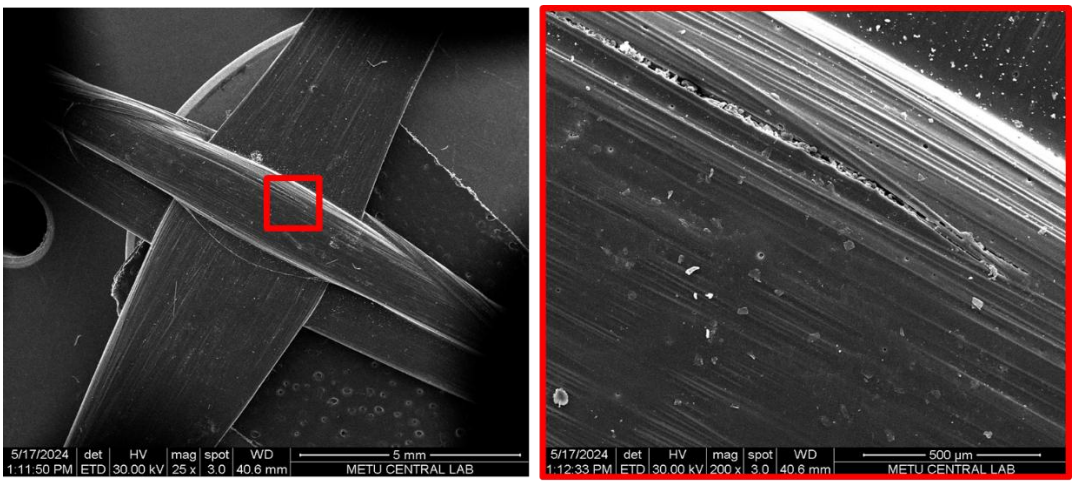

(a) (b)

Figure 3-4 SEM analysis: (a) yarns junction two warp yarns and one weft (b) illustration of SBR impregnation (defects are visible on filaments surface)

According to the manufacturer's datasheet, the textile is coated with styrene-butadiene rubber (SBR) due to its ability to improve ductility, bonding, and durability. SBR's elastomeric properties allow for high deformation without

cracking, enhancing mechanical interlock between the fabric and mortar. This results in better stress distribution and increased structural integrity. Additionally, the coating acts as a protective barrier, preventing direct contact between the mortar and filaments, thereby reducing the risk of filament degradation over time (Heins et al., 2023). However, SBR is sensitive to elevated temperatures (above 40°C), which poses a significant drawback for its use as a coating material in the construction industry. This temperature sensitivity presents a considerable challenge, particularly in warm climates, where maintaining material performance and durability can be more difficult (Rezig et al., 2020). It should be noted that, the application of SBR coatings requires careful control to ensure uniform coverage and proper adhesion, which can add complexity to the manufacturing process. Figure 3-4-b illustrates such a defect, which may be related to the processing of SBR as a coating material.

3.2.4.2 Laser Scanning

To accurately determine the geometrical properties of the textile yarns for subsequent mechanical characterization calculations (particularly shear bond stress) and to observe the cross-sectional geometry of the fabric yarns, a carbon textile sample was laser-scanned. This allowed for precise determination of the geometrical characteristics of the textile reinforcement. For that purpose, a 3D laser scanning procedure was employed using the Comet Yxlon FF35 CT system, located at the METU Design Factory (Figure 3-5). Scanning was made in high-power cone beam configuration using a 190 kV X-ray tube, acquiring 1080 projections in 360° rotation. The focus-object distance was 111 mm, and during the scan, the voxel size was 20.5 microns, hence acquiring high-resolution data. Environmental conditions were very controlled, and temperature fluctuated between 23.9°C and 24.1°C during the scanning process. Textile reinforcement was reconstructed in 3D with advanced reconstruction software from CERA-Comet (Comet's advanced reconstruction software), providing a highly detailed volumetric dataset. This dataset was processed using advanced algorithms, including auto-alignment and truncation correction,

ensuring an accurate and artifact-free model Figure 3-6. The resulting 3D model captured the intricate structure of the textile with an accuracy of approximately 20.5 microns, allowing for a detailed analysis of its geometry and structural integrity.

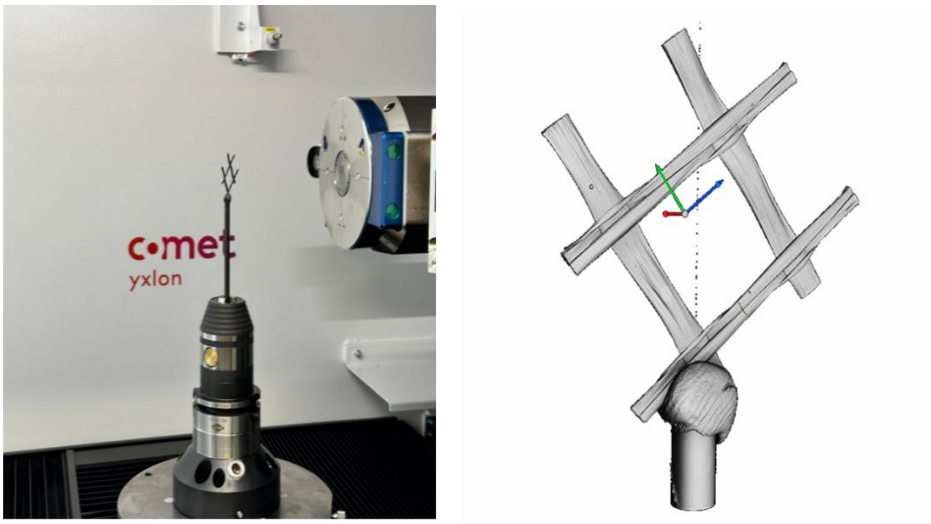

(a) (b)

Figure 3-5 Laser scanning: (a) textile specimen inside laser scanner, (b) its 3-D model

The 3-D model generated by the laser scanner facilitates precise examination of the textile structure and the geometric characteristics of the yarn, revealing that the weft yarns exhibit significant undulation and waviness along their length. Conversely, the warp yarns display a compact geometric configuration with less undulation and a more linear appearance. These findings are significantly important in the explanation of the mechanical performance of TRCC specimens under the uniaxial direct tensile and slip-bond tests.

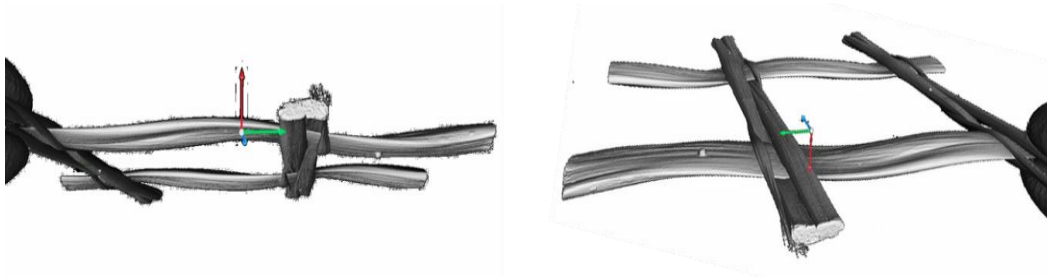

Figure 3-6 3-D Models of the textile from laser scanner

The cross-sectional geometry of warp (0°) was determined to have a width of 747.9 µm and a length of 2403.55 µm through the laser scanner analysis (Figure 3-7). Examination of the filament placement revealed a favorable level of density and a reduced occurrence of defects within the structure of carbon filaments. In weft yarn, cross-section dimensions are 1103.55 µm and 3326.09 µm for width and length diameters, respectively (Figure 3-8). From this data it can be concluded that weft yarns have a larger cross-sectional area and circumference, with a looser structure containing defects. The manufacturer's data indicates that both warp and weft yarns have the same cross-sectional area (A = 0.9 mm^2). However, laser scanning revealed a significant difference: the weft yarn exhibited an area of 2.8822 mm^2, approximately twice that of the warp yarn (1.4104 mm^2). This discrepancy can be attributed to the presence of spaces and defects within the geometry of the weft yarns, resulting in a larger measured cross-sectional area.

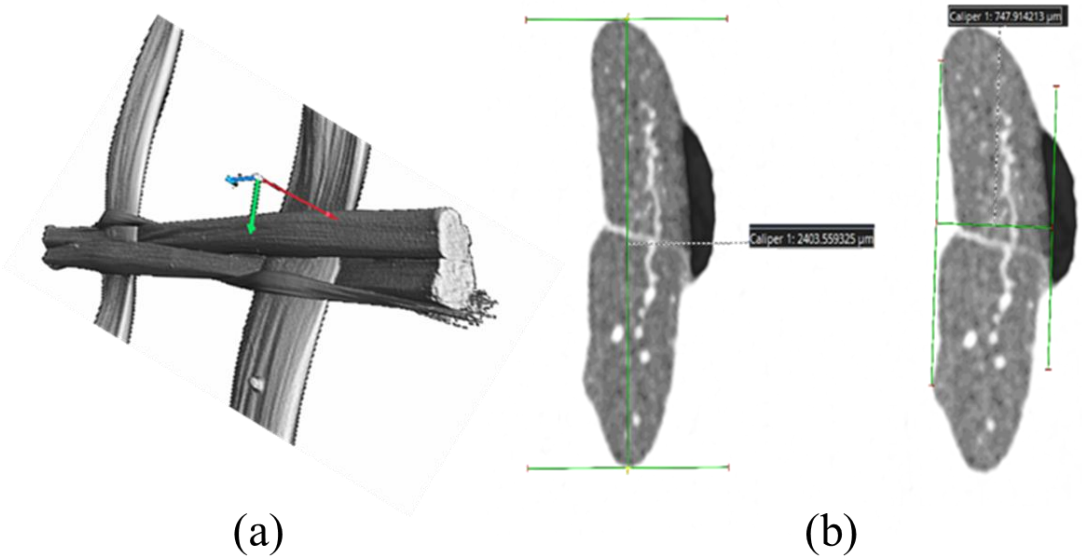

Figure 3-7 Laser scanning: (a) warp yarn 3-D model (b) dimension and cross-section geometry of warp yarns

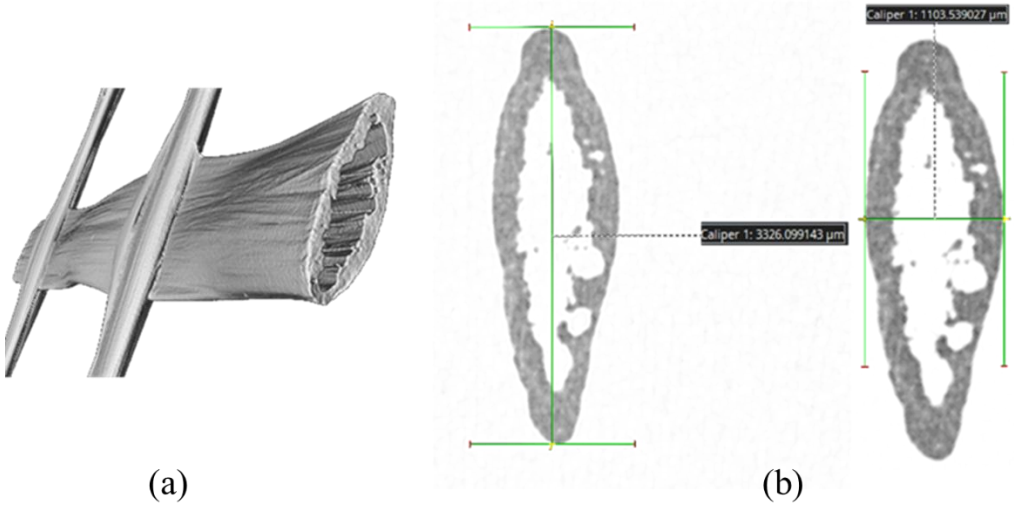

Figure 3-8 Laser scanning: (a) weft yarn 3-D model (b) dimension and cross-section geometry of weft yarns

3.2.4.3 Mechanical Characterization of the Textile

To determine the uniaxial tensile strength of individual yarns in both warp (0°) and weft (90°) directions, three 300 mm long specimens were tested for each direction. These tests were conducted under displacement control at a loading rate of 0.5 mm/sec using a 250 kN servo-hydraulic universal testing machine (MTS Landmark Series) located at the METU Department of Civil Engineering Materials of Construction Laboratories.

To minimize yarn damage during clamping, aluminum tabs were affixed to both ends of each specimen, as illustrated in Figure 3-9Analysis of the tensile test results presented in Figure 3-10 indicates a close agreement in the tensile strength of both warp (1933 MPa) and weft (1900 MPa) yarns. However, these experimentally determined values fall below the manufacturer's reported tensile strength. This discrepancy is likely attributed to localized yarn damage during the clamping process, despite the use of aluminum tabs, which may not have provided adequate protection against fiber-level damage.

Despite exploring various gripping methods, the use of aluminum tabs proved to be the most effective approach in minimizing yarn damage during testing. While the aluminum tabs mitigated some damage, discrepancies between weft and warp yarns were observed in the initial nonlinear portion of the stress-strain curves and in the overall strain capacity, with the weft direction exhibiting lower strain capacity. This disparity can be attributed to the undulated structure of the weft yarns, which requires straightening during tensile loading. This phenomenon, also documented by other researchers, contributes to the observed differences in mechanical behavior. Based on the recommendations outlined in ACI544.1R-20, the average modulus of elasticity and strain capacity of both yarns were determined to be 192 GPa and 1.0%, respectively.

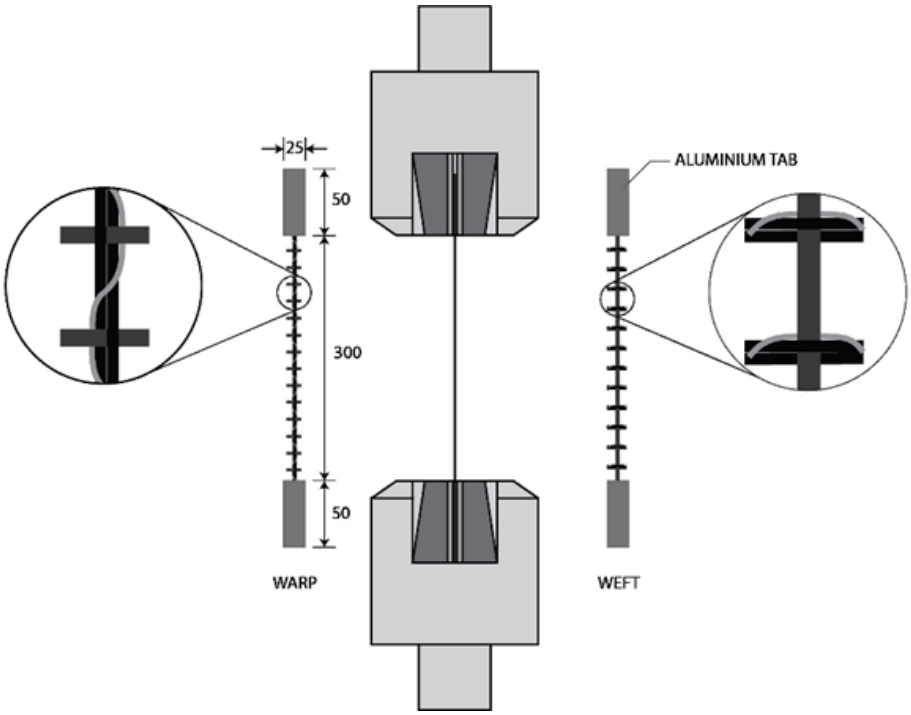

Figure 3-9 Schematic description of the uniaxial test setup of the yarns

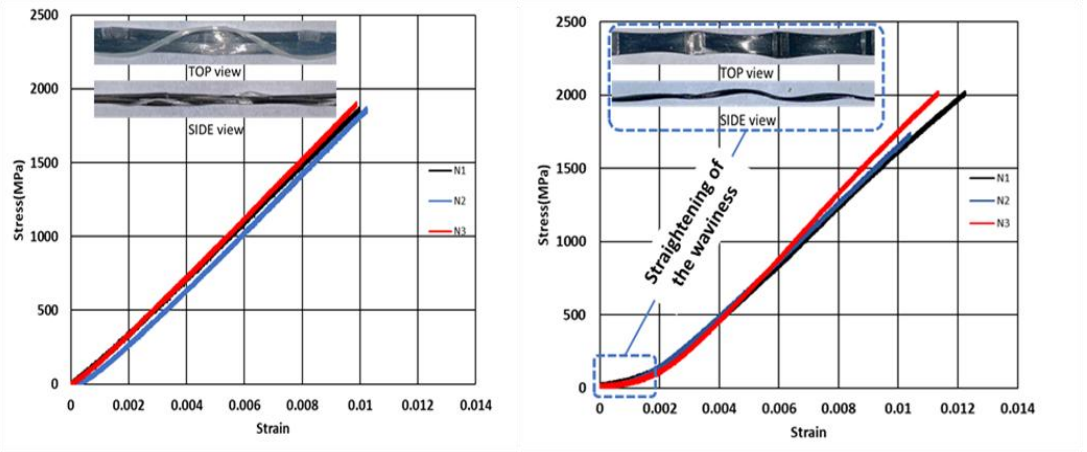

(a) Warp (0°) (b) Weft (90°)

Figure 3-10 Uniaxial tensile stress-strain response of the yarns in both directions

3.3 Cementitious Mortars

High workability and sufficient bonding to textiles are two fundamental requirements for cementitious mortars, facilitated by a high binder content (40-50%), a low water/binder ratio (30-40%), and a fine-grained aggregate. Throughout the experimental procedure, two fine-grained cementitious mortars (M45 and M7) were utilized with the proportions detailed in Table 3-6. M45 was developed based on the original M45 mortar, a renowned ECC matrix formulation known for its strain-hardening behavior, initially developed in the United States. The original M45 composition is characterized by a significant proportion of fly ash, the use of fine-grained aggregates, and the incorporation of short PVA fibers. However, in this investigation, short PVA fibers were omitted from the formulation. This decision was informed by the composition of M7, a reference mortar developed in Germany, where TRC technology was initially pioneered and extensively documented in the literature. Notably, M7, representative of early TRC developments, does not incorporate short fibers. The average direct tensile strength derived from 500×100×15 mm^3 prismatic specimens was 2.1 MPa (CoV of %26) and 4.4 MPa (CoV of %6) for M45 and M7, respectively. Conversely, the compressive strengths acquired from 50×50×50 mm^3 cubic specimens were 47.9 MPa (CoV of %18) and 72.7 MPa (CoV of %8) in the same sequence. Hence, it is apparent that M7 demonstrates relatively higher strength in comparison to M45.

Table 3-6. Mixture proportions of the cementitious mortars

Mix ID	**Theoretical Ingredient Amount (kg/m^3)**						**W/B**
	Cement	**Fly Ash**	**Silica Sand**		**Water**	**Superplasticizer**	
			(0-1 mm)	(0-0.25 mm)			
M45	556.5	667.8	-	445.2	360.6	6.7	0.30
M7	889.6	-	533.8	533.8	266.9	11.6	0.30

3.4 Testing Procedures

This thesis investigates the mechanical properties and long-term behavior of C-TRCC through a series of three distinct test types. The first phase involved uniaxial direct tensile tests to evaluate the initial mechanical properties of the composites. Subsequently, long-term creep behavior was assessed through direct tensile sustained loading tests. Finally, the slip-bond behavior between the textile and the matrix was examined using pull-out tests. This section provides a detailed description of each of these testing procedures.

3.4.1 Phase I: Uniaxial tensile testing of C-TRCC

3.4.1.1 Specimen preparation

C-TRCC specimens were fabricated utilizing cementitious mortars along with carbon textile measuring 100 mm in width, 500 mm in length, Figure 3-11 and a nominal thickness ranging from 10 to 20 mm as shown in Figure 3-12 (RILEM Technical Committee 232-TDT, Wolfgang Brameshuber et al., 2016).

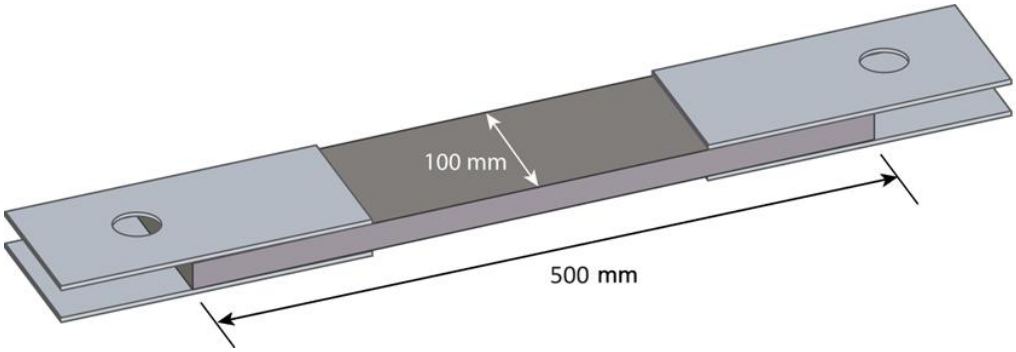

Figure 3-11 Schematic illustration of the uniaxial test specimen

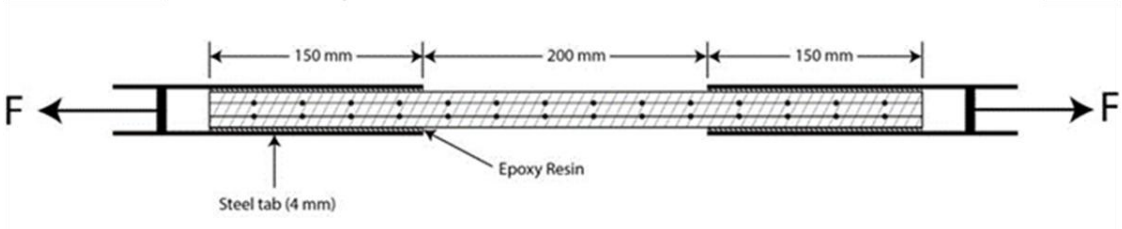

Figure 3-12 Cross-sectional view of the test specimen with two-layer carbon textile

The casting process, depicted in Figure 3-13, used a specially designed formwork equipped with an external vibrator to ensure proper consolidation of the mortar. Formwork attachments were employed to control the mortar cover thickness for all TRCC specimens within a range of 4 to 6 mm, depending on the number of textile layers. To minimize damage to the sensitive specimens, demolding occurred after two days, followed by 28 days of submerged curing in water at 23 ± 2 °C. The specimens were then air-dried for 24 hours before steel end plates were bonded to them using epoxy resin, with a bond length of 150 mm. After an additional day of epoxy curing, the specimens were considered ready for uniaxial tensile testing.

Figure 3-13 C-TRCC formwork: (a) textile placement in the forms (b) placement of cementitious mortar

The samples were labeled to specify the quantity of textile layers, the test's orientation, and the cementitious mortar type. For example, M45-C1-90 indicates a

specimen with a single layer (C1) of carbon textile reinforcement, M45 mortar, and testing performed in the weft direction (90°). Similarly, M7-C3-0 denotes a specimen with three layers (C3) of carbon textile, M7 mortar, and testing performed in the warp direction (0°).

3.4.1.2 Test setup

Throughout the experimental program, the clevis gripping testing method was selected (Arboleda, Carozzi, Nanni, & Poggi, 2016). Within this particular gripping approach, two metallic steel plates are affixed to both ends of the TRCC specimen, facilitating load transmission through these plates. To reduce eccentricity, the fixture was equipped with spherical ball joints at the two ends of the TRCC specimen. A 250 kN servo-hydraulic universal testing machine (MTS Landmark Series) was utilized, and an advanced video extensometer (AVE) system was complemented. In instances where necessary, images were captured for digital image correlation analysis. The tests were executed by applying a displacement-controlled loading regime at a 0.5 mm/min speed. A visual representation of the uniaxial tensile test setup is illustrated in Figure 3-14.

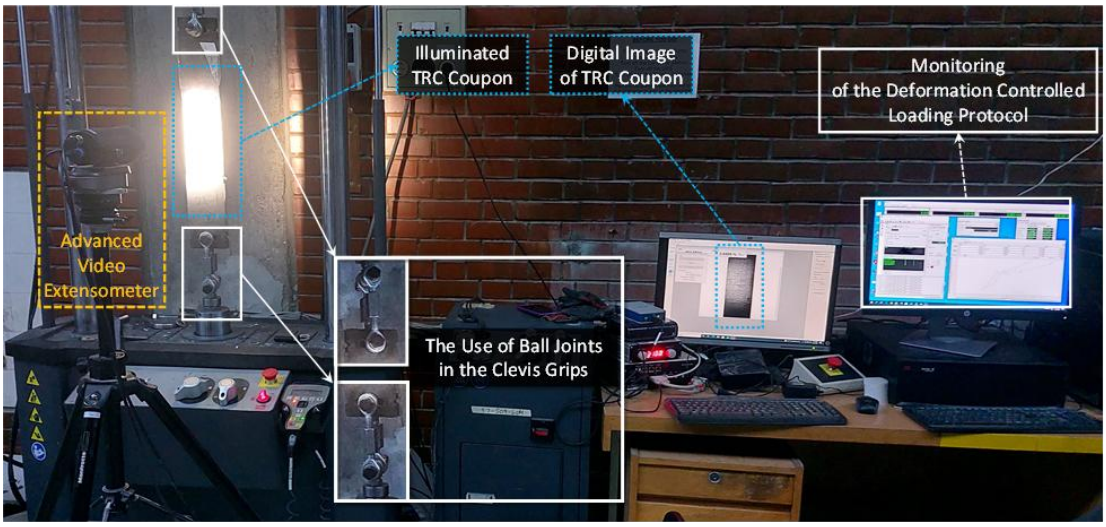

Figure 3-14 Uniaxial Tensile Test Set-up

Previous research has highlighted that the predominant failure mechanism in TRCC coupons involves the slippage of textiles around the steel plates and the TRCC interface (De Santis et al., 2018a). Given the sensitivity of the strain measurements to localized slip and the limited coverage of AVE measurements, the MTS testing system was employed to record axial displacements for comprehensive deformation analysis, as illustrated in Figure 3-15. To determine the strain within the region of interest (200 mm), the measured displacement across this region was normalized by dividing it by the region's length. This approach is commonly adopted in relevant(Truong & Kim, 2021) literature. To enhance the accuracy of this global strain measurement, the two steel end plates were welded together, and the combined stiffness of the testing setup was determined under uniaxial loading. This allowed for the precise calculation of the displacement within the region of interest by subtracting the deformation of the steel plates from the total measured displacement at each load increment. To mitigate potential inaccuracies arising from displacement measurement and the interaction between the coupon and the ball joint, all TRCC coupons were subjected to a preloading stage with a force of 0.2 kN prior to commencing displacement measurements.

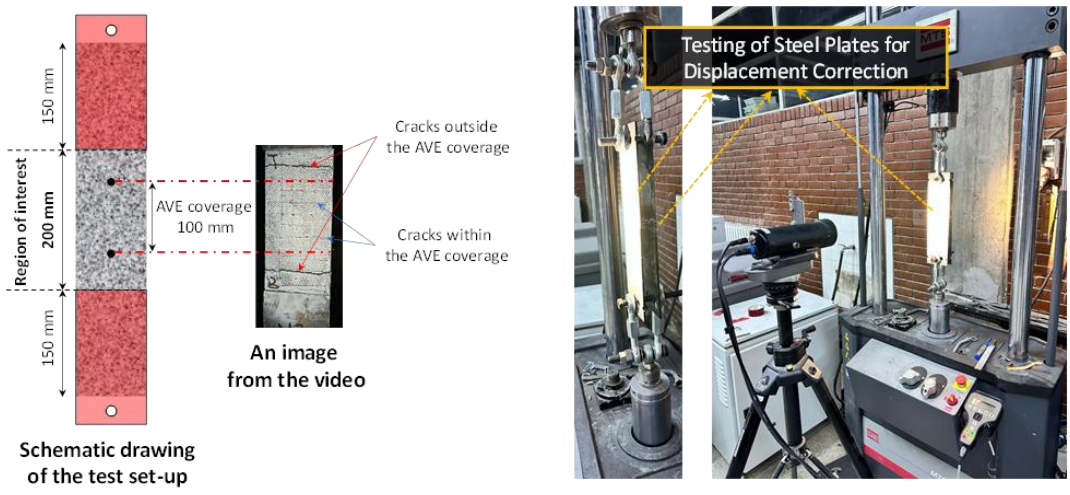

Figure 3-15 AVE measurements and correction of axial displacement after testing steel plates

3.4.2 Phase II: Slip-bond Behavior of C-TRCC (Yarn Pull-out tests)

For slip-bond testing, a yarn pull-out test was developed, adapting the clevis grip method employed in uniaxial direct tensile tests. This approach offers significant advantages over previous pull-out test methods, primarily the simplified direct measurement of displacement, which facilitates the interpretation of results. Furthermore, the dimensions of the specimens prepared for pull-out tests closely resemble those used in the uniaxial direct tensile tests, enhancing the comparability of the results. This testing program utilizes the yarn pull-out test as a primary method for evaluating slip-bond behavior in C-TRCC. The experimental program aims to investigate the influence of various factors on the slip-bond response of the embedded yarns. These factors include:

- Embedment Length: Specimens were tested at three different embedment lengths (150 mm, 100 mm, and 50 mm).
- Textile Structure: Specimens with one, two, and three embedded yarns were tested to evaluate the effect of transverse yarn interlock (also known as the group effect).
- Mortar Composition: Two different mortar formulations, M7 and M45, were used in the investigation.

3.4.2.1 Specimen Preparation

Specimens for the pull-out tests were designed to be 200 mm long, 100 mm wide, and 20 mm thick, with three different embedment lengths of 50 mm, 100 mm, and 150 mm, as shown in Figure 3-16. These dimensions were selected to simulate previous tests while providing sufficient embedding space for the carbon textile yarns. Specimens with one, two, and three embedded yarns (Figure 3-17) were prepared to investigate the influence of textile structure, particularly the mechanical interlock between adjacent yarns, on bond performance. To ensure proper gripping

during testing, a free yarn length of 100 mm was extended beyond the mortar block. Aluminum plates, measuring 50 mm x 100 mm, were affixed to the free ends of the yarns to prevent slippage and damage during loading.

Following the casting process, the specimens were cured in their molds for 24 hours. Subsequently, they were demolded and submerged in a curing bath for an additional 28 days. Upon completion of the curing period, holes were drilled into the specimens at distances of 50 mm, 100 mm, and 150 mm from the edge of the mortar block to accommodate the desired embedment lengths of the carbon textile yarns. Variations in the embedment lengths (50 mm, 100 mm, and 150 mm) allowed for an investigation of the influence of embedment length on bond strength, slippage, and failure modes. To ensure a robust connection to the testing apparatus, steel plates were bonded to the surfaces of the C-TRCC specimens using an epoxy resin.

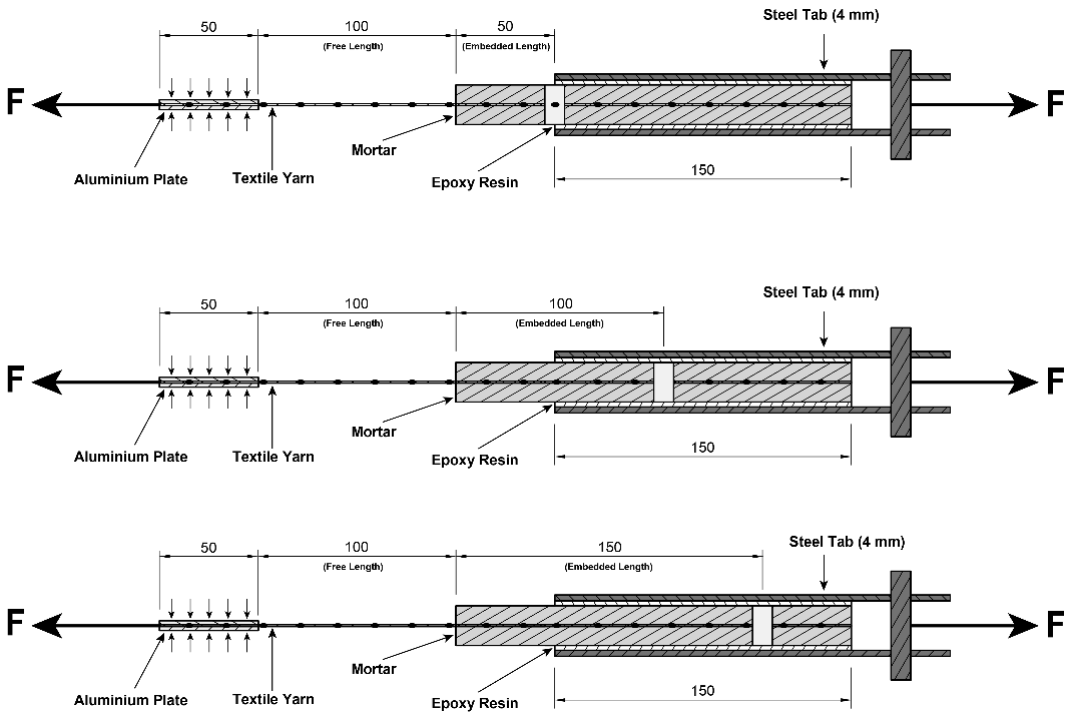

Figure 3-16 Schematic description of the yarn pull-out test specimens for three embedment lengths of 50, 100, and 150 mm

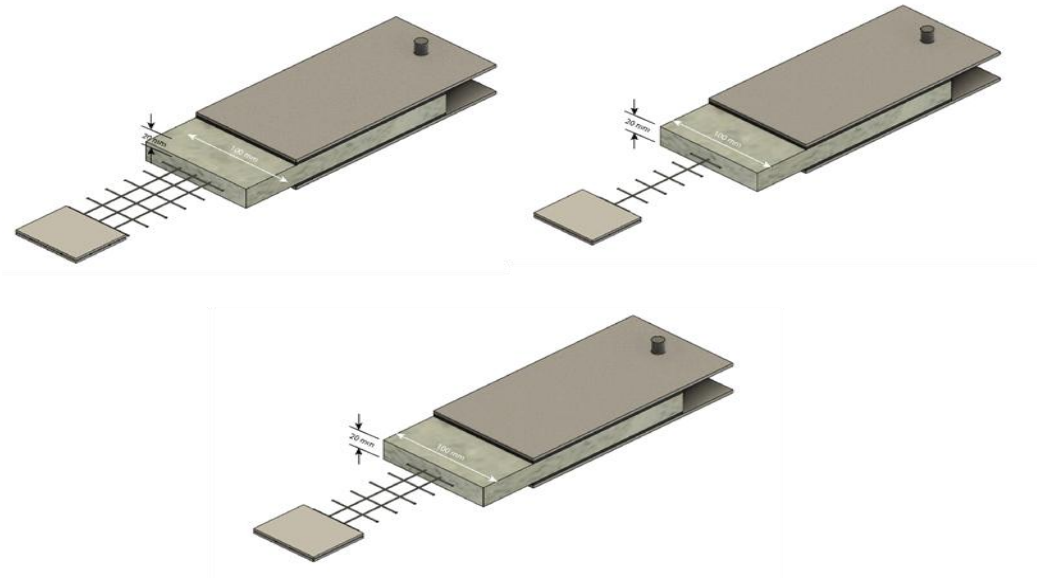

Figure 3-17 Schematic illustration of yarn pull-out testing for one, two, and three yarns

3.4.2.2 Yarn Pull-out Test Setup

In order to safeguard the carbon textile yarns from potential damage caused by the testing machine's clamps, two aluminum plates, each measuring 50 × 100 × 3 mm, were positioned on either side of the yarn within the designated clamping area. These plates are utilized to prevent possible damage to yarns in the griping area with uniform distribution of applied loads and inhibition of localized stress concentration. The aluminum plates facilitated a consistent grip throughout the experiment, thus reducing the probability of slippage and enabling the precise transfer of the applied tensile force to the yarns. Figure 3-18 illustrates the testing procedure and the placement of specimens in the testing machine, which is carefully controlled to minimize the potential for eccentricity during the loading stage. In this testing method, the specimen is not subjected to any lateral or axial load, which prevents any potential movement during the loading process.

The experiments were conducted using a servo-hydraulic system (MTS Landmark series), which had a maximum load capacity of 250 kN. In this testing procedure,

the applied speed is a constant displacement of 0.5 mm/min, to have similar testing conditions to uniaxial direct tensile tests Figure 3-19.

Figure 3-18 C-TRCC yarn pull-out tests specimen preparation and testing procedure.

A Linear Variable Differential Transformer (LVDT) was employed to measure the displacement in yarn pull-out tests. The LVDT was positioned vertically for the specimen's deformation axis, allowing for the precise tracking of the yarn's movement during the pull-out process. The core of the LVDT was attached to a rod that moved in conjunction with the specimen throughout the test, thereby providing real-time displacement data. This enabled precise monitoring of the yarn's slippage behavior as it was extracted from the cementitious matrix, which is a crucial aspect in evaluating slip-bond performance. The test commenced with a preloading phase, during which a 0.1 kN initial load was applied to guarantee optimal alignment and secure clamping of the yarns within the testing apparatus.

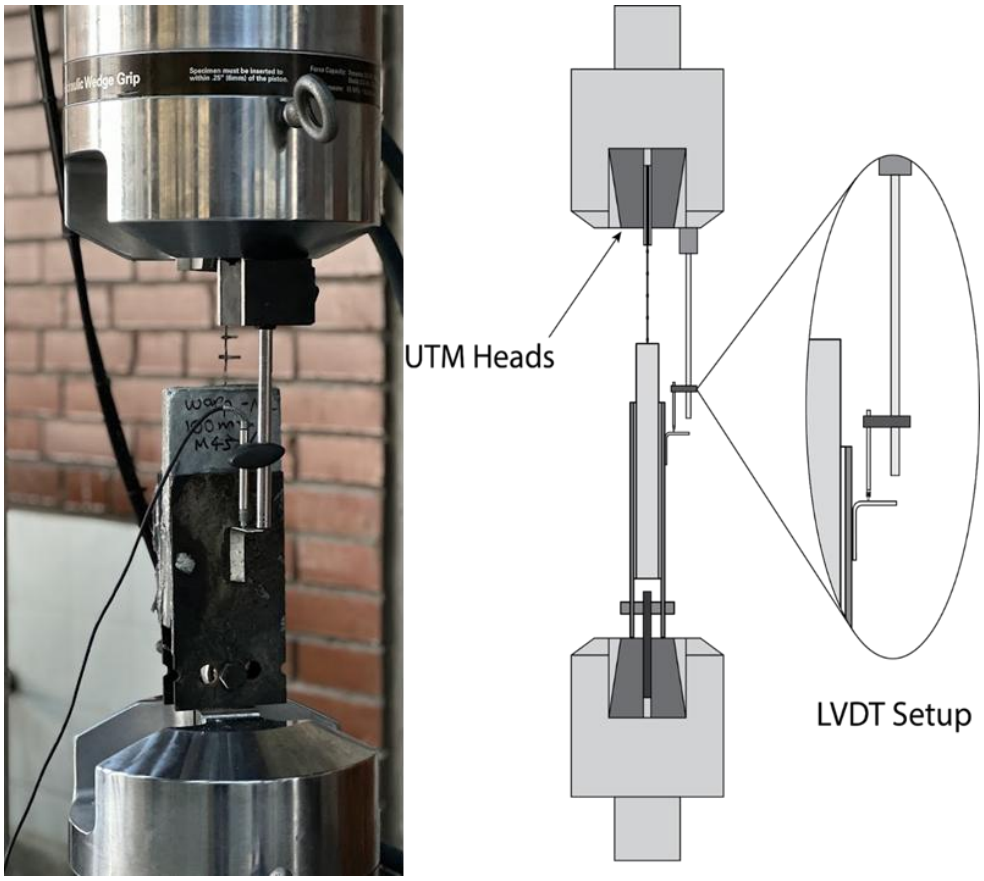

Figure 3-19 Yarn pull-out testing setup

3.4.3 Phase III: Creep Behavior of TRCC under Tensile Loading

3.4.3.1 Specimen Preparation

Given the extended duration of the creep tests, which limited the number of parameters that could be investigated simultaneously, two layers of carbon textile reinforcement were selected for this study. This choice was based on the expectation that a higher number of textile layers would enhance the overall strength and durability of the specimens, enabling them to withstand the prolonged loading conditions of the creep tests. Moreover, due to the limitations imposed by the creep

testing frame, the longitudinal dimension of the specimens was reduced to 450 mm. Therefore, C-TRCC specimens for creep testing were fabricated utilizing cementitious mortars along with two layers of carbon textile measuring 100 mm in width, 450 mm in length (Figure 3-20) and a nominal thickness of 25 mm (Figure 3-21). Specimen casting and testing procedures were the same as previous two phases. Prior to creep testing, a uniaxial direct tensile test was conducted on three specimens to determine the ultimate tensile strength of the specimens, which was subsequently used to apply the desired sustained load in the creep tests.

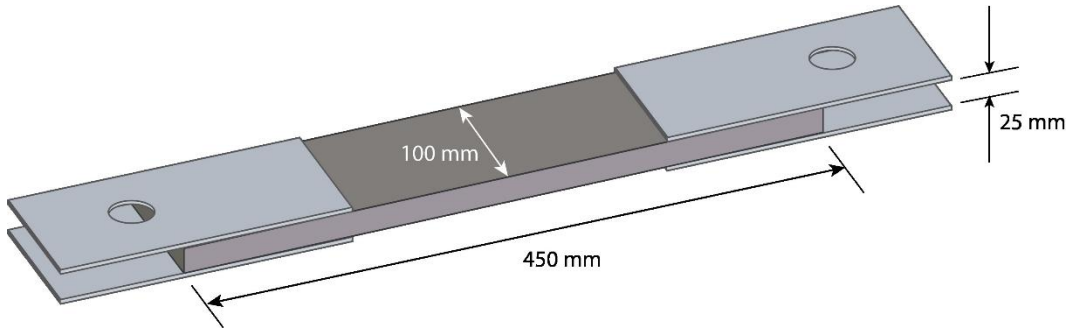

Figure 3-20 Schematic illustration of C-TRCC tensile creep specimen

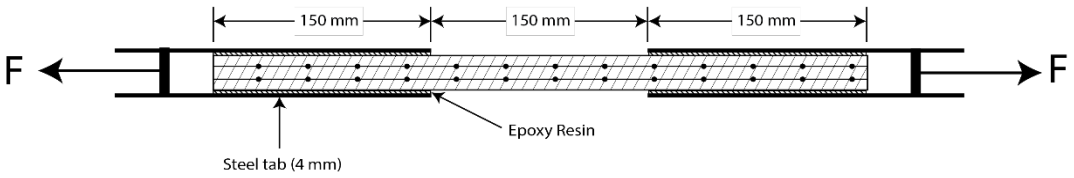

Figure 3-21 Schematic depiction of the cross-section tensile creep specimens

3.4.3.2 Creep Testing Frame

The tensile creep frame was a slightly modified form of a previous PhD thesis conducted at the materials of construction laboratory of METU-CE (Keskin, 2012). The tensile creep test setup is designed as a lever arm and utilizes I-profile steel beams to form the creep test frame. The total height of the loading frames is 1.7 m,

and the total length of the lever arm is 2.5 m. The load ratio (the ratio of the weight placed on the frame to the applied load) is approximately 1/7. The maximum weight that can be placed on the frame is 250 kg, corresponding to an applicable load of approximately 19.6 kN. For loading, 5 kg and 10 kg weights in steel plates are used, providing approximately 343 N of accuracy. Four frames were available, each capable of simultaneously testing two samples under a single load (Figure 3-22). In the connections between the frame and the specimens, ball-joints are again used at the joints, and any eccentricity that may occur in the specimens is minimized.

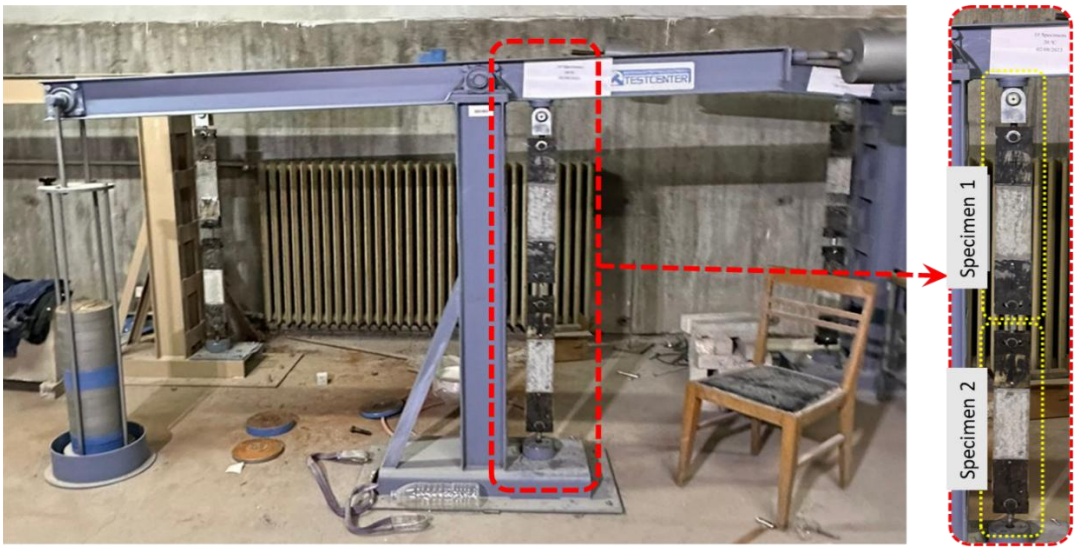

Figure 3-22 Creep test setup

Tensile creep tests were conducted in a controlled environment with a fixed temperature of 20 ± 2 °C and a relative humidity of 50 ± 5%. Following the bonding of the steel tabs, the length changes in the specimens were measured during manual load application using a DEMEC Digital strain gauge with a sensitivity of 1 μm (Figure 3-23). To ensure accurate deformation measurements, a one-minute waiting period was observed after every 10 kg increment of applied load.

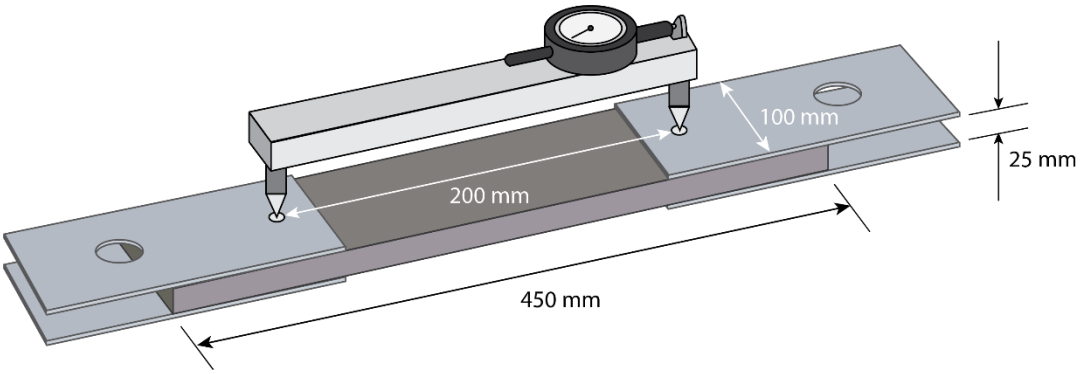

Figure 3-23 Schematic illustration of deformation measurement using DEMEC gage

The tensile creep behavior was investigated using three groups of specimens, each subjected to loads corresponding to 25%, 50%, and 75% of their ultimate tensile strength (UTS). These tests were conducted at two different temperatures, 20°C and 50°C, resulting in a test matrix of six conditions.

- Group 1: 25% of UTS at 20 °C and 50 °C
- Group 2: 50% of UTS at 20 °C and 50 °C
- Group 3: 75% of UTS at 20 °C and 50 °C

To maintain a constant temperature of 50°C on the C-TRCC specimens while testing at a specific creep load level, specialized metal plates with integrated electrical resistance heaters and a temperature control system were developed (Figure 3-24). These plates were attached to the specimens, and thermocouples positioned between the plates and the specimens were used to monitor and maintain a stable temperature of 50 ± 3°C. Figure 3-25 shows a close-up view of the heating system and a typical view during displacement measurement using the DEMEC gauge.

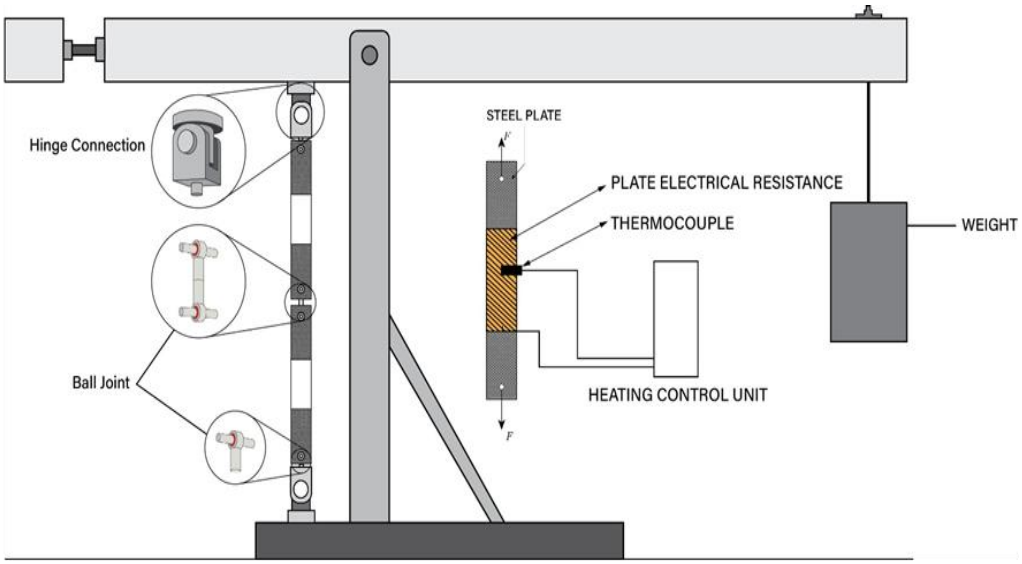

Figure 3-24 Schematic illustration of creep testing and the specimen heating system

(a)

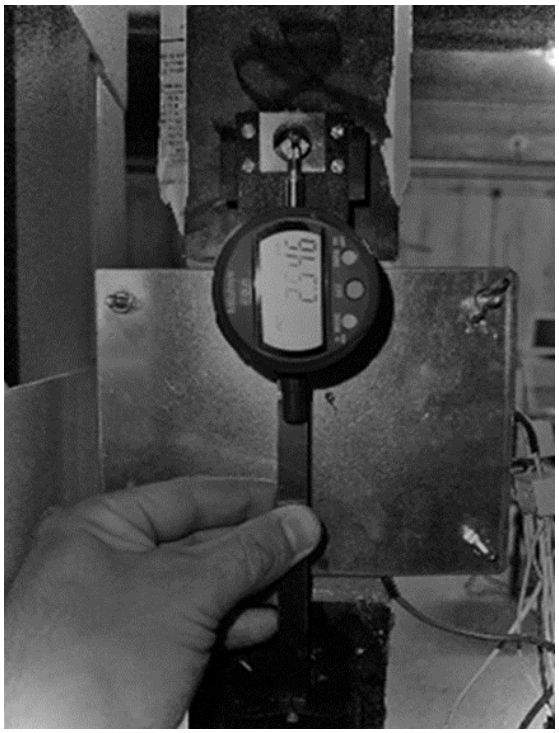

(b)

Figure 3-25 Pictures for (a) heating system, (b) Deformation measurement with DEMEC gage

CHAPTER 4

4 RESULTS AND DISCUSSION

The subsequent sections of this chapter present the results of the tests conducted in each of the three phases: uniaxial direct tensile tests (Phase I), slip-bond tests (Phase II), and tensile creep tests (Phase III).

4.1 Phase I: Uniaxial tensile test results

The results of the uniaxial tensile tests are presented in terms of the applied load versus global strain ($\Delta \boldsymbol{L}/\boldsymbol{L_0}$) as presented in Figure 4-1. As expected, increasing the number of textile layers resulted in an enhanced load-carrying capacity of the TRC specimens when tested in both directions. Additionally, a clear observation is the reduction in both load capacity and maximum global strain when the tests are conducted in the weft direction compared to the warp direction.

The results observed in Figure 4-1 are summarized in

Table 4-1 for a more precise comparison and to better analyze the findings. The analysis follows the procedure outlined in the AC434 guidelines, as described by De Santis et al., 2018, where the load is plotted in terms of the textile stress, and the parameters provided in the table are calculated accordingly.

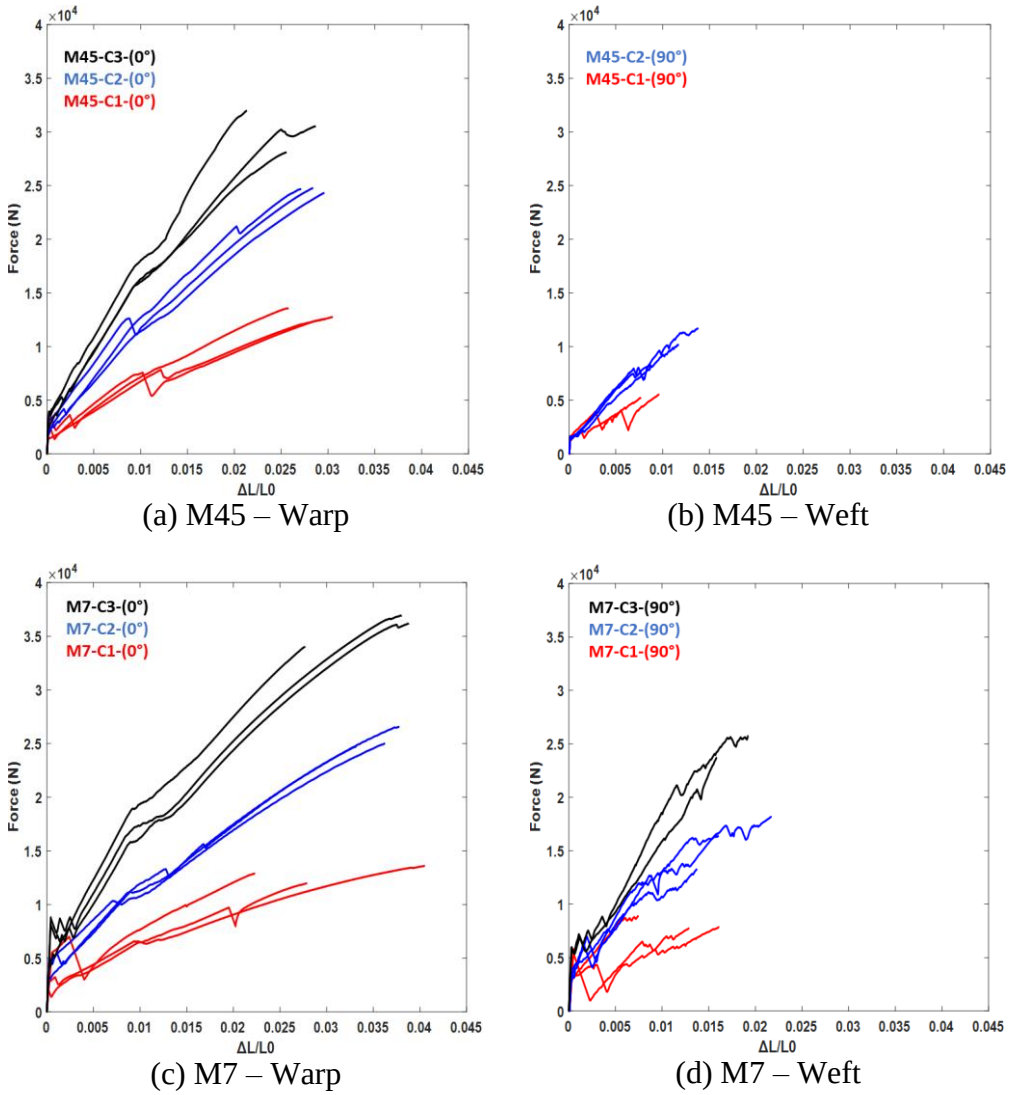

(a) M45 – Warp (b) M45 – Weft

(c) M7 – Warp (d) M7 – Weft

Figure 4-1 Load – global strain measurements of TRC specimens

As seen in

Table 4-1, the TRC specimens were tested in two different cementitious mortars (M4 and M7), in two different directions (warp and weft), and across three different reinforcement ratios (0.5%, 0.8%, and 1.0%). The cracking strength of the composite was between 1.6 to 2.5 MPa for M45 and between 3.1 to 4.4 MPa for M7, which aligns with the tensile strength of the unreinforced mortars which was found as 2.1 MPa (CoV of %26) and 4.4 MPa (CoV of %6) for M45 and M7, respectively. The considerably large CoV values for the cracking force/stress, specifically in one-layer coupons, is attributed to several factors, such as introducing microcracking during specimen fabrication and handling, additional tensile stresses due to bending resulting from misaligned grips, or geometrical imperfections as stated by previous research studies (De Santis & De Felice, 2015; Nanni et al., 2018). On the other hand, the ultimate tensile strength of the textiles ranged from 1865 to 2375 MPa in the warp direction and from 933 to 1528 MPa in the weft direction. Given that the manufacturer's reported tensile strength exceeds 2200 MPa for both warp and weft directions, it is clear that significant differences in the textile strength emerge when embedded in different mortars and when tested in various directions. The reasons for these observations are explained in the subsequent sections.

Although the textile strength was fully achieved in the warp direction, the reduced tensile strength in the weft direction suggests that the textile's full capacity was not fully utilized in this orientation regardless of the cementing matrix as observed in Figure 4-2(a). Moreover, the strain capacity of the C-TRCC is much higher than the bare textile especially when the textiles were tested in the warp direction as observed in Figure 4-2 (b).

Table 4-1 Analysis of the load-deformation data in accordance with AC434

Label	ρ_f (%)	@ Cracking		@ Ultimate			E_f (MPa)	Failure Mode
		F (N)	σ_{cr} (MPa)	F (N)	σ_t (MPa)	$\Delta L/L_0$ (%)		
M45 - Warp								
M45-C1-(0)	0.49 [8]	2520 [40]	2.50 [52]	12339 [4]	2285 [4]	2.9 [9]	843 [13]	I, I, II
M45-C2-(0)	0.80 [6]	2344 [27]	1.73 [25]	24611 [1]	2277 [1]	2.8 [4]	803 [5]	I, II, II
M45-C3-(0)	0.97 [7]	2242 [25]	2.01 [23]	30240 [7]	1865 [7]	2.5 [15]	753 [20]	III, III, III (splitting)
M45 - Weft								
M45-C1-(90)	0.52 [8]	1457 [52]	1.90 [60]	5398 [6]	996 [6]	0.9 [31]	1159 [27]	III, III, III (excessive spalling)
M45-C1-(90)	0.79 [6]	773 [7]	1.63 [8]	10106 [17]	933 [17]	1.1 [22]	823 [6]	III, III, III (excessive spalling)
M7 - Warp								
M7-C1-(0)	0.58 [8]	3537 [52]	3.84 [60]	12843 [6]	2375 [6]	3.0 [31]	828 [27]	I, I, I
M7-C2-(0)	0.79 [2]	4233 [25]	3.08 [26]	25474 [4]	2356 [4]	3.6 [7]	660 [4]	I, II, II
M7-C3-(0)	0.99 [3]	4782 [33]	4.36 [30]	35755 [4]	2206 [4]	3.5 [18]	645 [15]	II, II, II
M7 - Weft								
M7-C1-(90)	0.46 [10]	2922 [42]	3.48 [40]	7867 [8]	1455 [8]	1.6 [36]	902 [15]	III, III, III
M7-C2-(90)	0.72 [7]	3401 [16]	3.26 [7]	15983 [15]	1477 [15]	1.7 [24]	871 [10]	III, III, III (spalling)
M7-C3-(90)	0.95 [7]	3975 [1]	3.52 [8]	24782 [6]	1528 [6]	1.8 [14]	875 [8]	III, III

ρ_f: Reinforcement ratio; F: Force; σ_c: Composite stress; σ_t: Textile stress; $\Delta L/L_0$: Global strain; E_f: Cracked modulus of elasticity of the composite.
The values represent the mean of the 3 specimens tested, except for C3B-(90) where only two specimens were available, as the third specimen cracked during specimen preparation. Moreover, [ ] represent the CoV in %.

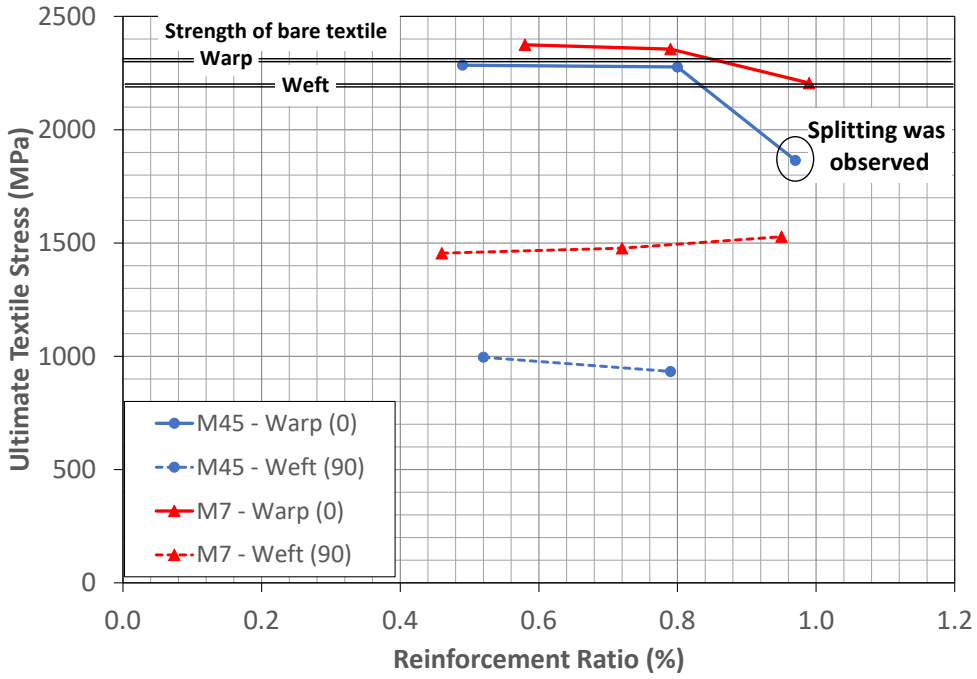

(a) Textile stress

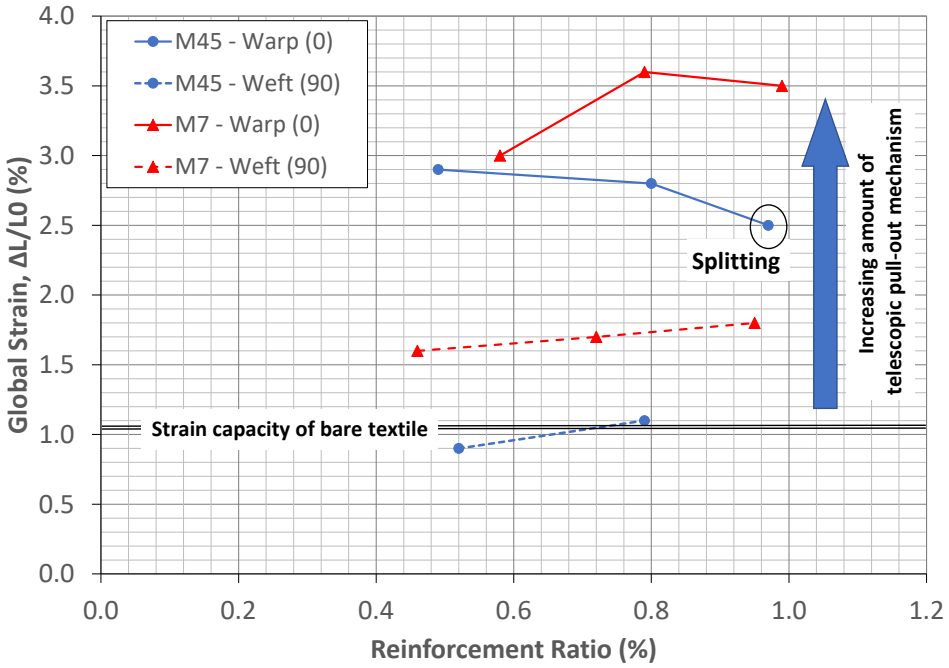

(b) Global strain

Figure 4-2 Effects of matrix type and textile direction on the performance of C-TRCC

These observations can be explained by investigating the failure modes observed in the C-TRCC specimens. Typical failure modes of C-TRCC are depicted in Figure 4-3 and presented in the last column of the table for each test case. After the first cracking of C-TRCC specimens, multiple cracking within the test region is typically observed. During the meantime a phenomenon called telescopic pull-out, as depicted in Figure 4-4, takes place within the yarn and the surrounding matrix, due to the insufficient bonding of the multifilament with each other (Arboleda, Carozzi, Nanni, Poggi, et al., 2016). Later, failure is characterized either by textile failure (Modes I and II) or slippage (Mode III), i.e. the telescopic pull-out failure of the textile within the grip zone. It should be noted that in Mode I type of failure, the textile fails at stress levels that fully utilizes the strength of the textile and the main crack is away from the grip zone. In Mode II type of failure, the failure again takes place in the textile but in the near vicinity of the grip zone. This is observed when there is a lack of development length of the textile within the grip zone or due to the occurrence of eccentricity in the loading equipment that may aggravate after multiple random cracking. In this failure mode, the textile may develop stresses close to the strength of the textile. However, in Mode III type of failure the textile cannot achieve its full capacity, and the maximum load is dictated by the bond between the textile and the matrix. The determining factors in C-TRCC failure modes are textile strength, specimen stiffness, geometry, and the interfacial bonding between the textile and the cementitious mortar (Al-Gemeel & Zhuge, 2019).

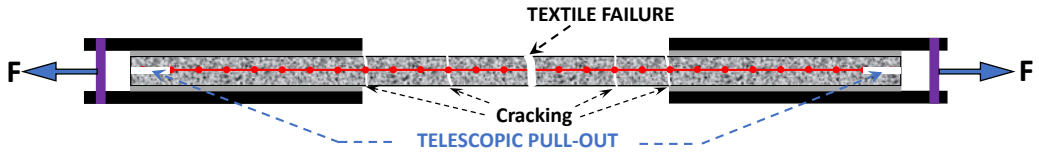

(a) Mode I – Textile failure

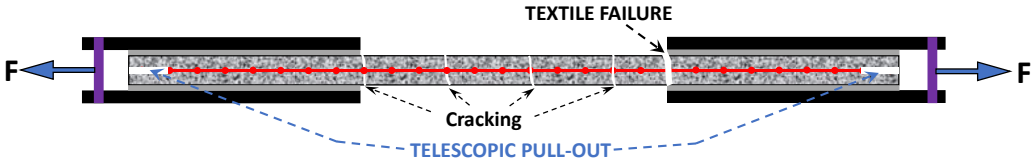

(b) Mode II – Textile failure possibly due to lack of development length

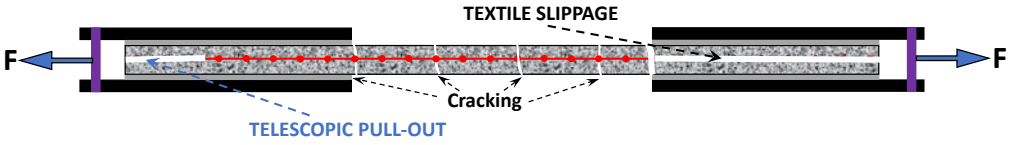

(c) Mode III – Textile slippage

Figure 4-3 Failure modes in C-TRC specimens

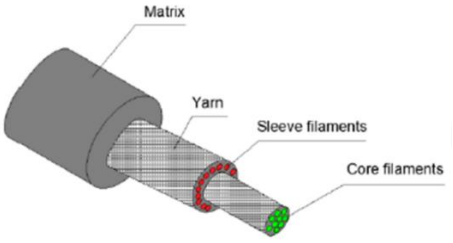

(a) Slippage phenomenon

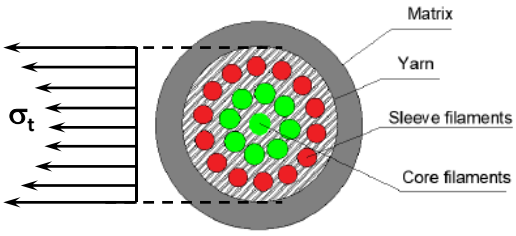

(b) The stress distribution within the textile

Figure 4-4 Slippage phenomenon observed in C-TRCC specimens

Besides the above-mentioned three failure modes, two different observations were also made. The first one is the splitting of the textile and the cementitious mortar within the grip zone as shown in Figure 4-5(a), which was observed when the carbon textiles were used in three layers. This led to the premature failure of the specimens leading to reduced failure load levels. Another observation was the spalling of the cover in the test zone of the C-TRCC specimens, which was observed when they were tested in the weft direction. Moreover, the spalling was limited in the strong cementitious matrix, i.e. matrix B, and was quite excessive in the softer one, i.e. M45, as respectively shown in Figure 4-5(b) and Figure 4-5 (c).

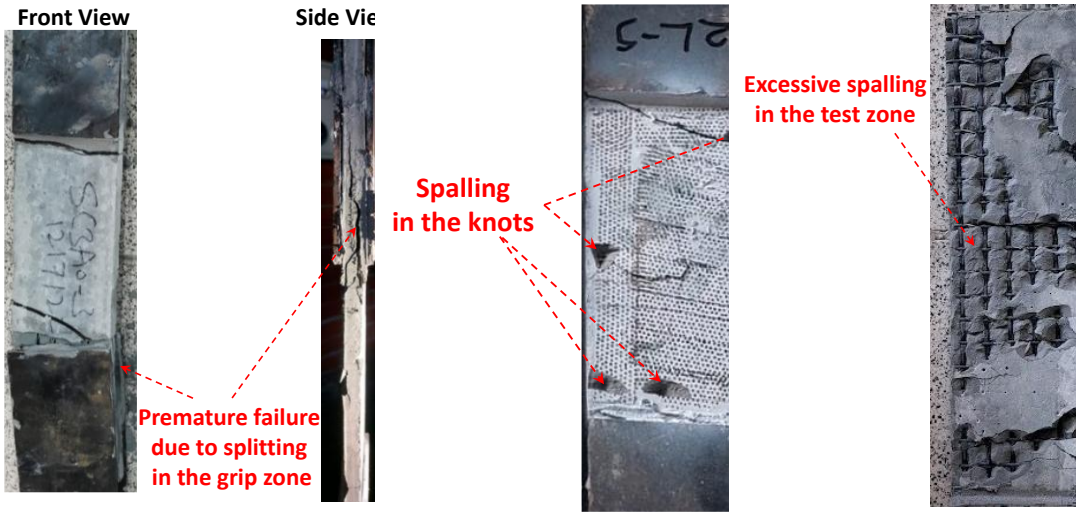

(a) M45-C3-(0) (b) M7-C2-(90) (c) M45-C2-(90)

Figure 4-5 Some other observations on the tested C-TRCC specimens

The debonding and spalling of the cementitious mortar is due to bond characteristics between the cementitious mortar and the textile which are influenced by the properties of the mortar and the geometric properties of yarns, such as yarn cross-section geometry and its variation along the yarn, undulation and waviness of yarns, and the contact pressure in the nodal point of yarns (Tekle et al., 2021)(Zhu et al., 2018)(Preinstorfer & Kollegger, 2020). The weft yarn has a flat (wider) elliptical cross-sectional shape with a voided internal structure. Due to this wider and thus

larger contact surface, the bonding of the textile yarn to the cover mortar increases. As the number of filaments involved in the bond increases, the number of remaining filaments involved in the telescopic pull-out phenomenon decreases, resulting in a reduction in the observed amount of global strain when the C-TRCC specimens were tested along the weft direction.

In addition to the reduction in the global strain, the other characteristic observation of excessive spalling in the test zone, Figure 4-5(c), when C-TRCC were tested in the weft direction, is due to their waviness, i.e. the deviation of the neutral axis of the fiber strand from the longitudinal axis of the textile reinforcement. Deviation forces that occur due to the presence of the waviness are predominantly oriented orthogonal to the textile reinforcement layer and induce a spalling type of failure in the C-TRCC (Preinstorfer & Kollegger, 2020). In order to complement the experimental program SEM investigation was performed at METU Central Laboratories as presented in Figure 4-6 for C-TRCC tested in warp direction and Figure 4-7 for weft direction.

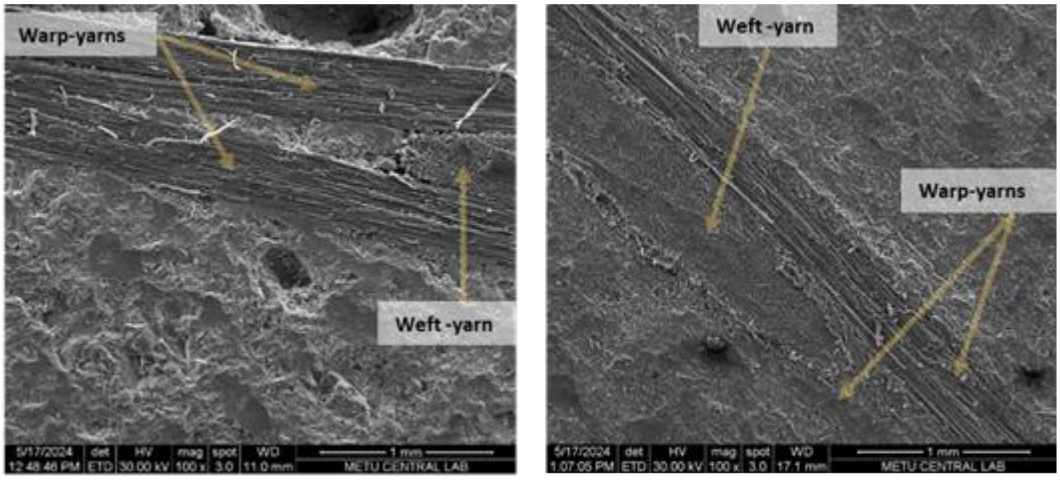

(a) Before testing (b) After testing

Figure 4-6 SEM pictures of C-TRCC when tested along the warp direction

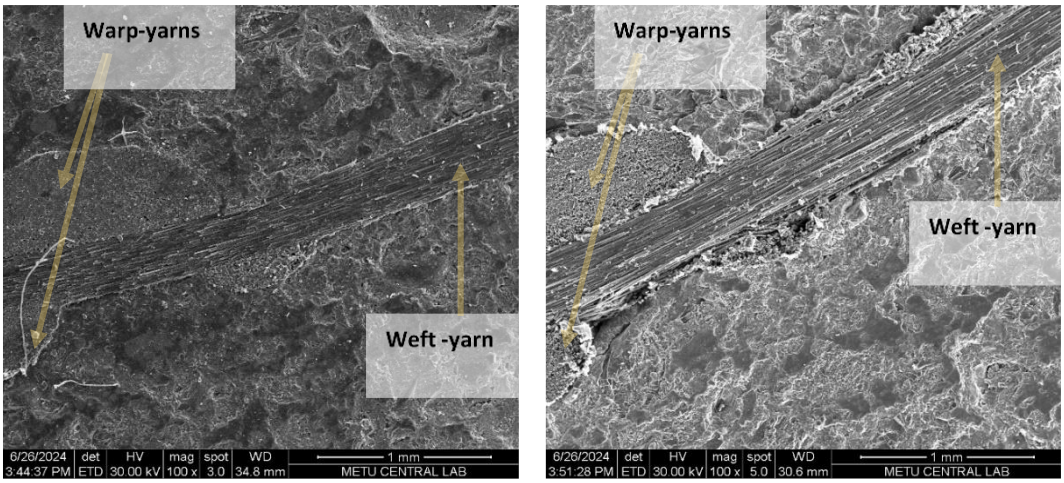

(a) Before testing (b) After testing

Figure 4-7 SEM pictures of C-TRCC when tested along the weft direction

The SEM images showed considerable alteration in the microstructures of the TRCC before and after mechanical testing. Before testing, warp and weft yarns appear integral and are well bonded in the concrete matrix, which gives strong interfacial bonding ability, critical for effective load transfer and development of crack resistance. The lack of cracks on the concrete matrix and the proper identification of yarns indicates that the textile reinforcement has played a substantial role in maintaining the integrity of C-TRCs. This condition considered the composite optimal in its performance with better mechanical properties like increased tensile strength and elevated crack resistance.

After testing, the images show deformations of yarns: separation from the concrete matrix. These are consistent with a weakening yarn-matrix bond due to the applied mechanical load. That agrees with the appearance of microcracks in the matrix and indicates that the material was loaded to the level of initiation of the crack propagation process. The visible signs of fiber breakages, pull-out, and debonding bring out significantly reduced structural integrity of the TRCC as exhibited by Figure 4-5(c) the reduction in its load-carrying capacity and development of increased chances of failure under further loading. These observations call for an

understanding and optimization of yarn-matrix interactions for performance improvement of the TRCC in structural applications.

When the scanning electron microscope images are digitally stitched together, the differences in waviness of the two yarns and the presence of debonding are shown in Figure 4-8. As the amount of textile reinforcement increases, these forces were so large that caused the splitting of the C-TRCC specimens in the grip zone like the one shown in Figure 4-5(a). The strength of the matrix of course is an important parameter for the spalling. With an increase in the strength of the matrix, like M7, the amount of spalling was limited, and mostly restricted to the knots as observed in Figure 4-5(b).

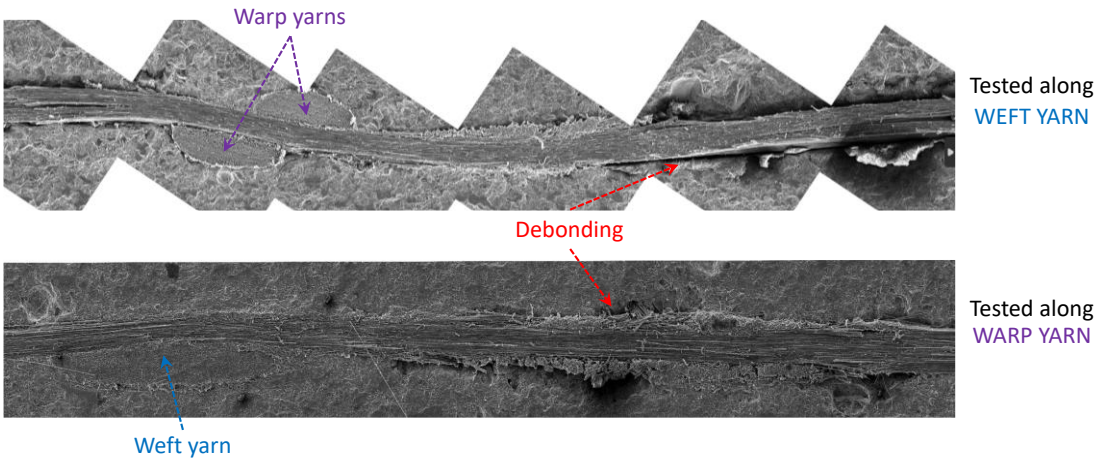

Figure 4-8 Digitally stitched SEM pictures of C-TRC coupons in M7

Tensile testing of C-TRCC specimens along the warp yarn axis revealed stress values approaching the ultimate tensile strength of the bare textile. This implies complete load transfer and effective distribution of stress within the composite structure. The most common mode of failure was Mode I, followed by Mode II, both of which exhibited telescopic pull-out failure.

The type of cementitious matrix used in C-TRCC coupons also has a substantial impact on their mechanical performance. The increased cement content in M7

results in a superior cracking strength, with values ranging from 3.1 MPa to 4.4 MPa, compared to M45, which has a lower cracking strength range of 1.7 MPa to 2.5 MPa, mainly due to the incorporation of fly ash. This phenomenon is attributed to the well-documented effects of fly ash on cement hydration kinetics, which can lead to delayed hydration and slower strength gain (Wen et al., 2023). On the other hand, a comparative analysis of ultimate tensile strength reveals relatively similar behavior between M45 and M7 coupons, especially in the warp direction. In the weft direction, however, there is a quite distinct difference that can be observed both from the ultimate textile stress and global strain. While the coupons of M7 have a textile strength of about 1500 MPa, this value is around 950 MPa for the coupons of M45. This is attributed to better bonding between textile and mortar, which is established from the higher cement content, along with the optimized particle size distribution of silica sand in M7, which contributed to better load transfer and a stronger textile/mortar bonding (Mechtcherine et al., 2016).

4.2 Phase II: Yarn Pull-out Test Results

This section presents the results of yarn pull-out tests conducted on the C-TRCC focusing on the influence of critical factors such as mortar composition (M7 and M45), embedment length (150 mm, 100 mm, and 50 mm), yarn architecture (Warp and Weft), and transverse yarn interlock also known as group effect (1Y, 2Y, and 3Y). Tests were conducted using the MTS universal testing machine in 0.5mm/s speed in a deformation control scheme. For each specimen tested, the load-slip curves are obtained and they are presented together with a picture of the specimen after testing as presented Appendix 1 for M7 and Appendix 2 for M45 mortar.

Later, using the data obtained from the load-slip curves, the nominal shear strength (τ_n) is calculated. However, this is calculated twice, first ($\tau_{n,1}$) by using the results of the yarn geometry as a circle based on manufacturer's data, and later ($\tau_{n,2}$) by assuming it as an ellipse as determined by laser scanning analysis. The relevant parameters related to the calculation processes are presented below.

$$\tau_{n,1} = \frac{F_{max}}{N\pi dl}$$

$$\tau_{n,2} = \frac{F_{max}}{NCl}$$

In the above equations,

- F_{max} is the maximum pullout load in full deboning of yarn,
- N is the number of yarns,
- l is the yarn embedded length,
- d is the yarn diameter calculated by the manufacturer's data and was determined as 1.0712 mm for warp and weft yarns,
- C is the circumference of the yarn as calculated by using Ramanujan's approximation for the circumference of an ellipse.

$$C \approx \pi\,[\,3(a + b) - \sqrt{((3a + b)(a + 3b))}]$$

Based on the laser scanning analysis, approximate circumference is calculated as 5.30 mm and 7.40 mm for warp and weft yarns, respectively.

Moreover, the ultimate tensile strength of textile yarns, σ_t, is calculated based on the following equation

$$\sigma_t = \frac{F_{max}}{A_t}$$

where,

- F_{max} is the maximum pull-out load,
- A_t is the yarn surface area that is provided by the manufacturer.

Finally, another parameter that was analyzed is the $S_{@f\_max}$, which is the related slip at maximum pull-out load. Using the data obtained during a pull-out test, the results will be given for C-TRCC specimens prepared with M45 and M7 mixtures separately in the following sections.

4.2.1 Yarn Pull-out Test Results of C-TRCC with M45 mortar

4.2.1.1 When Tested in the Warp Direction

The yarn pull-out test results for 1Y, 2Y, and 3Y specimens are provided in terms of force versus slip curves as presented in Figure 4-9 and Figure 4-10, for 150- and 100-mm embedment lengths, respectively.

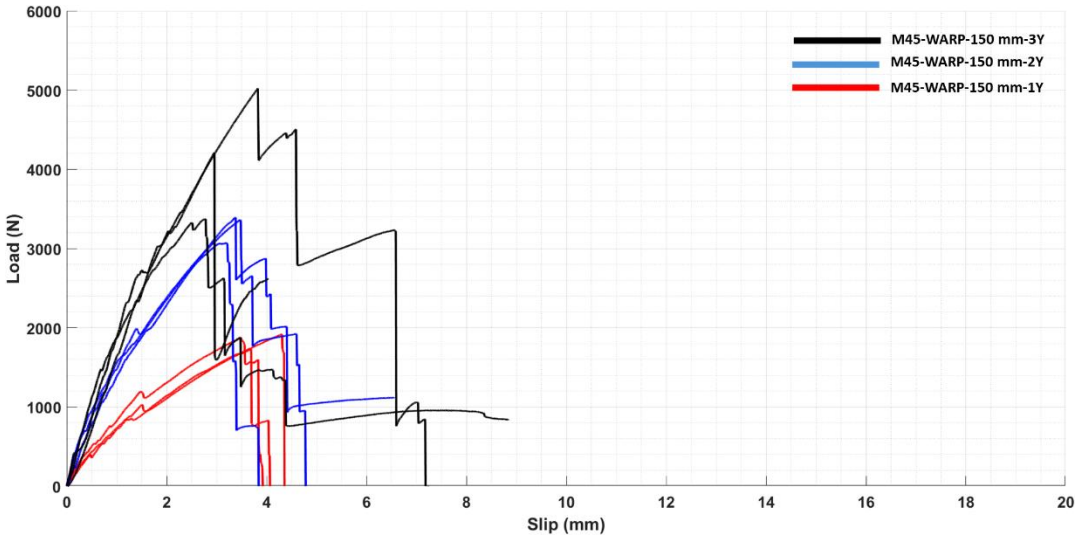

Figure 4-9 Load-slip curves for M45 mortar with 150 mm embedment length

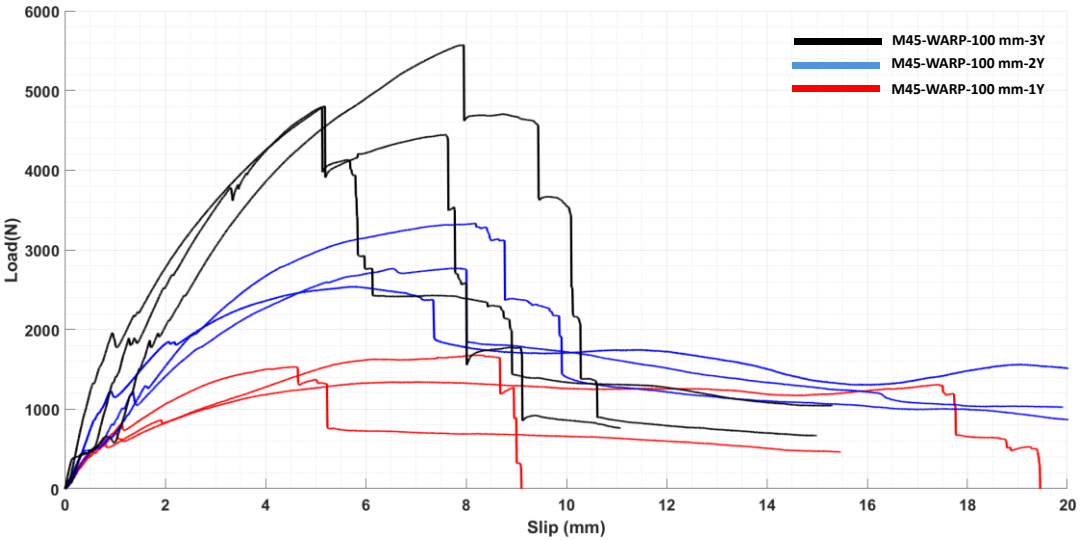

Figure 4-10 Load-slip curves for M45 mortar with 100mm embedment length

The data obtained from these tests are summarized in Table 4-2 with respect to the parameters explained earlier.

Table 4-2 Slip-bond test results for M45 when tested in the warp direction

# of Yarns	Embedment Length (mm)	F_{max} (N)	$\tau_{n,1}$ (MPa)	$\tau_{n,2}$ (MPa)	σ_t (MPa)	$Slip_{@Fmax}$ (mm)	Main Failure Mode
1Y	150	1851	3.7 [5.3]	2.3	2043	3.8 [11.2]	Rupture of Textile
	100	1533	4.6 [11.2]	2.9	1687	6.6 [28.1]	Slippage of Textile
2Y	150	3289	3.3 [5.4]	2.1	1821	3.3 [4.2]	Rupture of Textile
	100	2895	4.3 [14.1]	2.7	1601	7.3 [17.9]	Slippage of Textile
3Y	150	4215	2.8 [19.6]	1.8	1556	3.2 [17.8]	Rupture of Textile
	100	5067	5 [9.0]	3.2	1459	6.8 [26.5]	Rupture of Textile

As can be seen from those figures and the table, the pull-out tests for M45 mortar with warp yarns reveal key insights into the mechanical performance and bonding characteristics of the C-TRCC. Longer embedment lengths (150 mm) resulted in higher pull-out capacities compared to shorter ones (100 mm). For example, $\mathbf{F_{max}}$ for single-yarn specimens increased by 21%, from 1533 N to 1851 N, demonstrating the critical role of embedment length in enhancing pull out load. Shear bond strengths ($\tau_{n,1}$ and $\tau_{n,2}$) decreased with longer embedment lengths due to better stress distribution. Single-yarn specimens showed a reduction in $\tau_{n,1}$ from 4.6 MPa (100 mm) to 3.7 MPa (150 mm), indicating that longer embedment improves overall capacity but reduces shear bond stress. Specimens with 150 mm embedment lengths exhibited higher ultimate textile tensile stresses (σ_t) up to 2043 MPa, while shorter embedment led to greater slip at maximum force. For one yarn configuration slip increased from 3.8 mm (150 mm) to 6.6 mm (100 mm), suggesting less effective anchorage in shorter lengths. At 150 mm embedment length, textile rupture was the dominant failure mode, signifying optimal stress transfer. Conversely, slippage was

prevalent at 100 mm embedment, indicating insufficient anchorage. Multi -yarn configurations increased $\mathbf{F_{max}}$ values, with three-yarn specimens reaching up to 4215 N. However, this resulted in lower bond strengths per unit area due to stress concentrations, highlighting the group effect (Naaman & Shah, 1976). Shear bond strengths derived from experimental data were up to 50% lower than manufacturer estimates, emphasizing the need for precise experimental validation over theoretical models.

Based on the experimental results the observed failure modes needs to be clarified here. Three main failure modes were observed, rupture of textile, slippage of textile and splitting of mortar. However, a fourth failure mode can also be added that involves the telescopic pull-out dominant failure of the textile.

Rupture of textile yarns: The textile yarns break under the tensile loading indicating that the tensile capacity of the yarns has been attained. In this mode, the load-slip curve shows a sharp peak corresponding to the maximum pull-out load that is followed by an immediate drop (Figure 4-11

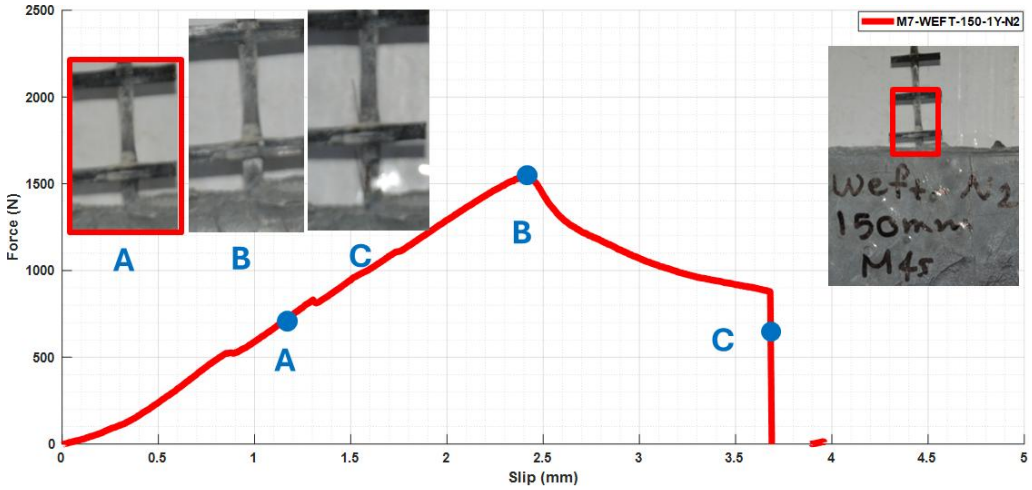

Figure 4-11 Textile rupture failure mode

Telescopic pull-out dominant rupture of textile yarns: After a partial debonding between yarn /mortar the outer filaments start to fail this continues in a progressive process until the yarn fails. The samples show a load-slip curve that has multiple stages. Each peak in the graph represents when a material layer starts to slip away, followed by a drop in the load (Figure 4-12).

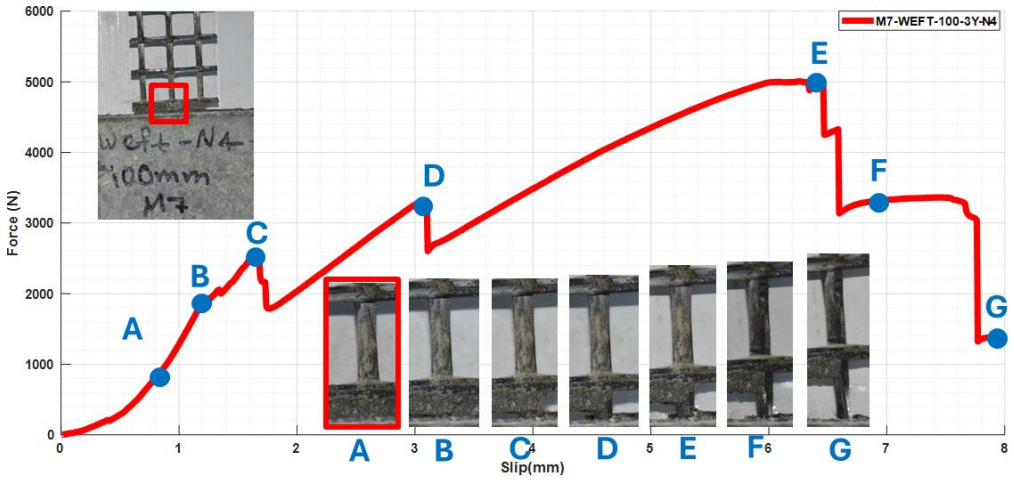

Figure 4-12 Telescopic failure dominant textile rupture failure

Slippage of textile yarns: In this mode, textile yarn is extracted from concrete without rupturing illustrating that the bonding strength between textile/mortar is lower than the tensile strength of the textile. The load slip curve typically indicates a peak load that is followed by a plateau or gradual decline while slip increases (Figure 4-13).

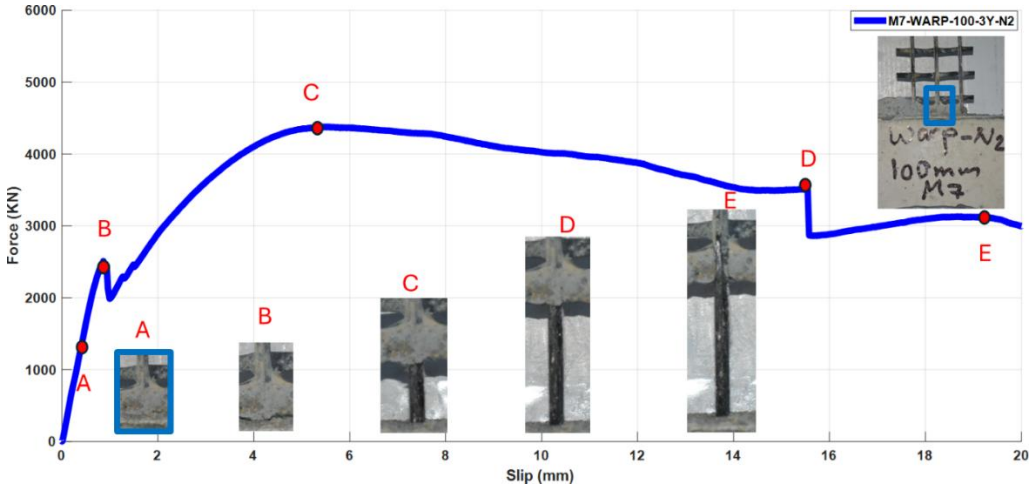

Figure 4-13 Textile pull-out failure mode

Splitting failure of mortar: Cracks develop in the mortar in the same direction as the embedded textile instead of a clean pull-out. The load-slip curve indicates an increase in load prior to reaching the textile tensile strength a sudden drop due to the cracking of mortar .

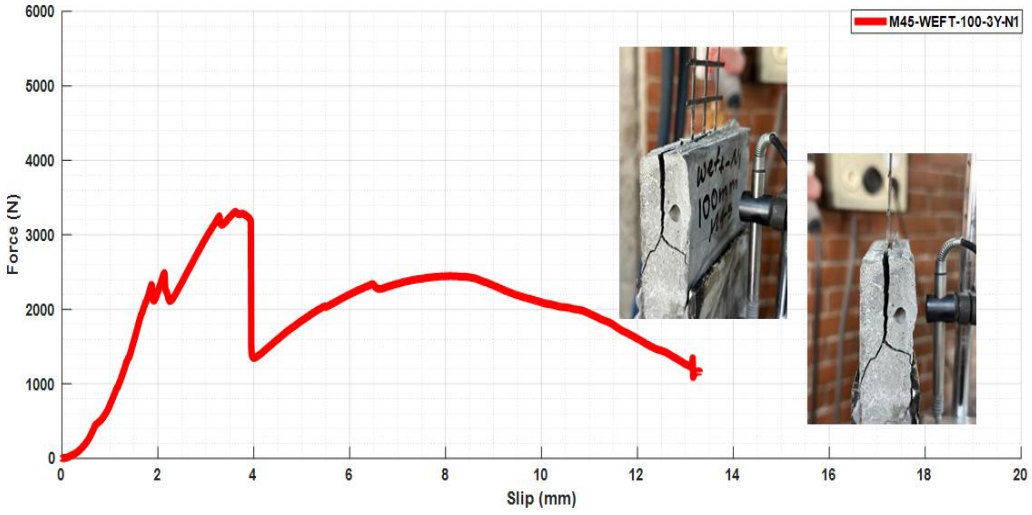

Figure 4-14 Splitting failure mode

It should be noted that 50 mm embedment lengths were not tested in the warp direction, as the slippage was the dominant failure mode in M45 mixtures.

4.2.1.2 When Tested in the Weft Direction

Similar to the warp direction tests, the yarn pull-out test results for the weft direction (1Y, 2Y, and 3Y specimens) are presented as force-slip curves in Figure 4-15 (150-mm embedment length) and Figure 4-16 (100-mm embedment length).

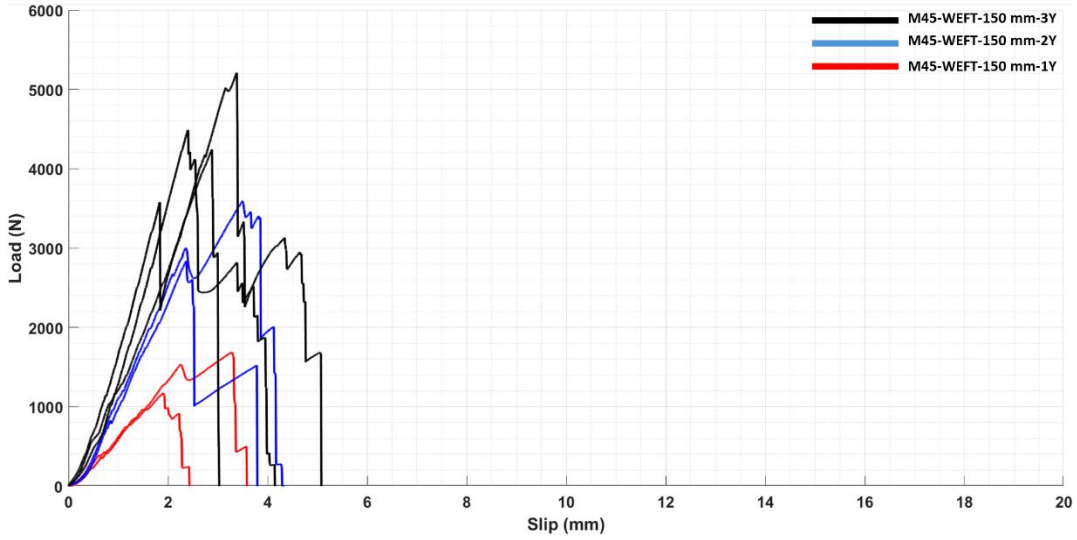

Figure 4-15 Load-slip curves for M45 mortar with 150mm embedment length

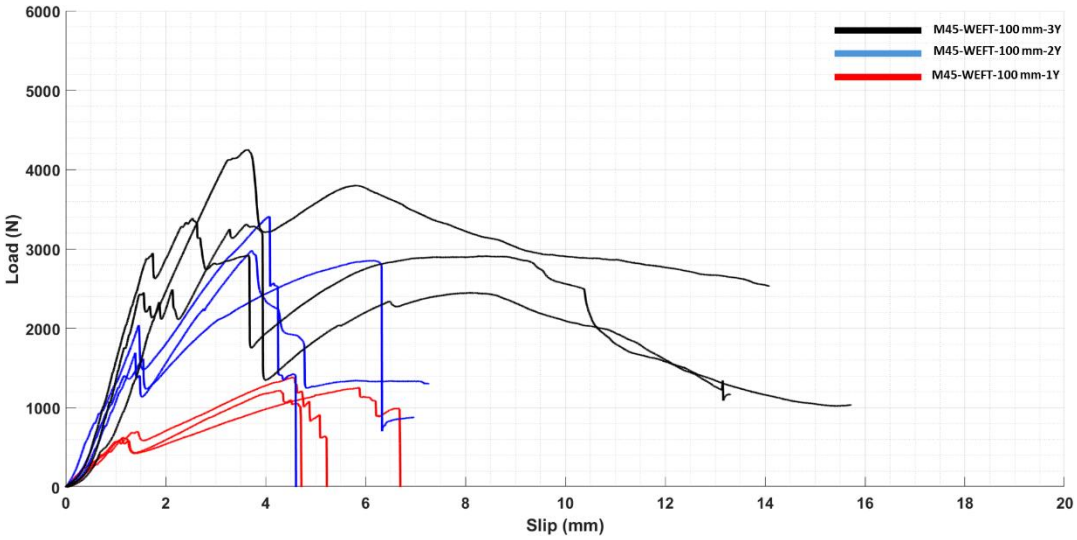

Figure 4-16 Load-slip curves for M45 mortar with 100 mm embedment length

When the data obtained from these tests are summarized in Table 4-3 with respect to the parameters explained earlier, the pull-out tests for M45 mortar with weft yarns reveal important trends in the slip-bond behavior of C-TRCC. As expected, longer embedment lengths (150 mm) generally increase pull-out strength. For example, in single-yarn specimens, F_{max} increased from 1297 N for 100 mm embedment to 1440 N for 150 mm, and the corresponding shear bond strengths ($\tau_{n,1}$ and $\tau_{n,2}$) decreased with increasing embedment length. Similarly, the ultimate textile strength (σ_t) were higher for specimens with longer embedment lengths, demonstrating more efficient stress transfer. For instance, single-yarn specimens achieved a σ_t of 1585 MPa at 150 mm embedment, compared to 1428 MPa at 100 mm. Conversely, slip at maximum force was higher for shorter embedment lengths, suggesting reduced anchorage effectiveness. This is evident from single-yarn specimens where slip increased from 2.6 mm at 150 mm embedment to 4.9 mm at 100 mm. The tests also highlighted issues with specimen integrity, particularly in single-yarn specimens Figure 4-15(a) and Figure 4-16(a). Several were lost during preparation or testing due to the weaker structure of the weft yarns, which affected the overall reliability and consistency of the results. These losses underscore the challenges posed by the structural characteristics of weft yarns in such experimental setups.

Table 4-3 Slip-bond test results for M45 when tested in the weft direction

# of Yarns	Embedment Length (mm)	F_{max} (N)	$\tau_{n,1}$ (MPa)	$\tau_{n,2}$ (MPa)	σ_t (MPa)	$Slip_{@Fmax}$ (mm)	Main Failure Mode
1Y	150	1440	2.9	1.3 [25.1]	1585	2.6 [37.9]	Rupture of Textile
	100	1297	3.9	1.8 [6.8]	1428	4.9 [17.3]	Rupture of Textile
2Y	150	3230	3.2	1.5 [16.5]	1786	2.9 [27.3]	Rupture of Textile
	100	3097	4.6	2.1 [9.4]	1712	4.6 [28.2]	Splitting of Mortar
3Y	150	4662	3.1	1.4 [10.8]	1721	2.9 [17.0]	Rupture of Textile
	100	3663	3.6	1.7 [14.3]	1352	3.3 [19.4]	Splitting of Mortar

Failure modes varied with embedment length and yarn configuration. At 150 mm, textile rupture was the predominant failure mode. At 100 mm, splitting of the mortar was observed in two-yarn and, three yarn configurations as shown in Figure 4-17 indicating a strong bonding with the weft yarns.

(a) 2Y

(b) 3Y

Figure 4-17 Splitting failure mode observed in (a) 2Y (b) 3Y configurations

The number of yarns also played a significant role in determining pull-out behavior. Multi-yarn specimens exhibited higher load values, with three-yarn specimens reaching up to 4662 N at 150 mm embedment. Moreover, the mechanical interlock in the warp and weft junction shows how warp and weft yarns interact to create a mechanical interlock, enhancing slip bod response and structural integrity under loading (Figure 4-18).

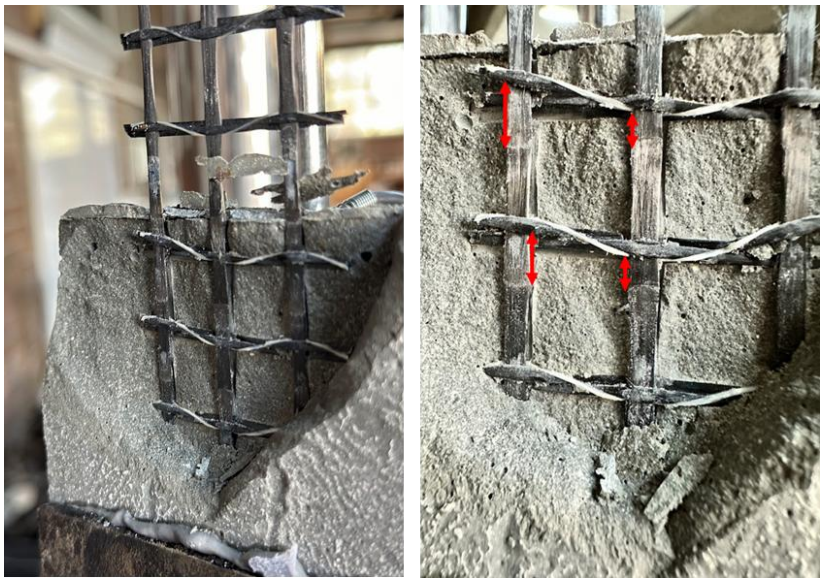

Figure 4-18 The mechanical interlock illustration in the warp and weft junction

It should be noted that 50 mm embedment lengths were not tested in the weft direction, as the slippage or splitting was the dominant failure mode in M45 mixtures.

4.2.2 Yarn Pull-out Test Results of C-TRCC with M7 mortar

4.2.2.1 When Tested in the Warp Direction

The yarn pull-out test results for 1Y, 2Y, and 3Y specimens are provided in terms of force versus slip curves as presented in Figure 4-19 and Figure 4-20, for 150- and 100-mm embedment lengths, respectively.

The data obtained from these tests are summarized in Table 4-4 with respect to the parameters explained earlier. One observation, as expected, is that longer embedment lengths significantly enhance the pull-out capacity. For instance, single-yarn samples demonstrated an increase in the maximum pull-out force ($\mathbf{F_{max}}$) from 1158 N at 100 mm embedment to 1839 N at 150 mm. The textile tensile stress (σ_t) exhibited a noticeable dependency on embedment length, with higher values recorded for specimens with longer embedment, indicating a rupture type of failure

mode. For example, single-yarn samples achieved a tensile stress of 2037 MPa at 150 mm compared to 1270 MPa at 100 mm. Conversely, shorter embedment exhibited greater slip at maximum force, increasing from 3.0 mm at 150 mm to 6.1 mm at 100 mm. Failure modes were also influenced by embedment length.

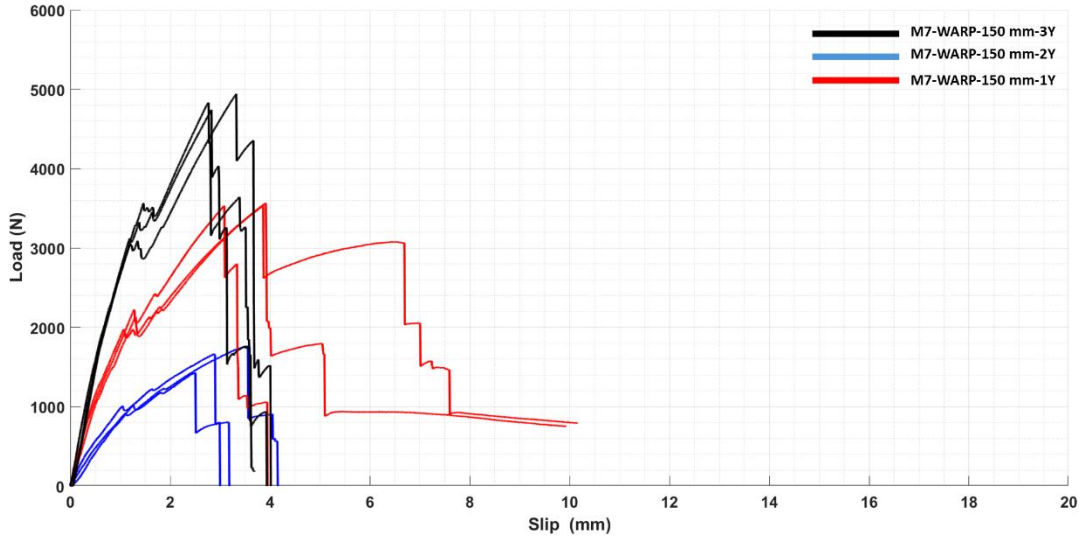

Figure 4-19 Load-slip curves for M7 mortar with 150mm embedment length

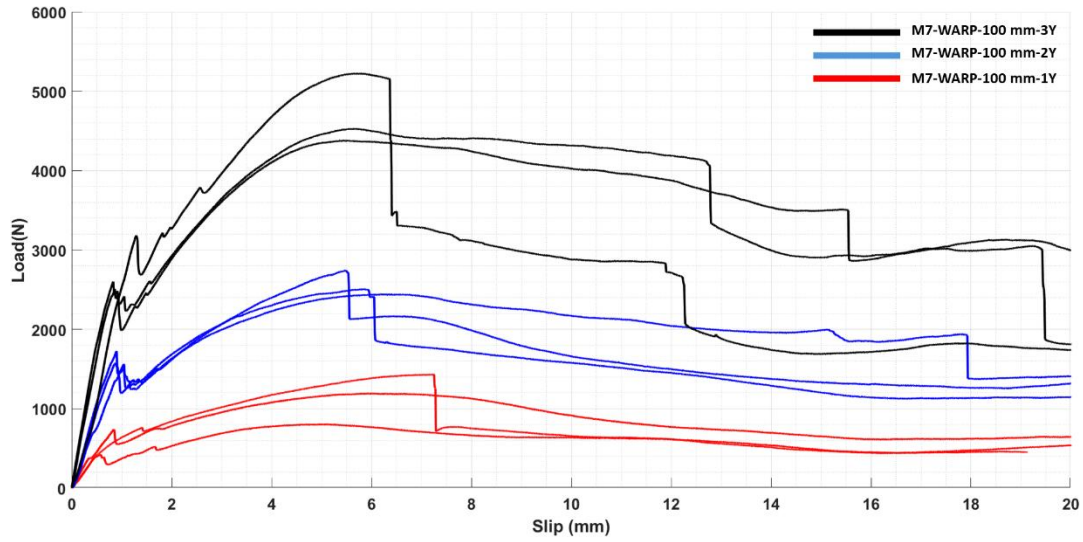

Figure 4-20 Load-slip curves for M7 mortar with 100 mm embedment length

Table 4-4 Slip-bond test results for M7 when tested in the warp direction

# of Yarns	Embedment Length (mm)	F_{max} (N)	$\tau_{n,1}$ (MPa)	$\tau_{n,2}$ (MPa)	σ_t (MPa)	$Slip_{@Fmax}$ (mm)	Main Failure Mode
1Y	150	1839	3.6 [3.0]	2.3	2037	3.0 [17.7]	Rupture of Textile
	100	1158	3.4 [27.4]	2.2	1270	6.1 [17.3]	Slippage of Textile
2Y	150	3558	3.5 [0.6]	2.2	1968	3.6 [12.9]	Rupture of Textile
	100	2582	3.8 [6.1]	2.4	1425	5.8 [6.2]	Slippage of Textile
3Y	150	4853	3.2 [2.0]	2	1792	3.0 [10.3]	Rupture of Textile
	100	4728	4.7 [9.5]	3	1745	5.6 [2.5]	Slippage of Textile

Specimens with 150 mm embedment predominantly exhibited textile rupture, signifying effective stress transfer and full utilization of the yarn's strength. In contrast, 100 mm embedment frequently resulted in textile slippage, Figure 4-21 indicative of insufficient bonding length. Multi-yarn configurations presented additional complexity, as three-yarn specimens achieved a maximum pull-out force of 4853 N at 150 mm. However, these configurations often led to stress concentrations, resulting in a reduction in bond strength per unit area which is known as group effect.

It should be noted that 50 mm embedment lengths were not tested in the warp direction, as the slippage was the dominant failure mode in M7 mixtures.

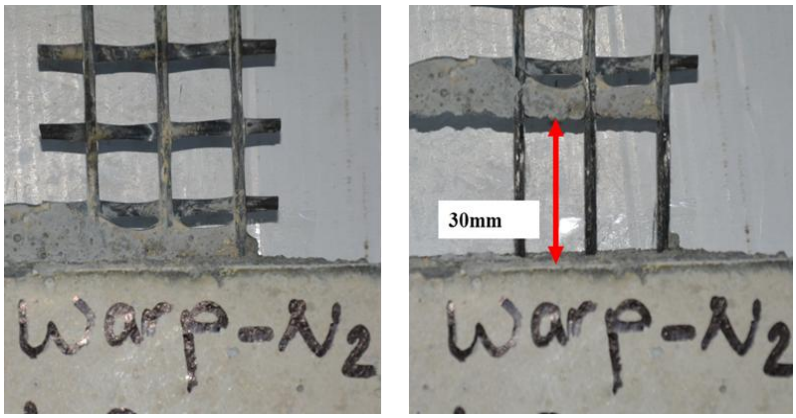

(a) Before testing (b) After testing

Figure 4-21 Textile slippage failure mode in M7 mortar

4.2.2.2 When Tested in the Weft Direction

The yarn pull-out test results for 1Y, 2Y, and 3Y specimens are provided in terms of force versus slip curves as presented in Figure 4-22, Figure 4-23 and Figure 4-24 for 150-, 100- and 50 mm embedment lengths, respectively. Similar to the previous sections, the data obtained from these tests are summarized in Table 4-5 with respect to the parameters explained earlier.

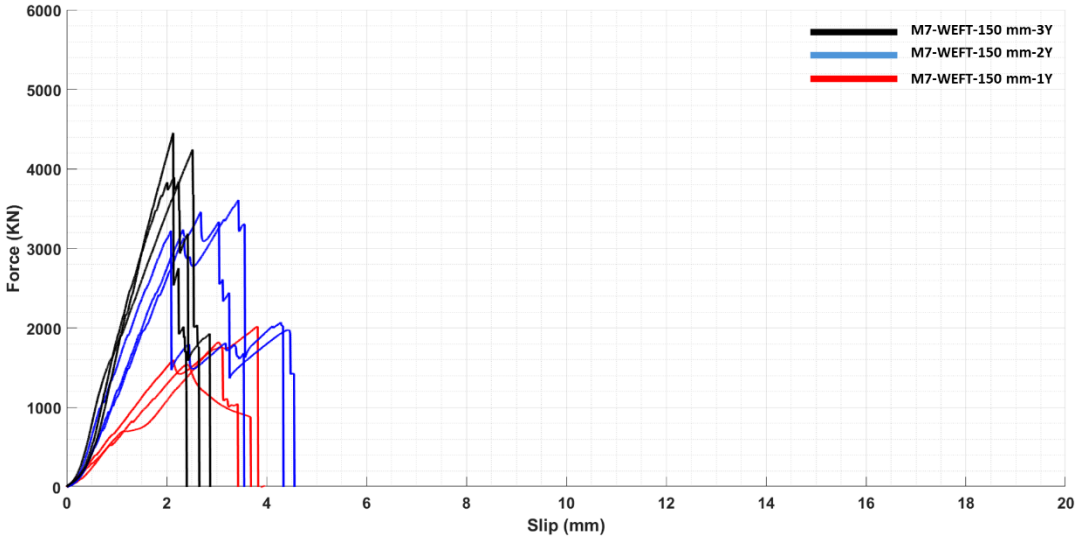

Figure 4-22 Load-slip curves for M7 mortar with 150mm embedment length

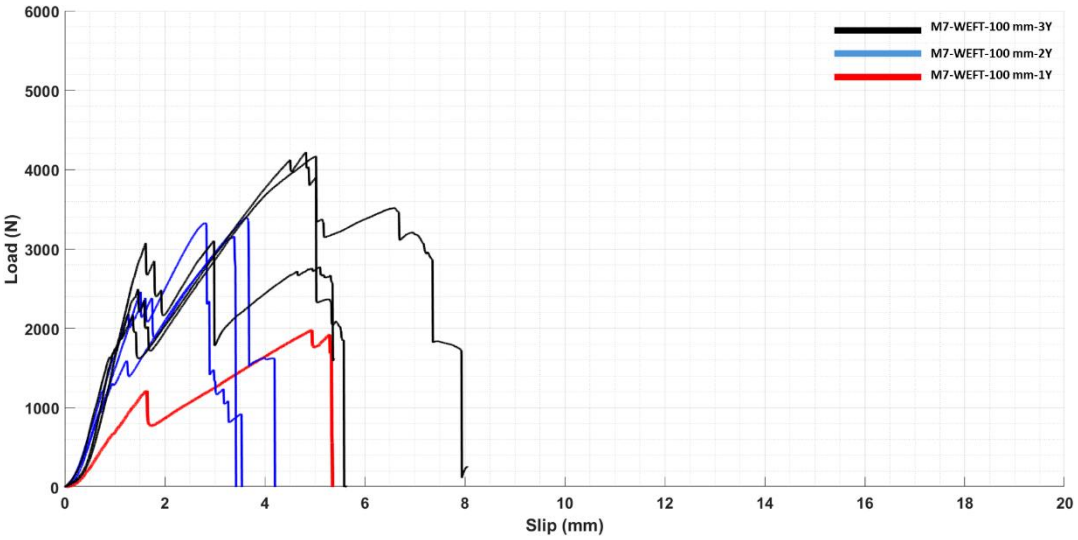

Figure 4-23 Load-slip curves for M7 mortar with 100mm embedment length

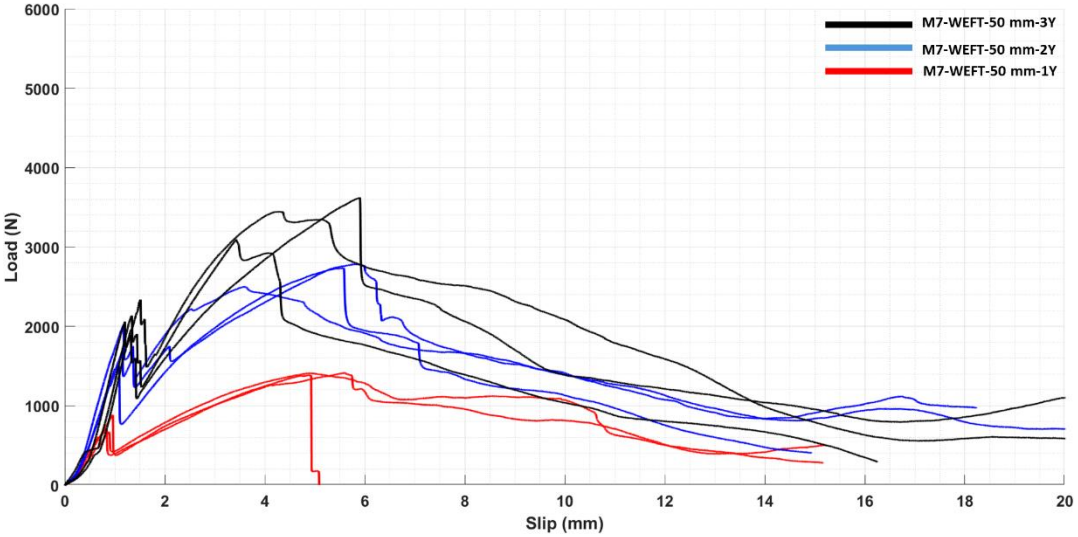

Figure 4-24 Load-slip curves for M7 mortar with 50 mm embedment length

As expected, the embedment length demonstrated a pronounced impact on the pull-out force. For instance, single-yarn specimens exhibited a substantial increase in maximum pull-out force $\mathbf{F_{max}}$, rising from 1416 N at 50 mm embedment to 1789 N at 150 mm embedment. This trend underscores the enhanced mechanical interlock provided by longer embedment lengths. Interestingly, while F_{max} increased, bond strength ($\boldsymbol{\tau_{n,1}}$ and $\boldsymbol{\tau_{n,2}}$) slightly declined with longer embedment, likely due to stress being distributed over a larger bonded area.

Table 4-5 Slip-bond test results for M7 when tested in the weft direction

# of Yarns	Embedment Length (mm)	F_{max} (N)	$\tau_{n,1}$ (MPa)	$\tau_{n,2}$ (MPa)	σ_t (MPa)	$Slip_{@Fmax}$ (mm)	Main Failure Mode
1Y	150	1789	3.5	1.6 [13.3]	1971	3.1 [22.8]	Rupture of Textile
	100	1999	6.0	2.7	2199	4.9	Rupture of Textile
		[Can't be determined, only 1 specimen tested]					
	50	1416	8.4	3.8 [1.1]	1559	5.1 [7.7]	Slippage of Textile
2Y	150	3196	3.2	1.4 [19.4]	1765	2.6 [33.8]	Rupture of Textile
	100	3309	4.9	2.2 [3.6]	1830	3.3 [12.8]	Rupture of Textile
	50	2689	8.0	3.6 [5.7]	1485	4.5 [24.4]	Slippage of Textile
3Y	150	4213	2.8	1.3 [6.7]	1554	2.3 [9.6]	Rupture of Textile
	100	4478	4.4	2 [10.5]	1654	5.4 [14.5]	Rupture of Textile
	50	3404	6.8	3.1 [7.9]	1254	4.5 [27.8]	Slippage of Textile

Textile tensile stress (σ_t) also showed notable variation with embedment length, reaching up to 1971 MPa for single-yarn specimens at 150 mm compared to 1559 MPa at 50 mm. Conversely, shorter embedment resulted in greater slip at maximum force, increasing from 3.1 mm at 150 mm to 5.1 mm at 50 mm, highlighting reduced anchorage stability.

The failure modes further emphasized the role of embedment length. Textile rupture dominated in specimens with 150 mm embedment, indicating effective stress transfer and optimal utilization of yarn strength. In contrast, shorter embedment often led to textile slippage, reflecting insufficient bonding length. Multi-yarn specimens achieved the highest pull-out forces, such as 4213 N for three-yarn configurations at

150 mm embedment, but also faced challenges like reduced bond strength per unit area due to stress concentrations. Moreover, the embedment lengths with 100 mm showed telescopic pull out dominant textile rupture Figure 4-25

The load-slip curves provided additional clarity. Longer embedment lengths displayed steeper initial slopes, signaling stronger bonding at the start of loading. Multi-yarn configurations, while reaching higher peak forces, exhibited more extensive slip, reflecting complex interactions between the yarns and the matrix.

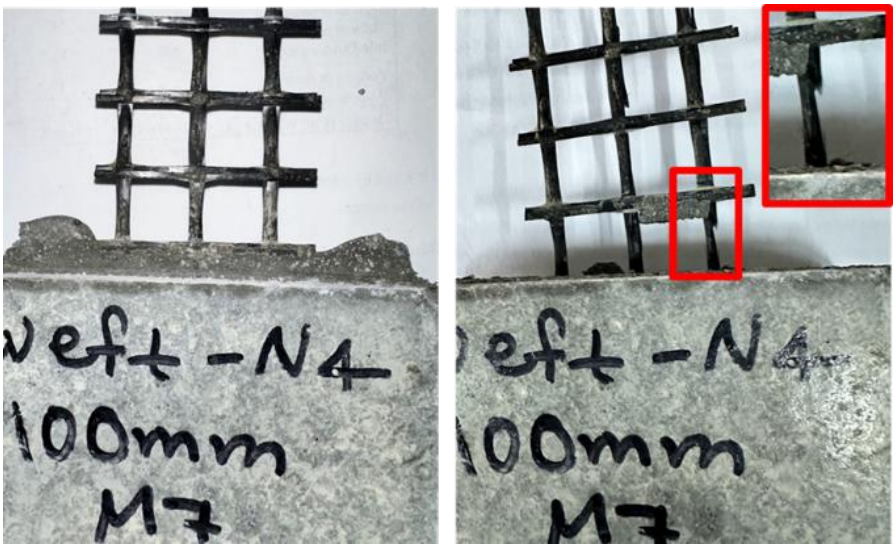

Figure 4-25 Telescopic pull-out dominant textile rupture in 3Y weft with 100 mm embedment length in M7 mortar

4.2.3 Discussion of results for M7 mortar pull-out tests

4.2.3.1 Pull-out load capacity

Maximum pull-out load results of CTRCC-M7 mortar reveal the influence of yarn configuration, yarn orientation, and embedment length on slip-bond behavior between the textile and mortar (Figure 4-26). Despite the absence of 50 mm warp

specimens which was due to slippage of specimens in the warp direction, the trends across the remaining data are clear and show meaningful conclusions.

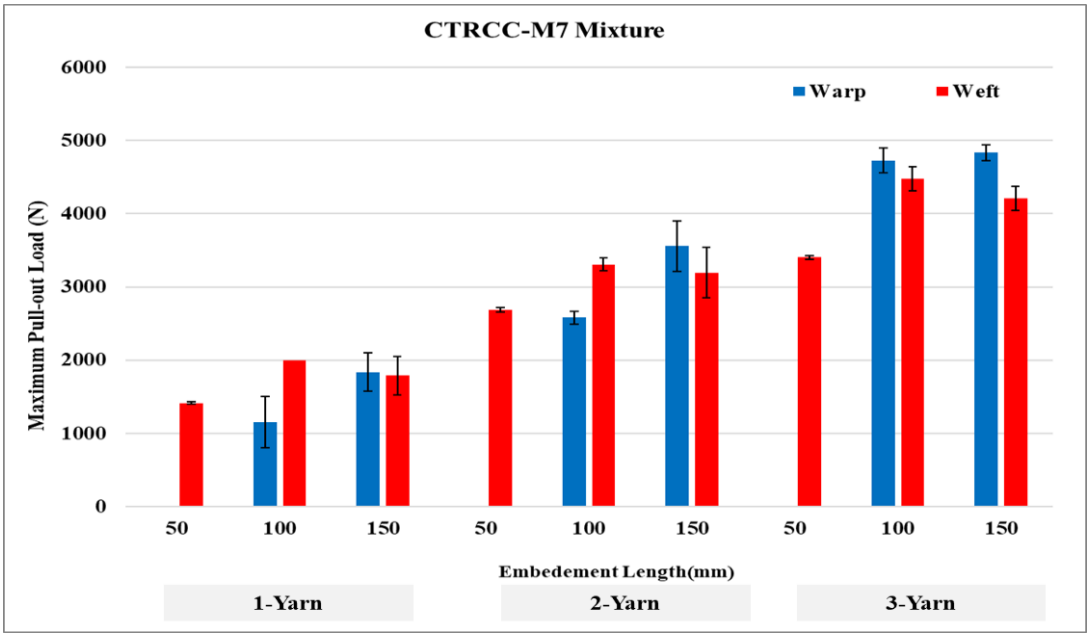

Figure 4-26 Maximum pull-out loads in the M7 mortar

With increasing number of yarns, the pull-out load capacity improved. For instance, in the 1Y configuration at 100 mm embedment, the weft orientation reaches a maximum pull-out load of 1,999 N. In contrast, the 2Y configuration at the same embedment length shows a much higher load of 3,309 N for the weft, representing a 65.6% increase. In the 3Y configuration, the load further increases to 4,833 N for the weft orientation at 100 mm embedment—an increase of 144% over the 1Y configuration. This consistent trend for different embedment lengths for both warp and weft direction results illustrates that higher volumes of textile inside the mortar contribute to better mechanical interlock and enhanced pull-out capacity (Alva Peled et al., 2006). Particularly in 3Y specimens mean value of the maximum pull-out load reached up to 4833 N for warp direction.

Considering embedment length, the length at which yarn is embedded in mortar, correlates with the pull-out load, and the longer embedment illustrate greater pull-out loads. For example, in the 2Y configuration with weft orientation, increasing embedment length from 50 mm to 100 mm raises the pull-out load from 2,689 N to 3,309 N, an increase of 23.1%. However, further increasing the embedment length to 150 mm yields a more modest gain, with the pull-out load reaching 3,558 N, only a 7.5% increase over the 100 mm length. The most significant increase in load occurs when embedment length is increased from 50 mm to 100 mm in the weft direction in which the failure mode of yarn changes (Alma'aitah & Ghiassi, 2022; Dalalbashi et al., 2018, 2021). This reducing return shows while an increase of embedment length increases the load-bearing capacity of yarns, an optimal length exists in which the additional embedment length offers minimal benefits (Banholzer, 2006.).

The weft direction specimens generally supply higher pull-out loads than warp direction, specifically at shorter embedment lengths and lower yarn numbers. For instance, in the 1Y configuration at 100 mm embedment, the pull-out load for weft orientation is 1,999 N, compared to 1,416 N for the warp—a difference of 41.2%. At 150 mm embedment, this difference is reduced, with the weft load at 1,829 N and warp at 1,789 N, a negligible difference of just 2.2%. In the 3Y configuration, the warp surpasses the weft at 150 mm embedment, reaching 4,478 N compared to 4,213 N. This is attributed to cross-sectional structure and the crimping nature of weft yarn. The results indicate that yarn direction effects on pull-out capacity are more obvious in shorter embedded lengths and lower yarn numbers. However, the differences in load capacity reduced in 3Y configuration and 150mm embedded lengths.

4.2.3.2 Nominal shear bond strength

Figure 4-27 presents the warp and weft nominal shear strength, calculated assuming a circular yarn shape based on the manufacturer's datasheet, consistent with previous literature (Williams Portal et al., 2014)(Alva Peled & Bentur, 2003).

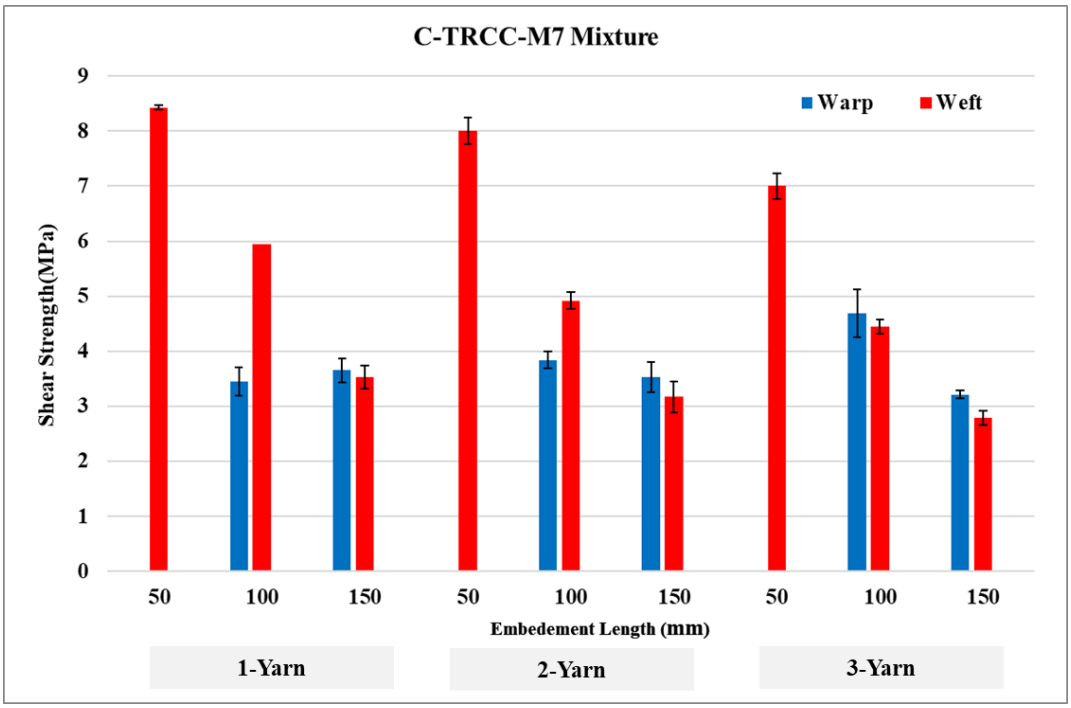

Figure 4-27 Shear bond strength based on manufacturer-provided dimensions for M7 mortar

Considering the embedment length, 1Y configuration, weft yarn specimens with 50 mm (experienced slippage) achieved an 8.4 MPa shear strength which is significantly higher than at longer embedment lengths (failure modes were yarn rupture). At 100 mm, weft shear strength drops by 29.4% to 6.0 MPa, and at 150 mm, it further declines to 3.5 MPa, reflecting a 55.5% decrease from 50 mm. On the other hand, there was no significant difference in nominal shear strength between slipped specimens with 100mm and yarn telescopic failure with 150 mm specimens with 3.4 MPa and 3.6 MPa, respectively.

For 2Y configuration weft yarns show 8.0 MPa at 50 mm, decreasing to 4.92 MPa (38.5% reduction) at 100 mm, and further to 3.17 MPa at 150 mm (60.4% lower than at 50 mm). Warp specimens in this configuration again indicate less sensitivity to embedment length, with shear strengths of 3.84 MPa at 100 mm and 3.53 MPa at 150 mm.

In 3Y configuration tests for weft direction, average shear strength is 6.8 MPa at 50 mm (slipped) which drops to 4.4 MPa at 100 mm (telescopic and yarn rupture) (a 33.0% reduction) and 2.79 MPa at 150 mm (yarn rupture) (60.1% decrease from 50 mm). However, in warp direction specimens show a peak at 4.44 MPa at 100 mm and decline slightly to 4.0 MPa at 150 mm, with a modest 9.9% decrease. The higher initial strength at 100 mm suggests that multiple yarns with moderate embedment may enhance warp performance, which provides an optimal bond strength. These findings align with the literature research results of (Shannag et al., 1997) that demonstrated that with an increase in the embedment length of steel fibers, the frictional shear stress values decreased.

Considering the yarn direction, weft specimens generally illustrate higher shear bonds for example the shear strength for slipped specimens (50mm) is around 8 MPa while this value for warp slipped specimens(100mm) is around 3.5 MPa.

That should be noted with increasing the yarn number difference in shear strength reduces. for instance, at 100 mm, the difference is only about 5.6%, with weft at 4.69 MPa and warp at 4.44 MPa, suggesting that higher yarn counts equalize performance across orientations at this embedment length.(Naaman & Shah, 1976) revealed that the shear frictional stress capacity of steel fibers significantly decreased as the number of fibers increased in the same area of concrete which is related to the group effect on pull-out capacity .

However, Figure 4-28 shows bond strength values derived from laser scanning, which assumes a more realistic elliptical yarn cross-section. These laser-scanned results, facilitated by advanced technology, offer greater accuracy. Both sets of results are presented here to highlight the significant differences arising from the yarn geometry assumptions. The comparison underscores the impact of approximating the yarn shape as a circle on the calculated bond strength.

The Figure 4-27 depicts the results based on circumferences delivered from laser scanning, with the assumption that the yarns are elliptical. This results in more accurate shear bond strength values for pull-out tests, as evidenced by the chart. Although the values are approximately half of those observed in previous charts, the trends are quite similar to those observed in the previous shear bond chart. For example, when the yarns were assumed to be circular, the weft 500mm specimens exhibited a shear bond strength of 8.43 MPa. In contrast, when the assumption was elliptical, the corresponding value was 3.83 MPa, representing a significant decrease of approximately 54.6% compared to the circular assumption.

Although the dimensions of the weft yarns are larger than those of the warp yarns, the shear bond strength values of the warp are higher than those of the weft yarns. This phenomenon can be attributed to the structural stability of the warp yarns, which demonstrate superior performance in pull-out tests(Alva Peled et al., 2008).

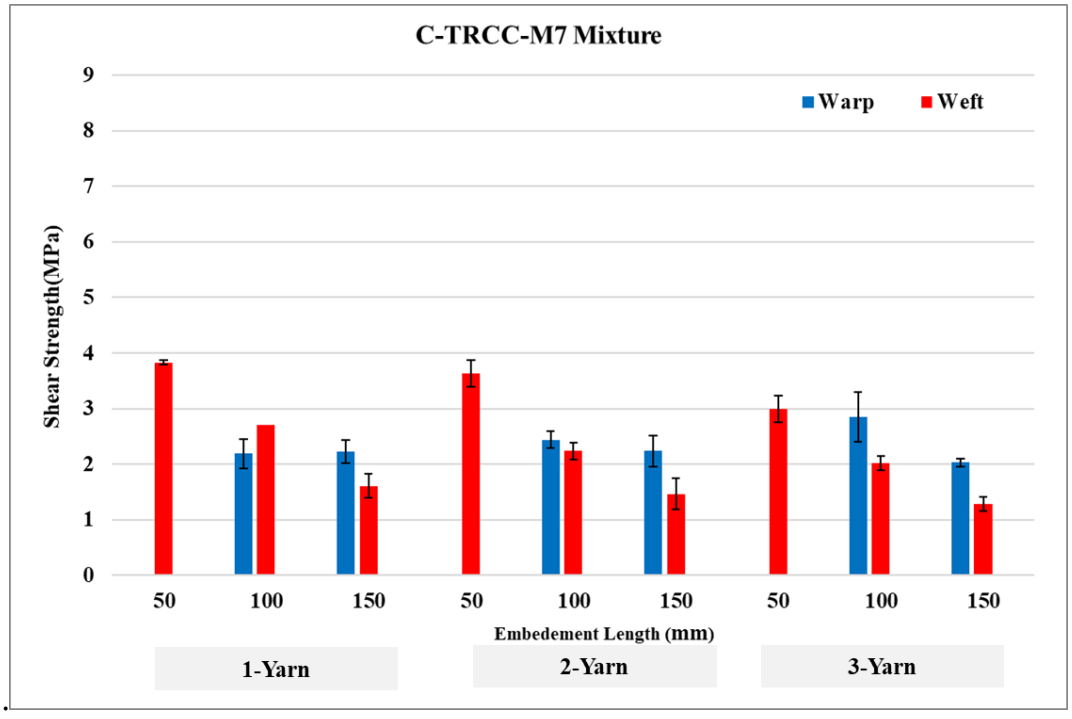

Figure 4-28 Shear bond strength based on laser scanning dimensions for C-TRCC with M7 pull-out tests

4.2.3.3 Tensile strength

The tensile strength of carbon textiles in the warp direction (see Figure 3 in Chapter 3) is 1933 MPa, while in the weft direction, it is 1900 MPa. As illustrated in Figure 4-22, specimens with an embedded length of 150mm exhibited a failure mode wherein the yarn ruptured or experienced a telescopic failure. This tensile strength was observed to be within the range of the yarn's ultimate tensile strength. However, in specimens exhibiting slippages specifically, warp 100mm and weft 50mm specimens due to yarn pull-out the yarns did not utilize their full tensile strength capacity, resulting in tensile strength values that were considerably lower, approximately 1500 MPa.

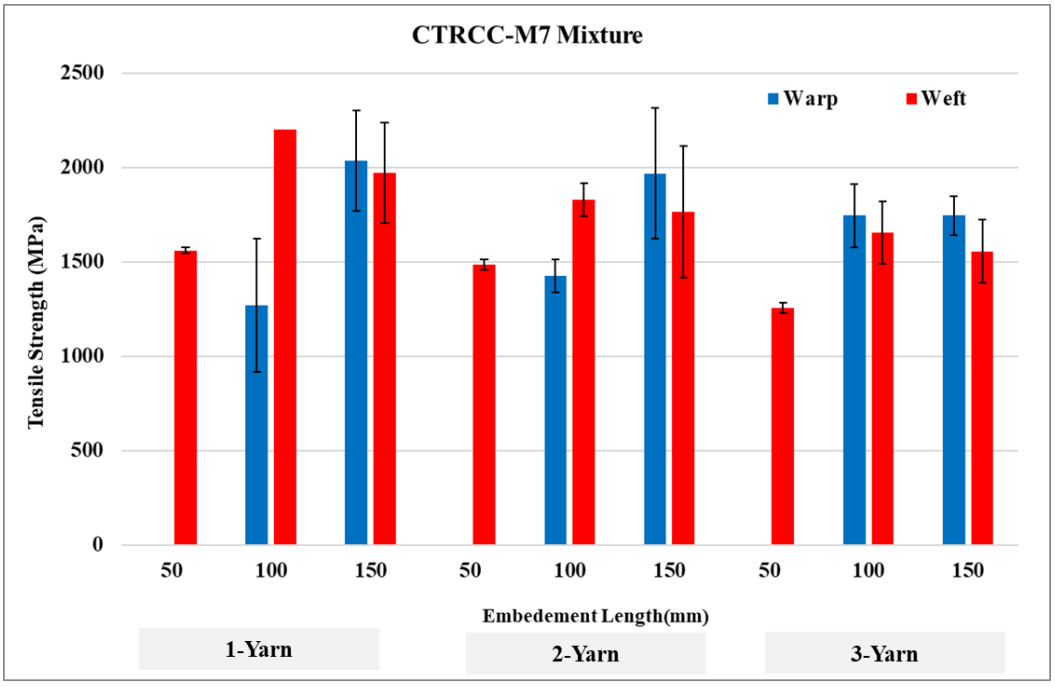

Figure 4-29 Tensile strength of C-TRCC with M7 pull-out tests

4.2.3.4 Slip at maximum pull-out load

In both orientations, the slip value at the maximum load is observed to decrease Figure 4-30 with increasing embedded length. To illustrate, in warp yarns with a 3-yarn configuration, the slip value decreases from approximately 3.5 mm at an embedded length of 100 mm to 2.2 mm at an embedded length of 150 mm, indicating a 37% reduction. The slip of specimens that experienced yarn pull-out in the weft direction remained at a stable value of 5 mm, while specimens of warp yarns that slipped exhibited a higher slip value of 6 mm when embedded for 100 mm.In comparing the overall slip values, it was observed that warp yarns exhibited higher values than weft yarns. In the case of specimens oriented in the ft direction, this can be attributed to the structural features of the yarns themselves. Warp yarns have a denser and more stable cross-sectional area, which allows them to be more stable and prone to telescopic failure. However, the structural defects of weft yarns cause a weaker performance.

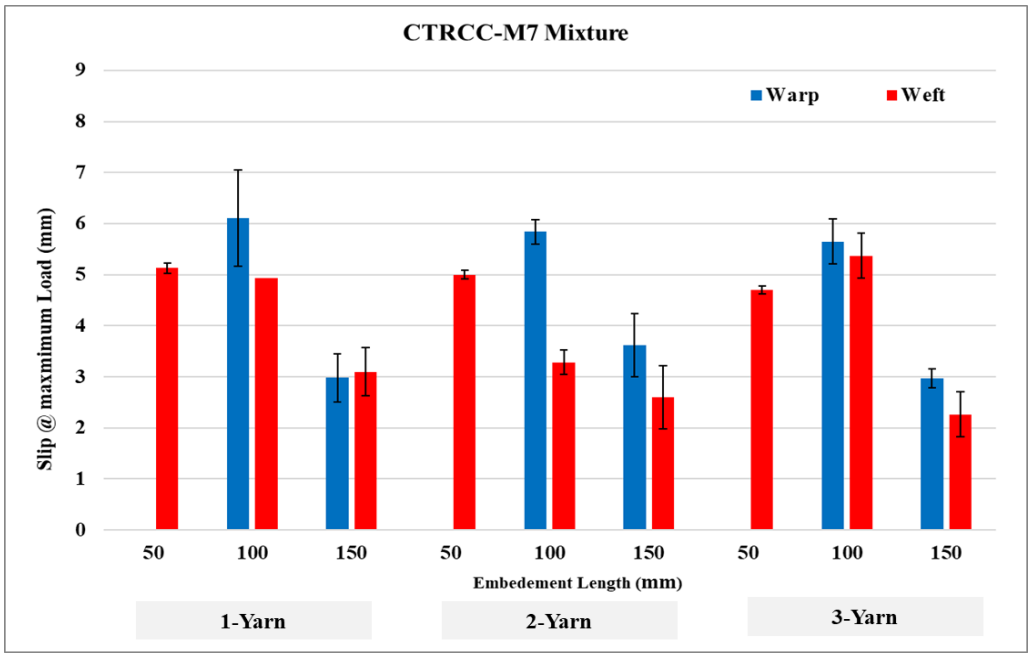

Figure 4-30 Slip@F_max of C-TRCC with M7 pull-out tests

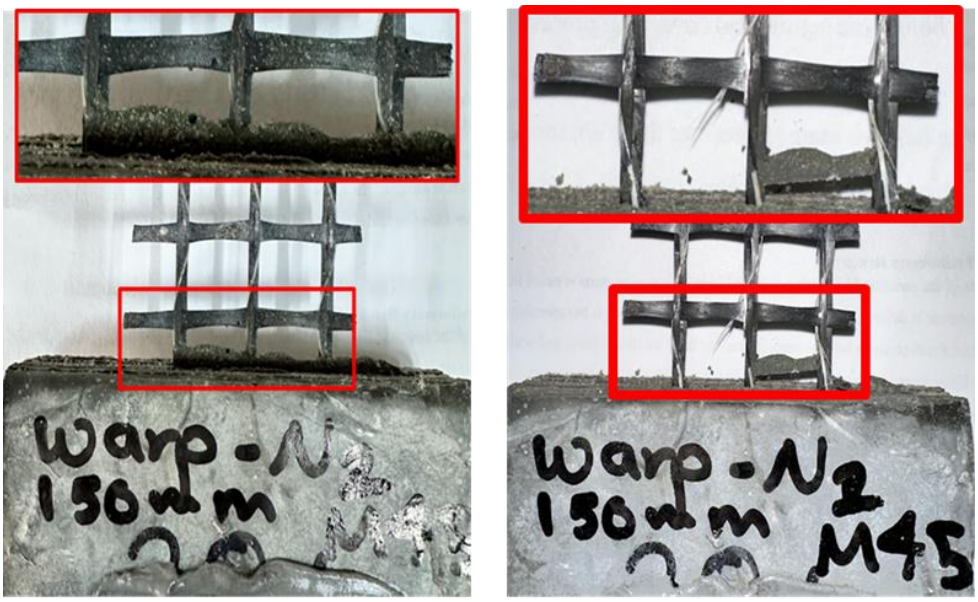

(a) (b)

Figure 4-31 Yarn telescopic failure mode in 3Y -150mm with M45 mortar

4.2.4 Discussion of results for M45 mortar pull out tests

CTRCC pull-out tests for M45 mortar conducted in three (1Y, 2Y, and 3Y) configurations for two (100mm, and 150mm) embedment lengths in warp and weft directions, and the mechanical characteristics such as pull-out load, shear bond strength, ultimate tensile strength, slip at pull out load, and energy absorption analyzed in average values bar charts as depicted in following figures

4.2.4.1 Maximum pull-out loads

This study aimed to investigate the effect of yarn configurations, embedment lengths, and textile orientations on the pull-out behavior of (CTRCC) with M45 mortar. The findings revealed a clear trend and relationship among these variables.

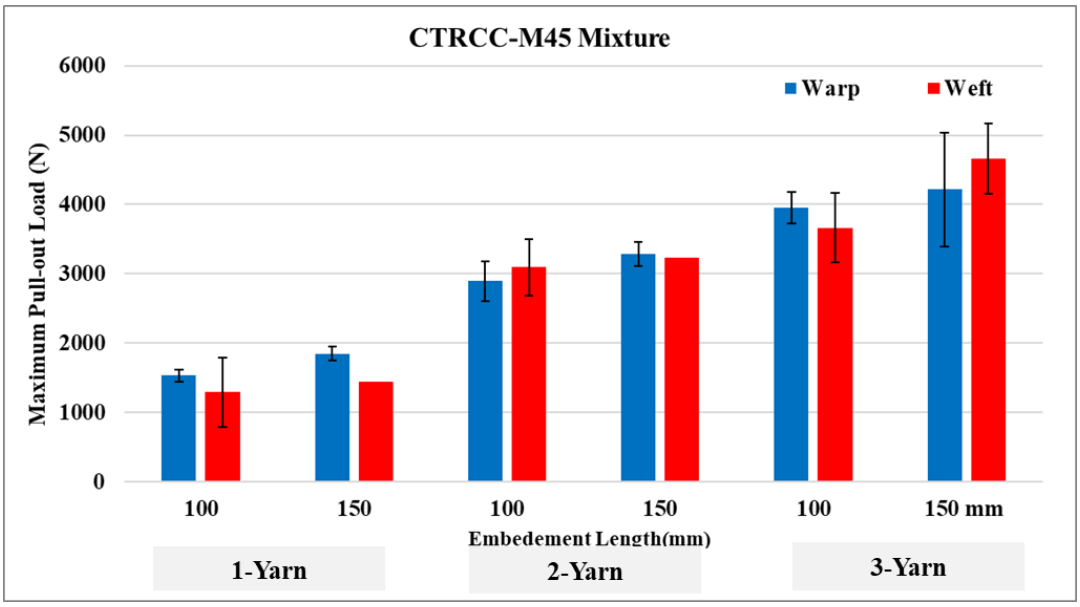

Figure 4-32 Maximum pull-out loads of C-TRCC with M45 mortar

Aa can be seen from Figure 4-32 The findings revealed that an increase in yarn number in the specimens had a notable impact on pull-out performance, with an increase in yarn number also increasing maximum pull-out loads. For example, in the weft direction, the pull-out load increased by up to 138% at a distance of 100mm from the 1Y to the 2Y configuration and by 124% at an embedment length of 150mm. The corresponding values for the warp are 89% and 78%, respectively. The increase in pull-out loads from 2Y to 3Y was only 18% in 100mm and 44% in 150mm embedded length, with the corresponding values for the warp direction being 36% and 28%.

An increase in the embedment length enhances the pull-out load values across all yarn configurations. However, the percentage of increase diminishes as the yarn number increases. For instance in warp direction with an increase of embedded length from 100mm to 150mm the pull-out load improved by 21%,14%, and 7% for 1Y,2Y, and 3Y respectively.

The other noticeable observation in pull-out loads of specimens is the difference between warp and weft yarns. At 1Y and specimens, warp yarns outperform weft. For example, at 2-Yarn and 150 mm, warp achieves 3289 N, which is higher than the 3230 N of weft despite smaller percentage improvements (13.6% vs. 4.3%).

The other noticeable fact is the damage to weft yarns during casting and specimen preparation for testing, which is related to the weft yarn's unstable and loose cross-sectional area, which caused progressive damage to specimens.

Figure 4-33 depicts the shear bond strength of CTRCC-M45 calculated with yarn dimensions which is provided by the manufacturer (both warp and weft yarns assumed as circular) for (100 mm and 150 mm) embedment lengths in 1-Yarn, 2-Yarn, 3-Yarn configurations.

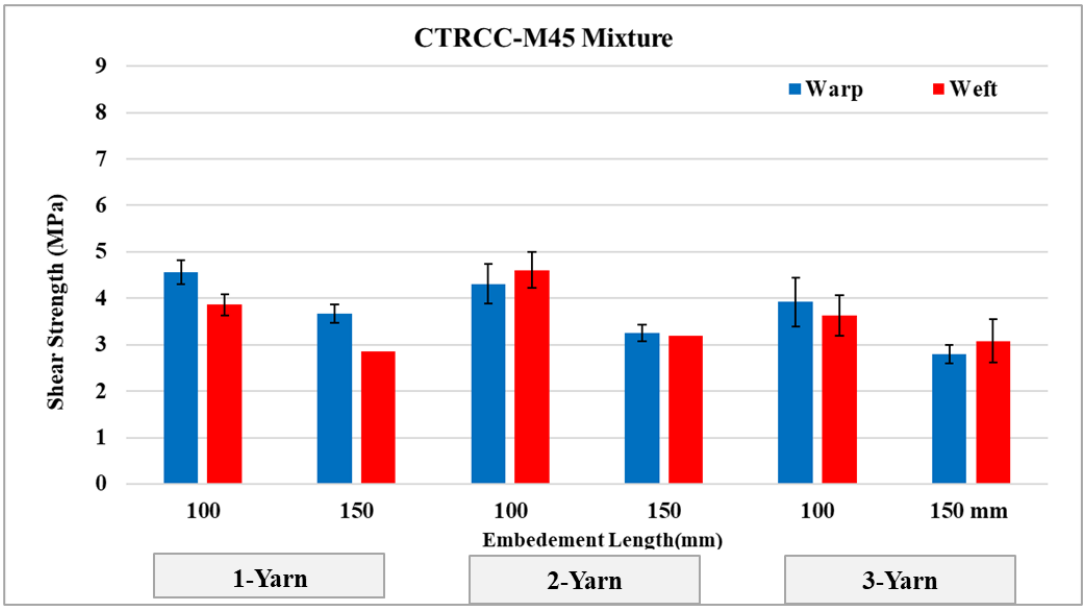

Figure 4-33 Shear bond strength calculated by manufacturer data C-TRCC with M45 mortar pull-out tests

4.2.4.2 Shear bond strength

In most of the test series, the warp yarn specimens exhibited higher shear bond strength values compared to the weft directions, which indicates superior bonding between the mortar and textile, attributable to the structural characteristics of the warp yarn.

For the 1Y with a 100 mm embedment length, the warp average shear strength is 4.56 MPa, which is 18.1% higher than the corresponding weft shear strength of 3.86 MPa. For the IY with a 150 mm embedment length, the warp shear strength decreases to 3.67 MPa, representing a 19.5% reduction compared to the 100 mm case. The weft also shows a decrease in performance, reaching 2.86 MPa, a 25.9% reduction from the 100 mm embedment.

In the Y2 specimens, shear bond strength in 100mm embedment length showed an 8.0% higher value for the weft with 4.61MPa compared to warp with 4.31 MPa. In the 150 mm, both direction specimens illustrated a reduction while warp reduced to 3.26 MPa **(**24.4% reduction), the weft experienced a 30.6% decline reaching to 3.20MPa.

The 3Y configuration exhibits a comparable pattern about warp direction, exhibiting an average shear bond strength of 3.92 MPa at 100 mm, which represents an 8% increase relative to the average shear bond strength of the weft specimens, which was 3.63 MPa. For an embedment length of 150 mm, the warp direction exhibited a higher reduction rate of 29%, reaching 2.79 MPa, while the weft achieved 3.08 MPa, with a reduction of 15.2%. This may be attributed to an increase in yarn number, resulting in a reduction in the influence of defects in individual yarns on the group yarn behavior observed in pull-out tests.

In all configurations, increasing the embedment length from 100 mm to 150 mm reduced the shear bond strength in both directions. This trend is more obvious in warp direction, particularly in the 1-Yarn and 3-Yarn configurations, where the decreases range from 20% to 29%. On the other hand, weft direction showed more

shear strength at higher yarn counts, with reductions as low as 15% in the 3Y configuration.

The results also depict the effect of the yarn number. The transition from 1Y to 2Y configurations generally enhances shear strength, particularly in the weft direction at 100 mm embedment, where the increase from 3.86 MPa to 4.61 MPa. However, in change the configuration from 2Y to 3Y depicts decreasing returns which shows that there is no linear correlation between increasing the yarn number and raising the shear bond strength.

Figure 4-34 presents the shear bond strength results calculated based on dimensions delivered from laser scanning assuming the yarns as an ellipse. n the previous graph, yarns were assumed to have circular cross-sections with a circumference of 3.36 mm, while in the updated graph, weft yarns are modeled as ellipses with a circumference of 7.4 mm, and warp yarns are ellipses with a circumference of 5.3 mm. These changes directly affect the effective bonding area and, consequently, the shear strength. The comparison between two shear bond values shows a significant difference in values in which the circular assumption due to smaller circumferences illustrates a lower strength. For example, the reduction in shear strength from circular to elliptical yarns is approximately 30 % for the warp direction and 43% for the weft direction at 100 mm embedment in the 1-yarn configuration.

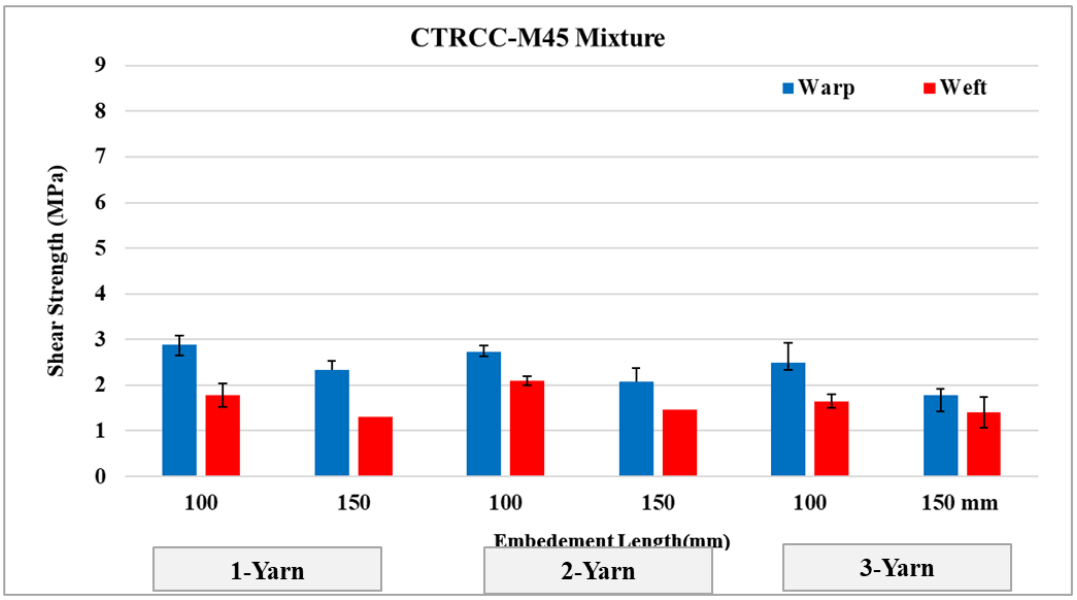

Figure 4-34 Shear bond strength calculated by laser scanning data C-TRCC with M45 mortar pull-out tests

4.2.4.3 Tensile strength

The presented data in the Figure 4-35 the tensile strength of pull-out tests of CTRCC-M45. Considering the ultimate tensile strength of carbon textile yarns based on the tests in the laboratory 1900 MPa for weft and 1933 MPa for warp direction. The calculated tensile strength for pull-out tests can be explained by the failure modes that the specimens experienced.

In the 1Y warp specimens, the tensile strength for 100 mm embedment length in which the failure mode was yarn pull out was an average value of 1683 MPa, and in 150 mm embedment lengths 2043 MPa in which the failure mode was yarn rupture. However, for weft direction, these values are quite lower with 1428 MPa, in 100mm and 1585 MPa and 1585 MPa for 150 mm embedment length which is attributed to damages on the textile yarn through the specimen preparation and testing procedure which is rooted in the defects on yarn geometry.

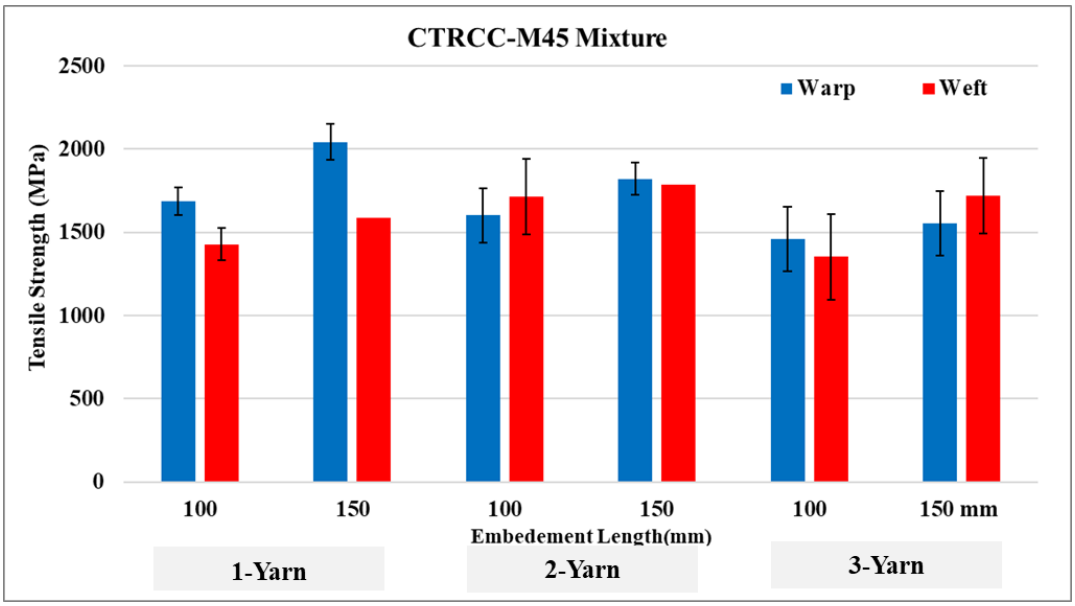

Figure 4-35 Tensile strength of C-TRCC with M45 mortar pull-out tests

In 2Y specimens, the warp direction in which the failure mode was yarn pull out the average tensile strength is 1021 MPa and with increasing the embedment length to 150 mm along with changing the failure mode to yarn rupture the tensile strength increased to 1821 MPa while the weft direction values are 1712 MPa and 1786 MPa, respectively. It should be noted that the weft specimen values are for two specimens' average; the rest of the five specimens prepared for the tests were damaged before and throughout the testing. The failure mode of 150 mm specimens was the yarn rupture.

In the 3Y tests, the tensile strength of warp specimens is 1459 MPa at 100 mm and 1556 MPa at 150 mm, both failing with telescopic failure mode. On the other hand for weft direction in 150 mm embedment lengths, the failure mode was the while for 100 mm splitting failure cover mortar that is attributed to the inadequate matrix strength, insufficient anchorage length the geometry and alignment of the yarns(Preinstorfer & Kollegger, 2020; Tekle et al., 2021) .

4.2.4.4 Slip at Maximum Pull-out Load

The graph Figure 4-36 shows the slip at the maximum the slip at maximum pull-out load for carbon textile-reinforced cementitious composites (CTRCC-M45) for different yarn numbers (1-Y, 2-Y, and 3-Y) and embedment lengths (100 mm and 150 mm) for warp and weft directions.

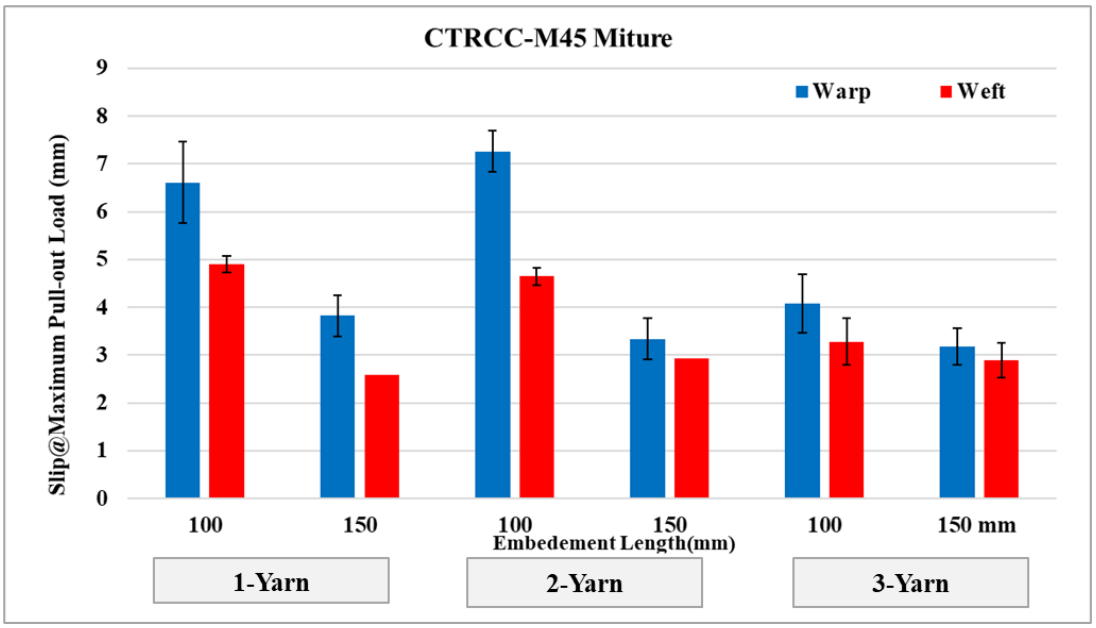

Figure 4-36 Slip at maximum pull-out load for C-TRCC with M45 mortar pull-out tests

In the 1-Yarn configuration, the warp exhibits a slip of 6.61 mm at 100 mm embedment, significantly higher than the weft's 4.90 mm, reflecting a 35% higher slip in the warp direction. At 150 mm embedment, the slip reduces to 3.82 mm for warp and 2.59 mm for weft, corresponding to reductions of 42.2% and 47.1%, respectively. These results reveal that increasing the embedment length decreases the related slip to the debonding point. Warp yarns also experienced higher slips related to the telescopic failure mode in this direction.

In two yarn specimens, the warp specimens slipped reduced from 7.26 mm to 3.34 mm (54%), changing the embedment length from 100 mm to 150 mm. For the weft direction, this reduction is relatively lower (37%), with the slip values declining from 4.65 mm to 2.93 mm.

For three yarn configurations warp direction changing the embedment length from 100 mm to 150 mm reduces the average slip values from 4.03 mm to 3.18 mm (22% reduction). The slip at maximum pull-out load for weft direction specimens decreases from 3.28 mm to 2.89 mm in similar conditions (12 %).

From the results, it can be observed that warp direction specimens showed consistently higher slip values than weft specimens which can be attributed to the failure mode of specimens in which the weft specimens due to yarn cross geometrical features (higher circumferences which results in higher bonding area between mortar and textile) while the defects in yarn structure cause damages and weaker performance) showed splitting.

4.3 Phase III: Tensile Creep Test Results

This section will present and discuss the results of tensile creep tests of C-TRCC specimens in both weft and warp directions. Specimens with two layers of carbon textile reinforcement for M7 and M45 were selected for creep tests due to better performance than other reinforcement ratios.

4.3.1 Preliminary Testing and Slippage

Prior to commencing the main test program, preliminary tests were conducted to validate the experimental load setup. For this purpose, dummy C-TRCC specimens were fabricated when the carbon fibers were utilized along the weft direction. An initial uniaxial tensile test was performed on three dummy specimens using an MTS

hydraulic testing machine with a 250 kN capacity. The test was conducted under displacement control at a loading rate of 0.5 m/s to determine the ultimate load-bearing capacity of the specimens. The results of these tests, presented in Figure 4-37, indicated an ultimate tensile strength of 21923 N. Based on this ultimate load, the creep loads for subsequent testing were determined as 25%, 50%, and 75% of the ultimate load.

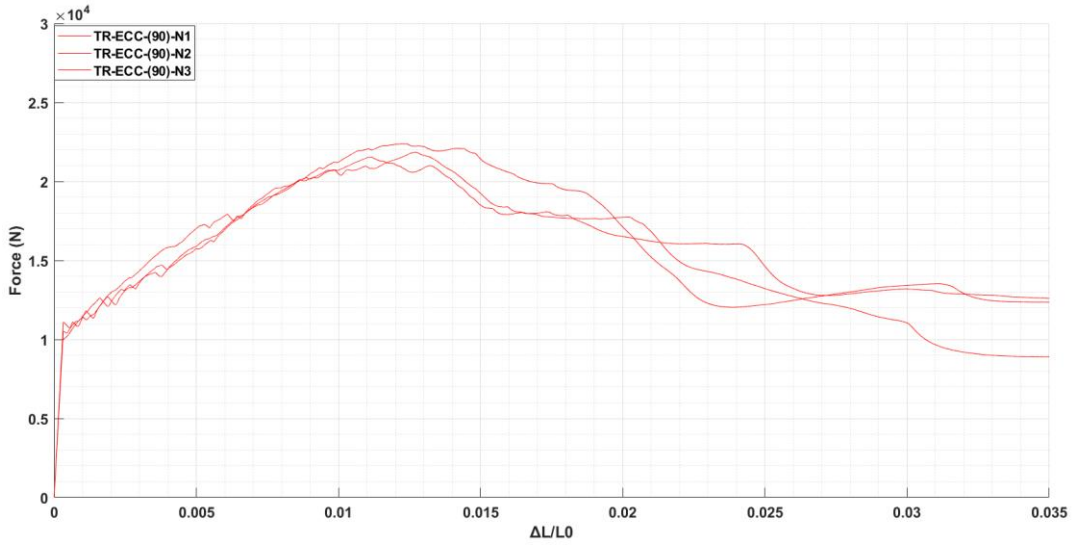

Figure 4-37 Load normalized deformation results of TRECC specimens

To accommodate the height limitations of the loading frames, the specimen length was reduced to 450 mm while maintaining a 200 mm region of interest for consistent strain measurements as the uniaxial tensile testing. To compensate for the reduced specimen length, the steel end plates were shortened to 125 mm. Two replicate specimens were tested at each creep load level (25%, 50%, and 75% of the ultimate load) and temperature condition (20°C and 50°C). Due to the limited number of available loading frames, the initial testing phase focused on 50% and 75% load levels at both temperature conditions.

For specimens subjected to 50% of the ultimate load, creep tests were conducted for 180 days. The creep strain time data presented in Figure 4-38 revealed a strong temperature dependence of tensile creep strain, with specimens tested at 50°C exhibiting significantly higher creep strain compared to those tested at 20°C. In both temperature conditions, creep strain stabilized after approximately 50 days. At 50°C, creep strain exhibited an initial rapid increase, reaching 6,500 με within the first few days. This rapid initial increase, followed by a more gradual increase to approximately 7,000 με over 180 days, is attributed to the influence of elevated temperatures, particularly the potential degradation of the SBR coating, which may become unstable above 40°C. In contrast, specimens tested at 20°C demonstrated significantly lower creep strain, with only a minor increase in strain observed over the 180-day testing period. These findings suggest that the long-term creep behavior of the C-TRCC specimens is significantly less pronounced at lower temperatures.

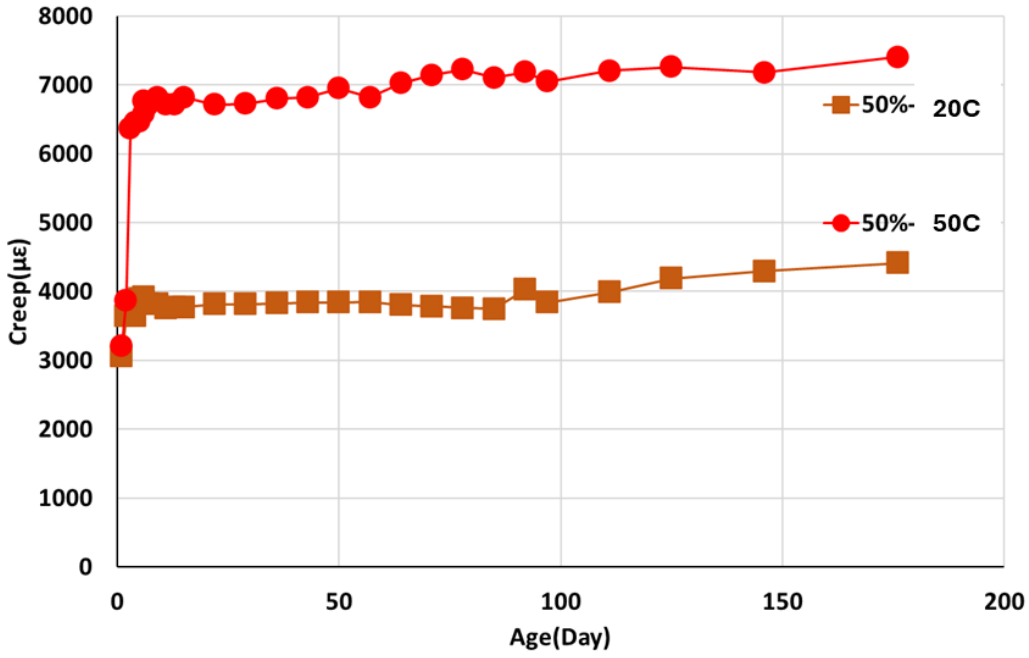

Figure 4-38 Tensile creep - time data at 50% creep loading for dummy specimens

However, during creep tests subjected to 75% of the ultimate load, the predominant failure mode involved the slippage of the textile reinforcement within the mortar matrix as observed in Figure 4-39. This failure mode, characterized by visible textile pull-out and matrix cracking, indicates that under high sustained loads, the bond between the carbon textile and the cement matrix was exceeded. This observation aligns with existing literature (Jon M. Rouse & Sarah L. Billington, 2007) which suggests that while the matrix may initially crack, the textile continues to carry the load. However, under prolonged or increased loading, the fiber-matrix bond weakens, leading to fiber pull-out and ultimately limiting the tensile capacity of the composite.

Figure 4-39 Pull out of carbon textile yarns in dummy specimens at 75% loading

To address this issue, the length of the steel end tabs was increased (Figure 4-40) to improve load transfer and minimize the risk of premature failure due to insufficient development length. While the overall specimen length was maintained at 450 mm,

the region of interest for strain measurements was reduced to 150 mm. This modified setup was utilized during the rest of the experimental program.

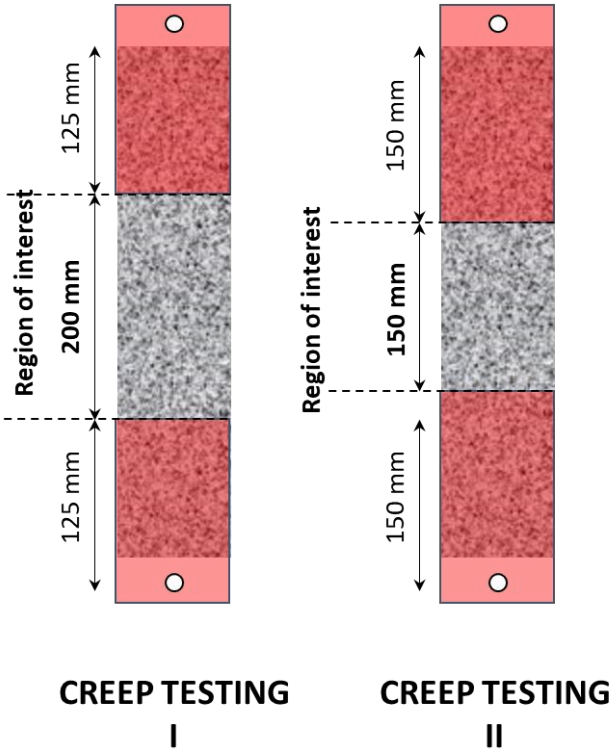

Figure 4-40 Modification of specimen dimensions for tensile creep testing

Given the extended duration of creep tests and the relatively high number of variables to be investigated, the scope of the creep testing phase was narrowed. Creep tests were conducted only on specimens reinforced with two layers of carbon textile in the warp direction, as this configuration exhibited superior performance in the initial uniaxial tensile tests. Furthermore, creep tests were performed using two different mortar compositions (M45, i.e. mortar A and M7, i.e. mortar B) and subjected to two distinct temperature conditions (20°C and 50°C). This focused approach allowed for a more in-depth investigation of creep behavior while maintaining manageable experimental constraints.

4.3.2 Uniaxial Tensile Strength of C-TRCC (Warp)

Before the start of creep testing, uniaxial tensile tests were conducted on the C-TRCC creep test specimens. The results, presented in Figure 4-41 and summarized in Table 4-6, demonstrate the typical stress-strain behavior of C-TRCC. Initially, the specimens exhibited a linear and elastic response, followed by multiple cracking. After the onset of cracking, the textile reinforcement carried the majority of the load. In this series of tests, the failure mode shifted from textile pull-out observed in previous tests on weft-direction specimens to a combination of telescopic failure within the textile layers followed by ultimate tensile rupture of the yarns (i.e. Mode I). This indicates that the specimens reached their maximum load-bearing capacity after experiencing a sequence of failure mechanisms, starting with telescopic failure within the textile layers and culminating in the final rupture of the yarns. Moreover, the M7 specimens exhibited higher cracking strength when compared to the M45 specimens.

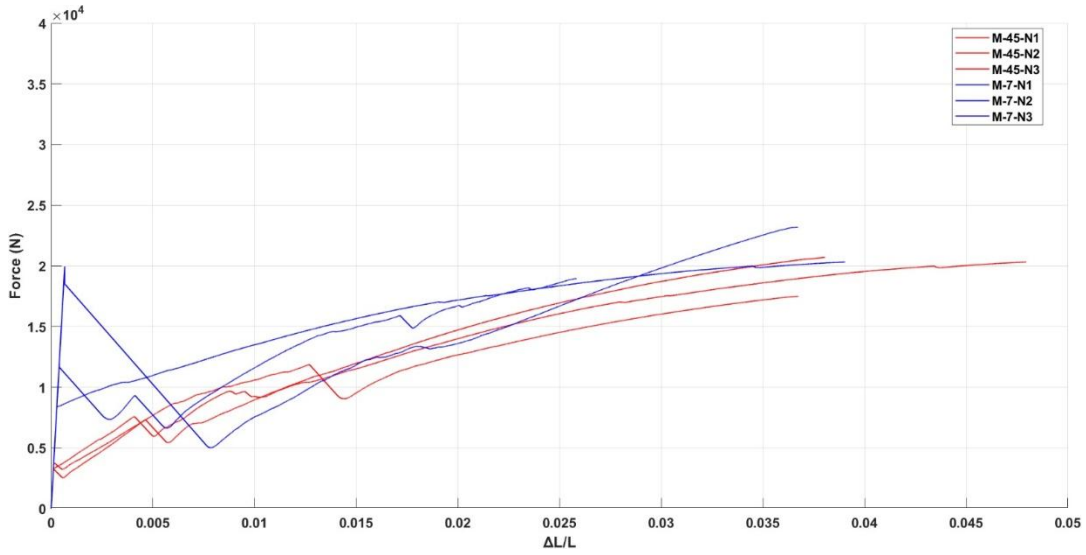

Figure 4-41 Force-normalized deformation of C-TRCC creep specimens

Table 4-6 Summary of the uniaxial tensile strength results of C-TRCC creep specimens

Label	ρ_f (%)	@ Cracking		@ Ultimate			Failure Mode
		F (N)	σ_c (MPa)	F (N)	σ_t (MPa)	$\Delta L/L_0$ (%)	
C2-M45	0.43	3460 [8]	1.38 [8]	19497 [9]	1805 [9]	4.1 [15]	I, I, I
C2-M7	0.43	13446 [49]	5.38 [49]	20813 [11]	1927 [11]	3.4 [27]	I, I, I

The creep test results will be presented for both M7 and M45 mortars will be presented separately in the subsequent sections.

4.3.3 Creep Testing of C-TRCC with M45 mortar (Mortar A)

Based on the ultimate load of 19.5 kN determined from uniaxial tensile tests, creep loads for subsequent testing were set at 25%, 50%, and 75% of this value. Manual creep loading was applied using 5 kg and 10 kg weights, and the resulting specimen displacements were measured and plotted in a load-strain graph (Figure 4-42). This graph illustrates the relationship between applied force and global strain during manual creep loading. Analysis of the load-strain graph revealed a correlation with the behavior observed in the MTS uniaxial tensile tests. Specifically, it was noted that at 25% loading, one crack developed in the specimens, while at 50% and 75% loading levels, two cracks were observed in each C-TRCC specimen.

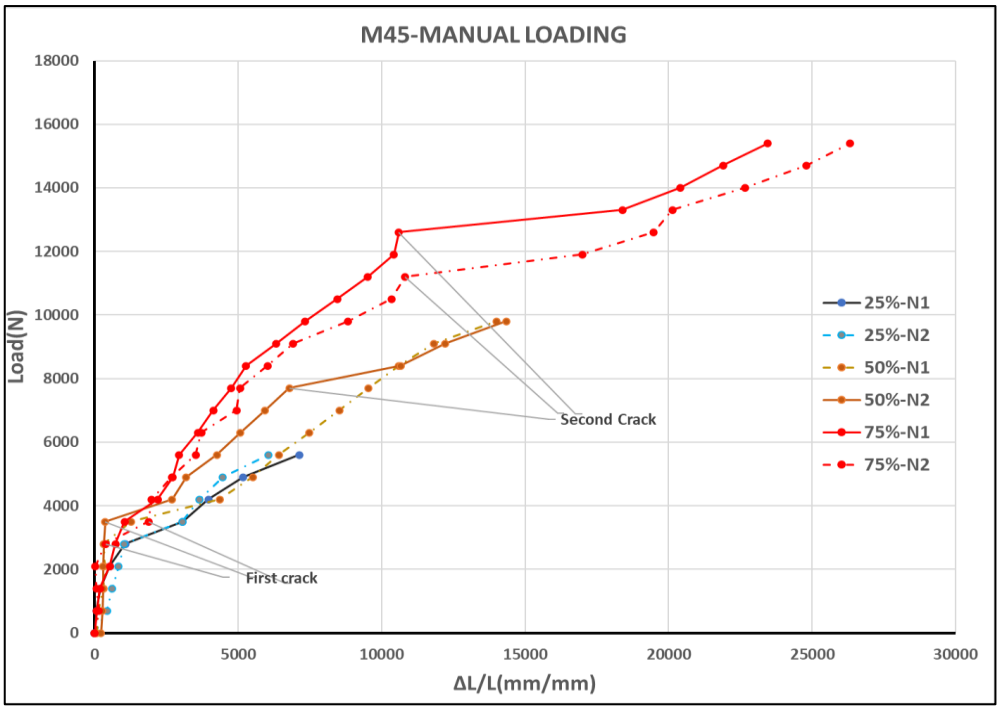

Figure 4-42 Creep loads and the number of cracks observed on each load level

After the initial creep loading shown in Figure 4-42, C-TRCC specimens were subjected to two different temperature regimes, i.e. 20°C and 50°C. Obtained creep strain time data is plotted in Figure 4-43 for each loading separately.

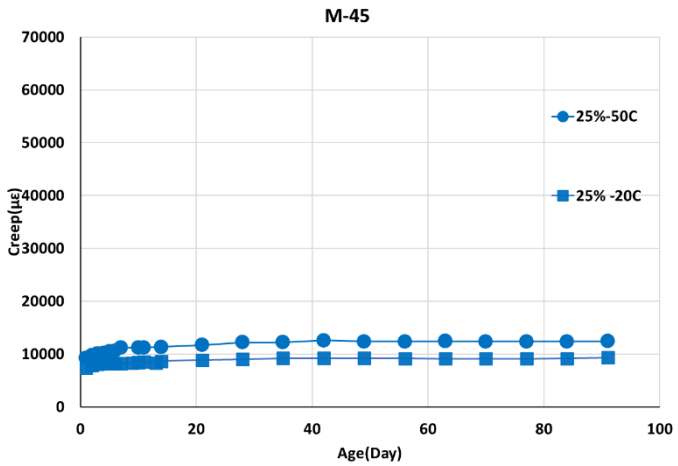

(a) 25 % Creep loading

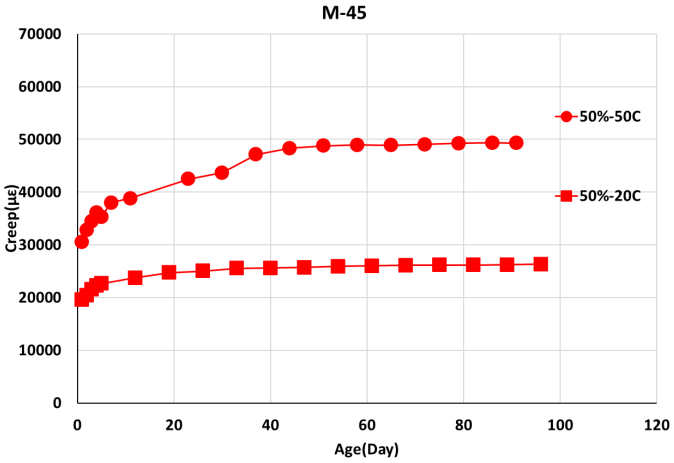

(b) 50% Creep loading

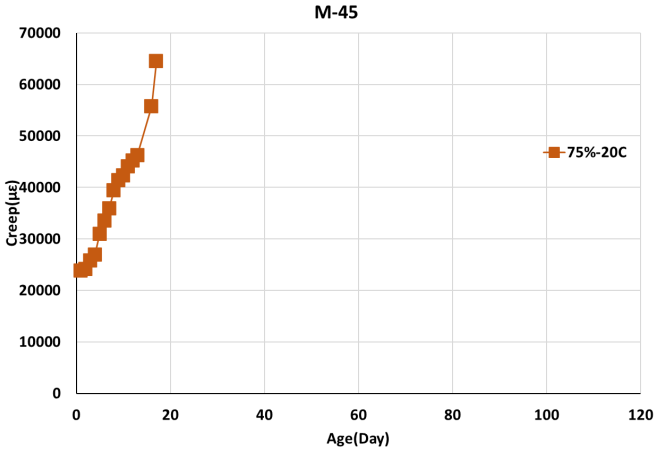

(c) 75% Creep loading

Figure 4-43 Creep test results of the C-TRCC specimens prepared with the M45 mortar

As observed in Figure 4-43(a), at 25% loading, after 10 days, the creep strain at 50°C reached 11237 με, significantly higher than the 8,410 με observed at 20°C, indicating a 53% increase in creep strain at the elevated temperature. By day 30, the strain at 50°C stabilized around 12,500 με, while at 20°C it stabilized at 8,283 με, which represents a 54% higher creep strain at 50°C. Over the 90-day test period, the difference in creep strain between the two temperature conditions remained relatively consistent, with the 50°C specimens exhibiting approximately 5,355 με higher creep strain compared to those at 20°C. This consistent difference

demonstrates that elevated temperatures significantly accelerate creep deformation in the material.

At 50% loading shown in Figure 4-43(b), however, at 50°C, creep strain exhibited a rapid increase, exceeding 42477με within the first 20 days, followed by a plateau around 50,000 με. In contrast, creep strain at 20°C showed a significantly slower increase, reaching 23257 με after 20 days and exhibiting minimal growth thereafter. Over the 90-day test period, the 50°C condition consistently exhibited significantly higher creep strain than the 20°C condition. By day 90, the 50°C condition maintained a consistent 25,000 με higher creep strain compared to the 20°C condition, representing a 100% increase. These results clearly demonstrate the significant impact of elevated temperature on the tensile creep performance of the C-TRCC composites.

Finally, at 75% loading as shown in Figure 4-43(c), when the specimens were subjected to 50 °C the specimens failed before any creep strain measurements were made and at 20 °C creep strain increased rapidly within the first 20 days, reaching 64487 με before failure. This rapid strain accumulation suggests that while the specimens could initially withstand this high load, the textile yarns eventually reached their strain capacity within 20 days. This early failure at elevated temperatures is likely to be attributed to the degradation of the SBR coating, which may compromise the integrity of the carbon yarns. The degradation of the coating could lead to individual yarn failure, ultimately resulting in rapid specimen failure.

4.3.4 Creep Testing of C-TRCC with M7 mortar (Mortar B)

(As observed in Figure 4-44(a), at 25% loading, the creep strain at 50°C increased steadily, reaching 10843 με after 10 days, significantly higher than the 300 με recorded at 20°C Which is attributed that specimens remained uncracked . By day 30, the strain at 50°C stabilized at approximately 9000 με, whereas the 20°C specimens showed a minimal increase to 350 με. Over the 90-day test period, the

50°C condition maintained a consistent difference of around 10000 με compared to the 20°C condition. This observation highlights the accelerated creep deformation at elevated temperatures, driven by the softening of the cement matrix and the degradation of the SBR coating, which weakens the bond between the textile and mortar.

As seen in Figure 4-44(b), for 50% loading the creep strain at 50°C exhibited a sharp increase, exceeding 33500 με within the first 20 days, and plateaued around 38013 με by the 90-day mark. In contrast, creep strain at 20°C grew at a much slower rate, reaching 20,381 με by day 90. The difference in creep strain between the two conditions consistently measured around 22,700 με, underscoring the influence of temperature in exacerbating the creep response. The softening of the matrix and the weakening of the SBR coating under high temperatures contributed significantly to the higher strain levels at 50°C.

At 75% loading, as depicted in Figure 4-44 Creep test results of the C-TRCC specimens prepared with M7 mortar(c), specimens subjected to 50°C failed within the first two days, preventing any meaningful strain measurements. This rapid failure was due to the degradation of the SBR coating and rupture of the textile reinforcement. At 20°C, the creep strain increased rapidly to approximately 38900 με within the first 15 days before failure occurred due to debonding of the steel plates. The early failure at 50°C highlights the vulnerability of the material to elevated temperatures, where both bond degradation and textile rupture significantly reduced the structural capacity.

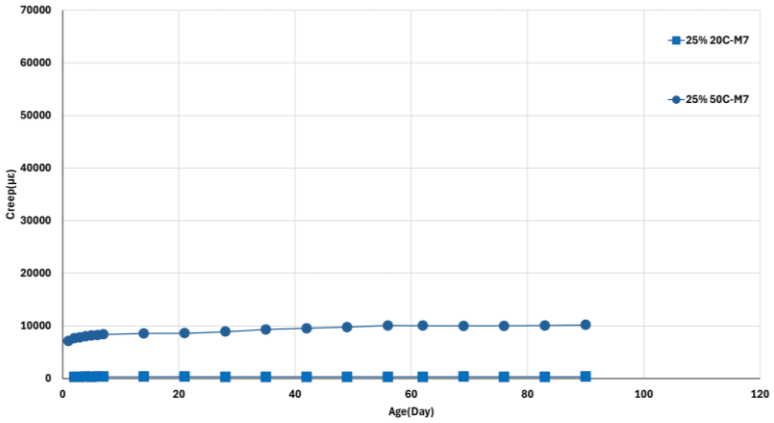

(a) 25% Creep loading

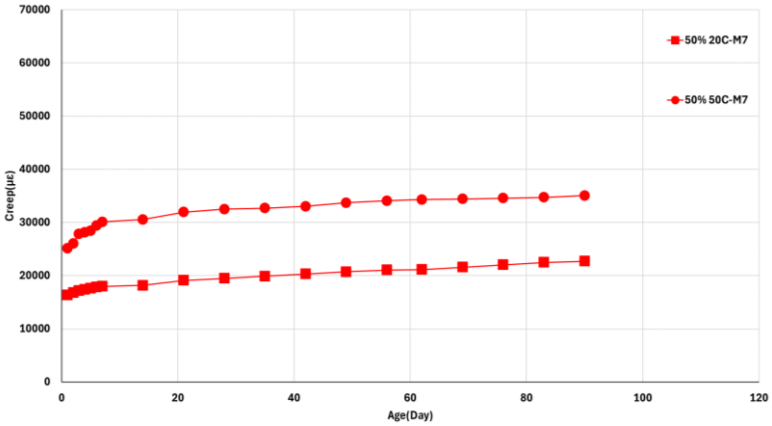

(b) 50% Creep loading

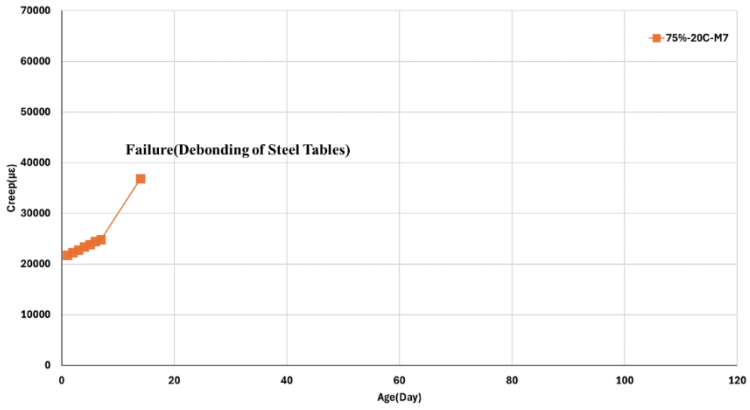

(c)75% Creep loading

Figure 4-44 Creep test results of the C-TRCC specimens prepared with M7 mortar

4.3.5 Discussion of Results

As observed in the above sections, the C-TRCC tensile sustained loading performance is influenced by mortar composition, load level and environmental conditions, i.e. temperature which was also mentioned by other researchers (Tošić et al., 2020). To gain a deeper understanding of the observed creep behavior, a comprehensive literature review will be conducted. This review will focus on existing research on the tensile creep behavior of TRCCs, with particular emphasis on the influence of key factors such as:

Matrix Composition: The impact of different matrix materials (e.g., cement type, admixtures, aggregate type) on creep behavior will be analyzed.

Textile Reinforcement: The effect of textile type (e.g., carbon, glass, aramid), weave pattern, and reinforcement density on creep performance will be investigated.

Temperature-Dependent Behavior: The literature will be reviewed to identify trends and mechanisms related to the influence of temperature on the creep behavior of TRCCs, including the effects of elevated temperatures on matrix properties, interfacial bond strength, and textile reinforcement.

4.3.5.1 Mortar Composition and Creep Behavior

The clear distinction between M45 and M7 mortars compositions such as fine aggregate size and volume and the different binder compositions could be responsible for the different tensile creep behavior between mortars. As a low-strength and ductile mortar, M45 demonstrates relatively higher creep strain even at lower load levels at both temperatures. In contrast, M7 has denser and stronger mortar which shows higher cracking strength and better resistance with tensile creep, especially in low loading. At the lower loading rates 25% the creep performance for elevated temperature was similar with around 10000 με. This shows both mortars maintain in the structural integrity in low-range sustained tensile loading. However,

in low temperatures, 20 °C M7 specimens depicted superior performance with no cracking under loading. At day of 100, for 50%- 20 °C again the M7 mortar's specimens showed better performance than M45. M45 showed about 20% higher creep rates than M7. However, this difference is more significant at 50%- 50 °C with about 43% which is attributed to the coupled effect of loading rate and implementation of elevated temperature. In conclusion, the M7 demonstrated superior resistance under tensile sustained loading coupled with elevated temperature.

4.3.5.2 Load Level and Impact of Temperature

Temperature is a determinant factor in tensile creep behavior in cementitious composites, and with higher temperatures, the creep accelerates (Forth, 2015). This is obvious from the test results of specimens exposed to 50°C, which showed that both mortars experienced substantially higher creep strain than 20°C. The other notable observation in tensile creep testing was the different cracking patterns)Figure 4-46 in specimens of 20°C and 50°C in which the number of cracks in elevated temperatures was higher than in lower temperatures which can be related to mortar's tendency to develop cracks at elevated temperatures and also fibers at this temperature are prone to creep which is stem from polymeric fibers can relax over time under sustained loading particularly when exposing to elevated temperatures that results in increased crack numbers and width in specimens exposed to elevated temperatures(Tošić et al., 2020). Accordingly, the specimens exposed to the elevated temperature of 50°C resulted in a considerable increase in tensile creep range, increased for both mortars, attaining noticeably higher levels than 50°C. This phenomenon can be attributed to the softening of cementitious mortar and SBR coating (Figure 4-45), which facilitates the bonding between textile yarns and mortar this finding aligns with the results of (Rezig et al., 2020) study of the effects of accelerated aging of SBR in temperatures lower than 100°C leads to a decrease in the mechanical properties of this material. In higher temperatures, the textile/mortar

bond declines, leading to telescopic failure (breaking of outer filaments while core filaments slip).

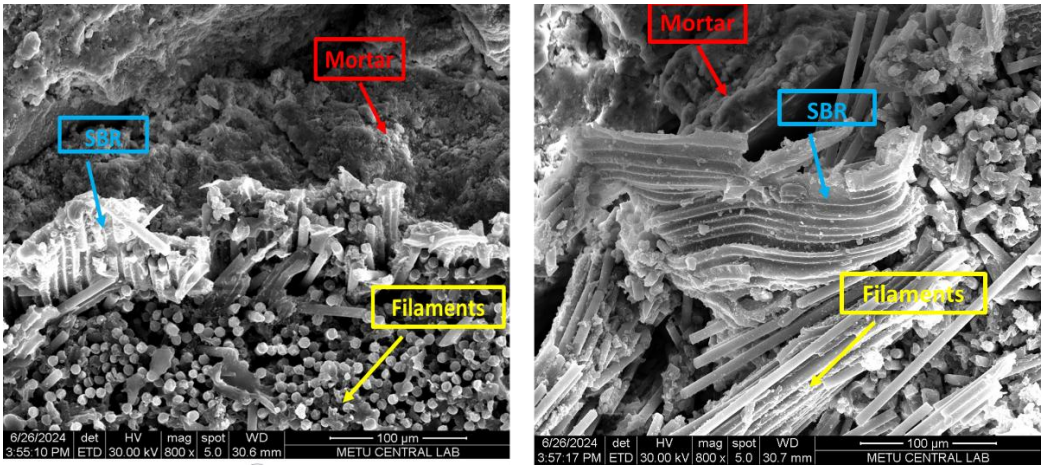

Figure 4-45 Tested Specimen SEM illustration degradation of SBR coating

Loading level increases lead to progressively greater creep values. In specimens with low loading levels (25%) maintaining structural stability, moderate level (50%) caused notable creep deformation, and high levels leading to rapid material degradation and early rupture, especially in materials with higher creep sensitivity. This comparison highlights the critical role of loading rate in determining a material's suitability for prolonged tensile loading, with M-45 showing a much higher susceptibility to creep-induced failure than M-7. This is in agreement with the outcomes of the research by (Zhao et al., 2015) that studied the tensile creep performance of pre-cracked steel fiber-reinforced concrete(SFRC) revealed specimens exposed to higher sustained loads showed higher creep deformations in the long term highlighting the sensitivity of tensile creep to loading rates.

(a) (b)

Figure 4-46 Cracking pattern in (a) 50°C,(b) 20°C

4.3.5.3 Failure and Strain Variability

One noticeable observation from the tensile sustained loading tests is significant variability in strain and failure modes. These differences are evident when testing the differences between C-TRCC specimens examined at various load conditions and temperatures. For example, specimens with 75%-50°C conditions undergo early failure because of the telescopic pull-out of carbon textile yarns, which reveals poor bonding behavior in the textile/mortar interface (Bentur et al., 2013). The other reason for weak bonding performance is SBR coating degradation at temperatures above 40°C, which causes slippage of filaments and premature failure of specimens(Rezig et al., 2020). On the other hand, for the same loading Level but 20°C, the specimens showed a constant increase in creep strain with failure after 20 days.

CHAPTER 5

5 CONCLUSIONS AND RECOMMENDATIONS

This study investigated the uniaxial tensile and the slip-bond behavior as well as the tensile creep performance C-TRCC. Main conclusions that can be drawn from the experimental program are as follows:

Phase I

- The textile strength was fully utilized in the warp direction (up to 2375 MPa) with a strain capacity of 2.8–3.6%. In contrast, the weft direction showed lower textile strength (933–1528 MPa), and elongation capacity (0.9–1.8%) regardless of the cement matrix. Additionally, C-TRCC demonstrated significantly higher elongation capacity than the bare textile, primarily due to telescopic pull-out failure in the yarn structure.
- High-strength mortar (M7) exhibited improved cracking strength (up to 4.4 MPa), limited spalling, and improved bonding performance in the weft direction. The softer mortar (M45) with lower cracking strength (1.7-2.5 MPa) illustrated excessive spalling, resulting in premature failure in the TRC coupons.
- The differing behaviors are attributed to distinct failure modes: textile failure (Modes I and II) in the warp direction and slippage (Mode III) in the weft direction. A spalling-type failure, influenced by the cementitious mortar's strength, was also observed.
- The anisotropic behavior of C-TRCC in two different directions was attributed to the yarn waviness and geometric discrepancies between the warp and weft directions, which was verified through advanced experimental

techniques such as 3D laser scanning and SEM imaging. These techniques enabled a detailed analysis of failure mechanisms and the impact of yarn architecture and mortar properties on the overall performance of C-TRCC.

Phase II

- There is a clear correlation between the number of yarns, the length of embedment, and the maximum pull-out capacity. As the yarn configuration is increased, a notable enhancement in the specimen's pull-out capacity is observed. In certain instances, the pull-out capacity increases up to 200% from 1Y to 2Y and 3Y. Warp direction specimens consistently illustrate higher pull-out capacities than the weft direction which is attributed to yarn architecture and cross-section structure the warp yarns have a denser cross-section with fewer defects than weft yarns. This trend is more obvious in longer embedment lengths.

- The presented values for shear bond strength reveal that warp-direction specimens have superior bonding performance than weft-direction specimens specifically in shorter embedment lengths**.** This research highlighted a substantial difference between the shear bond strengths which were calculated from manufacturer data (assuming both warp and weft as circular) and the shear bond strengths calculated from laser scanner models (which assumed an elliptical and are more accurate). the shear bond strengths calculated from the laser scanner model are up to 50% lower than manufacturer-provided dimensions emphasizing the importance of accurate geometric modeling for realistic assessments. The shear bond strength illustrated a decreasing trend with increasing the yarn number while in general 2Y specimens showed an enhanced shear bond strength compared to 1Y, 3Y configurations illustrated a decrease, which elaborate a non-linear relationship

- Specimens that failed through the yarn rupture showed tensile strength values near to the tensile strength of carbon yarns (achieved in the uniaxial direct

tensile on yarns) which confirms the load-carrying capacity of the textile yarns. On the other hand, specimens with telescopic failure or yarn pull-out illustrated reduced tensile strength values due to incomplete utilization of yarn tensile capacity. The yarn structural damage during the specimen preparation and testing procedure in the weft direction played as a limiting factor for tensile performance which is attributed to defects on the cross-section of this direction.

- Failure modes change from yarn pull-out in 1Y specimens to telescopic or splitting failure in 2Y and 3Y for identical embedment length. These failure modes are more regular in 2Y and 3Y. The splitting failure modes are observed in 100 mm embedded length of weft directions specimens with 2Y, and 3Y configurations which is attributed to waviness and higher surface contact with mortar. Notably, this failure mode appeared in M45 mortar which represents a weaker mortar in this research.

- In higher yarn configurations the values for slip values decrease, this trend is more obvious in the warp direction specimens.

Phase III

- The tensile creep behavior of C-TRCC specimens is significantly influenced by the environment's temperature. At elevated temperatures (50°C), the creep strain increased considerably at all load levels, illustrating the composite's sensitivity to thermal effects. This phenomenon is attributed to the softening of cementitious mortar and degradation of SBR coatings, which weaken the textile-matrix bond, and in most cases lead to telescopic pull-out failures.

- The mortar composition had a critical effect on the creep performance of C-TRCC specimens. The M7 mortar showed far better resistance to creep deformation compared to M45 specifically when specimens were exposed to lower temperature conditions (20°C). This might be attributed to M7 stronger

mortar which indicated higher cracking strength and maintained structural integrity under sustained loading compared to the M45 matrix.

- The load levels increase intensified creep strain and failure modes in specimens. At a 25% loading level specimens illustrated stable creep strain performance with minimum cracking in number and widening. However, at 50% and 75%, specimens were prone to failure in earlier times due to the widening of cracks and textile degradation.
- Considering the same specimen dimensions failure modes changed from textile pull-out (slippage) in weft-loaded specimens to textile rupture in warp-direction specimens. This is attributed to the unique architecture of yarns that leads to different behavior under tensile sustained loading.

Following the experimental program, the following recommendations are offered for future research in each of the experimental phases conducted:

Phase I: Mechanical Characterization. The impact of alternative textile impregnation materials on the mechanical behavior of C-TRCC, particularly for improved performance at elevated temperatures, can be investigated. The effects of varying yarn spacing and mesh configurations on the optimization of structural efficiency and tensile strength can be explored. The role of hybrid textiles, such as combinations of carbon and glass, in enhancing cost-effectiveness and mechanical properties can be examined.

Phase II: Slip-Bond Behavior. The effects of textile pre-treatment techniques, such as surface roughening or chemical treatments, on bond-slip characteristics can be investigated. The performance of TRCC under multi-directional loading, to assess slip-bond behavior in complex stress states, can be evaluated. Comparative studies on the influence of different mortar additives, such as nanoparticles and fibers, on the enhancement of bond strength and minimization of failure modes like splitting can be conducted.

Phase III: Tensile Creep Behavior. The creep behavior of TRCC under other environmental factors, such as high humidity or freeze-thaw cycles, can be studied to assess durability under diverse conditions.

REFERENCES

Alexander, A. E., & Shashikala, A. P. (2023). Experimental Investigations on the Uniaxial Tensile Behaviour of Carbon Textile Reinforced Geopolymer Mortar. *Lecture Notes in Civil Engineering*, *269*, 277–289. https://doi.org/10.1007/978-981-19-3371-4_25/TABLES/7

Alrefaei, Y., Rahal, K., & Maalej, M. (2018). Shear Strength of Beams Made Using Hybrid Fiber–Engineered Cementitious Composites. *Journal of Structural Engineering*, *144*(1), 04017177. https://doi.org/10.1061/(ASCE)ST.1943-541X.0001924

Al-Salloum, Y. A., Siddiqui, N. A., Elsanadedy, H. M., Abadel, A. A., & Aqel, M. A. (2011). Textile-Reinforced Mortar versus FRP as Strengthening Material for Seismically Deficient RC Beam-Column Joints. *Journal of Composites for Construction*, *15*(6), 920–933. https://doi.org/10.1061/(asce)cc.1943-5614.0000222

Arboleda, D., Carozzi, F. G., Nanni, A., & Poggi, C. (2016). Testing Procedures for the Uniaxial Tensile Characterization of Fabric-Reinforced Cementitious Matrix Composites. *Journal of Composites for Construction*, *20*(3), 1–11. https://doi.org/10.1061/(asce)cc.1943-5614.0000626

Arce, A., Azdejkovic, L., Lima, L. M. De, Papanicolaou, C. G., & Triantafillou, T. C. (2023). *Mechanical behavior of textile reinforced alkali-activated mortar*

based on fly ash , metakaolin and ladle furnace slag [version 1 ; peer review : 2 approved].

Barhum, R., & Mechtcherine, V. (2012). Effect of short, dispersed glass and carbon fibres on the behaviour of textile-reinforced concrete under tensile loading. *Engineering Fracture Mechanics*, *92*, 56–71. https://doi.org/10.1016/J.ENGFRACMECH.2012.06.001

Bielak, J., Li, Y., Hegger, J., & Chudoba, R. (2018). Numerical and experimental characterization of anchorage length for textile reinforced concrete. *RILEM Bookseries*, *15*, 409–417. https://doi.org/10.1007/978-94-024-1194-2_48/FIGURES/9

Bournas, D. A., Triantafillou, T. C., Zygouris, K., & Stavropoulos, F. (2009). Textile-Reinforced Mortar versus FRP Jacketing in Seismic Retrofitting of RC Columns with Continuous or Lap-Spliced Deformed Bars. *Journal of Composites for Construction*, *13*(5), 360–371. https://doi.org/10.1061/(asce)cc.1943-5614.0000028

Brameshuber, W. (2016). Manufacturing methods for textile-reinforced concrete. *Textile Fibre Composites in Civil Engineering*, 45–59. https://doi.org/10.1016/B978-1-78242-446-8.00004-5

Butler, M., Mechtcherine, V., & Hempel, S. (2009). Experimental investigations on the durability of fibre–matrix interfaces in textile-reinforced concrete. *Cement and Concrete Composites*, *31*(4), 221–231. https://doi.org/10.1016/J.CEMCONCOMP.2009.02.005

Butler, M., Mechtcherine, V., & Hempel, S. (2010). Durability of textile reinforced concrete made with AR glass fibre: Effect of the matrix composition. *Materials and Structures/Materiaux et Constructions*, *43*(10), 1351–1368. https://doi.org/10.1617/S11527-010-9586-8/FIGURES/22

Caggegi, C., Lanoye, E., Djama, K., Bassil, A., & Gabor, A. (2017). Tensile behaviour of a basalt TRM strengthening system: Influence of mortar and

reinforcing textile ratios. *Composites Part B: Engineering*, *130*, 90–102. https://doi.org/10.1016/j.compositesb.2017.07.027

Dalalbashi, A., Ghiassi, B., & Oliveira, D. V. (2021a). Textile-to-mortar bond behavior: An analytical study. *Construction and Building Materials*, *282*, 122639. https://doi.org/10.1016/j.conbuildmat.2021.122639

Dalalbashi, A., Ghiassi, B., & Oliveira, D. V. (2021). Textile-to-mortar bond behavior: An analytical study. *Construction and Building Materials*, *282*, 122639. https://doi.org/10.1016/j.conbuildmat.2021.122639

Dalalbashi, A., Ghiassi, B., Oliveira, D. V., & Freitas, A. (2018). Effect of test setup on the fiber-to-mortar pull-out response in TRM composites: Experimental and analytical modeling. *Composites Part B: Engineering*, *143*(December 2017), 250–268. https://doi.org/10.1016/j.compositesb.2018.02.010

D'Antino, T., & Papanicolaou, C. (Corina). (2018). Comparison between different tensile test set-ups for the mechanical characterization of inorganic-matrix composites. *Construction and Building Materials*, *171*, 140–151. https://doi.org/10.1016/J.CONBUILDMAT.2018.03.041

De Santis, S., Carozzi, F. G., de Felice, G., & Poggi, C. (2017a). Test methods for Textile Reinforced Mortar systems. *Composites Part B: Engineering*, *127*, 121–132. https://doi.org/10.1016/J.COMPOSITESB.2017.03.016

De Santis, S., Carozzi, F. G., de Felice, G., & Poggi, C. (2017b). Test methods for Textile Reinforced Mortar systems. *Composites Part B: Engineering*, *127*, 121–132. https://doi.org/10.1016/J.COMPOSITESB.2017.03.016

De Santis, S., & De Felice, G. (2015). Tensile behaviour of mortar-based composites for externally bonded reinforcement systems. *Composites Part B: Engineering*, *68*, 401–413. https://doi.org/10.1016/j.compositesb.2014.09.011

De Santis, S., Hadad, H. A., De Caso y Basalo, F., de Felice, G., & Nanni, A. (2018). Acceptance Criteria for Tensile Characterization of Fabric-Reinforced Cementitious Matrix Systems for Concrete and Masonry Repair. *Journal of Composites for Construction*, *22*(6), 1–14. https://doi.org/10.1061/(asce)cc.1943-5614.0000886

Deng, M., Dong, Z., & Zhang, C. (2020). Experimental investigation on tensile behavior of carbon textile reinforced mortar (TRM) added with short polyvinyl alcohol (PVA) fibers. *Construction and Building Materials*, *235*, 117801. https://doi.org/10.1016/J.CONBUILDMAT.2019.117801

Dissertation-Houman A. Hadad.pdf. (2018). *December*.

Donnini, J., Corinaldesi, V., & Nanni, A. (2016). Mechanical properties of FRCM using carbon fabrics with different coating treatments. *Composites Part B: Engineering*, *88*, 220–228. https://doi.org/10.1016/j.compositesb.2015.11.012

Durgadevi, S., Karthikeyan, S., Lavanya, N., & Kavitha, C. (2021). A review on retrofitting of reinforced concrete elements using FRP. *Materials Today: Proceedings*, *45*, 1050–1054. https://doi.org/10.1016/J.MATPR.2020.03.148

Elsanadedy, H. M., Almusallam, T. H., Alsayed, S. H., & Al-Salloum, Y. A. (2013). Flexural strengthening of RC beams using textile reinforced mortar - Experimental and numerical study. *Composite Structures*, *97*, 40–55. https://doi.org/10.1016/j.compstruct.2012.09.053

Endruweit, A., Zeng, X., Matveev, M., & Long, A. C. (2018). Effect of yarn cross-sectional shape on resin flow through inter-yarn gaps in textile reinforcements. *Composites Part A: Applied Science and Manufacturing*, *104*, 139–150. https://doi.org/10.1016/J.COMPOSITESA.2017.10.020

Esmaeili, J., Sharifi, I., Kasaei, J., Nourizadeh, M., & Ebrahimi Emamieh, A. (2019). Experimental and analytical investigation on strengthening of heat damaged concrete by textile reinforced concrete (TRC). *Archives of Civil and*

Mechanical Engineering, *19*(4), 1468–1483. https://doi.org/10.1016/j.acme.2019.09.008

Feng, G., Zhu, D., Guo, S., Rahman, M. Z., Jin, Z., & Shi, C. (2022). A review on mechanical properties and deterioration mechanisms of FRP bars under severe environmental and loading conditions. *Cement and Concrete Composites*, *134*(May), 104758. https://doi.org/10.1016/j.cemconcomp.2022.104758

Friese, D., Scheurer, M., Hahn, L., Gries, T., & Cherif, C. (2022). Textile reinforcement structures for concrete construction applications—a review. *Journal of Composite Materials*, *56*(26), 4041–4064. https://doi.org/10.1177/00219983221127181/ASSET/IMAGES/LARGE/10.1177_00219983221127181-FIG11.JPEG

Goliath, K. B., Cardoso, D. C. T., & Silva, F. de A. (2023). Influence of mechanical characterization technique on Carbon-TRC constitutive relations. *Journal of Building Engineering*, *67*, 106058. https://doi.org/10.1016/J.JOBE.2023.106058

Gries, T., Raina, M., Quadflieg, T., & Stolyarov, O. (2016). Manufacturing of Textiles for Civil Engineering Applications. *Textile Fibre Composites in Civil Engineering*, 3–24. https://doi.org/10.1016/B978-1-78242-446-8.00002-1

Hahn, L., Rittner, S., Nuss, D., Ashir, M., & Cherif, C. (2019). Development of methods to improve the mechanical performance of coated grid-like non-crimp fabrics for construction applications. *Fibres and Textiles in Eastern Europe*, *27*(1), 51–58. https://doi.org/10.5604/01.3001.0012.7508

Hausding, J., Lorenz, E., Ortlepp, R., Lundahl, A., & Cherif, C. (2011). Application of stitch-bonded multi-plies made by using the extended warp knitting process: reinforcements with symmetrical layer arrangement for concrete. *Http://Dx.Doi.Org/10.1080/00405000.2010.515729*, *102*(8), 726–738. https://doi.org/10.1080/00405000.2010.515729

Jesse, F., Will, N., Curbach, M., & Hegger, J. (2008). Load-bearing behavior of textile-reinforced concrete. *American Concrete Institute, ACI Special Publication, SP-250*, 59–68. https://doi.org/10.14359/20140

Keskin, S. B. (2012). *DIMENSIONAL STABILITY OF ENGINEERED CEMENTITIOUS COMPOSITES* A thesis submitted to the Graduate School of Natural and Applied Sciences at Middle East Technical University in partial fulfillment of the requirements for the Doctor of Philosophy degree in Civil Engineering.

Lepenies, I. (2003). *On the Analytical Solution of Pullout Phenomena in Textile*. *125*(January), 38–43. https://doi.org/10.1115/1.1526125

Li, Y., Bielak, J., Hegger, J., & Chudoba, R. (2018). An incremental inverse analysis procedure for identification of bond-slip laws in composites applied to textile reinforced concrete. *Composites Part B: Engineering*, *137*(November 2017), 111–122. https://doi.org/10.1016/j.compositesb.2017.11.014

Mattarollo, G., Randl, N., & Pauletta, M. (2023). Investigation of the Failure Modes of Textile-Reinforced Concrete and Fiber/Textile-Reinforced Concrete under Uniaxial Tensile Tests. *Materials*, *16*(5). https://doi.org/10.3390/ma16051999

Mechtcherine, V. (2016). Durability of structures made of or strengthened using textile-reinforced concrete. *Textile Fibre Composites in Civil Engineering*, 151–168. https://doi.org/10.1016/B978-1-78242-446-8.00007-0

Mercedes, L., Gil, L., & Bernat-Maso, E. (2018). Mechanical performance of vegetal fabric reinforced cementitious matrix (FRCM) composites.

Construction and Building Materials, *175*, 161–173. https://doi.org/10.1016/J.CONBUILDMAT.2018.04.171

Mobasher, B. (2016). Textile fiber composites: Testing and mechanical behavior. In *Textile fibre composites in civil engineering* (Issue Dic). Elsevier Ltd. https://doi.org/10.1016/B978-1-78242-446-8.00006-9

Nanni, A., De Caso Y Basalo, F. J., Ekenel, M., De Caso, F., & Basalo, A. N. (2018). Acceptance criteria for concrete and masonry strengthening using fabric-reinforced cementitious matrix (FRCM) and steel reinforced grout (SRG) composites. *American Concrete Institute, ACI Special Publication*, *2017-March*(SP 324). https://doi.org/10.14359/51702356

Peled, A., & Mobasher, B. (2007). Tensile Behavior of Fabric Cement-Based Composites: Pultruded and Cast. *Journal of Materials in Civil Engineering*, *19*(4), 340–348. https://doi.org/10.1061/(ASCE)0899-1561(2007)19:4(340)/ASSET/E91C4965-D84B-4400-91FC-31F4A0836528/ASSETS/IMAGES/LARGE/9.JPG

Peled, A., Mobasher, B., & Bentur, A. (2017Al-Salloum, Y. A., Siddiqui, N. A., Elsanadedy, H. M., Abadel, A. A., & Aqel, M. A. (2011). Textile-Reinforced Mortar versus FRP as Strengthening Material for Seismically Deficient RC Beam-Column Joints. *Journal of Composites for Construction*, *15*(6), 920–933. https://doi.org/10.1061/(asce)cc.1943-5614.0000222

Alexander, A. E., & Shashikala, A. P. (2020). Sustainability of Construction with Textile Reinforced Concrete- A State of the Art. *IOP Conference Series: Materials Science and Engineering*, *936*(1). https://doi.org/10.1088/1757-899X/936/1/012006

Alma'aitah, M., & Ghiassi, B. (2022). Development of cost-effective low carbon hybrid textile reinforced concrete for structural or repair applications. *Construction and Building Materials*, *341*, 127858. https://doi.org/10.1016/J.CONBUILDMAT.2022.127858

Alpes, G. (2016). *Effect of creep strains on the residual mechanical properties of concrete*.

Arboleda, D., Carozzi, F. G., Nanni, A., & Poggi, C. (2016). Testing Procedures for the Uniaxial Tensile Characterization of Fabric-Reinforced Cementitious Matrix Composites. *Journal of Composites for Construction*, *20*(3), 1–11. https://doi.org/10.1061/(asce)cc.1943-5614.0000626

Banholzer. (n.d.). *BOND BEHAVIOUR OF A MULTI-FILAMENT YARN EMBEDDED IN A CEMENTITIOUS MATRIX Obwohl das Verbundverhalten eines Multi-Filament-Garn/Feinbeton-Systems sicherlich*.

Banholzer, B. (2006). Bond of a strand in a cementitious matrix. *Materials and Structures/Materiaux et Constructions*, *39*(10), 1015–1028. https://doi.org/10.1617/s11527-006-9115-y

Barhum, R., & Mechtcherine, V. (2013). Influence of short dispersed and short integral glass fibres on the mechanical behaviour of textile-reinforced concrete. *Materials and Structures/Materiaux et Constructions*, *46*(4), 557–572. https://doi.org/10.1617/S11527-012-9913-3/FIGURES/18

Barıs¸barıs¸erdil, B. (2013). CFRP-confined concrete columns under different environmental conditions I ˙ smail O ¨ zgü r Yaman. *Icevirtuallibrary.Com*, *65*(12), 731–743. https://doi.org/10.1680/macr.12.00148

Bazant, Z. P. (1973). Creep of concrete: Plain, reinforced and prestressed: A. M. Neville and W. Dilger. 1970. North-Holland Publishing Company, Amsterdam, and American Elsevier Publishing Company, New York. 622 pp. $34.50. *Cement and Concrete Research*, *3*(2), 223–224. https://doi.org/10.1016/0008-8846(73)90052-5

Bentur, A., Yardimci, M. Y., & Tirosh, R. (2013). Preservation of telescopic bonding upon aging of bundled glass filaments by treatments with nano-particles. *Cement and Concrete Research*, *47*, 69–77. https://doi.org/10.1016/j.cemconres.2013.01.006

Bissonnette, B., Pigeon, M., & Vaysburd, A. M. (2007). Tensile creep of concrete: Study of its sensitivity to basic parameters. *ACI Materials Journal*, *104*(4), 360–368. https://doi.org/10.14359/18825

Brockmann, T., & Brameshuber, W. (2006). Mechanical and fracture mechanical properties of fine grained concrete for textile reinforced composites. *Advances in Construction Materials 2007*, 1–227. https://doi.org/26970

Butler, M., Mechtcherine, V., & Hempel, S. (2009). Experimental investigations on the durability of fibre–matrix interfaces in textile-reinforced concrete. *Cement and Concrete Composites*, *31*(4), 221–231. https://doi.org/10.1016/J.CEMCONCOMP.2009.02.005

Carozzi, F. G., & Poggi, C. (2015). Mechanical properties and debonding strength of Fabric Reinforced Cementitious Matrix (FRCM) systems for masonry strengthening. *Composites Part B: Engineering*, *70*, 215–230. https://doi.org/10.1016/j.compositesb.2014.10.056

Cohen, Z., & Peled, A. (2010). Controlled telescopic reinforcement system of fabric–cement composites — Durability concerns. *Cement and Concrete Research*, *40*(10), 1495–1506. https://doi.org/10.1016/J.CEMCONRES.2010.06.003

Dalalbashi, A., Ghiassi, B., & Oliveira, D. V. (2021). Textile-to-mortar bond behavior: An analytical study. *Construction and Building Materials*, *282*(February), 122639. https://doi.org/10.1016/j.conbuildmat.2021.122639

Dalalbashi, A., Ghiassi, B., Oliveira, D. V., & Freitas, A. (2018). Fiber-to-mortar bond behavior in TRM composites: Effect of embedded length and fiber configuration. *Composites Part B: Engineering*, *152*(March), 43–57. https://doi.org/10.1016/j.compositesb.2018.06.014

De Santis, S., Hadad, H. A., De Caso y Basalo, F., de Felice, G., & Nanni, A. (2018a). Acceptance Criteria for Tensile Characterization of Fabric-Reinforced Cementitious Matrix Systems for Concrete and Masonry Repair.

Journal of Composites for Construction, *22*(6), 1–14. https://doi.org/10.1061/(asce)cc.1943-5614.0000886

De Santis, S., Hadad, H. A., De Caso y Basalo, F., de Felice, G., & Nanni, A. (2018b). Acceptance Criteria for Tensile Characterization of Fabric-Reinforced Cementitious Matrix Systems for Concrete and Masonry Repair. *Journal of Composites for Construction*, *22*(6), 04018048. https://doi.org/10.1061/(ASCE)CC.1943-5614.0000886/ASSET/70D0E9B9-8072-42E2-8CC3-00E01BC1C385/ASSETS/IMAGES/LARGE/FIGURE11.JPG

Erdil, B., Akyuz, U., & Yaman, I. O. (2012). Mechanical behavior of CFRP confined low strength concretes subjected to simultaneous heating-cooling cycles and sustained loading. *Materials and Structures/Materiaux et Constructions*, *45*(1–2), 223–233. https://doi.org/10.1617/s11527-011-9761-6

Esmaeili, J., Sharifi, I., Kasaei, J., Nourizadeh, M., & Ebrahimi Emamieh, A. (2019). Experimental and analytical investigation on strengthening of heat damaged concrete by textile reinforced concrete (TRC). *Archives of Civil and Mechanical Engineering*, *19*(4), 1468–1483. https://doi.org/10.1016/j.acme.2019.09.008

Forth, J. P. (2015). Predicting the tensile creep of concrete. *Cement and Concrete Composites*, *55*, 70–80. https://doi.org/10.1016/j.cemconcomp.2014.07.010

Friese, D., Scheurer, M., Hahn, L., Gries, T., & Cherif, C. (2022). Textile reinforcement structures for concrete construction applications—a review. *Journal of Composite Materials*, *56*(26), 4041–4064. https://doi.org/10.1177/00219983221127181

Hahn, L., Rittner, S., Nuss, D., Ashir, M., & Cherif, C. (2019). Development of methods to improve the mechanical performance of coated grid-like non-crimp fabrics for construction applications. *Fibres and Textiles in Eastern Europe*, *27*(1), 51–58. https://doi.org/10.5604/01.3001.0012.7508

Heins, K., Lesker, S., Pütz, J., Hüntemann, M., & Gries, T. (2023). Effect of thermoplastic impregnation on the mechanical behaviour of textile reinforcement for concrete. *SN Applied Sciences*, *5*(3). https://doi.org/10.1007/s42452-023-05305-y

Jon M. Rouse, & Sarah L. Billington. (2007). Creep and Shrinkage of High-PerformanceFiber-Reinforced Cementitious Composites. *ACI Materials Journal*, *104*(2), 129–136.

Kapsalis, P., Tysmans, T., Van Hemelrijck, D., & Triantafillou, T. (2021). State-of-the-art review on experimental investigations of textile-reinforced concrete exposed to high temperatures. *Journal of Composites Science*, *5*(11). https://doi.org/10.3390/jcs5110290

Keskin, S. B. (2012a). *Dimensional Stability of Engineered Cementitious Composites*. *September*, 165. http://etd.lib.metu.edu.tr/upload/12614713/index.pdf

Keskin, S. B. (2012b). *DIMENSIONAL STABILITY OF ENGINEERED CEMENTITIOUS COMPOSITES A THESIS SUBMITTED TO THE GRADUATE SCHOOL OF NATURAL AND APPLIED SCIENCES OF MIDDLE EAST TECHNICAL UNIVERSITY IN PARTIAL FULFILLMENT OF THE REQUIREMENTS FOR THE DEGREE OF DOCTOR OF PHILOSOPHY IN* .

Kim, S. G., Park, Y. S., & Lee, Y. H. (2019). Comparison of concrete creep in compression, tension, and bending under drying condition. *Materials*, *12*(20). https://doi.org/10.3390/ma12203357

Li, V. C., & Li, V. C. (2019). Introduction to Engineered Cementitious Composites (ECC). In *Engineered Cementitious Composites (ECC)* (pp. 1–10). Springer Berlin Heidelberg. https://doi.org/10.1007/978-3-662-58438-5_1

Mader, E., Plonka, R., Schiekel, M., & Hempel, R. (2004). Coatings on Alkali-Resistant Glass Fibres for the Improvement of Concrete. *Journal of Industrial*

Textiles, *33*(3), 191–207. https://doi.org/10.1177/1528083704039833

Mattarollo, G., Randl, N., & Pauletta, M. (2023). Investigation of the Failure Modes of Textile-Reinforced Concrete and Fiber/Textile-Reinforced Concrete under Uniaxial Tensile Tests. *Materials*, *16*(5), 1999. https://doi.org/10.3390/ma16051999

Mechtcherine, V. (2016). Durability of Structures Made of or Strengthened Using Textile-Reinforced Concrete. In *Textile Fibre Composites in Civil Engineering*. Elsevier Ltd. https://doi.org/10.1016/B978-1-78242-446-8.00007-0

Mechtcherine, V., Schneider, K., & Brameshuber, W. (2016). Mineral-based matrices for textile-reinforced concrete. In *Textile fibre composites in civil engineering*. Elsevier Ltd. https://doi.org/10.1016/B978-1-78242-446-8.00003-3

Naaman, A. E., & Shah, S. P. (1976). Pull-Out Mechanism in Steel Fiber-Reinforced Concrete. *Journal of the Structural Division*, *102*(8), 1537–1548. https://doi.org/10.1061/JSDEAG.0004409

Nivetha, R., Vennila, A., & Dharshini, B. (2023). A review on various properties of textile reinforced concrete. *Materials Today: Proceedings*. https://doi.org/10.1016/J.MATPR.2023.05.430

Peled, A. (2016). Bonds in Textile-Reinforced Concrete Composites. *Textile Fibre Composites in Civil Engineering*, 63–99. https://doi.org/10.1016/B978-1-78242-446-8.00005-7

Peled, Alva, & Bentur, A. (2003). Quantitative Description of the Pull-Out Behavior of Crimped Yarns from Cement Matrix. *Journal of Materials in Civil Engineering*, *15*(6), 537–544. https://doi.org/10.1061/(asce)0899-1561(2003)15:6(537)

Peled, Alva, Mobasher, B., & Bentur, A. (2017). Textile reinforced concrete. In

Textile Reinforced Concrete. https://doi.org/10.1201/9781315119151

Peled, Alva, Sueki, S., & Mobasher, B. (2006). Bonding in fabric-cement systems: Effects of fabrication methods. *Cement and Concrete Research*, *36*(9), 1661–1671. https://doi.org/10.1016/j.cemconres.2006.05.009

Peled, Alva, Zaguri, E., & Marom, G. (2008). Bonding characteristics of multifilament polymer yarns and cement matrices. *Composites Part A: Applied Science and Manufacturing*, *39*(6), 930–939. https://doi.org/10.1016/j.compositesa.2008.03.012

Poston, R. W., Kesner, K., McDonald, J. E., Vaysburd, A. M., & Emmons, P. H. (2001). Concrete repair material performance - Laboratory study. *ACI Materials Journal*, *98*(2), 137–147. https://doi.org/10.14359/10197

Preinstorfer, P., El, M., Gözdem, K., Bahman, D., Müller, S., Mansur, R., Silva, D. C., Mobasher, B., Andrade, F. De, & Alva, S. (2024). Article of RILEM TC 292 - MCC : bond behaviour of textile - reinforced concrete — a review. *Materials and Structures*. https://doi.org/10.1617/s11527-024-02339-5

Preinstorfer, P., & Kollegger, J. (2020). New insights into the splitting failure of textile-reinforced concrete. *Composite Structures*, *243*(February), 112203. https://doi.org/10.1016/j.compstruct.2020.112203

Ranaivomanana, N., Multon, S., & Turatsinze, A. (2012). Comparative study of compressive and tensile basic creep behavior of concrete. *Brittle Matrix Composites 10, BMC 2010*, 243–252. https://doi.org/10.1533/9780857099891.243

Rawat, P., Liu, S., Guo, S., Zillur Rahman, M., Yang, T., Bai, X., Yao, Y., Mobasher, B., & Zhu, D. (2022). A state-of-the-art review on mechanical performance characterization and modelling of high-performance textile reinforced concretes. *Construction and Building Materials*, *347*, 128521. https://doi.org/10.1016/J.CONBUILDMAT.2022.128521

Rezig, N., Bellahcene, T., Aberkane, M., & Nait Abdelaziz, M. (2020). Thermo-oxidative ageing of a SBR rubber: effects on mechanical and chemical properties. *Journal of Polymer Research*, *27*(11), 1–13. https://doi.org/10.1007/s10965-020-02330-y

RILEM Technical Committee 232-TDT (Wolfgang Brameshuber), Brameshuber, W., Hinzen, M., Dubey, A., Peled, A., Mobasher, B., Bentur, A., Aldea, C., Silva, F., Hegger, J., Gries, T., Wastiels, J., Malaga, K., Papanicolaou, C., Taerwe, L., Curbach, M., Mechtcherine, V., Naaman, A., Orlowsky, J., … Jesse, F. (2016). Recommendation of RILEM TC 232-TDT: test methods and design of textile reinforced concrete: Uniaxial tensile test: test method to determine the load bearing behavior of tensile specimens made of textile reinforced concrete. *Materials and Structures/Materiaux et Constructions*, *49*(12), 4923–4927. https://doi.org/10.1617/s11527-016-0839-z

Santis, S. De, Hadad, H. A., Asce, S. M., De Caso Y Basalo, F., Asce, A. M., Gianmarco De Felice, ;, Nanni, A., & Asce, F. (2018). *Acceptance Criteria for Tensile Characterization of Fabric-Reinforced Cementitious Matrix Systems for Concrete and Masonry Repair*. https://doi.org/10.1061/(ASCE)CC.1943

Shannag, M. J., Brincker, R., & Hansen, W. (1997). Pullout behavior of steel fibers from cement-based composites. *Cement and Concrete Research*, *27*(6), 925–936. https://doi.org/10.1016/S0008-8846(97)00061-6

Soranakom, C., & Mobasher, B. (2009). Geometrical and mechanical aspects of fabric bonding and pullout in cement composites. *Materials and Structures/Materiaux et Constructions*, *42*(6), 765–777. https://doi.org/10.1617/s11527-008-9422-6

Steven H. Kosmatka, Beatrix Kerkhoff, and W. C. P., Kosmatka, S. H., Kerkhoff, B., & Panarese, W. C. (2002). *Design and Control Design and Control of*.

Tekle, B. H., Messerer, D., & Holschemacher, K. (2021). Bond induced concrete splitting failure in textile-reinforced fine-grained concrete. *Construction and*

Building Materials, *303*(June), 124503. https://doi.org/10.1016/j.conbuildmat.2021.124503

Tošić, N., Aidarov, S., & de la Fuente, A. (2020). Systematic Review on the Creep of Fiber-Reinforced Concrete. *Materials*, *13*(22), 5098. https://doi.org/10.3390/ma13225098

Truong, V. D., & Kim, D. J. (2021). A review paper on direct tensile behavior and test methods of textile reinforced cementitious composites. *Composite Structures*, *263*(February), 113661. https://doi.org/10.1016/j.compstruct.2021.113661

Venigalla, S. G., Nabilah, A. B., Nasir, N. A. M., Safiee, N. A., & Abd Aziz, F. N. A. (2022). Textile-Reinforced Concrete as a Structural Member: A Review. *Buildings 2022, Vol. 12, Page 474*, *12*(4), 474. https://doi.org/10.3390/BUILDINGS12040474

Ward, M. A., & Cook, D. J. (2015). The mechanism of tensile creep in concrete. *Https://Doi.Org/10.1680/Macr.1969.21.68.151*, *21*(68), 151–158. https://doi.org/10.1680/MACR.1969.21.68.151

Wen, C., Shen, D., Luo, Y., Wang, W., & Yao, P. (2023). Early-Age Cracking Potential of Fly Ash High Performance Concrete Internally Cured with Super Absorbent Polymers. *Journal of Testing and Evaluation*, *51*(4), 2422–2441. https://doi.org/10.1520/JTE20220421

Williams Portal, N., Fernandez Perez, I., Nyholm Thrane, L., & Lundgren, K. (2014). Pull-out of textile reinforcement in concrete. *Construction and Building Materials*, *71*, 63–71. https://doi.org/10.1016/j.conbuildmat.2014.08.014

Zhao, G., di Prisco, M., & Vandewalle, L. (2015). Experimental investigation on uniaxial tensile creep behavior of cracked steel fiber reinforced concrete. *Materials and Structures/Materiaux et Constructions*, *48*(10), 3173–3185. https://doi.org/10.1617/s11527-014-0389-1

Zhu, Z.-F., Wang, W.-W., Harries, K. A., & Zheng, Y.-Z. (2018). Uniaxial Tensile Stress–Strain Behavior of Carbon-Fiber Grid–Reinforced Engineered Cementitious Composites. *Journal of Composites for Construction*, *22*(6), 04018057. https://doi.org/10.1061/(asce)cc.1943-5614.0000891

). Textile reinforced concrete. In *Textile Reinforced Concrete*. https://doi.org/10.1201/9781315119151

Peled, A., Sueki, S., & Mobasher, B. (2006). Bonding in fabric-cement systems: Effects of fabrication methods. *Cement and Concrete Research*, *36*(9), 1661–1671. https://doi.org/10.1016/j.cemconres.2006.05.009

Peled, A., Zaguri, E., & Marom, G. (2008). Bonding characteristics of multifilament polymer yarns and cement matrices. *Composites Part A: Applied Science and Manufacturing*, *39*(6), 930–939. https://doi.org/10.1016/j.compositesa.2008.03.012

Penzel, P., May, M., Hahn, L., Scheerer, S., Michler, H., Butler, M., Waldmann, M., Curbach, M., Cherif, C., & Mechtcherine, V. (2022). Bond Modification of Carbon Rovings through Profiling. *Materials*, *15*(16). https://doi.org/10.3390/ma15165581

Preinstorfer, P., El, M., Gözdem, K., Bahman, D., Müller, S., Mansur, R., Silva, D. C., Mobasher, B., Andrade, F. De, & Alva, S. (2024). Article of RILEM TC 292 - MCC : bond behaviour of textile - reinforced concrete — a review. *Materials and Structures*. https://doi.org/10.1617/s11527-024-02339-5

Preinstorfer, P., & Kollegger, J. (2020). New insights into the splitting failure of textile-reinforced concrete. *Composite Structures*, *243*(February), 112203. https://doi.org/10.1016/j.compstruct.2020.112203

Quadflieg, T., Stolyarov, O., & Gries, T. (2017). Influence of the fabric construction parameters and roving type on the tensile property retention of high-performance rovings in warp-knitted reinforced fabrics and cement-based composites. *Journal of Industrial Textiles*, *47*(4), 453–471.

https://doi.org/10.1177/1528083716652831/ASSET/IMAGES/LARGE/10.1177_1528083716652831-FIG8.JPEG

Ricker, M., Rempel, S., Feiri, T., Schulze-Ardey, J., & Hegger, J. (2022). Statistical characterisation of reinforcement properties for textile-reinforced concrete: a novel approach. *Acta Polytechnica CTU Proceedings*, *36*, 175–184. https://doi.org/10.14311/APP.2022.36.0175

RILEM Technical Committee 232-TDT (Wolfgang Brameshuber), Brameshuber, W., Hinzen, M., Dubey, A., Peled, A., Mobasher, B., Bentur, A., Aldea, C., Silva, F., Hegger, J., Gries, T., Wastiels, J., Malaga, K., Papanicolaou, C., Taerwe, L., Curbach, M., Mechtcherine, V., Naaman, A., Orlowsky, J., … Jesse, F. (2016). Recommendation of RILEM TC 232-TDT: test methods and design of textile reinforced concrete: Uniaxial tensile test: test method to determine the load bearing behavior of tensile specimens made of textile reinforced concrete. *Materials and Structures/Materiaux et Constructions*, *49*(12), 4923–4927. https://doi.org/10.1617/s11527-016-0839-z

Silva, F. D. A., Butler, M., Hempel, S., Toledo Filho, R. D., & Mechtcherine, V. (2014). Effects of elevated temperatures on the interface properties of carbon textile-reinforced concrete. *Cement and Concrete Composites*, *48*, 26–34. https://doi.org/10.1016/J.CEMCONCOMP.2014.01.007

Spelter, A., Bergmann, S., Bielak, J., & Hegger, J. (2019). Long-Term Durability of Carbon-Reinforced Concrete: An Overview and Experimental Investigations. *Applied Sciences 2019, Vol. 9, Page 1651*, *9*(8), 1651. https://doi.org/10.3390/APP9081651

Steven H. Kosmatka, Beatrix Kerkhoff, and W. C. P., Kosmatka, S. H., Kerkhoff, B., & Panarese, W. C. (2002). *Design and Control Design and Control of*.

Tetta, Z. C., Koutas, L. N., & Bournas, D. A. (2015). Textile-reinforced mortar (TRM) versus fiber-reinforced polymers (FRP) in shear strengthening of

concrete beams. *Composites Part B: Engineering*, *77*, 338–348. https://doi.org/10.1016/j.compositesb.2015.03.055

Tietze, M., Kirmse, S., Kahnt, A., Schladitz, F., & Curbach, M. (2022). The ecological and economic advantages of carbon reinforced concrete—Using the C 3 result house CUBE especially the BOX value chain as an example . *Civil Engineering Design*, *4*(1–3), 79–88. https://doi.org/10.1002/cend.202200001

Tran, M. T., Vu, X. H., & Ferrier, E. (2021). Experimental and numerical investigation of carbon textile/cementitious matrix interfacebehaviourfrom pull-out tests. *Construction and Building Materials*, *282*, 122634. https://doi.org/10.1016/j.conbuildmat.2021.122634

Tran Manh, T., Do Ngoc, T., & Vu Xuan, H. (2021). A state-of-the art review of tensile behavior of the textile-reinforced concrete composite. In *Transport and Communications Science Journal* (Vol. 72, Issue 1, pp. 127–142). https://doi.org/10.47869/tcsj.72.1.14

Triantafillou, T. C. (2016). Textile Fibre Composites in Civil Engineering. In *Textile Fibre Composites in Civil Engineering*. Elsevier Inc. https://doi.org/10.1016/C2014-0-01415-3

Triantafillou, T. C., & Papanicolaou, C. G. (2006). Shear strengthening of reinforced concrete members with textile reinforced mortar (TRM) jackets. *Materials and Structures 2006 39:1*, *39*(1), 93–103. https://doi.org/10.1007/S11527-005-9034-3

Truong, B. T., Bui, T. T., Limam, A., Si Larbi, A., Le Nguyen, K., & Michel, M. (2017). Experimental investigations of reinforced concrete beams repaired/reinforced by TRC composites. *Composite Structures*, *168*, 826–839. https://doi.org/10.1016/J.COMPSTRUCT.2017.02.080

Truong, V. D., & Kim, D. J. (2021). A review paper on direct tensile behavior and test methods of textile reinforced cementitious composites. *Composite*

Structures, *263*(February), 113661. https://doi.org/10.1016/j.compstruct.2021.113661

Vakaliuk, I., Frenzel, M., & Curbach, M. (2022). *C 3 technology demonstration house : CUBE " from digital model to realis ation ." August 2021*.

Venigalla, S. G., Nabilah, A. B., Mohd Nasir, N. A., Safiee, N. A., & Abd Aziz, F. N. A. (2023). Experimental and numerical simulation of pull-out response in textile-reinforced concrete. *Structures*, *57*(September), 105132. https://doi.org/10.1016/j.istruc.2023.105132

Venigalla, S. G., Nabilah, A. B., Nasir, N. A. M., Safiee, N. A., & Abd Aziz, F. N. A. (2022a). Textile-Reinforced Concrete as a Structural Member: A Review. *Buildings 2022, Vol. 12, Page 474*, *12*(4), 474. https://doi.org/10.3390/BUILDINGS12040474

Venigalla, S. G., Nabilah, A. B., Nasir, N. A. M., Safiee, N. A., & Abd Aziz, F. N. A. (2022b). Textile-Reinforced Concrete as a Structural Member: A Review. *Buildings*, *12*(4). https://doi.org/10.3390/buildings12040474

Wei, L. L., Zhu, J. H., Ueda, T., Su, M. N., Liu, J., Liu, W., Tang, L. P., & Xing, F. (2020). Tensile behaviour of carbon fabric reinforced cementitious matrix composites as both strengthening and anode materials. *Composite Structures*, *234*, 111675. https://doi.org/10.1016/J.COMPSTRUCT.2019.111675

Williams, N., Fernandez, I., Nyholm, L., & Lundgren, K. (2014). Pull-out of textile reinforcement in concrete. *Construction and Building Materials*, *71*, 63–71. https://doi.org/10.1016/j.conbuildmat.2014.08.014

Williams Portal, N., Lundgren, K., Wallbaum, H., & Malaga, K. (2015). Sustainable Potential of Textile-Reinforced Concrete. *Journal of Materials in Civil Engineering*, *27*(7), 04014207. https://doi.org/10.1061/(asce)mt.1943-5533.0001160

Xu, S., Krüger, M., Reinhardt, H.-W., & Ožbolt, J. (2004). Bond Characteristics of Carbon, Alkali Resistant Glass, and Aramid Textiles in Mortar. *Journal of Materials in Civil Engineering*, *16*(4), 356–364. https://doi.org/10.1061/(asce)0899-1561(2004)16:4(356)

Yu, K., Li, L., Yu, J., Wang, Y., Ye, J., & Xu, Q. F. (2018). Direct tensile properties of engineered cementitious composites: A review. In *Construction and Building Materials* (Vol. 165, pp. 346–362). Elsevier Ltd. https://doi.org/10.1016/j.conbuildmat.2017.12.124

Zhang, M., & Deng, M. (2022). Tensile behavior of textile-reinforced composites made of highly ductile fiber-reinforced concrete and carbon textiles. *Journal of Building Engineering*, *57*(April), 104824. https://doi.org/10.1016/j.jobe.2022.104824

Zhu, M., Zhu, J. H., Ueda, T., Su, M., & Xing, F. (2020). A method for evaluating the bond behavior and anchorage length of embedded carbon yarn in the cementitious matrix. *Construction and Building Materials*, *255*, 119067. https://doi.org/10.1016/j.conbuildmat.2020.119067

6 APPENDIX-I

Pull-out Tests Results for M7 Mortar

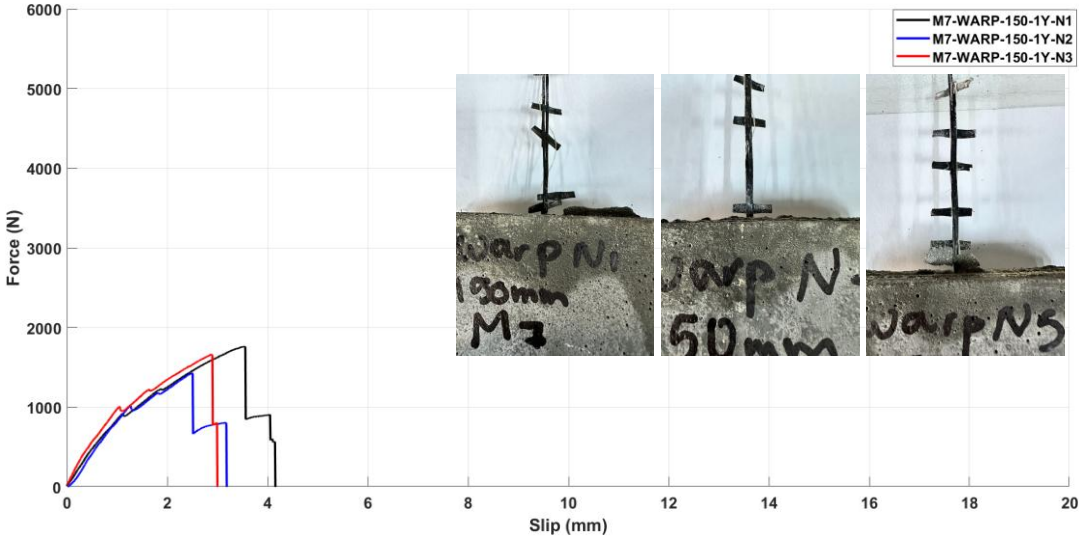

Figure 6-1 Load-slip curves for 1 yarn carbon textile tested in the warp direction with 150 mm embedment length into the M7 mortar

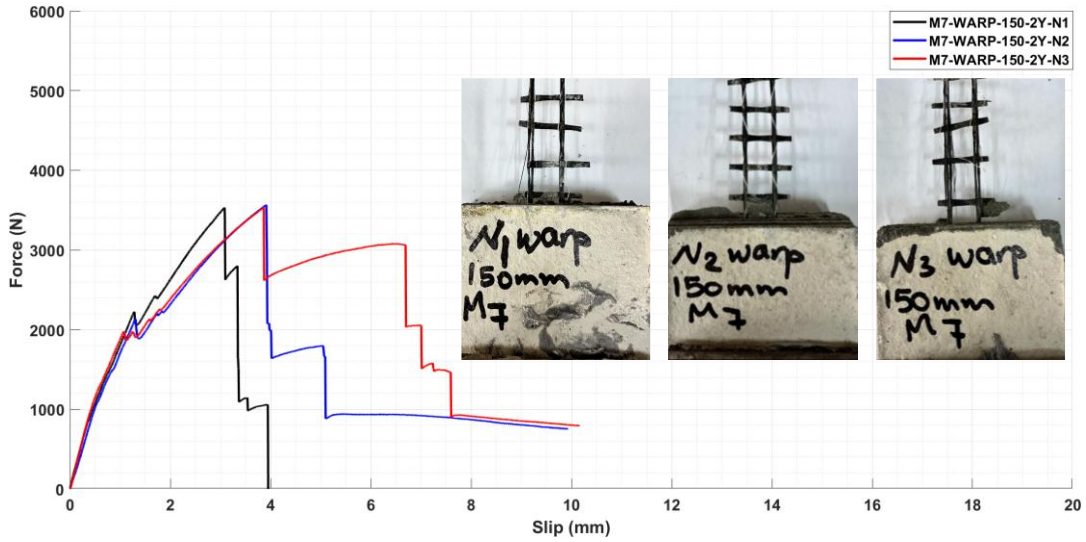

Figure 6-2 Load-slip curves for 2 yarn carbon textile tested in the warp direction with 150 mm embedment length into the M7 mortar

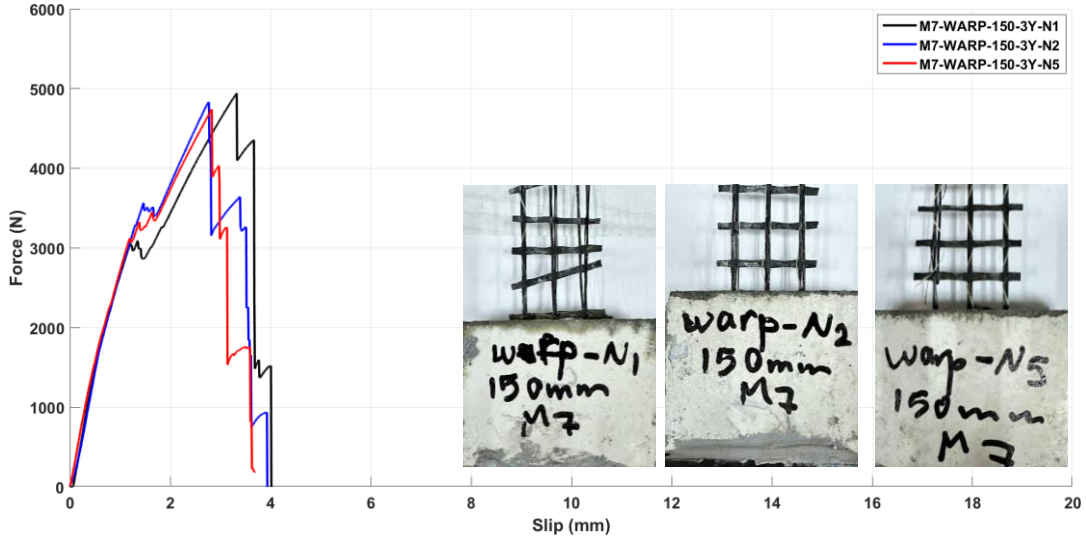

Figure 6-3Load-slip curves for 3 yarn carbon textile tested in the warp direction with 150 mm embedment length into the M7 mortar

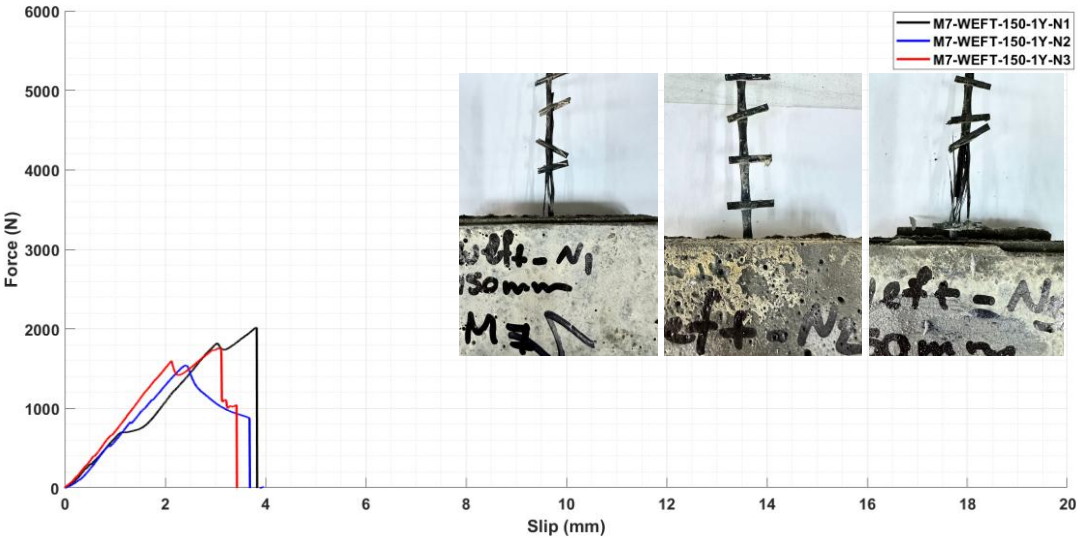

Figure 6-4 Load-slip curves for 1 yarn carbon textile tested in the weft direction with 150 mm embedment length into the M7 mortar

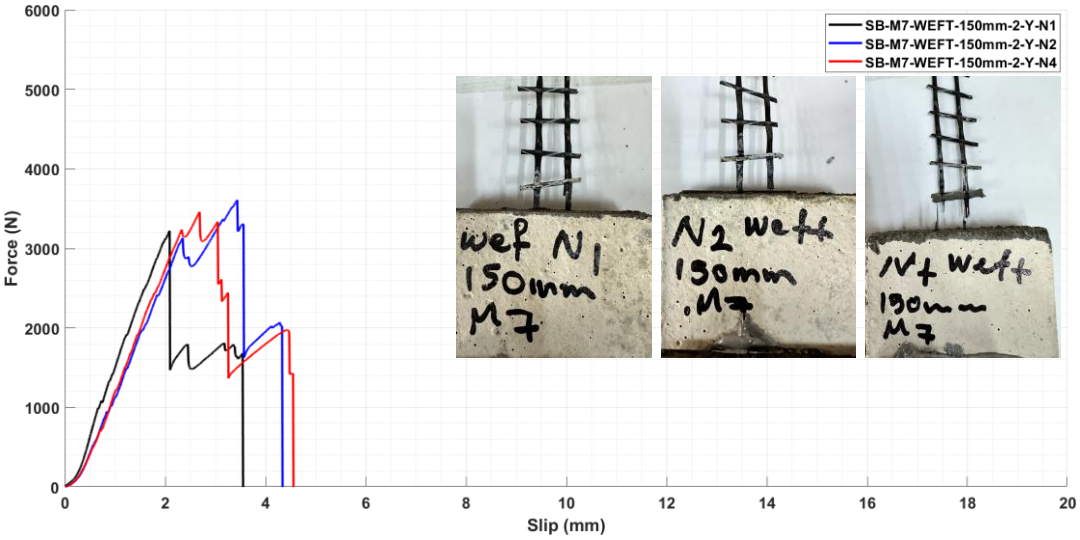

Figure 6-5 Load-slip curves for 2 yarn carbon textile tested in the weft direction with 150 mm embedment length into the M7 mortar

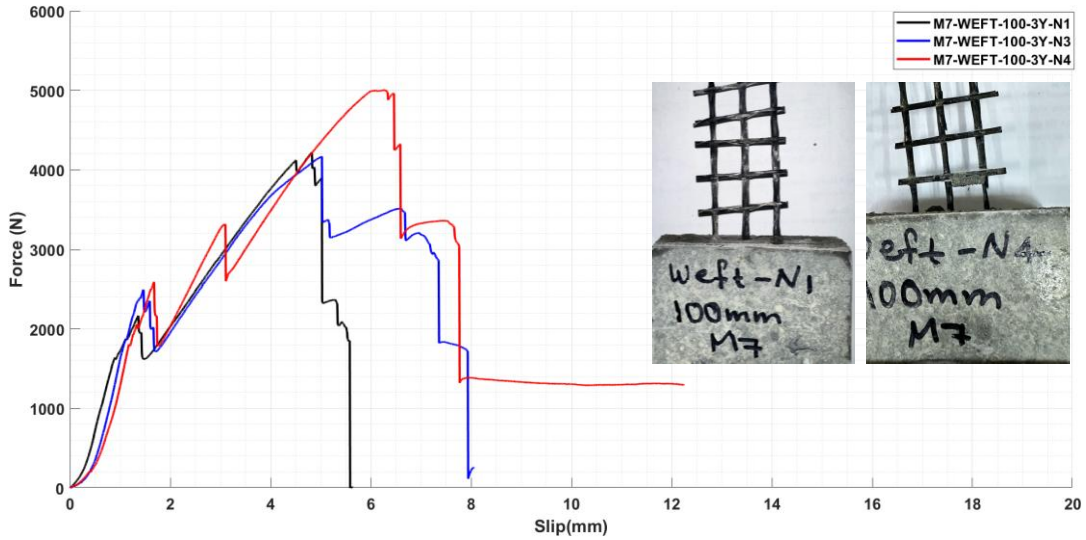

Figure 6-6 Load-slip curves for 3 yarn carbon textile tested in the weft direction with 150 mm embedment length into the M7 mortar

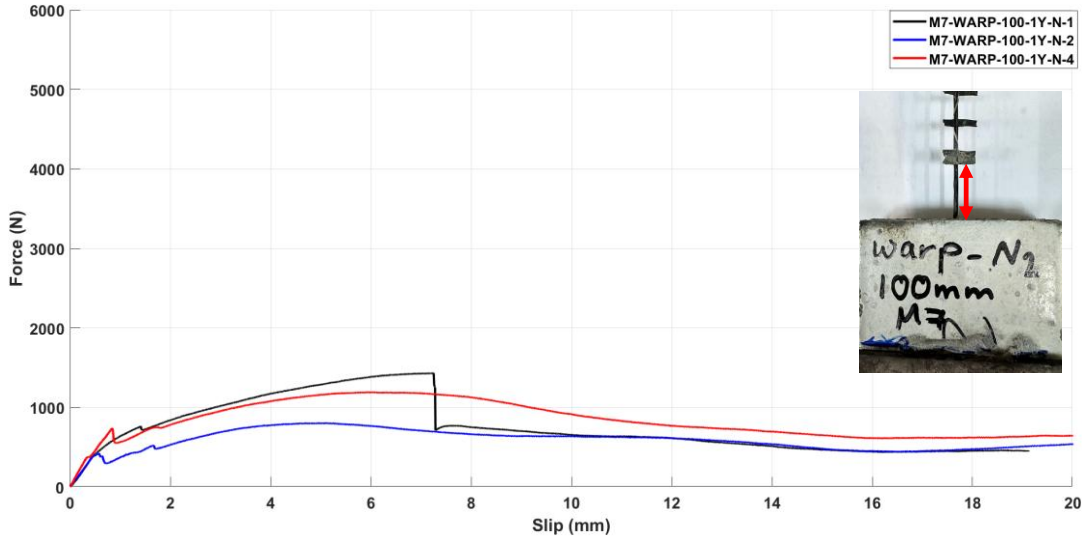

Figure 6-7 Load-slip curves for 1 yarn carbon textile tested in the warp direction with 100 mm embedment length into the M7 mortar

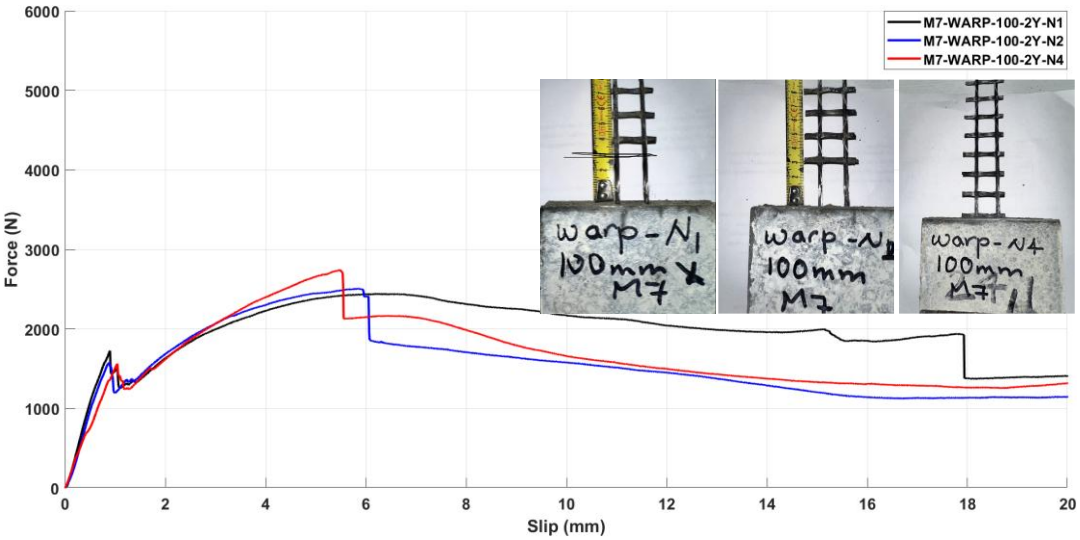

Figure 6-8 Load-slip curves for 2 yarn carbon textile tested in the warp direction with 100 mm embedment length into the M7 mortar

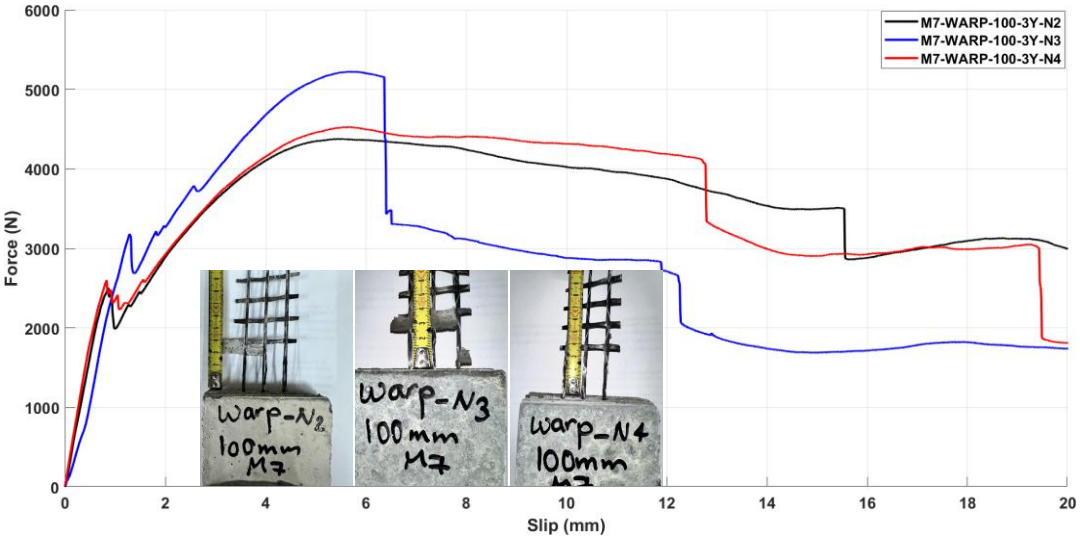

Figure 6-9 Load-slip curves for 3 yarn carbon textile tested in the warp direction with 100 mm embedment length into the M7 mortar

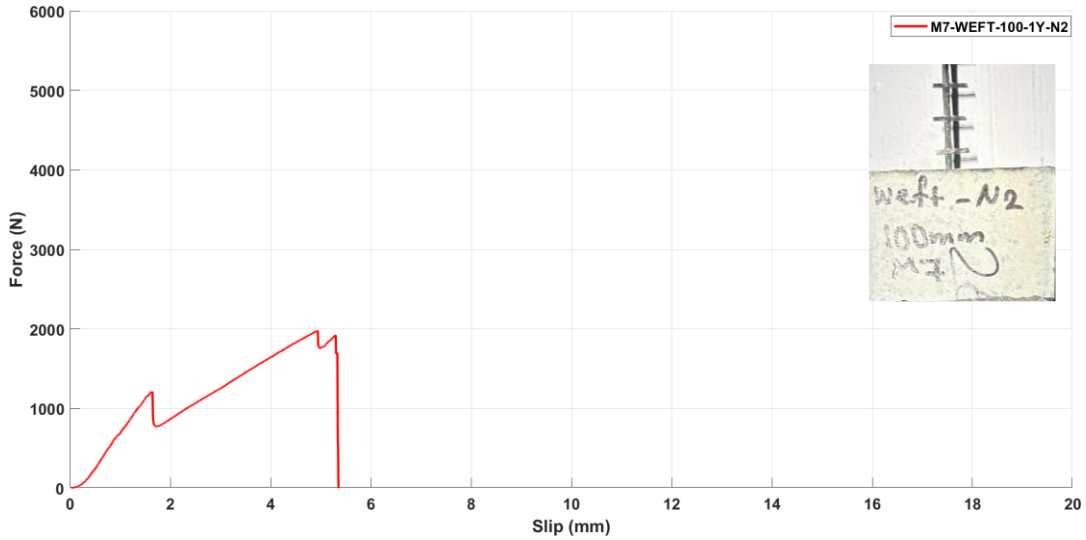

Figure 6-10 Load-slip curves for 1 yarn carbon textile tested in the weft direction with 100 mm embedment length into the M7 mortar

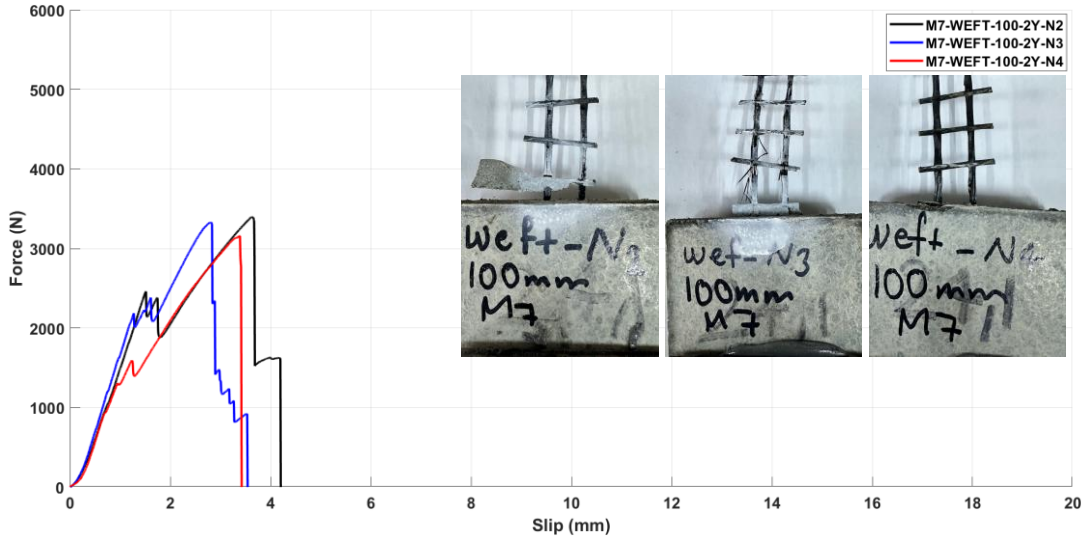

Figure 6-11 Load-slip curves for 2 yarn carbon textile tested in the weft direction with 100 mm embedment length into the M7 mortar

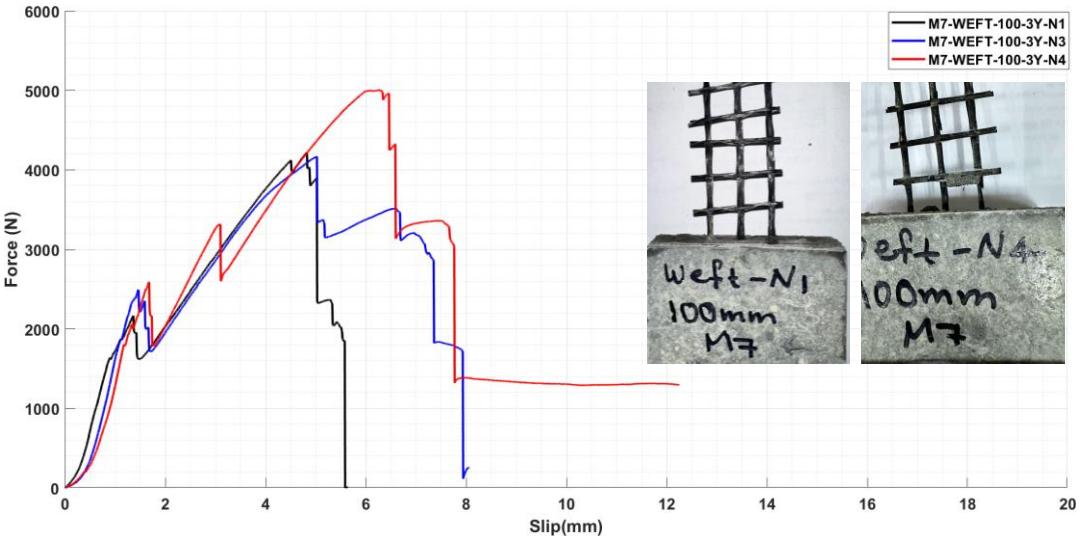

Figure 6-12 Load-slip curves for 3 yarn carbon textile tested in the weft direction with 100 mm embedment length into the M7 mortar

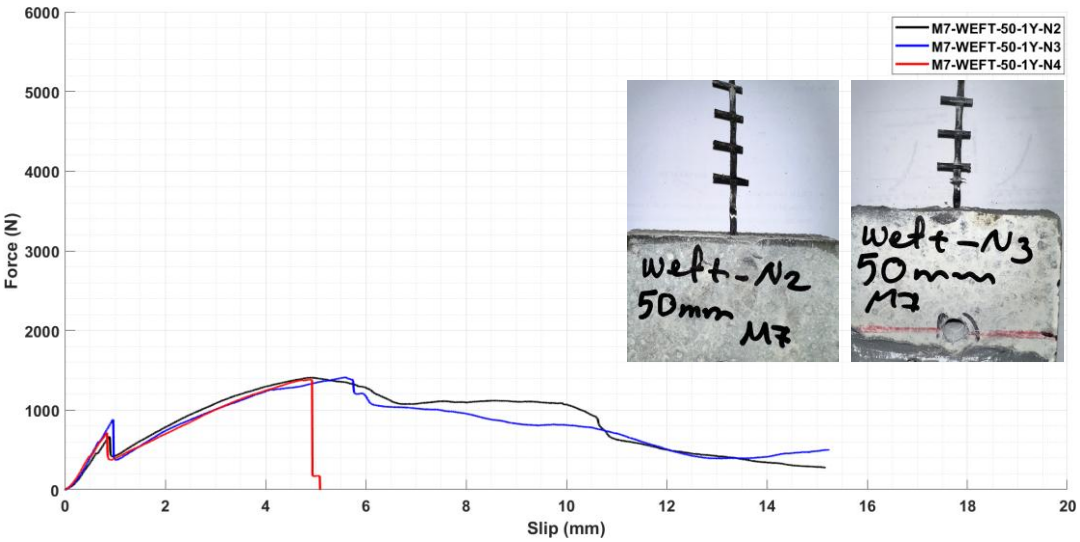

Figure 6-13 Load-slip curves for 1 yarn carbon textile tested in the weft direction with 50 mm embedment length into the M7 mortar

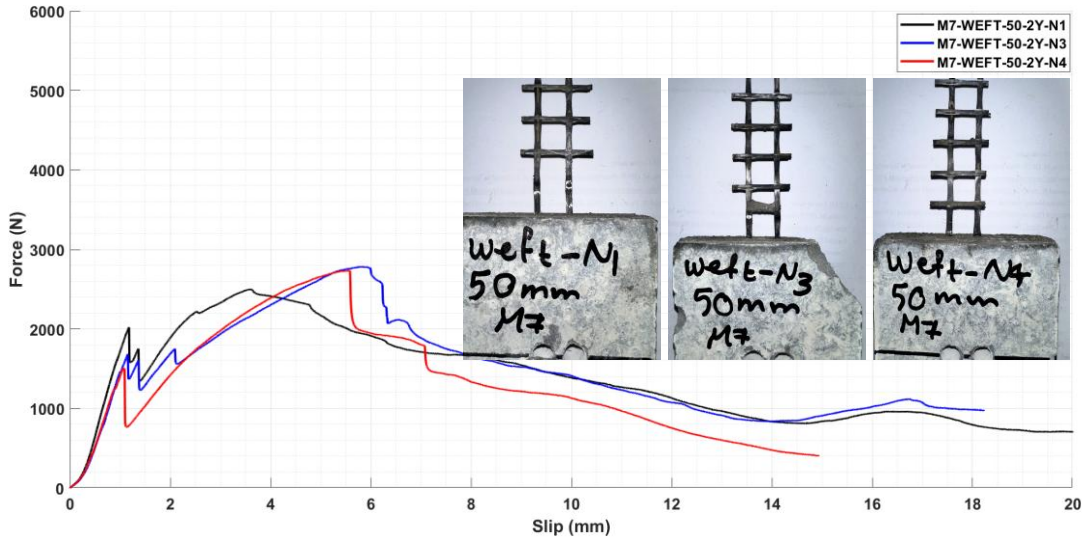

Figure 6-14 Load-slip curves for 2 yarn carbon textile tested in the weft direction with 50 mm embedment length into the M7 mortar

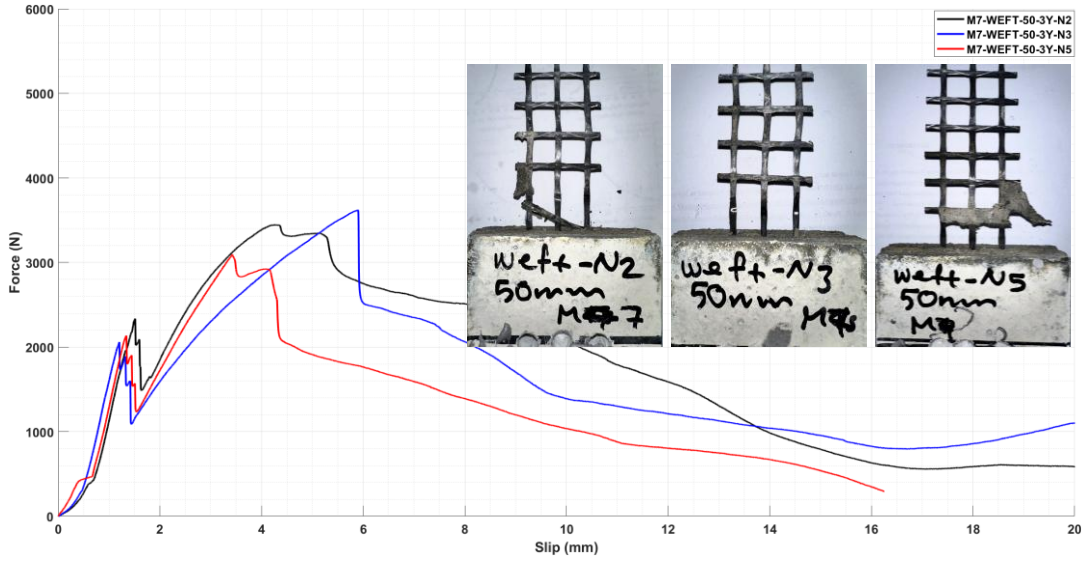

Figure 6-15 Load-slip curves for 3 yarn carbon textile tested in the weft direction with 50 mm embedment length into the M7 mortar

7 APPENDIX – II

Pull-out Tests Results for M45 Mortar

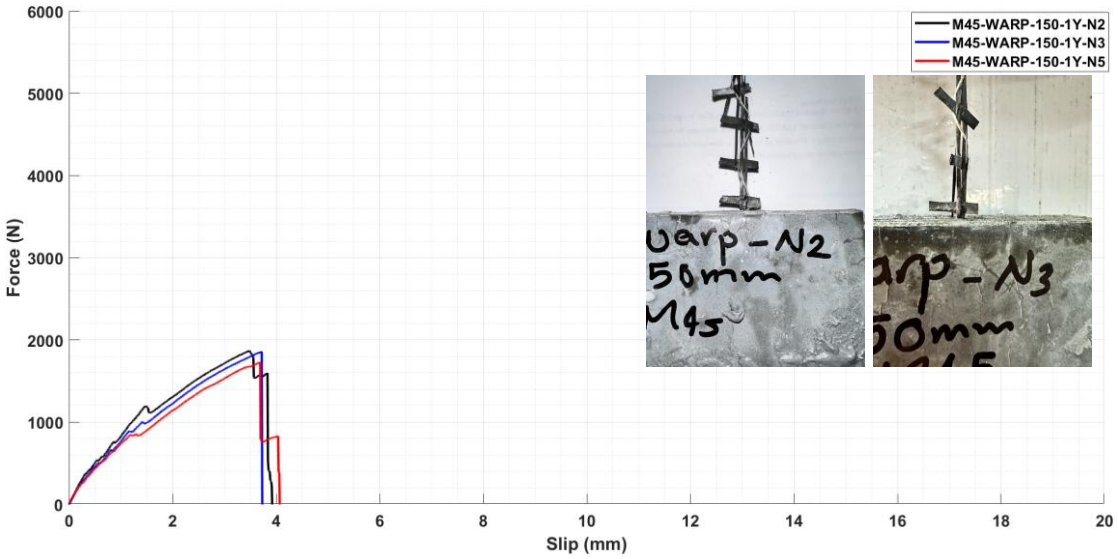

Figure 7-1 Load-slip curves for 1 yarn carbon textile tested in the warp direction with 150 mm embedment length into the M45 mortar

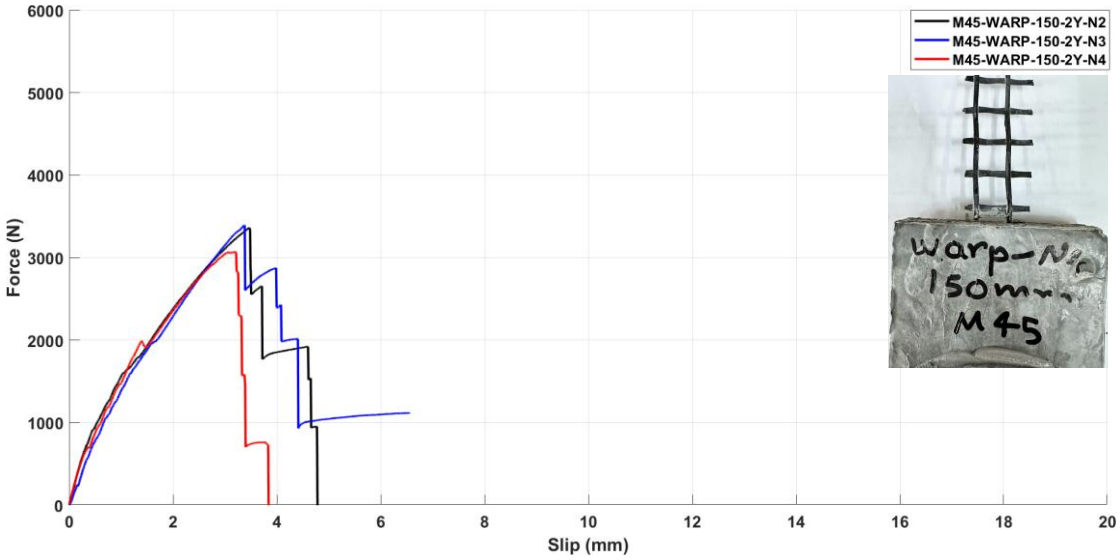

Figure 7-2 Load-slip curves for 2 yarn carbon textile tested in the warp direction with 150 mm embedment length into the M45 mortar

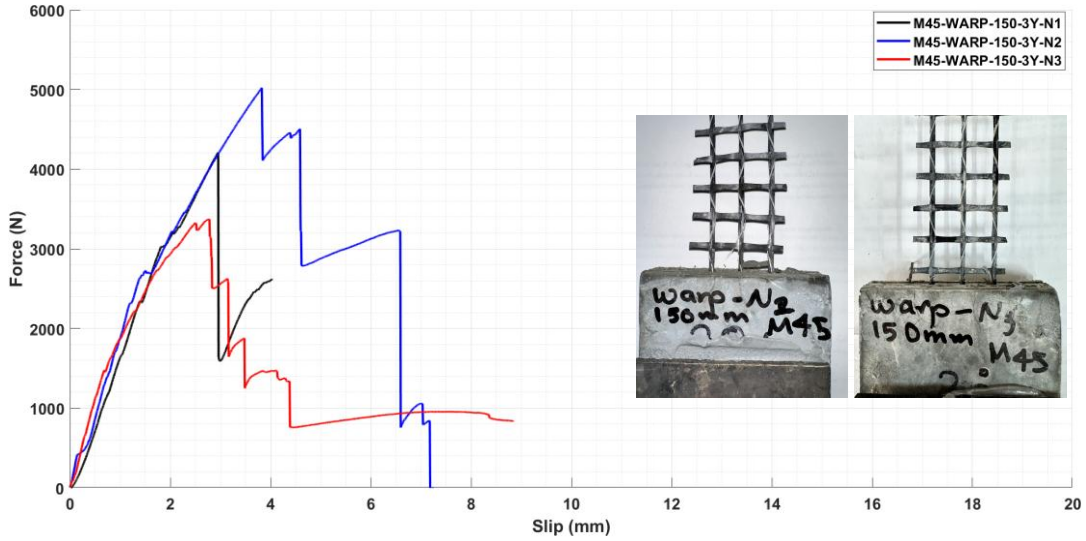

Figure 7-3 Load-slip curves for 3 yarn carbon textile tested in the warp direction with 50 mm embedment length into the M45 mortar

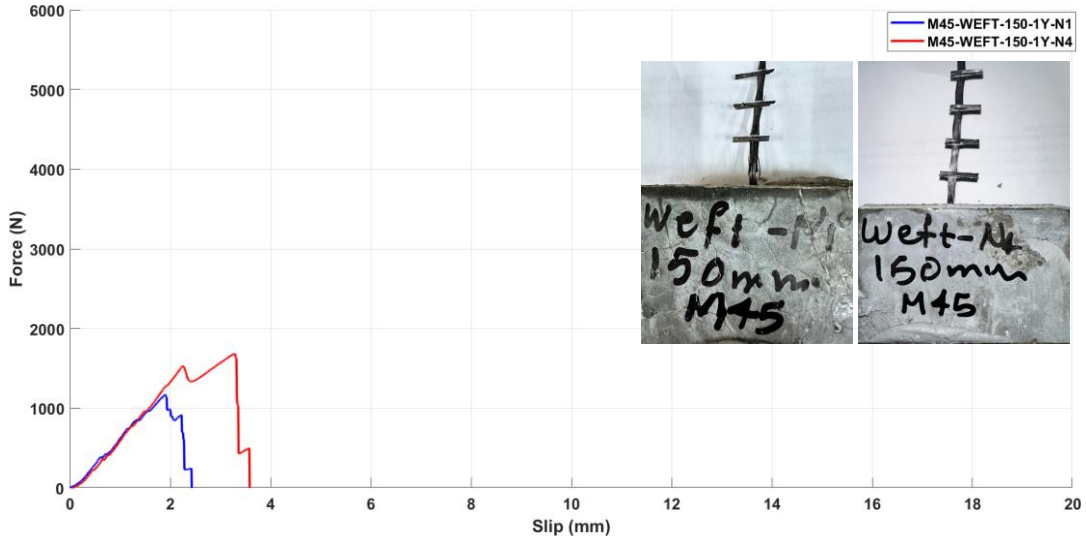

Figure 7-4 Load-slip curves for 1 yarn carbon textile tested in the weft direction with 150 mm embedment length into the M45 mortar

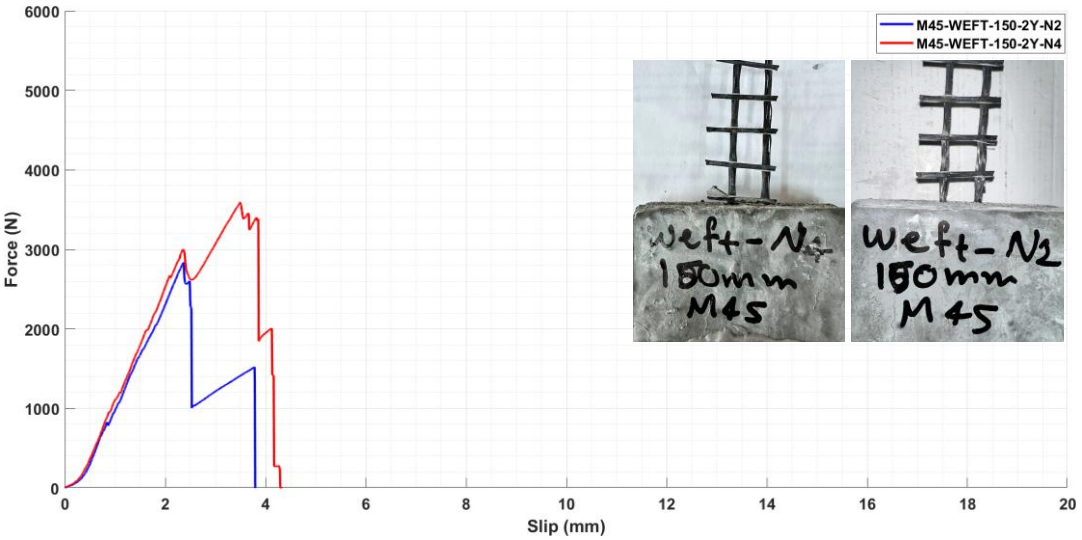

Figure 7-5 Load-slip curves for 2 yarn carbon textile tested in the weft direction with 150 mm embedment length into the M45 mortar

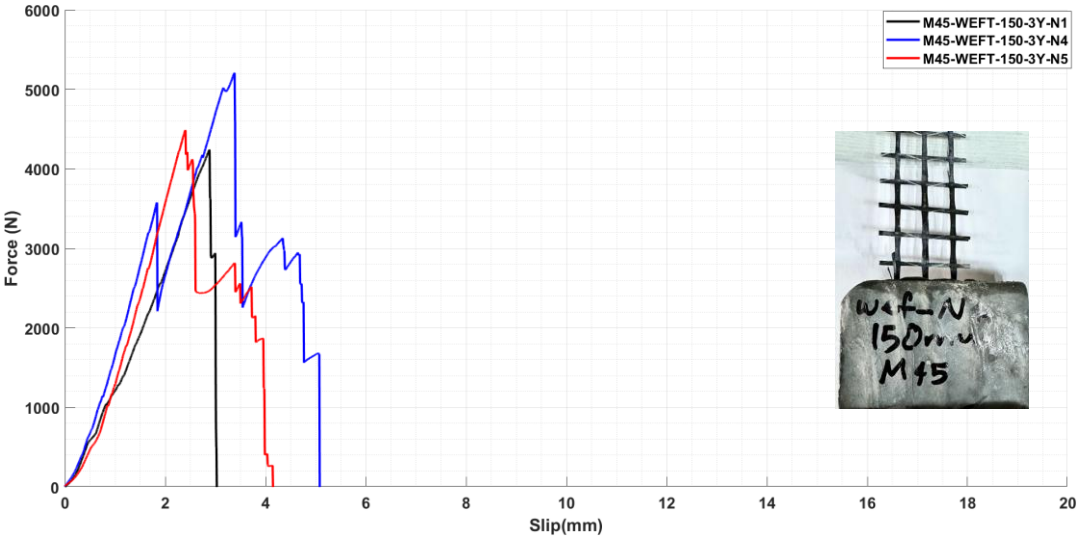

Figure 7-6 Load-slip curves for 3 yarn carbon textile tested in the weft direction with 150 mm embedment length into the M45 mortar

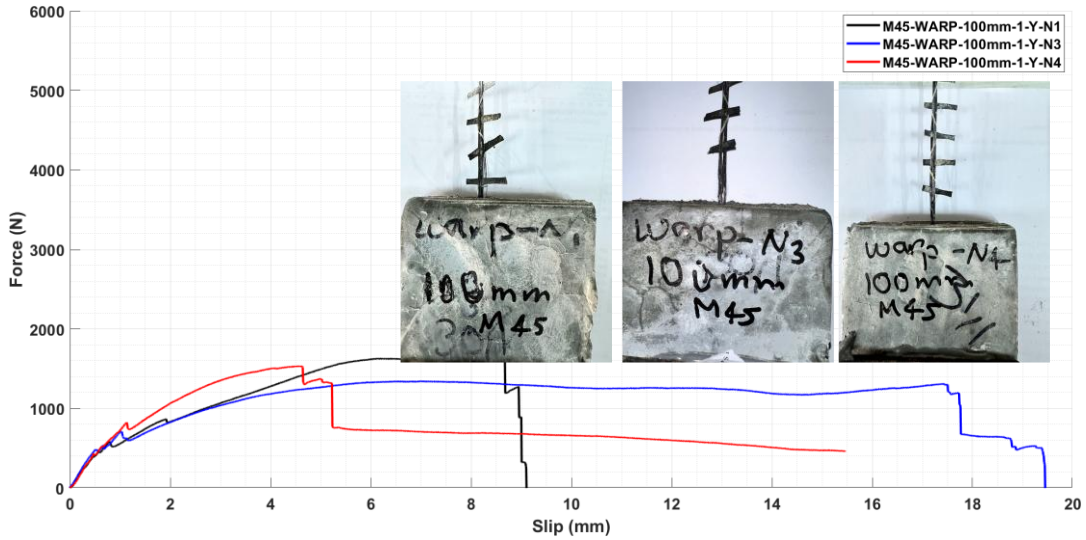

Figure 7-7 Load-slip curves for 1 yarn carbon textile tested in the warp direction with 100 mm embedment length into the M45 mortar

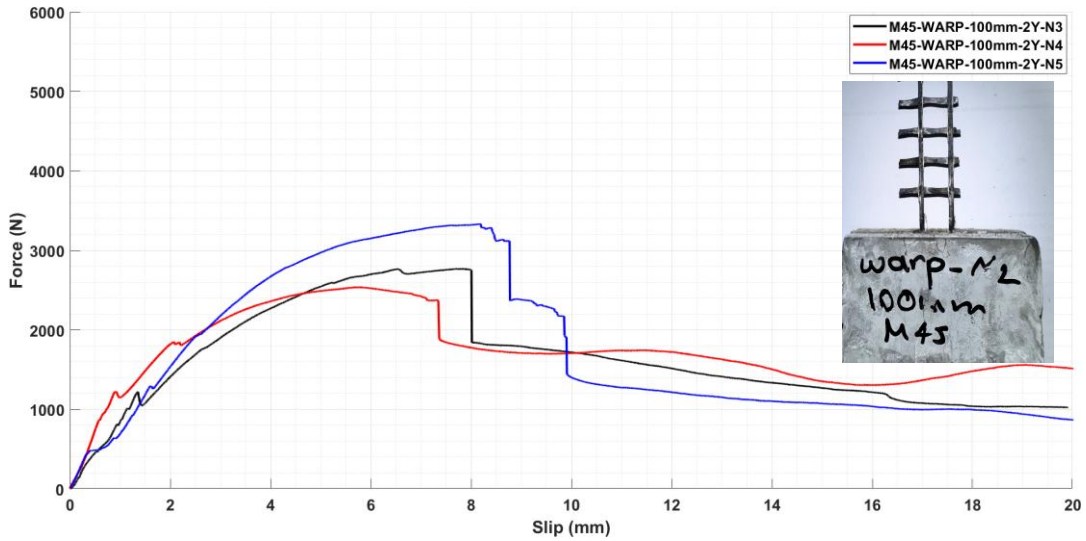

Figure 7-8 Load-slip curves for 2 yarn carbon textile tested in the warp direction with 100 mm embedment length into the M45 mortar

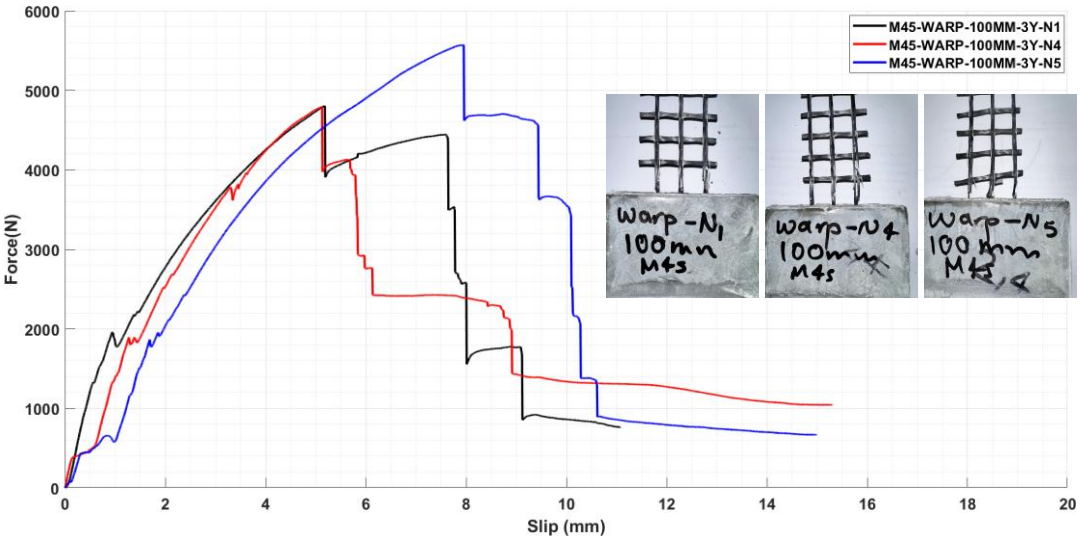

Figure 7-9 Load-slip curves for 3 yarn carbon textile tested in the warp direction with 100 mm embedment length into the M45 mortar

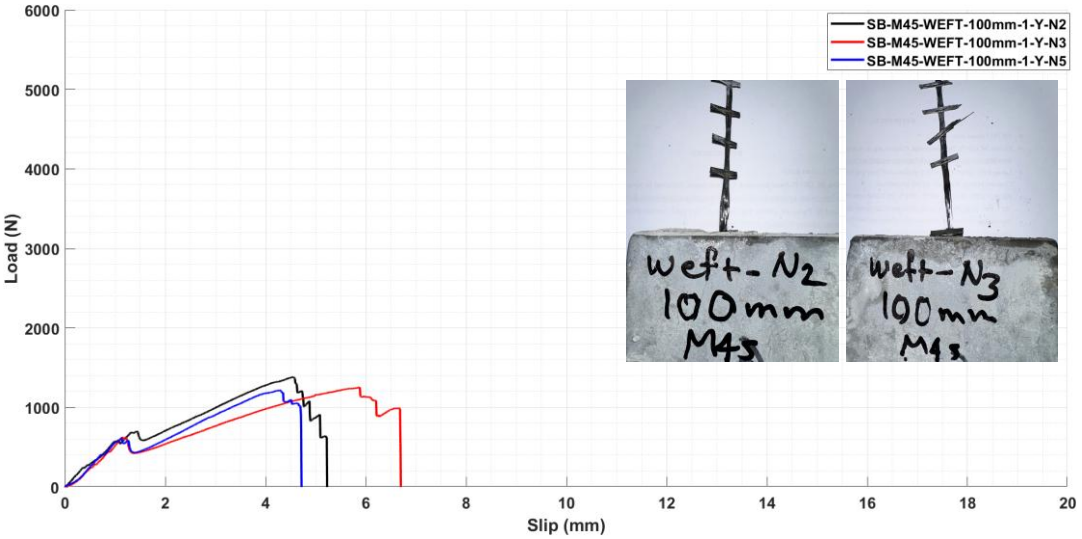

Figure 7-10 Load-slip curves for 1 yarn carbon textile tested in the weft direction with 100 mm embedment length into the M45 mortar

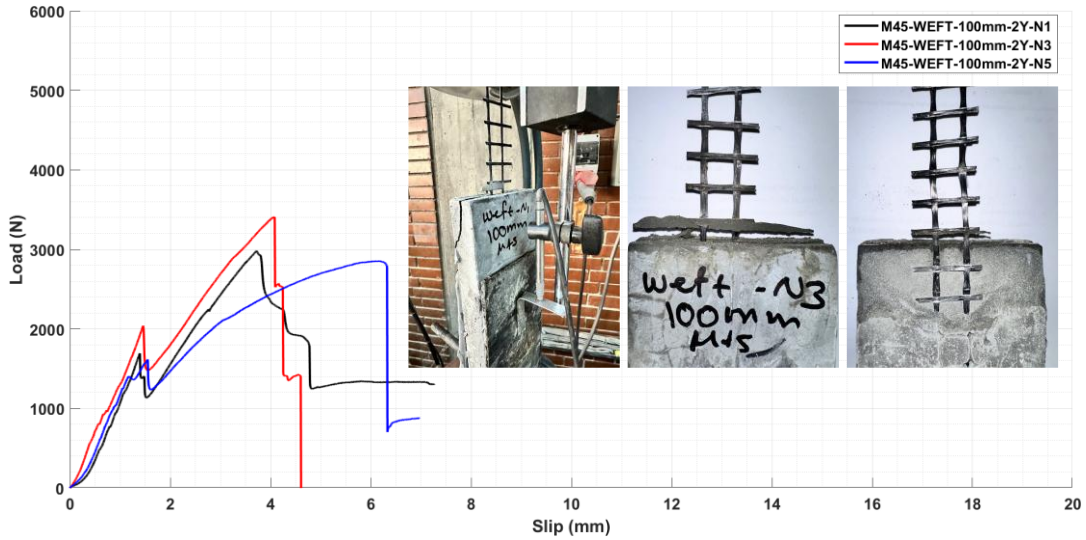

Figure 7-11 Load-slip curves for 2 yarn carbon textile tested in the weft direction with 100 mm embedment length

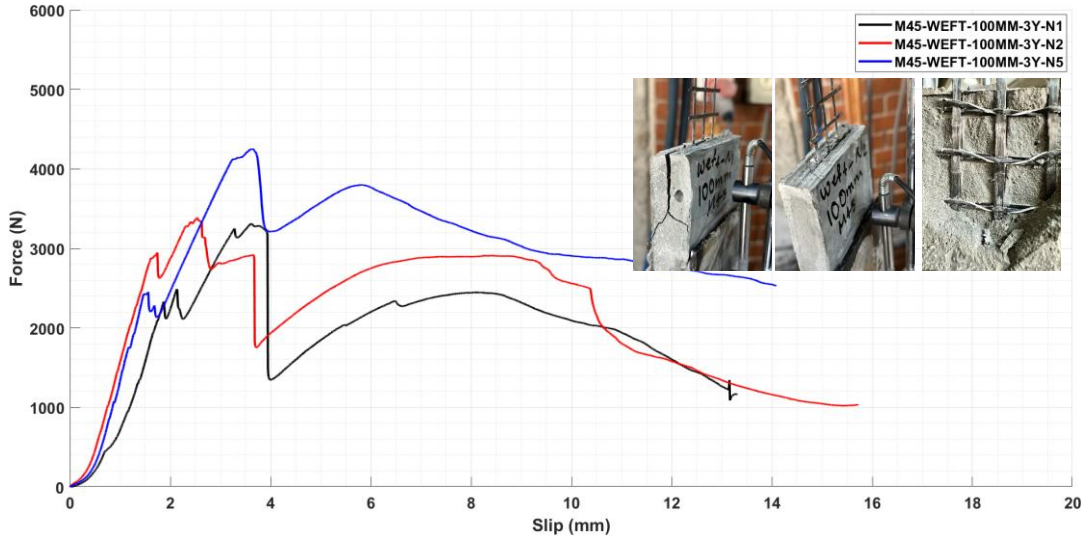

Figure 7-12 Load-slip curves for 3 yarn carbon textile tested in the weft direction with 100 mm embedment length

CURRICULUM VITAE (ONLY FOR DOCTORAL THESIS)

Surname, Name: Sharifi, Iraj

EDUCATION

Degree	Institution	Year of Graduation
MS	University of Tabriz Structural Engineering/Iran	2018
BS	Urima University Civil Engineering	2012
High School	Imam Jazar Sadiq/Iran	2006

FOREIGN LANGUAGES

Advanced English, Fluent Persian, Fluent Azerbayjani

PUBLICATIONS

1. Esmaeili, J., Sharifi, I., Andalibi, K., & Kasaei, J. (2017, September). Effect of different matrix compositions and micro steel fibers on tensile behavior of textile reinforced concrete. In IOP Conference Series: Materials Science and Engineering (Vol. 246, No. 1, p. 012031). IOP Publishing.

2. Esmaeili, J., Sharifi, I., Kasaei, J., Nourizadeh, M., & Ebrahimi Emamieh, A. (2019). Experimental and analytical investigation on strengthening of heat damaged concrete by textile reinforced concrete (TRC). Archives of Civil and Mechanical Engineering, 19, 1468-1483.)

3.Sharifi, I., Sherzai, M., Javanmard, A., Yalçındağ, F., & Yaman, İ. Ö. (Under review). Uniaxial tensile performance in the warp and weft directions of carbon textile-reinforced concretes with two different matrices. *Construction and Building Materials*.